

UCLA

UCLA Electronic Theses and Dissertations

Title

Solution Phase Routes to Functional Nanostructured Materials for Energy Applications

Permalink

<https://escholarship.org/uc/item/6vh6f6nd>

Author

Rauda, Iris Ester

Publication Date

2012

Peer reviewed|Thesis/dissertation

UNIVERSITY OF CALIFORNIA

Los Angeles

**Solution Phase Routes to Functional Nanostructured Materials
for Energy Applications**

A dissertation submitted in partial satisfaction of the
requirements for the degree Doctor of Philosophy
in Chemistry

by

Iris Ester Rauda

2012

ABSTRACT OF THE DISSERTATION

Solution Phase Routes to Functional Nanostructured Materials for Energy Applications

by

Iris Ester Rauda

Doctor of Philosophy in Chemistry

University of California, Los Angeles, 2012

Professor Sarah H. Tolbert, Chair

Solution-phase processing presents an attractive avenue for building unique architectures from a wide variety of materials that exhibit functional properties, making them ideal candidates for various energy applications. The most basic building block or precursor in solution-based syntheses is a soluble species that can either self-assemble, or coassemble with a structure directing agent or template, to create a unique architecture. Soluble inorganic-based building blocks ranging from atomic-scale charged molecular complexes to nanometer-scale preformed nanocrystals are utilized to construct functional inorganic materials. These nanostructured materials are excellent candidates for integrating into electronic and energy-storage devices, including photovoltaics and pseudocapacitors.

The goal of this work is to create inorganic nanostructured materials from solution-based methods. This work is divided into two parts: the first involves the

synthesis of inorganic semiconductor-based nanostructured materials; the second focuses on developing porous metal oxide-based pseudocapacitors.

The first part describes three distinct synthetic approaches to nanostructured semiconductors: the synthesis of complex metal chalcogenide semiconductors produced from highly soluble hydrazinium-based precursors using a porous template; low-temperature melt processing of an organic-inorganic hybrid semiconductor into porous templates to produce vertically-aligned arrays with a concentric multilayered structure; and solution-phase assembly of semiconductor nanocrystals of CdSe into nanoporous architectures via polymer templating. These nanostructured semiconductors are electrically interconnected through intimate contact between the molecular or nanoscale precursors achieved during solution-phase synthesis, making them suitable for a range of applications.

In the second part, porous metal-oxide based materials are constructed by the assembly of nanosized building blocks into 3D porous architectures via polymer templating. Two main approaches are described: first, a general route for templating both redox-active oxides (Mn_3O_4 , MnFe_2O_4) and conducting indium tin oxide (ITO) nanocrystals is described; second, nanocrystal-based porous architectures of a ITO are coated with redox-active V_2O_5 via atomic layer deposition to produce nanoporous composites. The porous architectures exhibit high surface areas, providing ample redox active sites, and an interconnected open porosity, facilitating solvent/ion diffusion to those sites. In the ITO- V_2O_5 composites, the electron-transfer reactions are facilitated by the increased conductivity leading to high pseudocapacitive contributions to charge storage that are accompanied by fast charging/discharging rates.

The dissertation of Iris Ester Rauda is approved.

Jane P. Chang

Richard B. Kaner

Sarah H. Tolbert, Committee Chair

University of California, Los Angeles

2012

To my loving family
Para mi querida familia

TABLE OF CONTENTS

List of Figures.....	xii
List of Schemes.....	xxx
List of Tables.....	xxxi
Acknowledgments.....	xxxii
Vita.....	xxxviii
Publications and Selected Presentations.....	xxxix
 CHAPTER 1. Introduction.....	 1
1.1 References.....	9
 CHAPTER 2. Copper Indium Diselenide Nanotubes and Nanowires Produced From Highly Soluble Hydrazinium-Based Precursors and Nanoporous Templates.....	 12
2.1 Introduction.....	12
2.2 Results and Discussion.....	14
2.2.1 Synthesis and Characterization of CuInSe ₂ Nanostructures.....	14
2.2.2 Conductivity Measurements.....	21
2.3 Conclusions.....	24
2.4 Experimental.....	25
2.4.1 Synthesis of CuInSe ₂ Precursor.....	25
2.4.2 Preparation of CuInSe ₂ Nanotubes and Nanowires	26

2.4.3	Methods.....	26
2.5	References.....	28
 CHAPTER 3. Directing Anisotropic Charge Transport of Layered Organic-Inorganic Hybrid Perovskite Semiconductors in Porous Templates.....		
		33
3.1	Introduction.....	33
3.2	Results and Discussion.....	35
3.2.1	Synthesis and Characterization of Hybrid Arrays.....	35
3.2.2	Conductivity Measurements.....	41
3.3	Conclusions.....	45
3.4	Experimental.....	46
3.4.1	Synthesis of Hybrid Perovskite.....	46
3.4.2	Preparation of Hybrid Thin-Films and Arrays.....	46
3.4.3	Methods.....	47
3.5	References.....	48
 CHAPTER 4. Nanoporous Semiconductors Synthesized Through Polymer Templating of Ligand-Stripped CdSe Nanocrystals.....		
		53
4.1	Introduction.....	53
4.2	Results and Discussion.....	57
4.2.1	Preparation of Mesoporous CdSe Nanocrystal-Based Films.....	57
4.2.2	Structural Characterization.....	60
4.2.3	Optical Properties.....	65

4.2.4	Composition.....	68
4.2.5	Ellipsometric Porosimetry Measurements.....	70
4.2.6	Electrical Properties.....	72
4.3	Conclusions.....	74
4.4	Experimental.....	75
4.4.1	Materials.....	75
4.4.2	Synthesis of Mesoporous CdSe Films.....	76
4.4.3	Methods.....	76
4.5	References.....	78

CHAPTER 5. Enhancing Pseudocapacitive Charge Storage in Polymer Templated

Mesoporous Materials.....	89
5.1	Introduction.....89
5.2	Electrochemical Capacitors.....91
5.3	Architectures for Fast Energy Storage.....95
5.3.1	Slurry-Cast Electrodes.....96
5.3.2	Nanomaterials on Conductive Scaffolds.....96
5.3.3	Thin-Film Electrodes.....97
5.4	Synthesis of Mesoporous Films.....98
5.5	Quantifying Capacitive Properties.....105
5.5.1	Differentiating Between Capacitance and Diffusion Currents.....106
5.5.2	Estimating Double-Layer Capacitance.....108
5.6	Design Rules for Pseudocapacitor Electrodes.....111

5.6.1	Small Nanosized Building Units for High Surface Area.....	113
5.6.2	Mesoporosity to Facilitate Solvent Diffusion.....	113
5.6.3	Flexible Architectures to Facilitate Volume Expansion.....	114
5.6.4	Nanosized Domains.....	115
5.7	Conclusions.....	116
5.8	References.....	118

CHAPTER 6. General Method for the Synthesis of Hierarchical Nanocrystal-

	Based Mesoporous Materials.....	122
6.1	Introduction.....	122
6.2	Results and Discussion.....	126
6.2.1	Preparation of Mesoporous Nanocrystal-Based Films.....	126
6.2.2	Synthetic and Structural Tunability.....	132
6.2.3	Structural Characterization.....	140
6.3	Conclusions.....	153
6.4	Experimental.....	154
6.4.1	Materials.....	154
6.4.2	Synthesis and Ligand-Exchange of Nanocrystals.....	155
6.4.3	Synthesis of Mesoporous Nanocrystal-Based Films.....	155
6.4.4	Methods.....	156
6.5	References.....	158

CHAPTER 7. High-Performance Pseudocapacitors Based on Atomic Layer Deposition of V₂O₅ onto Conductive Nanocrystal-Based ITO Mesoporous Scaffolds.....	171
7.1 Introduction.....	171
7.2 Results and Discussion.....	175
7.2.1 Synthesis of ITO-V ₂ O ₅ Composites.....	175
7.2.2 Structure and Electrochemical Properties of 2 nm V ₂ O ₅	178
7.2.3 Structure and Electrochemical Properties of 7 nm V ₂ O ₅	188
7.2.4 Pseudocapacitance in ITO-V ₂ O ₅ Composites.....	193
7.3 Conclusions.....	199
7.4 Experimental.....	201
7.4.1 Materials.....	201
7.4.2 Synthesis and Ligand-Exchange of Nanocrystals.....	202
7.4.3 Synthesis of Mesoporous Nanocrystal-Based Films.....	202
7.4.4 Synthesis of V ₂ O ₅ -ITO Composites.....	203
7.4.5 Methods.....	203
7.5 References.....	205
 CHAPTER 8. Conclusions.....	 212
 APPENDIX A. Detailed Experimental Procedures for the Synthesis of Hydrazine-based Metal Chalcogenide Precursors and Templated Nanocrystal-Based Mesoporous Films.....	 217

A.1	Detailed Synthesis of the Hydrazine-Based CuInSe ₂ Precursor.....	217
A.2	Detailed Synthesis of the Hydrazine-Based Sb ₂ S ₃ Precursor.....	219
A.3	Detailed Synthesis of CdSe Nanocrystal-Based Mesoporous Films.....	221
	A.3.1 Procedure for Meerwein's Salt Ligand-Exchange.....	221
	A.3.2 Procedure for Polymer Templating of CdSe Nanocrystals.....	223
A.4	Detailed Synthesis of Mn ₃ O ₄ Nanocrystal-Based Mesoporous Films.....	225
	A.4.1 Synthesis of Mn ₃ O ₄ Nanocrystals.....	225
	A.4.2 Procedure for NOBF ₄ Ligand-Exchange.....	225
	A.4.3 Procedure for Polymer Templating of Mn ₃ O ₄ Nanocrystals.....	227
A.5	References.....	230

LIST OF FIGURES

CHAPTER 2. Copper Indium Diselenide Nanotubes and Nanowires Produced From Highly Soluble Hydrazinium-Based Precursors and Nanoporous Templates

- Figure 2.1.** SEM images of free standing CuInSe_2 nanotubes after removal from porous alumina with (a–c) 200 nm sized pore and (d) 100 nm sized pore. The arrows in (b) point to a cross section of a nanotube with a wall thickness of 40 nm. The formation of tube structures after a single incorporation suggests the hydrazine solvent wets the inside of the alumina pore walls during the incorporation. The fact that tubes are produced in both 100nm and 200nm pores further shows that the pore entirely defines the final CuInSe_2 nanotube structure.....15
- Figure 2.2.** SEM images of free standing CuInSe_2 nanowires after removal from porous alumina with (a–c) 200 nm sized pore and (d) 100 nm sized pore. As previously described, in the first incorporation, the hydrazine wets the inside of the alumina pore walls to produce tubes. To form wires, multiple incorporations are required to fill the inner tube volume. Again, in this instance, the pore structure defines the final CuInSe_2 nanowire structure.....17

Figure 2.3. Typical X-ray diffraction patterns of CuInSe_2 nanowires (green pattern) and nanotubes (blue pattern) embedded in alumina template with 200nm pore size. The XRD reflections can be indexed to the chalcopyrite tetragonal phase of CuInSe_2 .	19
Figure 2.4. Energy dispersive X-ray spectra for CuInSe_2 nanowires (a) and nanotubes (b). From this data, the stoichiometry of both the nanowires and nanotubes was determined to be $\text{Cu}_{0.9}\text{In}_{1.0}\text{Se}_{1.9}\text{S}_{0.1}$.	20
Figure 2.5. TEM image of a free standing CIS nanotube (a) shows a typical tube wall structure with an empty volume, while the nanowire (b) shows a dense structure. HRTEM images of a nanotube (c) and a nanowire (d) show the expected lattice planes of the chalcopyrite structure.	22
Figure 2.6. Experimental current density versus voltage characteristics of CuInSe_2 nanowires embedded in a porous aluminum oxide template. (a) Typical J-V curve for the nanowires shows diodic behavior with a turn on voltage of 5 V. (b) A plot of $\log J$ vs. $\log V$ shows a space-charge limited conduction behavior with a trap space-charge limited region, a trap-filling region and a trap-free space-charge conductivity region. A fit to the trap-free space-charge limited region is shown as a dashed line with a slope = 2. Space-charge	

limited current fits to this data produce a mobility of 65 ± 10
 $\text{cm}^2 \text{V}^{-1} \text{sec}^{-1}$ 23

CHAPTER 3. Directing Anisotropic Charge Transport of Layered Organic-Inorganic Hybrid Perovskite Semiconductors in Porous Templates

Figure 3.1. (a) Schematic illustration of the organic-inorganic hybrid perovskite structure. In the $(\text{C}_6\text{H}_5\text{C}_2\text{H}_4\text{NH}_3)_2\text{SnI}_4$ system, the corner sharing SnI_6 octahedra form extended SnI_4^{2-} 2D inorganic semiconducting sheets that are charge stabilized by organic cation bilayers. (b) Schematic illustration of concentric layers (top) and a single rolled scroll of layers (bottom) within cylindrical pores.....36

Figure 3.2. (a) XRD pattern for a spin-coated hybrid film. The appearance of well-defined peaks corresponding to the (0 0 l) reflections suggests the hybrid is highly crystalline with organic-inorganic layers oriented in the plane of the substrate. (b) XRD data for hybrid-alumina arrays with the X-ray beam impinging on the plane of the alumina membrane in a θ - θ geometry. No (0 0 l) peaks are observed confirming the hybrid layers are not oriented in the plane of the substrate.....38

Figure 3.3. 2D transmission XRD results for hybrid-alumina arrays. (a) Data collected with the X-ray beam penetrating through the

plane of the membrane producing a ring (inset shows schematic of this geometry). This pattern confirms the presence of concentric layers that are oriented perpendicular to the plane of the membrane. (b) Data collected with the X-ray beam impinging on the membrane edge-on (inset shows schematic of this geometry). The red arrow points to the appearance of a single spot, further confirming the unidirectional orientation of the layers inside the channels.....40

Figure 3.4. Experimental current density-voltage characteristics of a hybrid thin-film device. (a) Typical J-V curve for the spin-coated film shows diodic behavior with a turn on voltage of 12 V. (b) A logarithmic plot of J vs. V showing a space-charge limited conduction behavior with a trap-free space-charge conductivity region. A fit to this region, where the slope = 2, is represented by the dashed line. SCLC fits to this data produce a carrier mobility of 12.8 cm² V⁻¹ sec⁻¹.....42

Figure 3.5. Experimental current density-voltage characteristics of the hybrid arrays embedded in alumina. (a) Under bias, the J-V curve shows diodic behavior with a turn on voltage of 10 V. (b) A logarithmic plot of J vs. V showing a space-charge limited conduction behavior with a trap-free space-charge conductivity region. A fit to this region, where the slope = 2,

is represented by the dashed line. SCLC fits to this data
 produce a carrier mobility of $0.4 \text{ cm}^2 \text{ V}^{-1} \text{ sec}^{-1}$43

CHAPTER 4. Nanoporous Semiconductors Synthesized Through Polymer Templating of Ligand-Stripped CdSe Nanocrystals

Figure 4.1. (a) TEM image of CdSe nanocrystals after treatment with Et_3OBF_4 . The nanocrystals are monodisperse and non-agglomerated. (b) TGA data for PBO-*b*-PEO at a constant heating rate of $1 \text{ }^\circ\text{C min}^{-1}$ under a flowing argon atmosphere. The data indicate that this diblock copolymer can be fully degraded under inert atmosphere by $350 \text{ }^\circ\text{C}$59

Figure 4.2. Top-view SEM images of CdSe nanocrystal-based mesoporous films templated with PBO-*b*-PEO. Parts (a) and (b) show low-magnification and high-magnification images, respectively, of films prepared by spin-coating. Parts (c) and (d) show low-magnification and high-magnification images, respectively, of films prepared by drop-casting. In both cases, both the larger black mesopores and the individual nanocrystals can be seen.....61

Figure 4.3. (a) Wide angle XRD patterns obtained by integrating 2D-WAXS data collected on CdSe nanocrystals after the ligand-exchange process with Et_3OBF_4 (A) and after templating with PBO-*b*-PEO and thermal treatment to $400 \text{ }^\circ\text{C}$ to form a

mesoporous CdSe nanocrystal-based film (B). Both before and after templating, the diffraction can be indexed to the wurtzite crystal structure of CdSe. Narrow peaks marked with * correspond to organic salts used in the ligand-stripping process. (b) 2D-SAXS pattern obtained on a CdSe nanocrystal-based mesoporous film. The image shows strong in-plane scattering, indicative of a well-defined pore size, but no long range periodicity of the pores. Scattering vector *S* components are given in 1/nm.....63

Figure 4.4. UV-visible absorption spectra of CdSe nanocrystals in several environments. As-synthesized samples dispersed in hexane are indicated with a solid black line. Data collected on samples dispersed in DMF after ligand stripping with Et₃OBF₄ are indicated with a dashed black line. Data for a dense film of untemplated CdSe nanocrystals after ligand stripping are indicated by a dashed gray line. Data for a templated mesoporous CdSe nanocrystal-based film are indicated by a solid gray line. All data is plotted as normalized absorbance versus wavelength.....66

Figure 4.5. XPS collected on a mesoporous CdSe nanocrystal-based film. (a) A high resolution spectrum of the Cd 3d core region shows peaks for the 3d_{3/2} and 3d_{5/2} core levels of Cd in CdSe. No peaks corresponding to CdO_x can be observed

(arrows mark expected location). (b) A high resolution spectrum for Se 3d core region shows peaks for the $3d_{3/2}$ and $3d_{5/2}$ core levels of Se in CdSe. Again, no peaks corresponding SeO_2 can be observed (arrows mark expected location).....69

Figure 4.6. (a) Toluene adsorption-desorption isotherm for a templated CdSe nanocrystal-based mesoporous film (filled triangles) and a dense film of untemplated nanocrystals (filled circles). The mesoporous film exhibits a 50% toluene-accessible porous volume while the dense film exhibits a 4% toluene-accessible porous volume. (b) Corresponding pore size distribution data obtained for the templated film in (a).....71

Figure 4.7. Experimental current density-voltage curve for a CdSe nanocrystal-based mesoporous film demonstrating typical diodic behavior. A space-charge limited current model was utilized to calculate a carrier mobility of $10^{-4} \text{ cm}^2 \text{ V}^{-1} \text{ sec}^{-1}$ from this data.....73

CHAPTER 5. Enhancing Pseudocapacitive Charge Storage in Polymer Templated Mesoporous Materials

Figure 5.1. (a) A power vs. energy density graph (Ragone Plot) of energy storage devices. (b) Mechanisms for capacitive charge storage at an electrode surface.....92

Figure 5.2. Morphology of KLE-templated $T\text{-Nb}_2\text{O}_5$ films with iso-oriented nanocrystalline pore walls. (a) Cross-sectional FESEM image of a razor-blade cut in a film held at a tilt of 45° . A higher-magnification image is shown in the inset of (a) confirming that the periodic structure observed on the top-surface persists throughout the film. (b) Bright-field TEM image. (c) Electron diffraction pattern obtained from the same sample shown in (b). The lattice-spacings correspond well with orthorhombic Nb_2O_5 (T -phase).....101

Figure 5.3. (a) 1D-WAXD data obtained on KLE-templated $T\text{-Nb}_2\text{O}_5$ (A), $L\text{-Ta}_2\text{O}_5$ (B), and TaNbO_5 (C) films. The stick pattern shows orthorhombic $T\text{-Nb}_2\text{O}_5$ according to JCPDS reference card no. 30-0873. A typical 2D-WAXD pattern for mesoporous $T\text{-Nb}_2\text{O}_5$ is shown in the inset of (a). (b) 2D-SAXS data obtained on cubic mesoporous Nb_2O_5 collected at angles of incidence $\beta = 10^\circ$ and 90° (inset). (c) 2D-SAXS pattern of KLE22-templated nanocrystal-based cubic mesoporous TiO_2 film acquired at an angle of incidence $\beta = 7^\circ$. (b–c) Scattering vector, s , components are given in $1/\text{nm}$103

Figure 5.4. (a) Low-magnification top-view FESEM images of a KLE23-templated nanocrystal-based mesoporous TiO_2 film. The inset in (a) shows a high-magnification top-view FESEM

image; the porosity is bimodal with 1–4 and 20–25 nm diameter pores. (b–d) Toluene adsorption-desorption isotherms for self-organized TiO₂ thin-films. (b) KLE22-templated sol-gel film, showing a standard isotherm for a sol-gel derived film with a monomodal pore structure. (c) KLE23-templated nanocrystal film with bimodal porosity. (d) Untemplated nanocrystal film with sub-4 nm pores that are formed by random nanocrystal aggregation.....104

Figure 5.5. (a) Typical cyclic voltammetric responses of KLE-templated nanocrystal-based TiO₂ films at various sweep rates. (b) Calculated *b*-values for a KLE-templated nanocrystal-based TiO₂ film as a function of potential for the cathodic (Li⁺ insertion) and anodic sweep (Li⁺ extraction). (c–d) Comparison of charging rates (c) and total stored charge at a sweep rate of 10 mV s⁻¹ (d) for various TiO₂ films. A and C refer to KLE-templated and untemplated nanocrystal films, while B refers to KLE-templated sol-gel films.....107

Figure 5.6. (a) Molybdate (α -MoO₃) unit cells showing the layer-like arrangement of molybdenum (green) and oxygen atoms (red). (b) Cyclic voltammetry at 0.1 mV s⁻¹ of mesoporous crystalline α -MoO₃: the pseudocapacitive contribution is shaded, as deduced from current analysis. (c) The capacitive contribution to the total stored charge plotted as

function of charging time for a mesoporous amorphous MoO_3 film and a mesoporous crystalline $\alpha\text{-MoO}_3$ film. The capacitive contribution for the mesoporous crystalline film is three times larger than the amorphous analogue.....109

Figure 5.7. Cyclic voltammetry ($v = 10 \text{ mV/s}$) of mesoporous $T\text{-Nb}_2\text{O}_5$ in Li^+ and TBA^+ non-aqueous electrolytes, where TBA^+ is used to estimate the double-layer capacitance. The results demonstrate the small contribution of double-layer capacitance to the overall charge storage.....110

Figure 5.8. Use of electrochemical impedance spectroscopy to separate pseudocapacitance and double-layer capacitance in mesoporous crystalline CeO_2 : (a) impedance response at 3.5 V and (b) after lithiation to 2 V. The inset in (a) represents the proposed circuit model. (c) Results of the fitting analysis demonstrate that pseudocapacitance accounts for a significant fraction of the charge storage. (d) Typical 1D-SAXS pattern for KLE-templated CeO_2 and Li_xCeO_2 films.....112

CHAPTER 6. General Method for the Synthesis of Hierarchical Nanocrystal-Based Mesoporous Materials

Figure 6.1. TEM images of ITO nanocrystals as-synthesized (a) and after the ligand-exchange process (b); MnFe_2O_4 nanocrystals as-synthesized (c) and after the ligand-exchange process (d); and Mn_3O_4 nanocrystals as-synthesized (e) and after the ligand-exchange process (f). In all cases, the particles do not agglomerate and maintain a uniform size and shape after the ligand removal process.....128

Figure 6.2. SEM images of various templated nanocrystal-based porous films. (a) Low-magnification and (b) high-magnification top-view SEM images of PEP-*b*-PEO templated ITO nanocrystals. (c) Low-magnification and (d) high-magnification top-view SEM images of PEP-*b*-PEO templated Mn_3O_4 nanocrystals. (e) Low-magnification and (f) high-magnification top-view SEM images of PEP-*b*-PEO templated MnFe_2O_4 nanocrystals.....130

Figure 6.3. SEM images of templated nanocrystal-based porous films demonstrating variability of the template and coating method. Low-magnification top-view SEM images of PB-*b*-PEO templated ITO nanocrystals prepared by dip-coating (a) and spin-coating (b). Low-magnification top-view SEM images of PBO-*b*-PEO templated Mn_3O_4 nanocrystals prepared by dip-coating (c) and spin-coating (d). (e) SEM

image of PEP-*b*-PEO templated ITO nanocrystals prepared
by drop-casting.....134

Figure 6.4. (a) SEM image of PEP-*b*-PEO templated MnFe_2O_4 nanocrystal-based films. (b) SEM image of MnFe_2O_4 films in (a) that were thermally converted to $(\text{Mn,Fe})_2\text{O}_3$ at 400 °C demonstrating retention of mesostructure. (c) WAXD data showing full conversion from MnFe_2O_4 to $(\text{Mn,Fe})_2\text{O}_3$138

Figure 6.5. (a) WAXD patterns of as-synthesized ITO nanocrystals (A), ITO nanocrystals after the ligand-exchange process (B) and a templated ITO nanocrystal-based film (C). (b) WAXD patterns of as-synthesized Mn_3O_4 nanocrystals (A), Mn_3O_4 nanocrystals after the ligand-exchange process (B), and a templated Mn_3O_4 nanocrystal-based film (C). (c) WAXD patterns of as-synthesized MnFe_2O_4 nanocrystals (A), MnFe_2O_4 nanocrystals after the ligand-exchange process (B), and a templated MnFe_2O_4 nanocrystal-based film (C).....141

Figure 6.6. 2D-SAXS patterns obtained on PEP-*b*-PEO templated ITO-based films (a), Mn_3O_4 -based films (b), MnFe_2O_4 -based films (c), and $(\text{Mn,Fe})_2\text{O}_3$ -based films (d). Patterns for PB-*b*-PEO templated ITO nanocrystal-based films (e) and PBO-*b*-PEO templated Mn_3O_4 nanocrystal-based films. Data were

collected at an angle of incidence $\beta = 1.25^\circ$ for (a), $\beta = 2.25^\circ$ for (b), $\beta = 0.80^\circ$ for (c), $\beta = 0.80^\circ$ for (d), $\beta = 0.80^\circ$ for (e), and $\beta = 0.60^\circ$ for (f). Scattering vector S components are given in 1/nm.....144

Figure 6.7. (a) SEM image of PEP-*b*-PEO templated ITO nanocrystals with a diameter of 4–5 nm. (b) TEM image of the NOBF₄-treated ITO nanocrystals. (c) A typical toluene adsorption-desorption isotherm showing characteristic mesoporous behavior for films shown in (a). (d) Pore size distribution data obtained from the isotherm in (c). (e) SEM image of 7–8 nm ITO nanocrystals templated with PEP-*b*-PEO. (f) TEM image of the NOBF₄-treated ITO nanocrystals. (g) Toluene adsorption-desorption isotherm showing characteristic mesoporous behavior. (h) Pore size distribution data obtained from the isotherm in (g).....146

Figure 6.8. Toluene adsorption-desorption isotherms for PB-*b*-PEO templated ITO nanocrystals with a diameter of 7–8 nm (a) and PEP-*b*-PEO templated Mn₃O₄ nanocrystals with a diameter of 4–5 nm (c). Corresponding pore size distribution data for PB-*b*-PEO templated ITO (b) and PEP-*b*-PEO templated Mn₃O₄ (d) obtained from the isotherms.....149

Figure 6.9. Comparison of capacity at various charging times calculated from cyclic voltammetric data at various sweep rates for a

PEP- <i>b</i> -PEO templated Mn ₃ O ₄ nanocrystal-based mesoporous film (squares) and an untemplated Mn ₃ O ₄ nanocrystal film (circles).....	152
---	-----

CHAPTER 7. General High-Performance Pseudocapacitors Based on Atomic Layer Deposition of V₂O₅ onto Conductive Nanocrystal-Based ITO Mesoporous Scaffolds

Figure 7.1. (a) Low-magnification SEM image of PEP-*b*-PEO templated ITO nanocrystal-based mesoporous films. Inset: higher-magnification image showing pore walls comprising individual ITO nanocrystals. (b) TEM image of ligand-stripped ITO nanocrystals with an average diameter of 4.6 ± 0.4 nm. (c) 2D-SAXS pattern obtained on a PEP-*b*-PEO templated ITO nanocrystal-based film, collected at an angle of incidence $\beta = 1.25^\circ$. The pattern shows strong in-plane scattering, indicative of a well-defined pore size, but no long range periodicity of the pores. Scattering vector S components are given in 1/nm.176

Figure 7.2. (a–c) Low-magnification SEM images of mesoporous ITO films coated with a 2 nm layer of V₂O₅ as-deposited (a) (inset: higher-magnification image showing individually coated nanocrystals); heated to 200 °C (b) (inset: higher-magnification image showing grain growth of the V₂O₅

around the nanocrystals); and, heated to 450 °C (c) (inset: higher-magnification image showing grain growth of the V_2O_5 around the nanocrystals). (d–f) Low-magnification SEM images of mesoporous ITO films coated with a 7 nm layer of V_2O_5 as-deposited (d) (inset: higher-magnification image showing spaces in between nanocrystals are filled in with V_2O_5); heated to 200 °C (e) (inset: higher-magnification image showing grain growth of V_2O_5 leads to partially fused pores); and, heated to 350 °C (f) (inset: higher-magnification image showing grain growth of the V_2O_5 leads to significant loss of mesostructure).....179

Figure 7.3. XPS spectra for porous ITO films coated with a 2 nm (a) and 7 nm (b) layer of V_2O_5 . The survey scans show the V 2p core regions, with peaks for both $2p_{3/2}$ and $2p_{1/2}$ core levels. The red arrows point to the V^{5+} peak and the blue arrows points to the V^{4+} peak after deconvolution of the $V2p_{3/2}$ peak.....181

Figure 7.4. Toluene adsorption-desorption isotherms showing characteristic mesoporous behavior for a mesoporous ITO nanocrystal-based film (a), mesoporous ITO film coated with a 2 nm layer of V_2O_5 heated to 200 °C (c), mesoporous ITO film coated with a 2 nm layer of V_2O_5 heated to 450 °C (e). Pore size distribution data obtained from the isotherms for a

mesoporous ITO nanocrystal-based film (b), mesoporous ITO film coated with a 2 nm layer of V_2O_5 heated to 200 °C (d), mesoporous ITO film coated with a 2 nm layer of V_2O_5 heated to 450 °C (f).....182–183

Figure 7.5. (a) Charge storage dependence on sweep rate for mesoporous ITO films coated with a 2 nm layer of V_2O_5 heated to 200 and 450 °C. (b) Comparison of charging rates calculated from cyclic voltammetric data at various sweep rates for mesoporous ITO films coated with a 2 nm layer of V_2O_5 heated to 200 and 450 °C.....185

Figure 7.6. (a) Charge storage dependence on sweep rate for porous ITO films coated with a 2 nm of V_2O_5 via ALD using water and ozone as the oxidant, both were heated to 200 °C. (b) Comparison of capacity versus charging times for porous ITO films coated with a 2 nm of V_2O_5 via ALD using water and ozone as the oxidant, both were heated to 200 °C.....187

Figure 7.7. Toluene adsorption-desorption isotherms showing characteristic mesoporous behavior for a mesoporous ITO film coated with a 7 nm layer of V_2O_5 heated to 200 °C (a), and a mesoporous ITO film coated with a 7 nm layer of V_2O_5 heated to 300 °C (c). Pore size distribution data obtained from the isotherms for a mesoporous ITO film coated with a 7 nm layer of V_2O_5 heated to 200 °C (b), and a mesoporous

ITO film coated with a 7 nm layer of V_2O_5 heated to 300 °C	
(d).....	190

Figure 7.8. (a) Charge storage dependence on sweep rate for mesoporous ITO films coated with a 7 nm layer of V_2O_5 heated to 200, 250, 300 and 350 °C. (b) Charge storage dependence on sweep rate for flat ITO coated with a 7 nm layer of V_2O_5 heated to 200, 250, 300 and 350 °C. (c) Comparison of charging rates calculated from cyclic voltammetric data at various sweep rates for mesoporous ITO films coated with a 7 nm layer of V_2O_5 heated to 200, 250, 300 and 350 °C. (d) Comparison of charging rates calculated from cyclic voltammetric data at various sweep rates for flat ITO coated with a 7 nm layer of V_2O_5 heated to 200 , 250, 300 and 350 °C.....	192
---	-----

Figure 7.9. Cyclic voltammetric responses for porous ITO films coated with 2 nm (a) and 7 nm (b) layer of V_2O_5 heated to 200°C at sweep rates of 1 mV/s. Cyclic voltammetric responses for the same films, 2 nm (d) and 7 nm (e) layer of V_2O_5 , at sweep rates of 10 mV/s. The capacitive contribution to the current is represented as the shaded area. Corresponding comparison of the total stored charge at sweep rates of 1 (c) and 10 (f) mV/s, where A and B represent 2 and 7 nm layer of V_2O_5 heated to 200°C.....	195
---	-----

Figure 7.10. (a) Comparison of normalized capacity versus sweep rate calculated from cyclic voltammetric data at various sweep rates for porous ITO coated with a 2 nm and 7 nm layer of V_2O_5 via ALD heated to various temperatures. (b) Comparison of the rate capability of porous ITO coated with a 2 nm and 7 nm layer of V_2O_5 , bare mesoporous ITO, and ITO- V_2O_5 composites including the mass loading for both ITO and V_2O_5198

LIST OF SCHEMES

CHAPTER 5. Enhancing Pseudocapacitive Charge Storage in Polymer Templated Mesoporous Materials

Scheme 5.1. Evaporative-induced self-assembly process for producing cubic mesoporous films. The building blocks can be either molecular precursors leading to sol-gel-based films, or pre-formed nanocrystals, leading to nanocrystal-based films.....	99
---	----

LIST OF TABLES

CHAPTER 6. General Method for the Synthesis of Hierarchical Nanocrystal-Based Mesoporous Materials

Table 6.1.	Summary of mesopore size arising from the block copolymer template and micropore size arising from nanocrystal size.....	150
-------------------	--	-----

ACKNOWLEDGEMENTS

I am privileged and fortunate for this opportunity to express the gratitude I feel towards those individuals that have made significant contributions to my personal and professional life. I would like to thank my family for their constant and unconditional love and support. There are no words that can describe the sacrifice my parents, Douglas and Cristina Rauda, made for me and my siblings in order to provide us with a comfortable life. My parents and siblings have been my rock during difficult times. As a family, we have endured several hardships, but with our love and commitment to each other, as well as God's blessings, we have overcome the obstacles of life and we are stronger than ever. I could not ask for better role models in life. I also thank the good Lord for all the blessings he has bestowed upon me.

I would also like to thank my advisor, Professor Sarah Tolbert, for her encouragement, guidance, and support throughout my time at UCLA. She has always believed in my ability to become a great scientist, even when I doubted myself. Her faith in me has been instrumental in my professional growth and development. She has taught by example how to mentor and engage students in science. She is an amazing teacher and I hope to someday inspire students the way she has inspired me. Sarah is not only my academic advisor, she is also my friend, and I am very fortunate to have been a student in her research group.

I thank my committee members, Professors Jane Chang and Richard Kaner, for their support. I also thank Professor Heather Maynard for serving on my oral

committee. I thank Professors Paula Diaconescu and Miguel Garcia-Garibay for supporting me with letters of recommendation.

I would especially like to thank my collaborators. In the Tolbert group I thank: Laura Saldarriaga for help with porosimetry measurements, Laura Schelhas for help with TEM and XPS measurements, Jean Benjauthrit for help with profilometry and other experiments. In the Dunn group I thank: Professor Bruce Dunn for his guidance, Veronica Augustyn and Jesse Ko for electrochemical measurements, and Daniel Membreno for conductivity measurements. I thank my collaborators at the University of Maryland, Professor Gary Rubloff and Xinyi Chen for providing ALD measurements. I thank Dr. Morgan Stefik and Professor Ulrich Wiesner for providing the block copolymer that was essential to my experiments. I thank my collaborators at the Molecular Foundry, Drs. Delia Milliron, Raffaella Buonsanti, and Brett Helms, for providing me with samples for my experiments.

I would also like to express my gratitude to Dr. Alan Hopkins for being my mentor during my internship at the Aerospace Corporation. I would like to thank Dr. Barbara Ige for allowing me to participate in the NSF AGEP STEM during my first summer at UCLA. I am also grateful to those who helped me during my time at UCLA: Dr. Ignacio Martini, Dr. Jane Strouse, Dr. Saeed Khan, Dr. Carolyn Knobler, Erica Eddings, Dr. Jia Ming Chen, Laurie Ultan-Thomas, Joe Rangel and Ricky Ruiz.

I want to thank the previous and current members of the Tolbert group: Anneliese Amacher, Chris Kang, Laura Schelhas, Rachel Huber, Amy Ferreira, Jean Benjauthrit, Brian Keck, Robert Thompson, David Watts, Abraham Buditama, Robert Boutelle, Shauna Robbennolt, Drs. Crissie Bauer, Robert Senter, Richard Farrell, Joe Nemanick,

Jessie Hierso, Tom Quickel, Van Le, Erik Richman, Andrew Clark, Chris Tassone, Scott Korlann, and Benny Ng. I want to thank my dear friend, Laura Saldarriaga, for her support and for helping me with many of my chapters. She worked tirelessly to help me get data, even when it was last minute. I thank my buddy, Will Molenkamp, for his words of wisdom and for always cheering me on. I thank my office mate and dear friend, Lisa Dudek, for always making me laugh with her stories. Lisa was always there to give me a boost of confidence when I really needed one. I am thankful we were able to share so many great memories in that window-less office. And, last but not least, I thank my roommate and best friend, Selma Duhovic, for all her support over the years. Selma is like a sister to me and I cannot imagine having gone through grad school without her. Over the years, we have laughed, cried, and built a strong bond that I hope will last always. I am going to miss her when the time comes to part ways, but, I know that love will keep us together. I look forward to hearing about her upcoming business endeavors, which I know will bring her great success and good fortune.

Previous Publications and Contributions of Co-Authors:

Chapter 2 is a version of: Iris E. Rauda, Sarah H. Tolbert, “Copper Indium Diselenide Nanotubes and Nanowires Produced From Highly Soluble Hydrazinium-Based Precursors and Nanoporous Templates.” I wrote the manuscript and Professor Sarah H. Tolbert helped edit the manuscript. This manuscript will be submitted for publication shortly after this dissertation is filed.

Chapter 3 is a version of: Iris E. Rauda, Sarah H. Tolbert, “Directing Anisotropic Charge Transport of Layered Organic-Inorganic Hybrid Perovskite Semiconductors in

Porous Templates.” I wrote the manuscript and Professor Sarah H. Tolbert helped edit the manuscript. This manuscript will be submitted for publication shortly after this dissertation is filed.

Chapter 4 is a version of: Iris E. Rauda, Laura C. Saldarriaga-Lopez, Brett A. Helms, Laura T. Schelhas, Daniel Membreno, Delia J. Milliron, Sarah H. Tolbert, “Nanoporous Semiconductors Synthesized Through Polymer Templating of Ligand-Stripped CdSe Nanocrystals.” Laura C. Saldarriaga-Lopez helped with ellipsometric porosimetry and UV-vis measurements. Brett A. Helms provided nanocrystal samples and helped with TEM and UV-vis measurements. Laura T. Schelhas helped with XPS measurements. Daniel Membreno helped with conductivity measurements. I wrote the manuscript. Drs. Brett A. Helms, Delia J. Milliron and Professor Sarah H. Tolbert helped edit the manuscript. This manuscript has been submitted for publication to *Advanced Materials*.

Chapter 5 is a version of: Iris E. Rauda, Veronica Augustyn, Bruce Dunn, Sarah H. Tolbert, “Enhancing Pseudocapacitive Charge Storage in Polymer Templated Mesoporous Materials.” Veronica Augustyn and I contributed equally to the writing of this review paper. Professors Bruce Dunn and Sarah H. Tolbert helped edit the manuscript. This manuscript has been accepted for publication in *Accounts of Chemical Research*.

Chapter 6 is a version of: Iris E. Rauda, Raffaella Buonsanti, Laura C. Saldarriaga-Lopez, Kanokraj Benjauthrit, Laura T. Schelhas, Morgan Stefik, Veronica Augustyn, Jesse Ko, Bruce Dunn, Ulrich Wiesner, Delia J. Milliron, Sarah H. Tolbert, “General Method for the Synthesis of Hierarchical Nanocrystal-Based Mesoporous

Materials.” *ACS Nano*, 2012, 6, 6386–6399. Copyright 2012 American Chemical Society. Dr. Raffaella Buonsanti provided nanocrystal samples and helped with TEM and SEM measurements. Laura C. Saldarriaga-Lopez helped with ellipsometric porosimetry. Kanokraj Benjauthrit helped synthesize samples and helped with SEM and XRD measurements. Laura T. Schelhas helped with TEM measurements. Dr. Morgan Stetik and Professor Ulrich Wiesner provided block copolymer materials. Veronica Augustyn, Jesse Ko and Professor Bruce Dunn helped with electrochemical measurements. I wrote the manuscript. Drs. Raffaella Buonsanti, Delia J. Milliron and Professor Sarah H. Tolbert helped edit the manuscript.

Chapter 7 is a version of: Iris E. Rauda, Veronica Augustyn, Xinyi Chen, Laura C. Saldarriaga-Lopez, Laura T. Schelhas, Gary Rubloff, Bruce Dunn, Sarah H. Tolbert, “High-Performance Pseudocapacitors Based on Atomic Layer Deposition of V_2O_5 onto Conductive Nanocrystal-Based ITO Mesoporous Scaffolds.” Veronica Augustyn helped with electrochemical measurements. Xinyi Chen helped with ALD measurements. Laura C. Saldarriaga-Lopez helped with ellipsometric porosimetry. Laura T. Schelhas helped with XPS and TEM measurements. I wrote most of the manuscript. Professor Sarah H. Tolbert helped edit the manuscript. This manuscript will be submitted for publication shortly after this dissertation is filed.

Professor Sarah H. Tolbert has directed the research presented in this dissertation. Most of the work in this dissertation was supported by: California NanoSystem Institute (CNSI); National Science Foundation (NSF); NSF Integrative Graduate Education and Research Traineeship Program (IGERT); Center for Molecularly Engineered Energy Materials (MEEM), an Energy Frontier Research Center

funded by the U.S. Department of Energy (D.O.E.), Office of Science, Office of Basic Energy Sciences; University of California Multicampus Research Programs and Initiatives (UC MRPI); and the UCLA Graduate Division. Portions of this research were performed as a user project at the Molecular Foundry, Lawrence Berkeley National Laboratory, which is supported by the Office of Science, Office of Basic Energy Sciences, of the U.S. D.O.E. Portions of this research were carried out at the Stanford Synchrotron Radiation Laboratory, a national user facility operated by Stanford University on behalf of the U.S. Department of Energy, Office of Basic Energy Sciences.

VITA

2002–2003	Minority Biomedical Research Support (MBRS) Undergraduate Fellowship, California State University, Los Angeles (CSULA)
2003	B.S. in Biology, CSULA
2003–2006	MBRS Graduate Fellowship, CSULA
2004	Phi Kappa Phi and Beta Beta Beta, CSULA
2005, 2006	Award for Special Recognition in Graduate Studies as a Graduate Honor Student, CSULA
2006	Graduate Scholarship awarded by Department of Chemistry, CSULA
2006	Graduate Student of the Year Award, CSULA
2006	M.S. in Chemistry, CSULA (GPA 4.0)
2006	Competitive Edge: Summer Transition Program to the Doctorate, NSF AGEP STEM, University of California Los Angeles (UCLA)
2006–2007	First Year Graduate Division Award Fellowship, UCLA
2007	Ludo Frevel Crystallography Scholarship
2007	The National GEM Consortium Fellowship (declined)
2007–2009	Materials Creation Training Program, NSF IGERT, UCLA
2007–2012	High School Nanoscience Outreach Program, UCLA
2007, 2010, 2011	Teaching Assistant, Department of Chemistry, UCLA
2009	Ford Fellowship Foundation Diversity Fellowship, Honorable Mention
2009	Internship, The Aerospace Corporation
2010, 2012	American Chemical Society Travel Award

PUBLICATIONS AND PRESENTATIONS

I. E. Rauda, L. C. Saldarriaga-Lopez, B. A. Helms, L. T. Schelhas, D. Membreno, D. J. Milliron, S. H. Tolbert, "Nanoporous Semiconductors Synthesized Through Polymer Templating of Ligand-Stripped CdSe Nanocrystals." **2012**, Accepted to *Advanced Materials*.

I. E. Rauda, V. Augustyn, B. Dunn, S. H. Tolbert. "Enhancing Pseudocapacitive Charge Storage in Polymer Templated Mesoporous Materials." **2012**, Accepted to *Accounts of Chemical Research*.

D. Jiang, **I. E. Rauda**, S. Han, F. Zhou. "Aggregation Pathways of the Amyloid- β (1–42) Peptide Depend of its Colloidal Stability and Ordered β -Sheet Stacking." *Langmuir* **2012**, 28, 12711–12721.

I. E. Rauda, R. Buonsanti, L. C. Saldarriaga-Lopez, K. Benjaurhrit, L. T. Schelhas, M. Stefik, V. Augustyn, J. Ko, B. Dunn, U. Wiesner, D. J. Milliron, S. H. Tolbert. "General Method for the Synthesis of Hierarchical Nanocrystal-Based Mesoporous Materials." *ACS Nano* **2012**, 6, 6386–6399.

I. E. Rauda, J. Benjauthrit, V. Augustyn, R. Buonsanti, X. Chen, G. Rubloff, D. Milliron, B. Dunn, S. Tolbert. "Synthesis of Hierarchical Nanocrystal-based Mesoporous Materials for Electrochemical Supercapacitors." Oral Presentation at the American Chemical Society Spring Meeting, San Diego, CA, **2012**.

A. J. Hong, J. Kim, K. Kkim, F. Xiu, J. Jeon, J. Park, Y. Wang, **I. E. Rauda**, L. Chen, Y. Yang, S. Tolbert, J. Zou, T. King, K. L. Wang. "Cr Metal Thin Film Memory." *J. Applied Physics*, **2011**, 110, 054501(1–5).

I. E. Rauda, S. Tolbert. "Template-assisted Preparation of Copper Indium Diselenide Nanotubes and Nanowires." Oral Presentation at the Materials Research Society Spring Meeting, San Francisco, CA, **2010**.

I. E. Rauda, S. Tolbert. "Copper Indium Diselenide Nanotubes and Nanowires via Incorporation into Porous Alumina Templates" Poster Presentation at the American Chemical Society Spring Meeting, San Francisco, CA, **2010**.

A. L. Briseno, S. Han, **I. E. Rauda**, F. Zhou, C.S. Toh, E. J. Nemanick, and N. S. Lewis. "Electrochemical Polymerization of Aniline Monomers Infiltrated into Well-Ordered Truncated Eggshell Structures of Polyelectrolyte Multilayers." *Langmuir*, **2004**, 20, 219–226.

J. Huang, V. M. Egan, R. B. Kaner, J. Yoon, R. L. Garrell, A. L. Briseno, **I. E. Rauda** and F. Zhou. "Enantioselective Discrimination of D- and L-Phenylalanine by Chiral Polyaniline Thin Films." *Adv. Mater.* **2003**, 15, 1158–1161.

CHAPTER 1

Introduction

The ability to precisely control the structure and composition of inorganic materials at the atomic and nanoscale is highly desirable, particularly for studying structure-property relationships in nanostructured materials. Solution-phase routes to produce nanostructured functional materials can provide simple and cost-effective avenues for fabricating materials for energy-related applications. The most basic building block or precursor in solution-phase syntheses is a soluble species that can either self-assemble, or co-assemble with a structure directing agent or template from solution, to generate uniquely architected materials that may exhibit structural- and/or compositional-dependent properties. In this work, soluble inorganic building blocks ranging from atomic-scale charged molecular complexes to nanometer-scale preformed nanocrystals are utilized to construct functional inorganic-based materials that are amenable for integrating into electronic and energy-storage devices, including photovoltaics and pseudocapacitors.

There is currently much effort placed into the fabrication of complex nanostructured semiconductors because these materials can serve as building blocks for a wide variety of technical and fundamental applications. Nanostructured semiconductors are particularly interesting functional materials because they have high optical absorption coefficients, tunable band gaps in the visible region, and demonstrate quantum confinement when they are nanodimensional.¹ When considering the

usefulness of a particular method to produce complex nanostructured materials, certain factors need to be addressed such as ease of manipulation, cost-effectiveness, time, and scalability. E-beam lithography, for example, offers a high degree of control over architecture; however, this technique is costly, time-consuming and offers limited scalability. Another method that can produce complex semiconductor nanostructures is simple solution phase chemistry. For example, thermal decomposition of organometallic precursors in a hot mixture of surfactants can produce an interesting structure like a CdSe tetrapod.² This method is quick, cheap and offers high scalability. The drawback here is the lack of ability to precisely define the final architecture. Tetrapods form for a variety of energetic reasons and other structures cannot be made easily. For such reasons, it is important to investigate new methods that will lead to a broader range of structures and architectures.

The first part of this work focuses on producing new complex nanostructured semiconductors using simple solution processing. Metal chalcogenides represent a class of semiconducting materials with attractive properties (e.g. good electrical mobility and band gap tunability) that make them ideal candidates for a wide range of electronic-based applications.³ In 2004, the development of solution-processing methods to fabricate high quality thin, continuous, and crystalline films of metal chalcogenide semiconductors using hydrazine as a solvent was reported by IBM.⁴ Using this method, copper indium diselenide (CuInSe_2) based thin-film photovoltaic devices have demonstrated high power conversion.⁵ The approach uses excess chalcogen to improve the solubility of selected main group metal chalcogenides in hydrazine through the formation of highly soluble hydrazinium-based precursors that can be solution

processed and decomposed to the starting metal chalcogenide at low temperature. Chapter 2 describes the synthesis of copper indium diselenide (CuInSe_2) nanostructures by incorporating a highly soluble hydrazinium-based precursor into a nanoporous aluminum oxide template.⁶ The precursor is then thermally decomposed at low temperature and with minimal volume change to yield the CuInSe_2 semiconductor within the template, which is etched away, leaving behind CuInSe_2 . By controlling the number of incorporations, both nanotubes and nanowires can be produced which have dimensions that are defined by the template, indicating that the final architecture of CuInSe_2 can be tuned. Moreover, the nanowires exhibit good conductivity along the wire axis, suggesting they form an electronically interconnected network. The results demonstrate this approach offers a new method for producing CuInSe_2 nanostructures from a solution-based precursor.

In another interesting approach, hybrid organic-inorganic semiconductors have recently been prepared by low-temperature melt-processing.^{7,8} These materials are comprised of alternating layers of organic cations and 2-dimensional (2D) semiconducting sheets that exhibit high carrier mobilities along the 2D sheets leading to anisotropic conductivity in the material.^{9–11} Despite these interesting electronic properties, these materials have not been built into nanometer scale architectures. Chapter 3 thus describes an approach to confine these anisotropic semiconductors within porous templates with cylindrical channels oriented perpendicular to the plane of the substrate. Because of this crystallographic anisotropy, the material forms vertically-aligned arrays with a concentric multilayered structure where the 2D conducting sheets are oriented along the channel direction. In agreement with this idea, conductivity

measurements demonstrate that the oriented arrays exhibit charge transport in the direction perpendicular to the substrate confirming that nanostructured materials can be made using the unique hybrid semiconductors and that control of nanoscale architecture also results in control over anisotropic conductivity.

In chapter 4, we move away from hard templates like anodic alumina and instead discuss the synthesis of nanoporous semiconductor materials from cadmium selenide (CdSe) nanocrystals through polymer (soft) templating. In recent years, the utilization of large amphiphilic diblock copolymers has led to the synthesis of nanoporous materials through the self-assembly of preformed nanocrystals of oxide systems.^{12–15} In our approach, we use a block copolymer, which forms micelles in polar solvents, to template colloidal CdSe nanocrystals into mesoporous hierarchical architectures that exhibit a high surface area and a bimodal porosity. One unique feature about this approach is the fact that the CdSe nanocrystals are stripped of their native ligands to yield bare and highly dispersible nanocrystals. This is accomplished through a ligand-exchange process that utilizes Meerwin's salt (Et_3OBF_4) as the stripping agent.¹⁶ The nanocrystals are then templated with the suitable block copolymer via an evaporation-induced self-assembly process. Next, the polymer is decomposed under inert conditions resulting in CdSe-based mesoporous films that retain their semiconducting properties, including quantum confined excitonic absorption and modest carrier mobilities. The films exhibit a bimodal porosity with the presence of both mesopores, arising from the polymer template, and micropores that arise from the nanocrystals embedded in the pore walls. These mesoporous CdSe nanocrystal-based materials have an accessible high surface area resulting from the bimodal porosity. More

importantly is that in this work, the CdSe nanocrystal building blocks serve only as a model system and, because the assembly process is independent of any CdSe reactivity, the approach should be general for a wide range of colloidal semiconductor nanocrystals.

The second part of this work focuses on the synthesis of mesoporous pseudocapacitors from various redox-active and conductive metal-oxide-based materials via solution-phase syntheses. Pseudocapacitors are electrochemical energy storage devices that have recently attracted much attention because they have the ability to attain high energy densities while maintaining high power densities.¹⁷ Pseudocapacitors store charge through faradaic processes that involve surface or near surface redox reactions. These charge storage mechanisms are different than those in traditional batteries because they are not limited by the diffusion of ions/electrolyte into the bulk. Therefore, pseudocapacitors have the potential to provide greater power, faster charge/discharging times, and longer charge/discharge cycling stability than traditional batteries.¹⁸

The surface confined processes associated with pseudocapacitors can greatly benefit from the high surface area of nanodimensional and porous materials because the surface redox-active sites become accessible to the electrolyte. Recently, we reported the synthesis of polymer-templated mesoporous nanocrystal-based anatase titanium oxide (TiO₂) thin-films that demonstrated enhanced pseudocapacitive charge storage.¹⁵ Anatase nanocrystals (diameter < 10 nm) were co-assembled with a block copolymer by an evaporation-induced self-assembly process, followed by removal of the template, to yield a mesoporous inorganic composite with high surface area. In that

work, enhancement of electrochemical properties resulted when the films were both made from nanocrystals and mesoporous. The porosity allowed facile electrolyte diffusion throughout the material while the nanocrystals embedded in the pore walls provided a high surface area with ample redox-active sites.

Here, we build from our previously established TiO_2 work on mesoporous pseudocapacitors and we explore a wider range of metal-oxide nanocrystal systems. In chapter 5 we introduce and discuss several design rules that lead to enhanced pseudocapacitive charge storage in mesoporous transition metal oxide materials. We propose that an ideal pseudocapacitor electrode architecture should be comprised of a redox-active material (i.e. metal oxide) that has a nanodimensional structure to accommodate shorter ion diffusion lengths. In addition, the material should have a high surface area in order to maximize all the redox-active sites, and, have an open interconnected porosity to facilitate solvent diffusion to all the redox-active sites. Finally, electrical conductivity should be integrated and wired into the redox-active component in order to simultaneously achieve both higher energy and power densities in one structure.

In chapter 6, we build from these design rules and describe a general route for assembling pre-formed nanocrystals into hierarchical mesoporous architectures by extending this synthetic approach to a wider range of nanocrystal systems including manganese oxide (Mn_3O_4), manganese ferrite (MnFe_2O_4), and tin-doped indium oxide (ITO).¹² We use an established ligand-exchange method and use NOBF_4 to strip ligands off of the surface of nanocrystals, allowing them to be templated with diblock copolymers.¹⁹ We demonstrate the generality of this approach by varying the

composition and size of the nanocrystal building blocks and in each case, nearly identical porous networks are produced with no modification of the synthetic procedure. In addition, nanocrystals are templated with a range of diblock copolymers containing variable block compositions and molecular weights. The significance of the work is that the bimodal porosity, which combines mesopores and micropores as discussed above, can be synthetically tuned. Moreover, we show that templated Mn_3O_4 nanocrystal-based films exhibit enhanced charge storage behavior compared to untemplated nanocrystals, again demonstrating the efficacy of the electrode architecture. More importantly, we achieve a high degree of synthetic versatility and tunability because the mesoporosity can be tuned by varying the polymer template, and, the microporosity can be tuned by varying the size of the nanocrystal.

While we establish that nanocrystal-based mesoporous materials are good architectures for maximizing pseudocapacitive charge storage, limitations from electrical conductivity are likely to occur when scaling these materials into bulk-scale electrodes, necessitating the need to wire electrical conductivity into these materials. Therefore, in chapter 7, we use solution-phase methods to construct porous conductive scaffolds by templating ITO nanocrystals into mesoporous architectures and subsequently coat the ITO with vanadium oxide (V_2O_5) via atomic layer deposition (ALD) to produce pseudocapacitor electrode composites. Recent work has led to the ability to coat flat conductive substrates and multi-walled carbon nanotubes (MWCNT) with a thin layer of V_2O_5 resulting in highly conformal and crystalline V_2O_5 films and MWCNT/ V_2O_5 core/shell structures that demonstrate good electrochemical energy storage.^{20,21} In our approach, we coat highly porous ITO nanocrystal-based scaffolds with V_2O_5 coatings

with variable film thicknesses. We study the effects of material crystallinity by heating the deposited V_2O_5 layers to various temperatures and conclude that thin layers at lower annealing temperatures are all capacitive. The significance of this work is that we can use this newly designed nanocomposite for important fundamental studies like determining the ideal active layer thickness or extent of material crystallinity and the implications on pseudocapacitive energy storage. Collectively, this work can provide us with a basic understanding of the fundamental processes that govern charge storage behavior in nanocrystal-based nanoporous systems. Chapter 8 concludes with a summary of the entire work and addresses the implications and future directions of the work. Finally, an Appendix section at the end describes detailed experimental procedures for the synthesis of various nanostructured materials described in this dissertation including the hydrazine-based $CuInSe_2$ precursor and several templated nanocrystal-based mesoporous films.

1.1 References

- ¹ Alivisatos, P. Semiconductor Clusters, Nanocrystals, and Quantum Dots. *Science* **1996**, 271, 933–937.
- ² Manna, L.; Scher, E. C.; Alivisatos, A. P. Synthesis of Soluble and Processable Rod-, Arrow-, Teardrop-, and Tetrapd-Shaped CdSe Nanocrystals. *J. Am. Chem. Soc.* **2000**, 122, 12700–12706.
- ³ Kazmerski, L. L. Status and Assessment of Photovoltaic Technologies. *Intern. Mater. Rev.* **1989**, 34, 185–210.
- ⁴ Mitzi, D. B.; Kosbar, L. L.; Murray, C. E.; Copel, M.; Afzali, A. High-Mobility Ultrathin Semiconducting Films Prepared by Spin Coating. *Nature* **2004**, 428, 29–303.
- ⁵ Liu, W.; Mitzi, D. B.; Yuan, M.; Kellock, A. J.; Chey, S. J.; Gunawan, O. 12 % Efficiency CuIn(Se,S)₂ Photovoltaic Device Prepared Using a Hydrazine solution Process. *Chem. Mater.* **2010**, 22, 1010–1014.
- ⁶ Milliron, D. J.; Mitzi, D. B.; Copel, M.; Murray, C. E. Solution-Processed Metal Chalcogenide Films for *p*-Type Transistors. *Chem. Mater.* **2006**, 3, 587–590.
- ⁷ Mitzi, D. B.; Medeiros, D. R.; DeHaven, P. W. Low-Temperature Melt Processing of Organic-Inorganic Hybrid Films. *Chem. Mater.* **2002**, 14, 2839–2841.
- ⁸ Mitzi, D. B.; Dimitrakopoulos, C. D.; Rosner, J.; Medeiros, D. R.; Xu, Z.; Noyan, C. Hybrid Field-Effect Transistor Based on a Low-Temperature Melt-Processed Channel Layer. *Adv. Mater.* **2002**, 14, 1772–1776.
- ⁹ Kagan, C. R. ; Mitzi, D. B. ; Dimitrakopoulos, C. D. Organic-Inorganic Hybrid Materials as Semiconducting Channels in Thin-Film Field-Effect Transistors. *Science*, **1999**, 286, 945–947.

-
- ¹⁰ Mitzi, D. B.; Feild, C. A.; Harrison, W. T. A.; Guloy, A. M. Conducting Tin Halides with a Layered Organic-Based Perovskite Structure. *Nature*, **1994**, *369*, 467–469.
- ¹¹ Mitzi, D. B.; Wang, S.; Feild, C. A.; Chess, C. A.; Guloy, A. M. Conducting Layered Organic-Inorganic Halides Containing (100)-Oriented Perovskite Sheets. *Science*, **1995**, *267*, 1473–1476.
- ¹² Rauda, I. E.; Buonsanti, R.; Saldarriaga-Lopez, L. C.; Benjauthrit, K.; Schelhas, L. T.; Stefik, M.; Augustyn, V.; Ko, J.; Dunn, B.; Wiesner, U.; Milliron, D. J.; Tolbert, S. H. General Method for the Synthesis of Hierarchical Nanocrystal-Based Mesoporous Materials. *ACS Nano* **2012**, *6*, 6386–6399.
- ¹³ Buonsanti, R.; Pick, T. E.; Krins, N.; Richardson, T. J.; Helms, B. A.; Milliron, D. J. Assembly of Ligand-Stripped Nanocrystals into Precisely Controlled Mesoporous Architectures. *Nano Lett.* **2012**, *12*, 3872–3877.
- ¹⁴ Warren, S. C.; Messina, L. C.; Slaughter, L. S.; Kamperman, M.; Zhou, Q.; Gruner, S. M.; DiSalvo, F. J.; Wiesner, U. Ordered Mesoporous Materials from Metal Nanoparticle-Block Copolymer Self-Assembly. *Science* **2008**, *320*, 1748–1752.
- ¹⁵ Brezesinski, B.; Wang, J.; Polleux, J.; Dunn, B.; Tolbert, S. H. Templated Nanocrystal-Based Porous TiO₂ Films for Next-Generation Electrochemical Capacitors. *J. Am. Chem. Soc.* **2009**, *131*, 1802–1809.
- ¹⁶ Rosen, E. L.; Buonsanti, R.; Llodes, A.; Sawvel, A. M.; Milliron, D. J.; Helms, B. A. Exceptionally Mild Reactive Stripping of Native Ligands from Nanocrystal Surfaces by Using Meerwein's Salt. *Angew. Chem. Int. Ed.* **2012**, *51*, 684–689.

-
- ¹⁷ Conway, B. E.; Pell, W. G. Double-layer and Pseudocapacitance Type of Electrochemical Capacitors and their Applications to the Development of Hybrid Devices. *J. Solid State Electrochem.* **2003**, *7*, 637–644.
- ¹⁸ Miller, J. R.; Simon, P. Electrochemical Capacitors for Energy Management. *Science* **2008**, *321*, 651–652.
- ¹⁹ Dong, A.; Ye, X.; Chen, J.; Kang, Y.; Gordon, T.; Kikkawa, J. M.; Murray, C. B. A Generalized Ligand-Exchange Strategy Enabling Sequential Surface Functionalization of Colloidal Nanocrystals. *J. Am. Chem. Soc.* **2011**, *133*, 998–1006.
- ²⁰ Chen, X.; Pomerantseva, E.; Banerjee, P.; Gregorczyk, K.; Ghodssi, R.; Rubloff, G. Ozone-Based Atomic Layer Deposition of Crystalline V₂O₅ Films for High Performance Electrochemical Energy Storage. *Chem. Mater.* **2012**, *24*, 1255–1261.
- ²¹ Chen, X.; Zhu, H.; Chen, Y-C.; Shang, Y.; Cao, A.; Hu, L.; Rubloff, G. MWCNT/V₂O₅ Core/Shell Sponge for High Areal Capacity and Power Density Li-Ion Cathodes. *ACS Nano* **2012**, DOI: 10.1021/nn302417x.

CHAPTER 2

Copper Indium Diselenide Nanotubes and Nanowires Produced From Highly Soluble Hydrazinium-Based Precursors and Nanoporous Templates

2.1 Introduction

Copper indium diselenide (CuInSe_2 or CIS) has received much attention in the field of photovoltaics because of its direct band gap (~ 1 eV), high optical absorption coefficient ($3\text{--}6 \times 10^5 \text{ cm}^{-1}$) and stable electro-optical properties.¹ CuInSe_2 , a ternary semiconductor, belongs to the I-III-VI₂ group of semiconductors and takes on a tetragonal chalcopyrite crystal structure. To date, CuInSe_2 ^{2,3} and related CuInGaSe_2 ^{4,5} thin-film photovoltaic devices have demonstrated high power conversion efficiencies that make them exciting candidates for next generation solar cell technologies. Both *p*-type and *n*-type CuInSe_2 has been prepared and characterized electronically, optically and structurally.^{6–11} While several techniques are available to synthesize both bulk single-crystals and thin-films of CIS,^{12–16} it is more of a challenge to generate complex yet still well-defined morphologies. Thoughtfully designed and structurally controlled semiconducting materials are desirable because they can serve as building blocks for a wide variety of functional composites. In the case of CuInSe_2 , nanodimensional architectures are interesting because charge-transport within the material can be directed by tailoring the nanoscale architecture. Some interesting morphologies that have been prepared include CuInSe_2 nanorings,¹⁷ nanocrystals with a trigonal shape,¹⁸ nanocables,¹⁹ nanowhiskers,²⁰ and nanowires.^{21–23} CuInSe_2 nanotube arrays were

synthesized on conductive glass substrates by using ZnO nanorod arrays as sacrificial templates involving multiple ion exchange steps.²⁴ Other template-assisted approaches have utilized porous anodic alumina, leading to CuInSe₂ nanotubes arrays via galvanic displacement methods,²⁵ as well as nanowire arrays via electrodeposition techniques.^{26,27} In this paper, we add to this palate of nanostructured CIS with a new solution phase route to nanowires and nanotubes arrays.

In 2004, IBM developed a solution-based method for fabricating high quality thin, continuous, and crystalline films of metal chalcogenide semiconductors using hydrazine as a solvent.²⁸ This simple approach uses excess chalcogen to improve the solubility of selected main group metal chalcogenides in hydrazine through the formation of highly soluble hydrazinium-salts that can be solution processed and then decomposed to reform metal chalcogenide at low temperature.²⁸ Several metal chalcogenide semiconductors have been prepared by this chemistry, including CuInSe₂, CuInTe₂, In₂Se₃, ZnTe, SnSe₂ and SnS₂.^{28–32} Recently, this method was further used to prepare CuIn(Se,S)₂² and CuInGaSe₂⁵ thin-film photovoltaic devices that demonstrated good performances. This hydrazine-precursor method offers several attractive features including a low temperature annealing step, low volume change after thermal decomposition, high throughput processing (spin-coating, printing, or stamping) and cost-effectiveness.

Despite the great versatility of this chemistry, to date, these soluble precursors have only been reported for the production of thin (or thick) films. In this work, we utilize this solution-phase route to prepare CuInSe₂ nanotubes and nanowires via a template assisted method. We incorporated the CuInSe precursor solution into

nanoporous aluminum oxide templates and thermally decomposed the precursor to the CuInSe₂ semiconductor. Depending on the amount of solution used, either tubes or wires could be generated. The alumina was then chemically etched away, leaving behind arrays of high aspect ratio tubes or wires. X-ray diffraction studies confirm formation of the chalcopyrite phase of CuInSe₂ and energy-dispersive X-ray studies confirm the 1:1:2 CuInSe₂ stoichiometry. Moreover, electrical conductivity measurements suggest the nanowires are electrically interconnected along their entire length.

2.2 Results and Discussion

2.2.1 Synthesis and Characterization of CuInSe₂ Nanostructures

In our work, the hydrazine-based CuInSe₂ precursor was prepared by dissolving copper(I) sulfide, elemental sulfur, indium(III) selenide and selenium in hydrazine.²⁹ CuInSe₂ nanotubes were produced from a single incorporation into the porous alumina (Figure 2.1). Figure 2.1a–c shows typical SEM images at various magnifications of free standing CuInSe₂ nanotubes after removal from a porous alumina template with a pore diameter of 200 nm. Figure 2.1d shows nanotubes prepared using templates with 100 nm pore diameter. In Figure 2.1b, the arrows point to a cross section of a CuInSe₂ nanotube with a wall thickness of 40 nm. Typical wall thicknesses varied from 20 nm to 40 nm for tubes prepared in 200 nm pores and from 10 nm to 25 nm in 100 nm pores. The outer diameter of the tubes was defined by the pore size leading to tubes with outer diameters of 200 nm ± 20 nm (Figure 2.1a–c) and 100 nm ± 10 nm (Figure 2.1d).

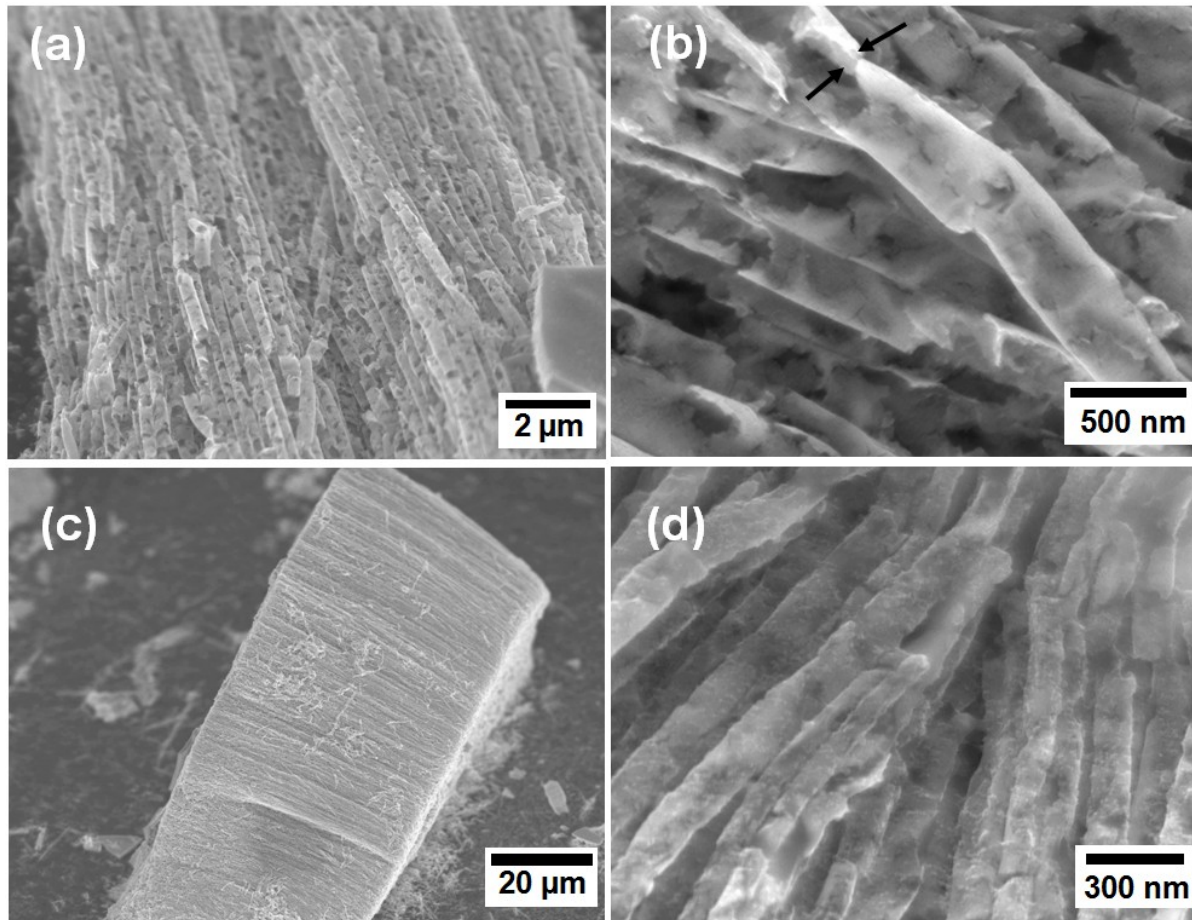


Figure 2.1. SEM images of free standing CuInSe_2 nanotubes after removal from porous alumina with (a–c) 200 nm sized pore and (d) 100 nm sized pore. The arrows in (b) point to a cross section of a nanotube with a wall thickness of 40 nm. The formation of tube structures after a single incorporation suggests the hydrazine solvent wets the inside of the alumina pore walls during the incorporation. The fact that tubes are produced in both 100nm and 200nm pores further shows that the pore entirely defines the final CuInSe_2 nanotube structure.

Average inner diameters varied from 120 nm to 160 nm for tubes prepared in 200 nm pores and from 50 nm to 80 nm in 100 nm pores.

Remarkably, the tubes extend the entire 60 μm length of the pores in the template as shown in Figure 2.1c. It should be noted from the SEM images in Figure 2.1 that the nanotubes are not completely dense and some regions are not fully connected, however, the tubes remain intact upon the template removal process. Because we obtain homogeneous nanotubes from this synthesis, we conclude that the hydrazine-CuInSe₂ precursor wets the inner walls of the pores. The areas that are discontinuous might be attributed the contraction of the tube during the thermal conversion process and/or the chemical etching of the template.

CuInSe₂ nanowires were produced using multiple incorporations to fill the entire tube volume. Figure 2.2 shows SEM images at various magnifications of free standing CuInSe₂ nanowires produced from 200 nm pores (Figure 2.2a–c) and 100 nm pores (Figure 2.2d). As in the case of the nanotubes discussed above, the outer diameter of the nanowires was defined by the pore size leading to tubes with outer diameters of 200 nm \pm 20 nm (Figure 2.2a–c) and 100 nm \pm 10 nm (Figure 2.2d). The nanowires also exhibit high aspect ratios with lengths up to 60 μm (Figure 2.2c). As shown in the high magnification image (Figure 2.2b), the nanowires appear to be more continuous and structurally more robust than the nanotubes. It is evident from our results that the final architecture and dimensions of the nanotubes and nanowires are defined by the template. The pores of the alumina membrane are cylindrical leading to nanotubes and nanowires. Therefore, producing a wide range of interesting and complex

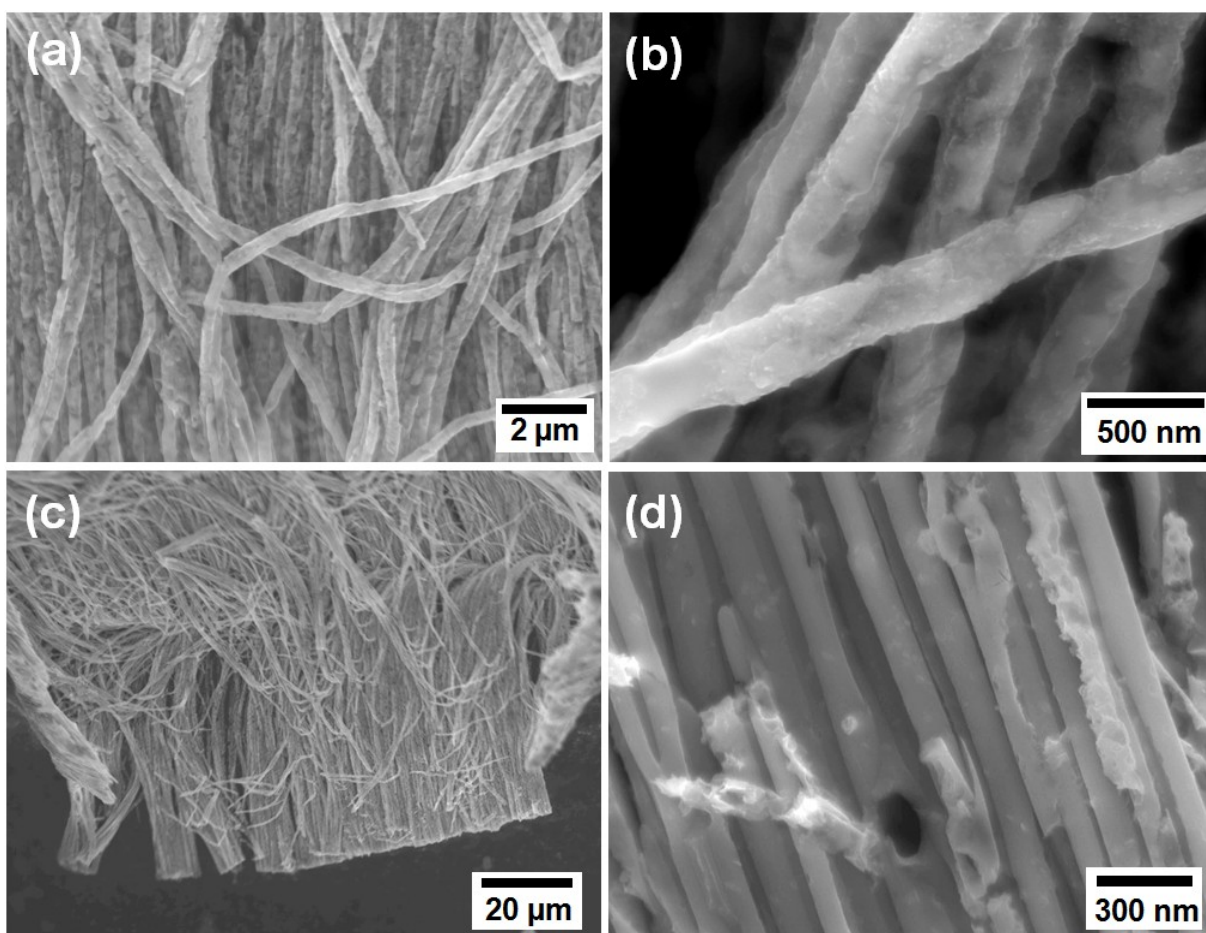


Figure 2.2. SEM images of free standing CuInSe_2 nanowires after removal from porous alumina with (a–c) 200 nm sized pore and (d) 100 nm sized pore. As previously described, in the first incorporation, the hydrazine wets the inside of the alumina pore walls to produce tubes. To form wires, multiple incorporations are required to fill the inner tube volume. Again, in this instance, the pore structure defines the final CuInSe_2 nanowire structure.

nanostructures should be feasible by varying the structures and dimensions of the template.

The phase and crystal structure of the nanotubes and nanowires were determined from X-ray diffraction and HRTEM analysis. Figure 2.3 depicts the XRD patterns of CuInSe₂ nanowires (green pattern) and nanotubes (blue pattern) embedded in a 200 nm pore alumina template. The XRD reflections can be indexed to the chalcopyrite tetragonal phase of CuInSe₂ (JCPDS reference card no. 73-351). Scherrer analysis of the diffraction data results in an average crystalline domain size of 12 ± 2 nm for the nanotubes and 13 ± 2 nm for the nanowires. No other phases or impurities are observed, consistent with energy-dispersive x-ray spectroscopy data in Figure 2.4 which gives an atomic stoichiometry of Cu_{0.9}In_{1.0}Se_{1.9}S_{0.1}. The slight Cu deficiency that is introduced results in a *p*-type material.²⁹ In agreement with previous reports, the excess sulfur required for the synthesis of the precursor is preferentially lost during the thermal decomposition step.²⁹

Diffraction peak intensities provide some information about domain alignment within the crystalline CuInSe₂ material. All data was collected on samples contained in the alumina pores with the x-ray beam impinging on the plane of the alumina membrane in a θ - θ geometry. The most intense diffraction peak observed for the nanowires is the (204)/(220). In the case of the nanotubes, both (112) and the (204)/(220) have similar intensities. The (312)/(116) peak is the weakest peak for both nanowires and nanotubes. The data for the both nanowires and nanotubes deviate from the relative intensities observed in bulk powders where the (112) is the strongest peak followed by the (204)/(220). These results suggests preferential orientation of the (204)/(220)

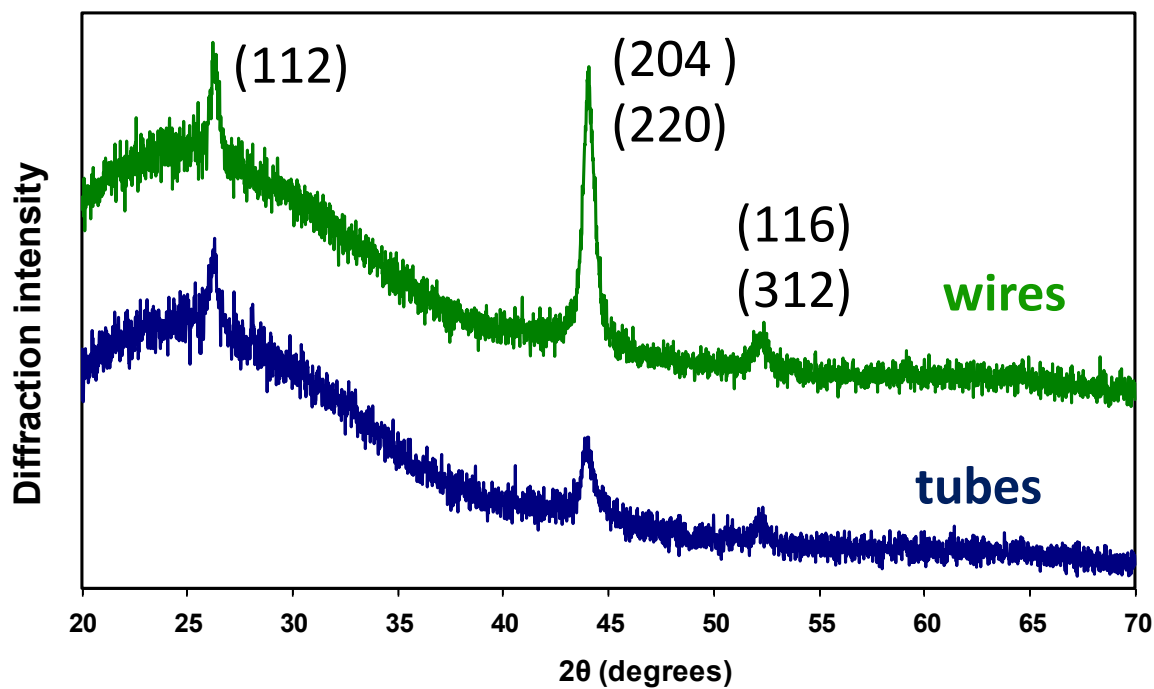


Figure 2.3. Typical X-ray diffraction patterns of CuInSe₂ nanowires (green pattern) and nanotubes (blue pattern) embedded in alumina template with 200nm pore size. The XRD reflections can be indexed to the chalcopyrite tetragonal phase of CuInSe₂.

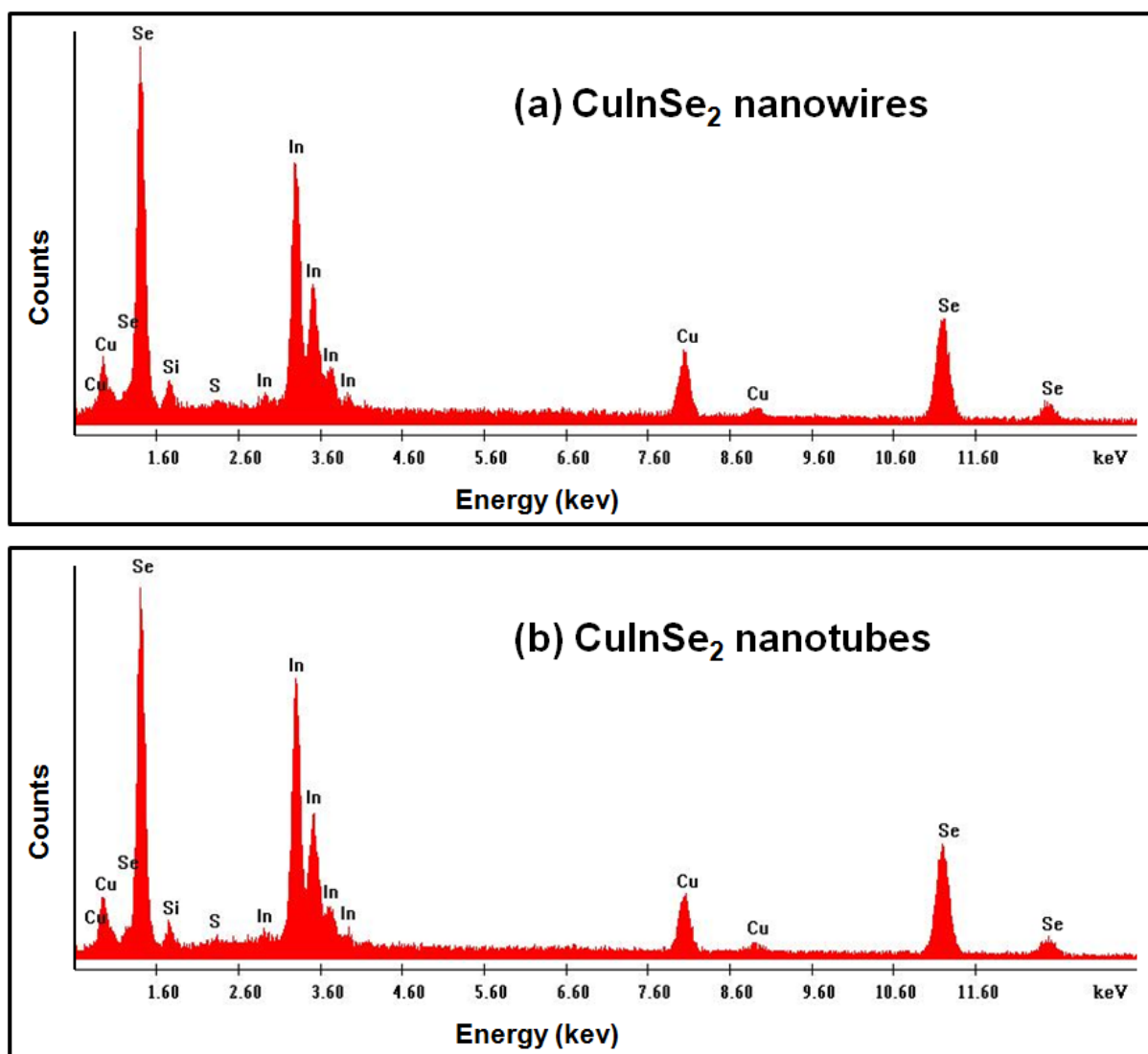


Figure 2.4. Energy dispersive X-ray spectra for CuInSe_2 nanowires (a) and nanotubes (b). From this data, the stoichiometry of both the nanowires and nanotubes was determined to be $\text{Cu}_{0.9}\text{In}_{1.0}\text{Se}_{1.9}\text{S}_{0.1}$.

direction along the tube/wire long axis. The preferred orientation effects are greater for the nanowires compared to the nanotubes.

Figure 2.5a–d shows TEM images of free standing nanotubes and nanowires. The morphology of the nanotubes (Figure 2.5a) is apparent from the dark edges of increased density going through the tube wall. In contrast, the nanowires (Figure 2.5b) appear completely dense. HRTEM images of the same nanowire (Figure 2.5c) and nanotube (Figure 2.5d) indicate both structures are polycrystalline in nature. In both Figure 2.5c and 2.4d, the lattice fringe spacing of 0.33 nm matches well to the interplanar spacing of the (112) plane of the chalcopyrite CuInSe_2 crystal structure. In Figure 2.5c the lattice fringe spacing of 0.25 nm matches well to the interplanar spacing of the (211) plane, and the lattice fringe spacing of 0.21 nm matches well to the interplanar spacing of the (220) plane. The average crystal domain sizes from HRTEM analysis are in agreement with the domain sizes calculated using the Scherrer equation from XRD data.

2.2.2 Conductivity Measurements

To investigate the electrical properties of CuInSe_2 nanostructures produced in this work, a $\text{Ag/CuInSe}_2/\text{Ag}$ Schottky diode was fabricated. Previously, *p*-type CuInSe_2 was prepared using the hydrazine-precursor method and a slight copper deficiency was introduced by carefully controlling the Cu:In ratio during synthesis.²⁹ Similar *p*-type CuInSe_2 is used in this work. Figure 2.6 depicts current density-voltage characteristics of a CuInSe_2 nanowire array still embedded in the original alumina template. Ag paint was used for both top and bottom contacts. Under bias, the current density-voltage curve in Figure 2.6a shows diodic behavior with a turn-on voltage of 5 V. A logarithmic

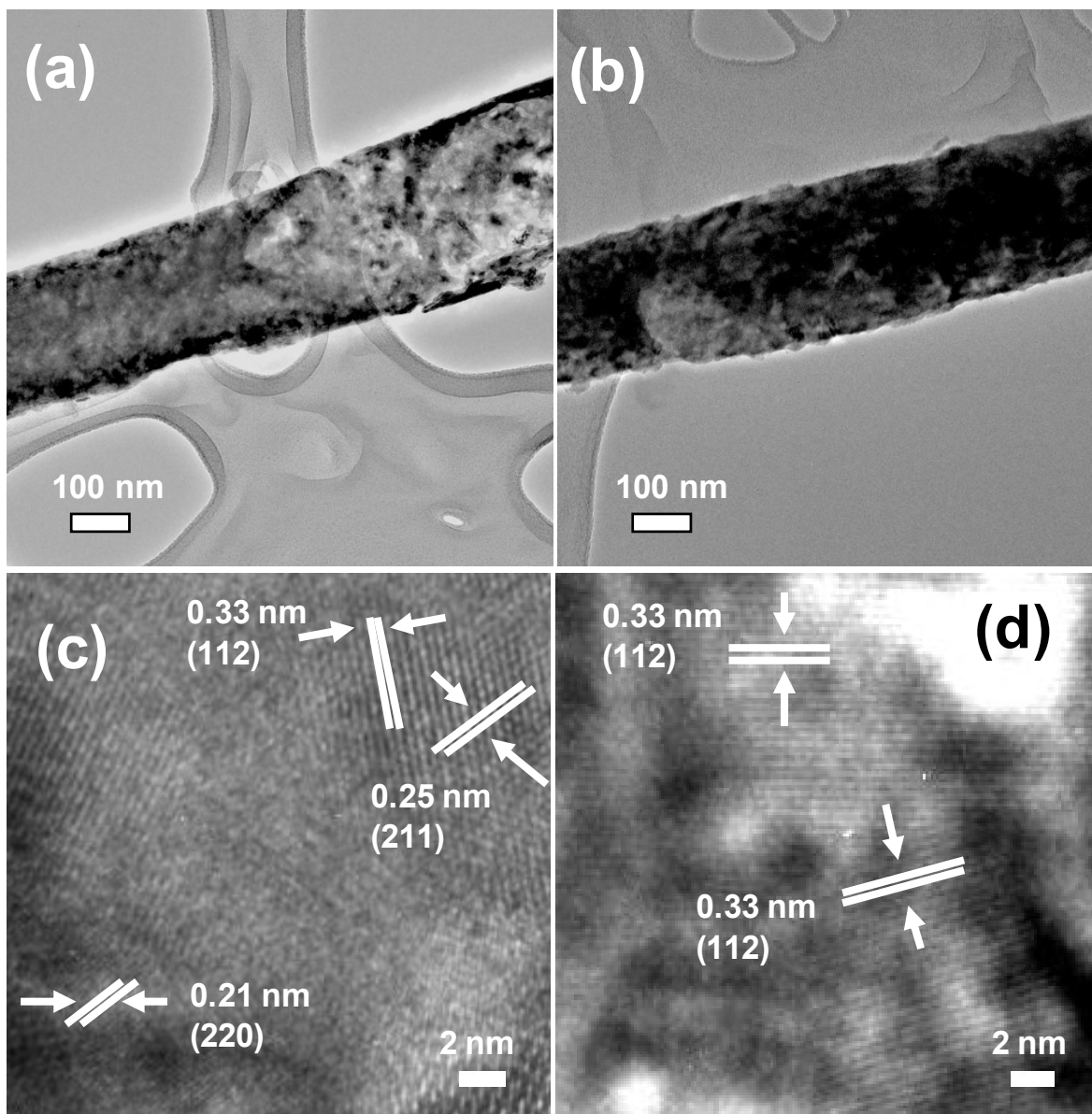


Figure 2.5. TEM image of a free standing CIS nanotube (a) shows a typical tube wall structure with an empty volume, while the nanowire (b) shows a dense structure. HRTEM images of a nanotube (c) and a nanowire (d) show the expected lattice planes of the chalcopyrite structure.

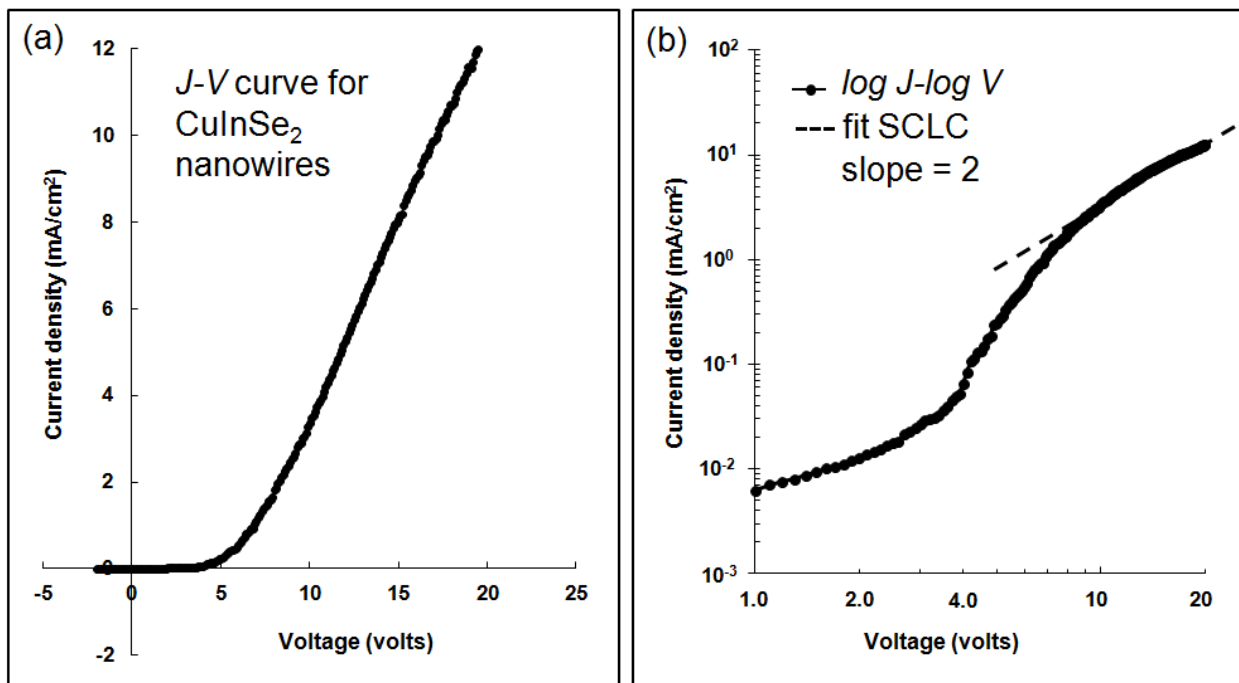


Figure 2.6. Experimental current density versus voltage characteristics of CuInSe₂ nanowires embedded in a porous aluminum oxide template. (a) Typical J-V curve for the nanowires shows diodic behavior with a turn on voltage of 5 V. (b) A plot of log J vs. log V shows a space-charge limited conduction behavior with a trap space-charge limited region, a trap-filling region and a trap-free space-charge conductivity region. A fit to the trap-free space-charge limited region is shown as a dashed line with a slope = 2. Space-charge limited current fits to this data produce a mobility of $65 \pm 10 \text{ cm}^2 \text{ V}^{-1} \text{ sec}^{-1}$.

current density-voltage plot is shown in Figure 2.6b. The curve shows a space-charge limited conduction behavior with a trap-space charge limited region, a trap filling region and a trap free space charge conductivity region, consistent with previous reports.¹¹ A fit to the trap-free space charge limited region is shown as a dashed line with a slope = 2. SCLC fits to this data produce a mobility of $65 \pm 10 \text{ cm}^2 \text{ V}^{-1} \text{ sec}^{-1}$. This value is within the standard range of mobilities reported in the literature for room temperature measurements on p-type CuInSe_2 , including mobilities of $84 \text{ cm}^2 \text{ V}^{-1} \text{ sec}^{-1}$ for bulk, and $19 \text{ cm}^2 \text{ V}^{-1} \text{ sec}^{-1}$ for thin-films.^{33,34} These results suggest the CuInSe_2 material is electrically interconnected throughout the entire length of the nanowires. Current-voltage data obtained for CuInSe_2 nanotubes like those shown in Figure 2.1a–d showed lower current and poor reproducibility. This indicates that these nanotubes generally contain at least one break or discontinuity somewhere along their $60 \text{ }\mu\text{m}$ length. By carefully controlling the volume of precursor incorporated, it is likely that nanotubes that maintain a porous interior without breaks could be produced.

2.3 Conclusions

In conclusion, we have prepared CuInSe_2 nanotubes and nanowires via a simple template-assisted approach. Single incorporation of the CuInSe_2 soluble precursor leads to nanotubes while multiple incorporations that fill the entire tube volume lead to nanowires. The CuInSe_2 nanotubes and nanowires are identified as the chalcopyrite phase of CuInSe_2 . The nanowires are electrically interconnected and demonstrate typical charge carrier mobilities. These results suggest this approach offers a new method for producing novel complex CuInSe_2 structures from a solution-based

precursor. Because the final architecture appears to be controlled mostly by the wetting of the hydrazine solution, wire formation does not require that all of the multiple incorporations make use of the same precursor solutions. By infiltrating the tubes with a variety of different solutions, it may be possible to construct hetero-structured materials that exhibit unique properties. Perhaps more importantly, this method should be general to all of the metal chalcogenide semiconductors that have been prepared by this hydrazinium salt chemistry because incorporation and wetting are controlled by hydrazine and not the precursor.

2.4 Experimental

2.4.1 Synthesis of CuInSe₂ Precursor

The hydrazine-based CuInSe₂ precursor was synthesized according to a previously established procedure.²⁹ In a typical synthesis of CuInSe₂ precursor, Cu₂S (159 mg, 1.0 mmol), S (64 mg, 2.0 mmol), In₂Se₃ (467 mg, 1.0 mmol) and Se (79 mg, 1.0 mmol) were dissolved in 8 mL of anhydrous hydrazine in a single reaction. *Caution: hydrazine is highly toxic and should be handled with appropriate protective equipment to prevent contact with either the vapors or liquid.* The dissolution of the reactants in anhydrous hydrazine to form the soluble CuInSe₂ precursor results in a yellow solution. The yellow precursor solution was allowed to stir overnight. The CuInSe₂ precursor formed large particles which were filtered before incorporating into the porous template. Both the CuInSe₂ precursor synthesis and infiltration steps were carried out in a N₂ filled glove box.

2.4.2 Preparation of CuInSe₂ Nanotubes and Nanowires

In a typical preparation of CuInSe₂ nanotubes, 0.1 mL of the precursor solution was drop cast onto a commercially available porous alumina template (200 nm or 100 nm pore size, 60 μ m thickness, 25 mm diameter). A glass slide was placed on top to allow the solution to enter the pores by capillary action and the solvent was allowed to evaporate. The incorporation process was repeated several times to fill the entire pore volume to produce nanowires. The precursor-filled template was then thermally annealed at 350 °C for 20 minutes to allow complete conversion of the hydrazinium salt to crystalline CuInSe₂. Both the incorporation and thermal annealing steps were carried out in a N₂ filled glove box.

2.4.3 Methods

Ag/CuInSe₂/Ag Schottky diodes were fabricated with CuInSe₂ nanotubes and nanowires embedded in the alumina template. The CuInSe₂-alumina sample was sandwiched between Ag paint electrodes. Current-voltage characteristics were measured with a Keithly 2400 SourceMeter. A space-charge limited current model (SCLC) was used to extract the charge carrier mobility.

CuInSe₂ characterization was performed using (i) powder X-ray diffraction (XRD), (ii) scanning electron microscopy (SEM) with an energy-dispersive X-ray (EDX) spectroscopy attachment, and (iii) transmission electron microscopy (TEM). All XRD measurements were performed with the CuInSe₂ embedded into the alumina template. XRD measurements were performed with a Panalytical X'Pert PRO diffractometer. SEM samples were prepared by placing the CuInSe₂-alumina onto a piece of carbon

tape attached to a Si substrate and then immersing the entire sample into 3M NaOH for 3 h to remove the alumina template. The sample was rinsed several times with deionized water before imaging. TEM samples were similarly prepared by immersing the CuInSe₂-alumina into 3M NaOH for 3 h and rinsing several times with water. The alumina-free CuInSe₂ nanostructures suspended in ethanol were then drop-cast onto a copper grid and allowed to air dry before measurement. Low magnification and high magnification TEM images were collected on a FEI Titan using an accelerating voltage of 300 kV.

2.5 References

- ¹ Kazmerski, L. L. Status and Assessment of Photovoltaic Technologies. *Intern. Mater. Rev.* **1989**, *34*, 185–210.
- ² Liu, W.; Mitzi, D. B.; Yuan, M.; Kellock, A. J.; Chey, S. J.; Gunawan, O. 12% Efficiency CuIn(Se,S)₂ Photovoltaic Device Prepared Using a Hydrazine solution Process. *Chem. Mater.* **2010**, *22*, 1010–1014.
- ³ AbuShama, J. A. M.; Johnston, S.; Moriarty, T.; Teeter, G.; Ramanathan, K.; Noufi, R. Properties of ZnO/CdS/CuInSe₂ Solar Cells with Improved performance. *Prog. Photovoltaics* **2004**, *12*, 39–45.
- ⁴ Repins, I.; Contreras, M. A.; Egaas, B.; DeHart, C.; Scharf, J.; Perkins, C. L.; To, B.; Noufi, R. 19.9%-Efficient ZnO/CdS/CuInGaSe₂ Solar Cell with 81.2% Fill Factor. *Prog. Photovoltaics* **2008**, *16*, 235–239.
- ⁵ Mitzi, D. B.; Yuan, M.; Liu, W.; Kellock, A. J.; Chey, S. J.; Deline, V.; Schrott, A. G. A High-Efficiency Solution-Deposited Thin-Film Photovoltaic Device. *Adv. Mater.* **2008**, *20*, 3657–3662.
- ⁶ Rife, J. C.; Dexter, R. N.; Bridenbaugh, P. M.; Veal, B. W. Optical Properties of the Chalcopyrite Semiconductors ZnGeP₂, ZnGeAs₂, CuGaS₂, CuAlS₂, CuInSe₂, and AgInSe₂. *Phys. Rev. B.* **1977**, *16*, 4491–4500.
- ⁷ Neumann, H.; Bullett, D. W.; Sommer, H.; Tomlinson, R. D.; John, W. Valence Bands of the Cu-III-VI₂ Chalcopyrites Studied by Photoemission Spectra, X-Ray Emission Spectra, and Electronic Structure Calculations. *Phys. Stat. Sol.* **1984**, *121*, 641–647.

-
- ⁸ Worz, M.; Pschorr-Schoberer, E.; Flierl, R.; Preis, H.; Gebhardt, W. Photoelectron Spectroscopy of Chalcopyrites and Zn Based II-VI Semiconductor Heterostructures. *J. Appl. Phys.* **1998**, *84*, 2871–2875.
- ⁹ Agilan, S.; Mangalaraj, D.; Narayandass, S. K.; Rao, G. M.; Velumani, S. Structure and Temperature Dependence of Conduction Mechanisms in Hot Wall Deposited CuInSe₂ Thin Films and Effect of Back Contact Layer in CuInSe₂ Based Solar Cells. *Vacuum* **2010**, *84*, 1220–1225.
- ¹⁰ Prasad, J. J. B.; Rao, D. K.; Sridevi, D.; Majhi, J.; Reddy, K. V.; Sobhanadri, J. Characteristics of *n*-CuInSe₂/Au Schottky Diodes. *Solid-State Electronics* **1985**, *28*, 1251–1254.
- ¹¹ Yalcin, N.; Al-Saffar, I. S.; Tomlinson, R. D. Space-Charge-Limited Current Effects in *n*-Type CuInSe₂/Au Schottky Diodes. *J. Appl. Phys.* **1981**, *52*, 5857–5858.
- ¹² Guillemoles, J. F.; Cowache, P.; Massaccesi, S.; Thouin, L.; Sanchez, S.; Lincot, D.; Vedel, J. Solar Cells with Improved Efficiency Based on Electrodeposited Copper Indium Diselenide Thin Films. *Adv. Mater.* **1994**, *6*, 379–381.
- ¹³ Singh, R. P.; Singh, S. L. Electrodeposited Semiconducting CuInSe₂ Films: II. Photo-electrochemical Solar Cells. *J. Phys. D: Appl. Phys.* **1986**, *19*, 1759–1769.
- ¹⁴ Prabahar, S.; Balasubramanian, V.; Suryanarayanan, N.; Muthukumarasamy, N. Compositional and Electrical Resistivity Studies on Thermal Evaporation Copper Indium Diselenide Thin Films. *J. Ovonic Research* **2009**, *5*, 207–211.
- ¹⁵ Yamanaka, S.; Konagai, M.; Takahashi, K. Characterization of Copper Indium Diselenide Thin Films by Raman Spectroscopy for Solar Cell Applications. *Japanese J. of Appl. Phys.* **1989**, *28*, L 1337–1340.

-
- ¹⁶ Arsene, M. A.; Albacete, A.; Voillot, F.; Peyrade, J. P.; Barra, A.; Galibert, J.; Wasim, S. M.; Hernandez, E. Synthesis and Growth of Large Stoichiometric Single Crystals of Copper Indium Diselenide by Horizontal Varying Gradient Zone Freeze Technique. *J. Crystal Growth* **1996**, *158*, 97–102.
- ¹⁷ Guo, Q.; Kim, S. J.; Kar, M.; Sharaman, W. N.; Birkmire, R. W.; Stach, E. A.; Agrawal, R.; Hillhouse, H. W. Development of CuInSe₂ Nanocrystal and Nanoring Inks for Low-Cost Solar Cells. *Nano Lett.* **2008**, *8*, 2987–2987.
- ¹⁸ Koo, B.; Patel, R. N.; Korgel, B. A. Synthesis of CuInSe₂ Nanocrystals with Trigonal Pyramidal Shape. *J. Am. Chem. Soc.* **2009**, *131*, 3134–3135.
- ¹⁹ Xu, J.; Lee, C. S.; Tang, Y. B.; Chen, X.; Chen, Z. H.; Zhang, W. J.; Lee, S. T.; Zhang, W.; Yang, Z. Large-Scale Synthesis and Phase Transformation of CuSe, CuInSe₂, and CuInSe₂/CuInS₂ Core/Shell Nanowire Bundles. *ACS Nano* **2010**, *4*, 1845–1850.
- ²⁰ Li, B.; Xie, Y.; Huang, J.; Qian, Y. Synthesis by a Solvothermal Route and Characterization of CuInSe₂ Nanowhiskers and Nanoparticles. *Adv. Mater.* **1999**, *11*, 1456–1459.
- ²¹ Peng, H.; Schoen, D. T.; Meister, S.; Zhang, X. F.; Cui, Y. Synthesis of Phase Transformation of In₂Se₃ and CuInSe₂ Nanowires. *J. Am. Chem. Soc.* **2007**, *129*, 34–35.
- ²² Schoen, D. T.; Peng, H.; Cui, Y. Anisotropy of Chemical Transformation from In₂Se₃ to CuInSe₂ Nanowires through Solid State Reaction. *J. Am. Chem. Soc.* **2009**, *131*, 7973–7975.

-
- ²³ Peng, H.; Xie, C.; Schoen, D. T.; McIlwrath, K.; Zhang, X.; F. Ciu, Y. Ordered Vacancy Compounds and Nanotube Formation in CuInSe₂-CdS Core-Shell Nanowires. *Nano Lett.* **2007**, *7*, 3734–3738.
- ²⁴ Xu, J.; Luan, C. Y.; Tang, Y. B.; Chen, X.; Zapien, J. A.; Zhang, W. J.; Kwong, H. L.; Meng, X. M.; Lee, S. T.; Lee, C. S. Low-Temperature Synthesis of CuInSe₂. *ACS Nano* **2010**, *4*, 6064–6070.
- ²⁵ Zhou, T.; Zheng, M.; Ma, L.; He, Z.; Li, M.; Li, C.; Shen, W. Size Control of CuInSe₂ Nanotube Arrays via Nanochannel-Confined Galvanic Displacement. *J. Mater. Chem.* **2011**, *21*, 17091–17093.
- ²⁶ Phok, S.; Rajaputra, S.; Singh, V. Copper Indium Diselenide Nanowire Arrays by Electrodeposition in Porous Alumina Templates. *Nanotechnology* **2007**, *18*, 475601(1–8).
- ²⁷ Liu, P.; Singh, V. P.; Rajaputra, S.; Phok, S.; Chen, Z. Characteristics of Copper Indium Diselenide Nanowires Embedded in Porous Alumina Templates. *J. Mater. Res.* **2010**, *25*, 207–212.
- ²⁸ Mitzi, D. B.; Kosbar, L. L.; Murray, C. E.; Copel, M.; Afzali, A. High-Mobility Ultrathin Semiconducting Films Prepared by Spin Coating. *Nature* **2004**, *428*, 299–303.
- ²⁹ Milliron, D. J.; Mitzi, D. B.; Copel, M.; Murray, C. E. Solution-Processed Metal Chalcogenide Films for *p*-Type Transistors. *Chem. Mater.* **2006**, *3*, 587–590.
- ³⁰ Mitzi, D. B.; Copel, M.; Murray, C. E. High-Mobility *p*-Type Transistor Based on a Spin-Coated Metal Telluride Semiconductor. *Adv. Mater.* **2006**, *18*, 2448–2452.

-
- ³¹ Mitzi, D. B.; Copel, M.; Chey, S. J. Low-Voltage Transistor Employing a High-Mobility Spin-Coated Chalcogenide Semiconductor. *Adv. Mater.* **2005**, *17*, 1285–1289.
- ³² Mitzi, D. B. Polymorphic One-Dimensional $(\text{N}_2\text{H}_4)_2\text{ZnTe}$: Soluble Precursors for the Formation of Hexagonal or Cubic Zinc Telluride. *Inorg. Chem.* **2005**, *44*, 7078–7086.
- ³³ Champness, C. H.; Cheung, T.; Shih, I. Room Temperature Transport Measurements on Bridgman-Grown *p*-Type $\text{CuIn}_{1-x}\text{Ga}_x\text{Se}_2$. *Solar Energy Materials & Solar Cells* **2007**, *91*, 791–800.
- ³⁴ Shah, N. M.; Ray, J. R.; Kheraj, V. A.; Desai, M. S.; Panchal, C. J.; Rehani, B. Structural, Optical, and Electrical Properties of Flash-Evaporated Copper Indium Diselenide Thin Films. *J. Mater. Sci.* **2009**, *44*, 316–322.

CHAPTER 3

Directing Anisotropic Charge Transport of Layered Organic-Inorganic Hybrid Perovskite Semiconductors in Porous Templates

3.1 Introduction

Layered organic-inorganic hybrid perovskites represent a unique class of materials that exhibit interesting electronic, optical, and magnetic properties.^{1–8} The properties of these materials result from the intimate combination of organic and inorganic components within their structure.^{9–12} For example, the metal-halide based hybrid perovskites are comprised of 2-dimensional (2D) sheets of corner-sharing metal-halide octahedral layers that are separated by organic cation layers to form an alternating layered structure. The extended covalent nature of the inorganic layers results in unidirectional charge transport along the 2D semiconducting sheets. The ability to tailor the band gap of these materials has been demonstrated through chemical modifications to the organic cations by various functional moieties resulting in tunable optoelectronic properties.^{13–17} Hybrid perovskites have been integrated into several types of devices including field-effect transistors, photoconductors, and light-emitting diodes.^{18–22} These materials can thus be thought of as something akin to a chemically tunable, easily synthesized semiconductor superlattice.

While there are many exciting aspects to these hybrid perovskites, structurally, they are fairly limited. Thin films uniformly show layers oriented parallel to the substrate, resulting in materials with good in-plane conductivity and poor out of plane conductivity.

While the semiconducting layers are quantum confined in one direction, there are few reports of producing these materials in any form other than bulk crystals or powders, and thin films.²³ The ability to manipulate both the crystallographic orientation and the direction of anisotropic conductivity would be highly desirable in order to fully exploit their unique electrical properties. It could also be interesting to use these materials to fabricate nanostructures, such as nanowires or nanoscrolls. In this work, our goal is thus to build nanostructures with a controllable conductive axis using host/guest chemistry in combination with some of the unique processing capabilities of hybrid perovskites.

One of the most important features of these metal-halide based semiconducting perovskites is their low-temperature melt-process capability.^{24,25} The presence of organic cations in the crystal structure renders these materials highly soluble in a range of polar solvents, making them ideal candidates for solution-phase deposition. The potential to melt-anneal those solution processed inorganic semiconductors at low temperature is cost beneficial, scalable and does not require the utility of high vacuum conditions, making it an attractive and versatile engineering method. This was demonstrated in the fabrication of a high performance thin-film transistor (TFT) device using the 2D layered organic-inorganic perovskite $(\text{C}_6\text{H}_5\text{C}_2\text{H}_4\text{NH}_3)_2\text{SnI}_4$ as the semiconducting channel using all solution-phase deposition methods.¹⁸ The spin-coated thin-film formed a p-channel transistor that demonstrated characteristics comparable to amorphous silicon and state-of-the-art vacuum-deposited organic semiconductors.¹⁸ In that work, the TFT demonstrated high mobility parallel to the substrate, a result which stemmed from the highly-oriented 2D inorganic sheets.

Directing the charge transport perpendicular to the substrate becomes interesting for building other types of devices that rely on electronic conductivity along this direction.

Controlling the anisotropic behavior of functional materials has been effectively accomplished through confinement of the material within porous anodic alumina templates with highly ordered cylindrical nanochannels. Reports include anisotropic magnetic behavior in quasi-1-dimensional nanostructures,²⁶ anisotropic thermal expansion of Bi nanowires,²⁷ and anisotropic photoluminescence in select lanthanides.²⁸ Materials synthesis within a cylindrical nanochannel resulted in the formation of mesoporous silicas with unique helical architectures.²⁹ Here, we build upon this rich literature to fabricate vertically-aligned concentric cylinder or scroll arrays of the layered organic-inorganic hybrid perovskite semiconductor $(\text{C}_6\text{H}_5\text{C}_2\text{H}_4\text{NH}_3)_2\text{SnI}_4$ via confinement into a porous template with cylindrical channels. The arrays exhibit anisotropic electrical conductivity in the direction out-of-plane with respect to the substrate that stems from control over the crystallographic orientation of the semiconductor within the pores of the template.

3.2 Results and Discussion

3.2.1 Synthesis and Characterization of Hybrid Arrays

The synthesis and melting temperature (213.4 °C) of the $(\text{C}_6\text{H}_5\text{C}_2\text{H}_4\text{NH}_3)_2\text{SnI}_4$ perovskite were previously reported in the literature.^{13,24} Figure 3.1a shows a schematic illustration of the perovskite structure consisting of infinite corner-sharing SnI_6 octahedra that form extended SnI_4^{4-} 2D sheets that are charge stabilized by organic cation bilayers. All syntheses and processing were performed in a glove box or using

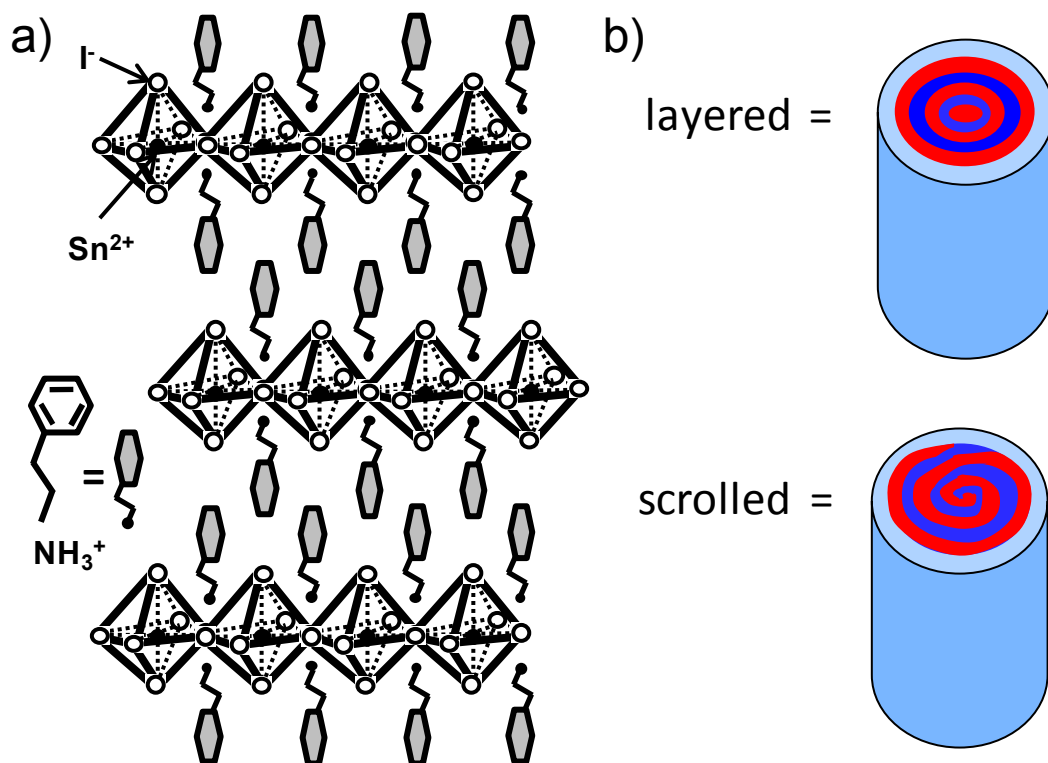


Figure 3.1. (a) Schematic illustration of the organic-inorganic hybrid perovskite structure. In the $(\text{C}_6\text{H}_5\text{C}_2\text{H}_4\text{NH}_3)_2\text{SnI}_4$ system, the corner sharing SnI_6 octahedra form extended SnI_4^{2-} 2D inorganic semiconducting sheets that are charge stabilized by organic cation bilayers. (b) Schematic illustration of concentric layers (top) and a single rolled scroll of layers (bottom) within cylindrical pores.

standard Schlenk techniques under inert atmosphere as the hybrid is an air-sensitive material. The hybrid formed red crystals that were dissolved in methanol at 20 mg/ml; this solution was then used to spin-coat thin-films onto silicon substrates. The films were then melt-annealed after spin coating at few degrees above the melting temperature of 213.4 °C. Figure 3.2a shows the X-ray diffraction (XRD) pattern of a spin-coated thin-film that exhibits well-defined peaks corresponding to the (0 0 l) reflections. The presence of strictly (0 0 l) peaks suggests that the hybrid is both crystalline and highly oriented with the organic-inorganic layers preferentially aligned in the plane of the substrate. Because of the lamellar structure of the hybrid, it self-assembles with the organic-inorganic layers parallel to the planar surface, characteristic of a highly anisotropic material. The interlayer distance between the inorganic sheets was determined to be 16.3 Å which is in agreement with previous reports.¹⁸ Moreover, the absence of any additional peaks confirms the perovskite is phase pure and free from impurities.

Our approach to produce the hybrid-alumina arrays involved depositing the perovskite from a methanolic solution and subsequently melting it to fill porous alumina channels that are 200 nm in diameter and 60 µm in length. Upon melting, the hybrid self-assembles to form concentric 2D layered arrays that are preferentially aligned along the direction of the alumina channels with a pore filling volume of 85–90%. To verify the crystallographic orientation we performed a series of XRD experiments. Figure 3.2b shows data that was collected on hybrid-alumina arrays with the X-ray beam impinging on the plane of the alumina membrane in a θ – θ geometry. The absence of (0 0 l) reflections suggests that the hybrid organic-inorganic layers are not oriented along the

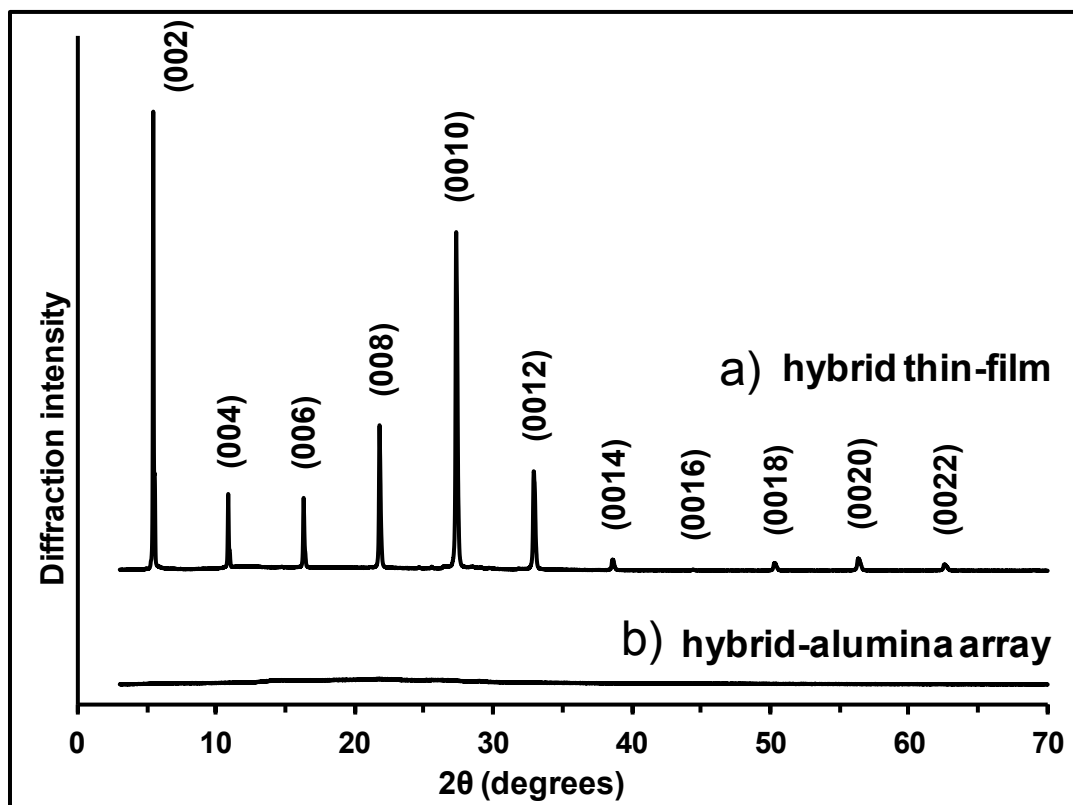


Figure 3.2. (a) XRD pattern for a spin-coated hybrid film. The appearance of well-defined peaks corresponding to the (0 0 l) reflections suggests the hybrid is highly crystalline with organic-inorganic layers oriented in the plane of the substrate. (b) XRD data for hybrid-alumina arrays with the X-ray beam impinging on the plane of the alumina membrane in a θ – θ geometry. No (0 0 l) peaks are observed confirming the hybrid layers are not oriented in the plane of the substrate.

plane of the substrate. A null result like this does not, however, confirm the crystallographic orientation within the channels.

To determine the crystallographic orientation of the material within the porous channels, we performed a series of 2D XRD studies. Figure 3.3a shows a diffraction pattern from a 2D transmission experiment where the X-ray beam impinged on the sample normal to the plane of the substrate and penetrated through the plane of hybrid-alumina arrays. The inset shows a schematic representation of the geometry used for this experiment. The appearance of a full diffraction ring with homogeneous intensity confirms that the sample contains layers oriented perpendicular to the substrate and that all possible orientations of layers within the plane are present. Given the geometry of the sample, the easiest way to generate that combination of lattice planes would be a sample composed of concentric layers or a single rolled scroll of layers with the scroll or wire axis oriented out-of-plane with respect to the substrate. Figure 3.1b shows schematic illustrations of such layered and scrolled structures.

To further confirm this geometry, Figure 3.3b depicts data that was collected from an experiment where the X-ray beam impinged on the sample edge-on with the plane of the anodic alumina oriented vertically in space. Again, the inset shows a schematic representation of the geometry used for this experiment. The presence of a single spot along the z-axis further confirms the preferred crystallographic orientation of the layers within the nanochannels – no scattering is observed in the x-direction as that represents the non-periodic axis of the concentric or rolled layers. For both Figures 3.3a and 3.3b, the peak position corresponds to an interlayer distance of 16.3 Å which is in agreement with the calculated distance from Figure 3.1a. No other diffracted rings or spots are

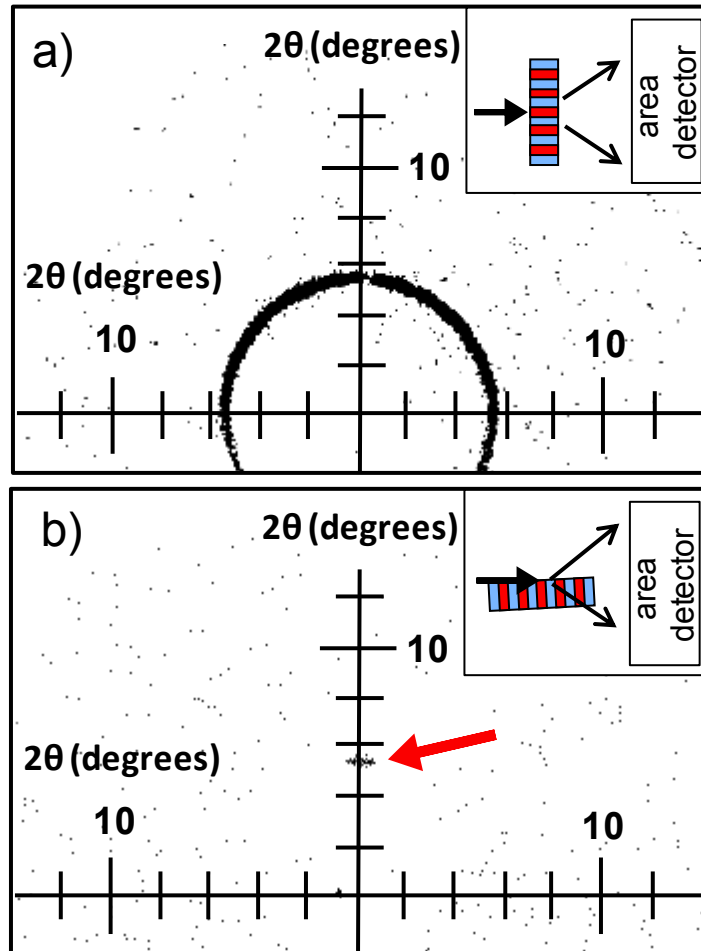


Figure 3.3. 2D transmission XRD results for hybrid-alumina arrays. (a) Data collected with the X-ray beam penetrating through the plane of the membrane producing a ring (inset shows schematic of this geometry). This pattern confirms the presence of concentric layers that are oriented perpendicular to the plane of the membrane. (b) Data collected with the X-ray beam impinging on the membrane edge-on (inset shows schematic of this geometry). The red arrow points to the appearance of a single spot, further confirming the unidirectional orientation of the layers inside the channels.

observed in Figure 3.3a–b, also suggesting the concentric layers are highly crystalline and oriented along the direction of the channels. Taken together, the data from all the XRD studies confirm that the control over the crystallographic orientation of the semiconductor has been achieved arising from confinement of a highly anisotropic material within the unidirectional porous channels.

3.2.2 Conductivity Measurements

We next investigated the electrical properties of the hybrid in both thin-film form and array configurations. Because the conductivity is so anisotropic, we expect to see reasonable conductivities only in plane for thin film samples and out-of-plane for the arrays. The band gap of $(\text{C}_6\text{H}_5\text{C}_2\text{H}_4\text{NH}_3)_2\text{SnI}_4$ perovskite has been reported to be 2.19 eV, typical of a wide-band gap semiconductor.³⁰ To measure the in-plane conductivity of the hybrid with respect to the substrate, we deposited two Ag paint electrodes on top of the spin-coated films. Figure 3.4a shows current density-voltage characteristics of a typical hybrid thin-film device. Under bias, the current density-voltage curve shows diodic behavior with a turn-on voltage of 12 V. In Figure 3.4b, a logarithmic plot of current density vs. voltage shows a characteristic space-charge limited conduction behavior. In Figure 3.4b, the dashed line shows a fit to the trap-free space-charge conductivity region where the slope = 2, producing a charge carrier mobility of $12.8 \text{ cm}^2 \text{ V}^{-1} \text{ sec}^{-1}$. This value is within the range of reported mobilities for $(\text{C}_6\text{H}_5\text{C}_2\text{H}_4\text{NH}_3)_2\text{SnI}_4$ perovskite TFT devices in which the hybrid formed a *p*-type channel.⁷

To measure conductivity on the hybrid-alumina arrays, samples were sandwiched between two Ag paint electrodes and conductivity was measured through plane. In Figure 3.5a, a representative plot of current density-voltage is shown, again

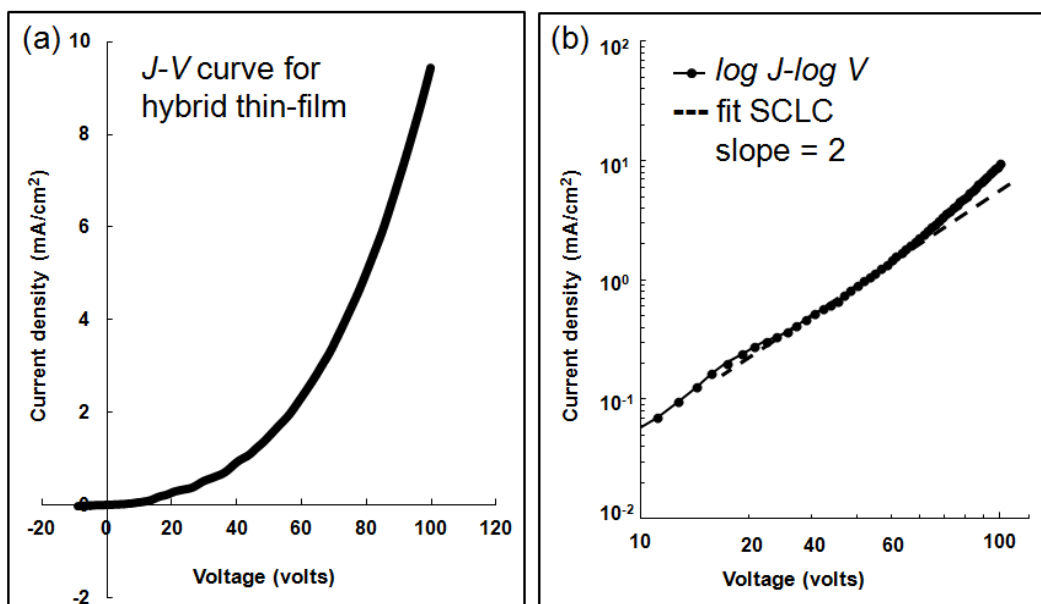


Figure 3.4. Experimental current density-voltage characteristics of a hybrid thin-film device. (a) Typical J-V curve for the spin-coated film shows diodic behavior with a turn on voltage of 12 V. (b) A logarithmic plot of J vs. V showing a space-charge limited conduction behavior with a trap-free space-charge conductivity region. A fit to this region, where the slope = 2, is represented by the dashed line. SCLC fits to this data produce a carrier mobility of $12.8 \text{ cm}^2 \text{ V}^{-1} \text{ sec}^{-1}$.

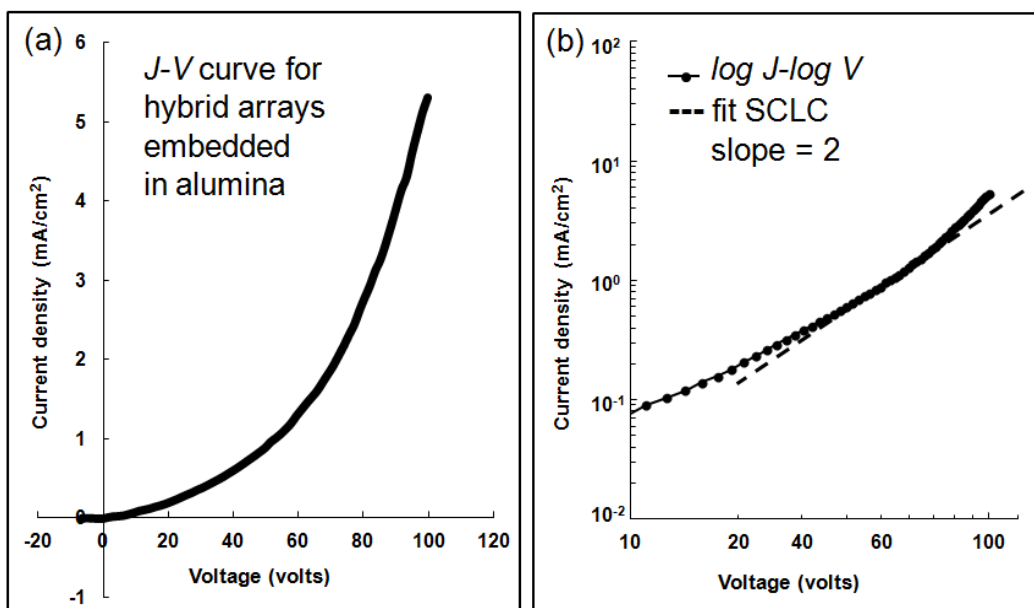


Figure 3.5. Experimental current density-voltage characteristics of the hybrid arrays embedded in alumina. (a) Under bias, the J-V curve shows diodic behavior with a turn on voltage of 10 V. (b) A logarithmic plot of J vs. V showing a space-charge limited conduction behavior with a trap-free space-charge conductivity region. A fit to this region, where the slope = 2, is represented by the dashed line. SCLC fits to this data produce a carrier mobility of $0.4 \text{ cm}^2 \text{ V}^{-1} \text{ sec}^{-1}$.

demonstrating typical diodic behavior with a similar turn-on voltage as in Figure 3.4a. The hybrid-alumina array device also shows a space-charge limited conduction behavior, shown in Figure 3.5b. SCLC fits to the data, where the slope = 2, produces a carrier mobility of $0.4 \text{ cm}^2 \text{ V}^{-1} \text{ sec}^{-1}$. While the current density and the carrier mobility are both greater for the thin-films compared to the hybrid-alumina arrays, the values differ by only a little over one order of magnitude.

The difference between the carrier mobilities can be explained by considering the morphology, grain structure, and grain boundary defects within the perovskite structure for each device. For instance, it is expected that the spin-coated films should exhibit a more homogenous morphology upon deposition with better connected grains and less defect sites, leading to better device performance. This is because the spin-coating process produces one continuous film that is homogeneously connected to both electrical contacts, minimizing defects along the conduction pathway. In contrast, for the hybrid-alumina arrays, the connectivity of the grains can become compromised when confined inside the pore channels, leading to an increased potential for traps and defects along the 2D concentric layers. We expect the embedded hybrid to experience higher resistance due to the curvature of the layers, thus leading to the observed significant reduction in mobility. Also, any pores that are not 100% filled will not contribute to the conductivity at all and we know that the pores are only 85–90% filled, leading to the conclusion that a significant number of pores could be only partly filled. Nonetheless, the electrical conductivity of the confined layered semiconductor is reasonable and in general agreement with reported values for hybrid thin-film devices.¹⁸ Collectively, the results presented here demonstrate that melting processing an

anisotropic semiconductor into unidirectional porous channels is an effective approach to creating nanowires from hybrid-perovskite materials. The materials retain much of the electrical conductivity of the original layered perovskites, but the conductive axis is now oriented along the wire direction, rather than in the plane of the substrate.

3.3 Conclusions

In this work, we have thus shown a new method to fabricate nanowire structures from the layered perovskite semiconductor $(\text{C}_6\text{H}_5\text{C}_2\text{H}_4\text{NH}_3)_2\text{SnI}_4$ by incorporating the material into porous alumina with cylindrical nanochannels. In our study, XRD experiments show that the organic-inorganic layers are preferentially aligned along the direction of the alumina channels, forming highly oriented concentric or rolled multilayered arrays. In agreement with this structural data, electrical measurements indicated that the conductive direction is changed from in-plane, as found in traditional spin-coated thin-films, to out-of-plane, in the hybrid-alumina arrays. This was accomplished by conversion of a traditional layered material to a new nanoscale architecture – nanorolls or nanorods composed of concentric layers.

Our results suggest this simple approach may be extended to other organic-inorganic layered perovskites that are prepared by similar solution/melt processes. In addition, it should be possible to prepare arrays with a broad range of well-defined dimensions by varying the dimensions of the alumina channels. It would also be interesting to explore other transport properties in these materials. While we cannot determine from XRD if the materials produced here are composed of rolls or concentric layers, if they are composed of concentric layers, they could show very interesting

magnetic field dependent conductivity. Less immediate, but also interesting to consider are wire arrays produced using non-cylindrical pores. For example, well defined pore arrays can be produced by combining lithographic patterning with highly directional etching.^{31,32} It is likely that the perovskite layers would similarly conform to such non-cylindrical pores after melt processing, producing semiconductor nanowires with a unique combination of curved and straight sections defined by the pores. The resulting materials could show exciting combinations of electrical, magnetic and optical behavior.

3.4 Experimental

3.4.1 Synthesis of Hybrid Perovskite

Crystals of $(\text{C}_6\text{H}_5\text{C}_2\text{H}_4\text{NH}_3)_2\text{SnI}_4$ were synthesized following previously reported procedures.^{13,18} In a typical synthesis, 1.118 g of SnI_2 (3 mmol) was transferred to a Schlenk flask under inert atmosphere. To this flask, 10 mL of anhydrous butanol was added through a syringe. Next, 0.79 mL of phenethylamine (6 mmol) was added to the flask and the solution was cooled to $-5\text{ }^\circ\text{C}$, upon which 2 mL of concentrated hydroiodic acid was added slowly. The solution was thoroughly mixed and heated to $94\text{ }^\circ\text{C}$ to allow complete dissolution of the SnI_2 . Finally, the solution was cooled to $0\text{ }^\circ\text{C}$ at $3\text{ }^\circ\text{C}/\text{hour}$. The red $(\text{C}_6\text{H}_5\text{C}_2\text{H}_4\text{NH}_3)_2\text{SnI}_4$ crystals were filtered and recrystallized twice from a mixture of anhydrous methanol and toluene. The crystals were dried under vacuum and stored in an argon-atmosphere glove box.

3.4.2 Preparation of Hybrid Thin-Films and Arrays

Perovskite solutions were prepared by dissolving 20 g of hybrid crystals in 1 mL of anhydrous methanol. This solution was used to spin-coat films onto clean silicon or

glass substrates, followed by melt-annealing at a few degrees above the melting temperature of ~ 214 °C. To prepare the hybrid-alumina arrays the perovskite solution was used to infiltrate the alumina membrane and allowed to dry. The commercially available alumina membranes had cylindrical channels that were 200 nm in diameter and 60 μm in length. Several infiltration steps were carried out until a 85–90% pore filling was obtained, determined by weighing the amount of hybrid. The hybrid-alumina composite was then heated a few degrees above the melting temperature, ~ 214 °C, to allow the hybrid to melt into the alumina nanochannels.²⁴ All processing steps were carried out in a N_2 filled glove box.

3.4.3 Methods

1D-WAXD measurements were performed on an XPert PRO MPD diffractometer from Panalytical instruments. 2D-WAXD measurements were carried out on a D8-GADDS diffractometer from Bruker instruments (Cu $\text{K}\alpha$ radiation) equipped with an energy dispersive solid-state area detector.

Hybrid thin-film devices were prepared by depositing two Ag paint electrodes onto spin-coated thin-films. Hybrid-alumina array devices were fabricated by sandwiching the membrane in between two Ag paint electrodes. Current-voltage characteristics were measured with a Keithly 2612A System SourceMeter. A space-charge limited current model (SCLC) was used to extract the charge carrier mobility.

3.5 References

- ¹ Mitzi, D. B.; Feild, C. A.; Harrison W. T. A.; Guloy, A. M. Conducting Tin Halides with a Layered Organic-Based Perovskite Structure. *Nature* **1994**, *369*, 467–469.
- ² Mitzi, D. B.; Wang, S.; Feild, C. A.; Chess, C. A.; Guloy A. M. Conducting Layered Organic-Inorganic Halides Containing (100)-Oriented Perovskite Sheets. *Science* **1995**, *267*, 1473–1476.
- ³ Li, Y.; Zheng, G.; Lin, C.; Lin J. New Organic-Inorganic Perovskite Materials with Different Optical Properties Modulated by Different Inorganic Sheets. *Crystal Growth & Design* **2008**, *8*, 1990–1996.
- ⁴ Vishwakarma, A. K.; Ghalsasi, P. S.; Navamoney, A.; Lan, Y.; Powell, A. K. Structural Phase Transition and Magnetic Properties of Layered Organic-Inorganic Hybrid Compounds: *p*-Haloanilinium Tetrachlorocuparate(II). *Polyhedron* **2011**, *30*, 1565–1570.
- ⁵ Mitzi, D. B. Synthesis, Crystal Structure, and Optical and Thermal Properties of $(C_4H_9NH_3)_2MI_4$ (M = Ge, Sn, Pb). *Chem. Mater.* **1996**, *8*, 791–800.
- ⁶ Mitzi, D. B.; Brock P Structure and Optical Properties of Several Organic-Inorganic Hybrids Containing Corner-Sharing of Bismuth Iodide Octahedra. *Inorg. Chem.* **2001**, *40*, 2096–2104.
- ⁷ Zhang, S.; Audebert, P.; Wei, Y.; Lauret, J. S.; Galmichec, L.; Deleporte E. Synthesis and Optical Properties of Novel Organic-Inorganic Hybrid UV (R-NH₃)₂PbCl₄ Semiconductors. *J. Mater. Chem.* **2011**, *21*, 466–474.

-
- ⁸ Kitazawa, N.; Watanabe, Y. Optical Properties of Natural Quantum-Well Compounds $(\text{C}_6\text{H}_5\text{-C}_n\text{H}_{2n}\text{-NH}_3)_2\text{PbBr}_4$ ($n=1\text{-}2$). *J. Phys. and Chem. of Solids* **2010**, *71*, 797–802.
- ⁹ Mitzi, D. B. Thin-Film Deposition of Organic-Inorganic Hybrid Materials. *Chem. Mater.* **2001**, *13*, 3283–3298.
- ¹⁰ Mitzi, D. B. Solution-Processed Inorganic Semiconductors. *J. Mater. Chem.* **2004**, *14*, 2355–2365.
- ¹¹ Wang, S.; Mitzi, D. B.; Field, C. A.; Guloy, A. Synthesis and Characterization of $[\text{NH}_2\text{C(I)=NH}_2]_3\text{MI}_5$ ($\text{M} = \text{Sn, Pb}$): Stereochemical Activity in Divalent Tin and Lead Halides Containing Single (100) Perovskite Sheets. *J. Am. Chem. Soc.* **1995**, *117*, 5297–5302.
- ¹² Mitzi, D. B. Organic-Inorganic Perovskites Containing Trivalent Metal Halide Layers: The Templating Influence of the Organic Cation Layer. *Inorg. Chem.* **2000**, *39*, 6107–6113.
- ¹³ Mitzi, D. B.; Dimitrakopoulos, C. D.; Kosbar L. L. Structurally Tailored Organic-Inorganic Perovskites: Optical Properties and Solution-Processed Channel Materials for Thin-Film Transistors. *Chem. Mater.* **2001**, *13*, 3728–3740.
- ¹⁴ Xu, Z.; Mitzi, D. B. SnI_4^{2-} -Based Hybrid Perovskites Templated by Multiple Organic Cations: Combining Organic Functionalities through Noncovalent Interactions. *Chem. Mater.* **2003**, *15*, 3632–3637.
- ¹⁵ Mercier, N.; Poiroux, S.; Riou, A.; Batail P. Unique Hydrogen Bonding Correlating with a Reduced Band Gap and Phase Transition in the Hybrid Perovskites $(\text{HO}(\text{CH}_2)_2\text{NH}_3)_2\text{PbX}_4$ ($\text{X} = \text{I, Br}$). *Inorg. Chem.* **2004**, *43*, 8361–8366.

-
- ¹⁶ Knutson, J. L.; Martin, J. D.; Mitzi D. B. Tuning the Band Gap in Hybrid Tin Iodide Perovskite Semiconductors Using Structural Templating. *Inorg. Chem.* **2005**, *44*, 4699–4705.
- ¹⁷ Sourisseau, S.; Louvain, N.; Bi, W.; Mercier, N.; Rondeau, D.; Boucher, F.; Buzare, J. Y.; Legein C. Reduced Band Gap Hybrid Perovskite Resulting from Combined Hydrogen and Halogen Bonding at the Organic-Inorganic Interface. *Chem. Mater.* **2007**, *19*, 600–607.
- ¹⁸ Kagan, C. R. ; Mitzi, D. B. ; Dimitrakopoulos C. D. Organic-Inorganic Hybrid Materials as Semiconducting Channels in Thin-Film Field-Effect Transistors. *Science* **1999**, *286*, 945–947.
- ¹⁹ Li, C. R.; Deng, H. T.; Wan, J.; Zheng, Y. Y.; Dong W. J. Photoconductive Properties of Organic-Inorganic Hybrid Perovskite $(\text{C}_6\text{H}_{13}\text{NH}_3)_2(\text{CH}_3\text{NH}_3)_{m-1}\text{Pb}_m\text{I}_{3m+1}:\text{TiO}_2$ Nanocomposites Device Structure. *Mater. Lett.* **2010**, *64*, 2735–2737.
- ²⁰ Era, M.; Morimoto, S.; Tsutsui, T.; Saito S. Organic-Inorganic Heterostructure Electroluminescent Device using a Layered Perovskite Semiconductor $(\text{C}_6\text{H}_5\text{C}_2\text{H}_4\text{NH}_3)_2\text{PbI}_4$. *Appl. Phys. Lett.* **1994**, *65*, 676–678.
- ²¹ Chondroudis, K.; Mitzi, D. B. Electroluminescence from an Organic-Inorganic Perovskite Incorporating a Quaterthiophene Dye within Lead Halide Perovskite Layers. *Chem. Mater.* **1999**, *11*, 3028–3030.

-
- ²² Koutselas, I.; Bampoulis, P.; Maratou, E.; Evagelinou, T.; Pagona, G.; Papavassiliou, G. C. Some Unconventional Organic-Inorganic Hybrid Low-Dimensional Semiconductors and Related Light-Emitting Devices. *J. Phys. Chem. C* **2011**, *115*, 8475–8483.
- ²³ Cheng, Z. Y.; Wang, Z.; Xing, R. B.; Han, Y. C.; Lin, J. Patterning and Photoluminescent Properties of Perovskite-Type Organic/Inorganic Hybrid Luminescent Films by Soft Lithography. *Chem. Phys. Lett.* **2003**, *376*, 481–486.
- ²⁴ Mitzi, D. B.; Medeiros, D. R.; DeHaven, P. W. Low-Temperature Melt Processing of Organic-Inorganic Hybrid Films. *Chem. Mater.* **2002**, *14*, 2839–2841.
- ²⁵ Mitzi, D. B.; Dimitrakopoulos, C. D.; Rosner, J.; Medeiros, D. R.; Xu, Z.; Noyan, C. Hybrid Field-Effect Transistor Based on a Low-Temperature Melt-Processed Channel Layer. *Adv. Mater.* **2002**, *14*, 1772–1776.
- ²⁶ Lukatskaya, M. R.; Trusov, L. A.; Eliseev, A. A.; Lukashin, A. V.; Jansen, M.; Kazin, P. E.; Napolskii, K. S. Controlled Way to Prepare Quasi-1D Nanostructures with Complex Chemical Composition in Porous Anodic Alumina. *Chem. Commun.* **2011**, *47*, 2396–2398.
- ²⁷ Zhu, Y.; Dou, X.; Huang, X.; Li, L.; Li, G. Thermal Properties of Bi Nanowire Arrays with Different Orientations and Diameters. *J. Phys. Chem. B* **2006**, *110*, 26189–26193.
- ²⁸ Gaponenko, N. V.; Hluzd, Y. V.; Maliarevich, G. K.; Molchan, I. S.; Thompson, G. E.; Dabboussi, S.; Elhouichet, H.; Prislopski, S. Y.; Lutich, A. A. Room-Temperature Photoluminescence from Porous Anodic Alumina Films with Embedded Terbium and Europium Species. *Mater. Lett.* **2009**, *63*, 621–624.

-
- ²⁹ Wu, Y.; Cheng, G.; Katsov, K.; Sides, S. W.; Wang, J.; Tang, J.; Fredrickson, G. H.; Moskovits, M.; Stucky, G. D. Composite Mesostructures by Nano-Confinement. *Nat. Mater.* **2004**, *3*, 816–822.
- ³⁰ Papavassiliou, G. C.; Koutselas, I. B.; Terzis, A.; Whangbo, M. H. Structural and Electrical Properties of the Natural Quantum-Well System $(\text{C}_6\text{H}_5\text{CH}_2\text{NH}_3)_2\text{SnI}_4$. *Solid State Commun.* **1994**, *91*, 695–698.
- ³¹ Chamran, F.; Yeh, Y.; Min, H-S.; Dunn, B.; Kim, C-J. Fabrication of High-Aspect-Ratio Electrode Arrays for Three-Dimensional Microbatteries. *J. Microelectromechanical Systems* **2007**, *16*, 844–852.
- ³² Sun, G.; Hur, J. I.; Zhao, X.; Kim, C-J. Fabrication of Very-High-Aspect-Ratio Micro Metal Posts and Gratings by Photoelectrochemical Etching and Electroplating. *J. Microelectromechanical Systems* **2011**, *20*, 876–884.

CHAPTER 4

Nanoporous Semiconductors Synthesized Through Polymer Templating of Ligand-Stripped CdSe Nanocrystals

4.1 Introduction

The push to develop new functional materials for both catalysis and energy related applications has produced a surge of interest in producing mesoporous architectures from functional materials. When nanostructured materials are made mesoporous with an open and interconnected pore structure, the surface area of that material becomes accessible to the solvent environment, allowing materials to be optimized for specific chemical transformations and redox reactions. Examples of processes that could benefit from functional mesoporous materials vary from catalysis and photocatalysis to solar energy harvesting and electrochemical charge storage.¹⁻⁷

One particularly exciting family of systems for many of these applications, particularly those involving absorption of solar radiation, is main-group semiconductor nanocrystals. These materials have been shown to exhibit a broad range of exciting optical and electronic properties, making them suitable for integration into a diverse family of devices.⁸⁻¹¹ The literature includes a vast number of synthetic routes to produce stable semiconductor nanocrystals with controlled compositions, shapes, and sizes.¹²⁻¹⁸ In general, these syntheses leave the surface of nanocrystals capped with organic ligands that act to stabilize the nanocrystals and prevent aggregation. Monodisperse nanocrystals of this type can be crystallized into highly periodic arrays,

containing many different types of nanocrystal.^{19, 20} While compositionally and topologically diverse materials can be created, the resulting materials are often neither conductive nor porous because of the surface passivating groups. In many cases, removal of these surface stabilizing groups leads to undesirable agglomeration or etching.^{21,22} Conductivity problems have been partially resolved by depositing a dense film of nanocrystals, followed by a ligand-exchange with a very small, organic ligand.^{23–25} Materials have also been synthesized with inorganic ligands that can be thermally processed to produce nanocrystals embedded in a conductive matrix.^{26–29} While these methods can be used to solve the conductivity problem, the resulting materials are mostly dense and so they do not provide solvent access to the tremendous intrinsic interfacial area of these nanocrystal based materials.

Recently, some very beautiful sol-gel methods for assembling colloidal nanocrystals of various semiconductors into porous aerogels have been reported.^{30–33} This sol-gel method has been used to prepare highly porous aerogels from various chalcogenide semiconductor nanocrystals, including CdSe,³⁰ CdTe,^{31,32} CdS,³⁰ PbS,³⁰ ZnS³⁰ and Ag₂Se³³. These aerogels have been shown to exhibit typical absorption of quantum-confined semiconductors. These sol-gel method produce the desirable combination of high surface area and open porosity, although the pores are fairly large with a broad pore size distribution that ranges from mesopores to macropores (~2–120 nm).^{32,33} For the preparation of such aerogels, an efficient and specific surface reaction is also usually necessary in order to gelate the colloids; to date the method has only been applied to chalcogenide based systems. As a result, while this aero-gel work marks a major advance in the field, there is still a need for a general method for building

mesoporous semiconductor, particularly in thin film format, with smaller and more homogeneous porosity from a broader range of semiconductor nanocrystals.

While aerogels like those described above may be the most familiar form of porous materials, another route to produce mesoporous materials is through solution-phase self-assembly of soluble building blocks, typically molecular inorganic precursors, with a structure directing template such as amphiphilic surfactants or block copolymers.^{34–39} In many cases, sol-gel chemistries are utilized, producing oxide-based inorganic materials through an evaporation-induced self-assembly process (EISA).^{40–44} In this simple approach, the organic template forms micelles, and upon evaporation of the solvent, the inorganic precursors co-assemble with the micelles and self-organize into an organic-inorganic composite. The template is then thermally decomposed, usually in air, to yield a mesoporous architecture.

In recent years, the utilization of large diblock copolymers as templating agents has led to the synthesis of porous materials with crystalline walls that exhibit large mesopores with good solvent accessibility to the pore volume.^{45–50} Unfortunately, the surface area of these large pore materials tends to be fairly modest as wall thicknesses are in the 10–20 nm range, rather than the 5 nm range. To address this problem, significant recent advances have been made in the synthesis of nanoporous materials from assembly of pre-formed nanocrystal building blocks into hierarchical mesoporous architectures.^{5,51–56} Such materials combine the accessibility of large-pore materials, with the surface area of much smaller-pore systems. Nanocrystal-based nanoporous materials have now been made from systems as diverse as oxides, metals, and fluorides.^{5,54–56} The one thing shared by all systems made to date, however, is the fact

that they are air stable. This is because decomposition of the polymer template is generally carried out in oxidative conditions.

While there are many interesting applications for noble metal and oxide nanocrystal-based porous materials, the ability to assemble non-oxide nanocrystals, such as main-group semiconductors, into porous films would significantly broaden the spectrum of applications for these high surface area porous materials. In particular, applications such as solar energy harvesting and photocatalysis generally require mid-to-low band gap semiconductors, and these are difficult to produce in oxide systems. However, as discussed above, semiconductor nanocrystals have organic surface ligands that make them unsuitable for polymer templating in polar solvents.

Huge strides have recently been made in solving these problems using soluble, ligand-free nanocrystals. A series of recent reports indicate that it is now possible to strip native ligands off the surface of nanocrystals to produce bare, stable nanocrystals that are soluble in polar organic solvents.^{57–59} Such nanocrystals can be easily processed into conductive films.⁶⁰ More importantly, we have recently demonstrated that these ligand-free nanocrystals can be templated to form high surface area nanoporous architectures using block copolymer templating.^{51,52} While our previous work was a major step toward realizing materials that combine electrical connectivity, high surface area, and open porosity, the materials were still limited by one major constraint – only oxidatively stable materials could be produced as the polymer template was thermally degraded in air at elevated temperature.

In this work, we build from our previous nanocrystal templating results by extending this approach to oxidatively unstable materials. This work focuses on the

synthesis of mesoporous materials from ligand-stripped cadmium selenide (CdSe) nanocrystals as a model system, but the method should be general to the broad family of main group semiconductor nanocrystals. We specifically utilize recently developed chemistries that use Meerwein's salt (Et_3OBF_4) to gently strip ligands from the surface of CdSe nanocrystals.⁵⁹ The ligand-stripped CdSe nanocrystals are then combined with a block copolymer that can be thermally decomposed to volatile species under inert conditions. We show that mesoporous CdSe-based materials retain their semiconducting properties, including quantum confined excitonic absorption and modest carrier mobilities. These standard properties are then complemented by new features, such as homogeneous open porosity and high surface area. This work thus builds a bridge between the structural complexity of templated porous materials, and the electronic and optical complexity of semiconductor nanocrystals. While this work utilizes one of the most common semiconductor nanocrystals, CdSe, it is important to point out that nothing in the assembly methods used here takes advantage of CdSe specific chemistries. Because the assembly process itself is independent of the synthesis and reactivity of the CdSe itself, our approach should be applicable across the wide range of semiconductor nanocrystals which can be prepared as ligand-free dispersions using the Meerwein's salt process.

4.2 Results and Discussion

4.2.1 Preparation of Mesoporous CdSe Nanocrystal-Based Films

As discussed above, in order to template nanocrystals, they must be stripped of their native ligands in order to form stable dispersions in polar solvents. Here, we utilize

previously reported methods to produce ligand-stripped or “bare” CdSe nanocrystals.^{59, 61} Briefly, oleate-passivated CdSe (CdSe-OA) nanocrystals were synthesized according to literature procedures using the automated synthesis robot, WANDA.⁶² In a typical ligand-exchange process, a solution of Et₃OBF₄ in acetonitrile (MeCN) is added to CdSe-OA nanocrystals dispersed in hexane, forming a biphasic solution. The reaction mixture is vortexed, resulting in oleate ligand stripping with subsequent charge stabilization by BF₄⁻ anions. The resultant “bare” nanocrystals are then washed and redispersed in dimethylformamide (DMF). Figure 4.1a shows a transmission electron microscope (TEM) image of CdSe nanocrystals after the ligand-exchange process with an average diameter of 4.1 ± 0.3 nm. The image shows that the nanocrystals are not agglomerated or fused together after Et₃OBF₄ treatment.^{59,61} This is important, because to effectively assemble nanocrystals into robust networks, they must be bare and individually dispersed. Previous work has shown that the size of a species that can be organized by a block copolymer is directly related to the molecular weight of the polymer itself.⁵³ The modest sized polymer used here cannot organize a large nanocrystal or aggregates of nanocrystals (which are equivalent). Bare nanocrystals are required because the nanocrystals must fuse into a robust network at temperatures below the thermal degradation point of the polymer template with minimal volume change.

Because CdSe can oxidize to form both CdO and SeO₂, another important element for templating CdSe nanocrystals is to use a polymer template that can be decomposed under non-oxidizing conditions. Here, we use the diblock copolymer poly(butylene oxide)-*block*-poly(ethylene oxide), (PBO(5000)-*b*-PEO(6500), $M_n = 11500$

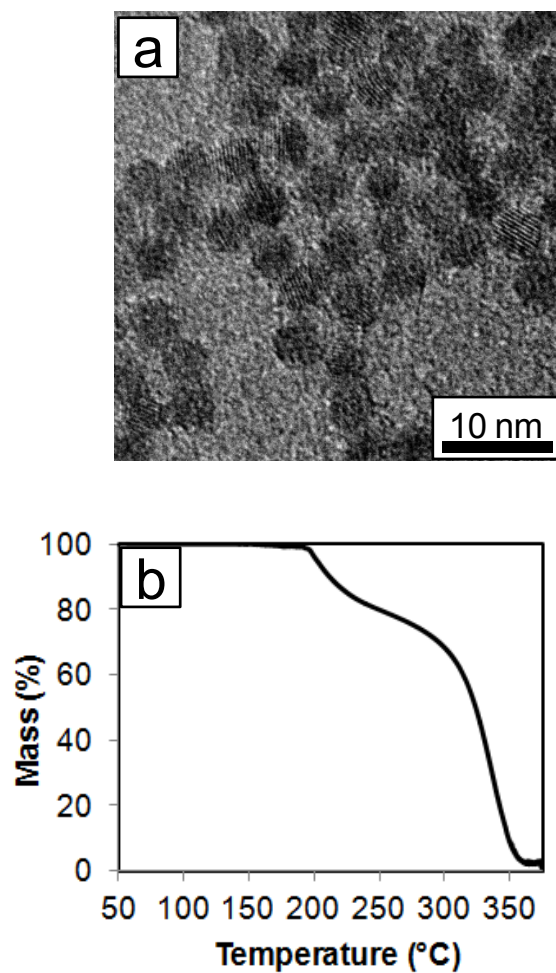


Figure 4.1. (a) TEM image of CdSe nanocrystals after treatment with Et_3OBF_4 . The nanocrystals are monodisperse and non-agglomerated. (b) TGA data for PBO-*b*-PEO at a constant heating rate of $1\text{ }^\circ\text{C min}^{-1}$ under a flowing argon atmosphere. The data indicate that this diblock copolymer can be fully degraded under inert atmosphere by $350\text{ }^\circ\text{C}$.

g mol⁻¹), which has ether functional groups along the backbone for both blocks. This ether functionality provides an oxygen source during thermal degradation of the polymer that leads to the production of volatile species from both blocks. Unlike typical pluronic surfactants, however, which are based on combination of PEO with poly(propylene oxide),^{38,40} the hydrophobic contrast between PBO and PEO is quite good and so strong segregation of blocks is observed in a range of polar organic solvents. Figure 4.1b shows a thermal gravimetric analysis (TGA) trace for PBO-*b*-PEO heated under argon. The data confirm that the polymer is fully decomposed by 350 °C in the absence of oxygen. This is important because chemically unstable materials, like CdSe nanocrystals, are unable to withstand oxidizing environments. In a typical synthesis of CdSe mesoporous films, a dispersion of ligand-stripped CdSe nanocrystals in DMF was combined with polymer, also dissolved in DMF. From this solution, films were prepared by spin-coating onto polar substrates, followed by thermal treatment to 400 °C under argon.

4.2.2 Structural Characterization

Figure 4.2 shows (a) low- and (b) high-magnification scanning electron microscope (SEM) images of CdSe nanocrystal-based mesoporous films with an average thickness of 120 ± 20 nm, as determined by profilometry measurements. The films show the appearance of locally disordered mesopores. As discussed above, the size of the polymer determines the size of nanocrystals it can assemble; therefore, it is likely that a larger polymer would produce more ordered pores.⁵³ It is important to note, however, that while the films do not show periodic pores, they do demonstrate macroscopic homogeneity of the mesopores, with the mesopores having an average

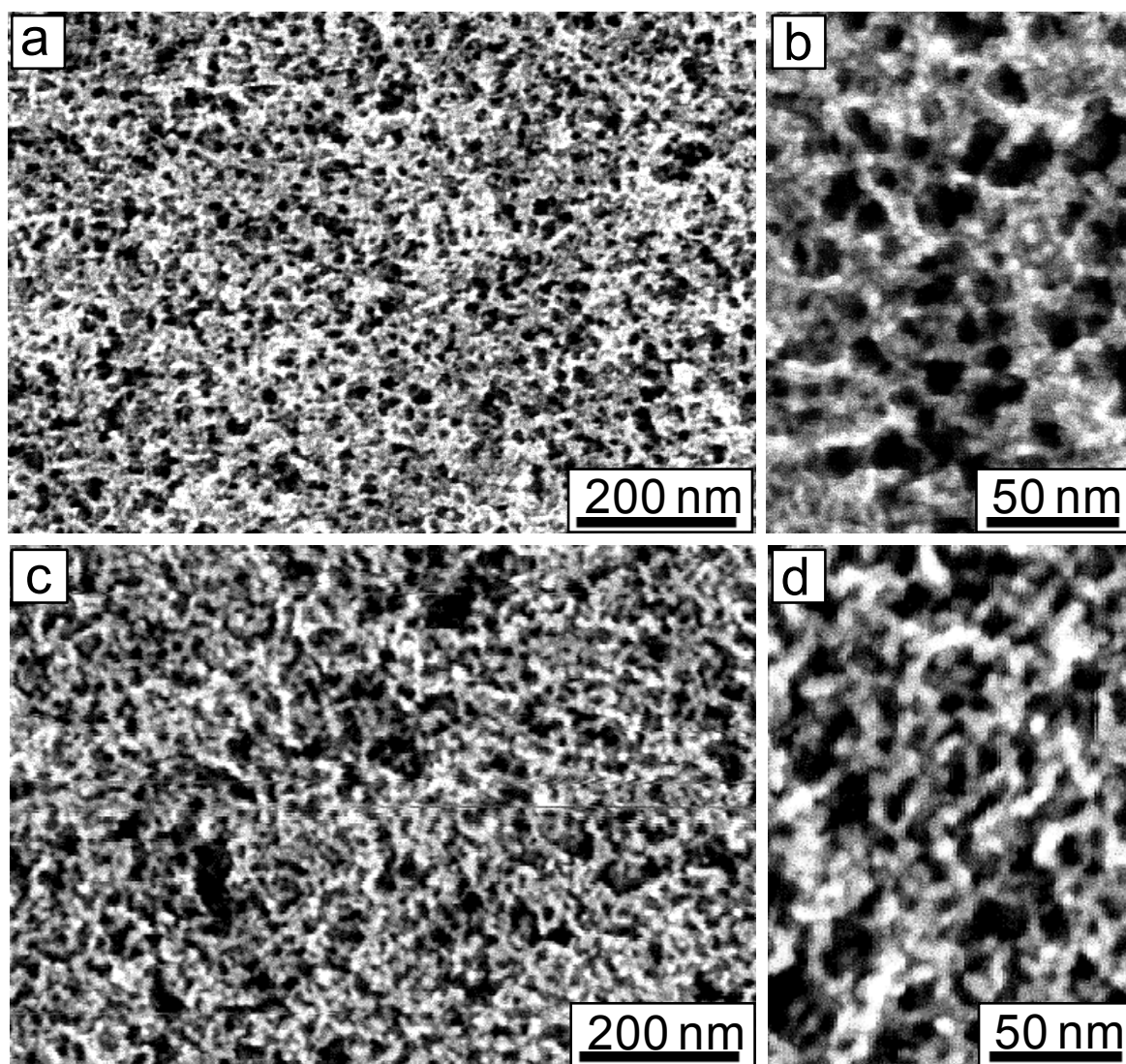


Figure 4.2. Top-view SEM images of CdSe nanocrystal-based mesoporous films templated with PBO-*b*-PEO. Parts (a) and (b) show low-magnification and high-magnification images, respectively, of films prepared by spin-coating. Parts (c) and (d) show low-magnification and high-magnification images, respectively, of films prepared by drop-casting. In both cases, both the larger black mesopores and the individual nanocrystals can be seen.

diameter of 15 ± 2 nm, judging by SEM. Moreover, the films are crack-free with visibly open porosity at the film surface. A closer look at Figure 4.2b shows the presence of individual nanocrystals comprising the pore-walls. The agglomerated nanocrystals in the walls give rise to micropores, which significantly increase the surface area of these materials compared to materials with dense walls. Figure 4.2 also shows (c) low- and (d) high-magnification SEM images of a CdSe mesoporous film that was prepared by drop-casting, leading to a film that is 1.2 ± 0.2 μm thick. The thick films are also crack-free, show open mesopores at the surface with an average diameter of 15 ± 2 nm, and have individual nanocrystals embedded in the pore-walls.

To determine the crystal structure of both CdSe nanocrystals and the templated mesoporous CdSe films, two-dimensional wide angle X-ray scattering (2D-WAXS) measurements were performed on beamline 11-3 at the Stanford Synchrotron Radiation Laboratory (SSRL). 2D-WAXS measurements were carried out in reflection mode with the incoming beam at or near grazing incidence. Here we define β as the angle between the X-ray beam and the plane of the substrate. Figure 4.3a shows WAXS patterns for CdSe nanocrystals after ligand-exchange with Et_3OBF_4 (A) and mesoporous film of CdSe nanocrystals after templating with PBO-*b*-PEO (B), collected at $\beta = 2.0^\circ$. The main peaks for both samples can be indexed to the hexagonal or wurtzite phase of CdSe (JCPDS reference card no. 02-0330). Deviations in peak intensities from the ideal wurtzite structure, however, indicate some stacking faults and structure that is actually intermediate between wurtzite and the related cubic zinc blende structure. The pattern for the ligand-exchanged nanocrystals (A) shows significant peak broadening, consistent with their small size. Domain sizes calculated by Scherrer

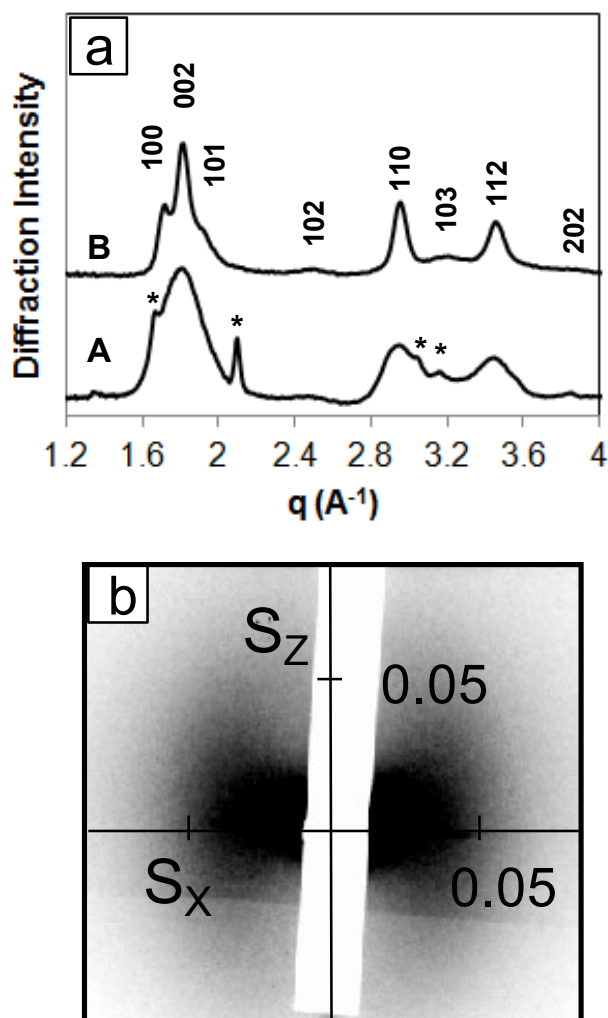


Figure 4.3. (a) Wide angle XRD patterns obtained by integrating 2D-WAXS data collected on CdSe nanocrystals after the ligand-exchange process with Et₃OBF₄ (A) and after templating with PBO-*b*-PEO and thermal treatment to 400 °C to form a mesoporous CdSe nanocrystal-based film (B). Both before and after templating, the diffraction can be indexed to the wurtzite crystal structure of CdSe. Narrow peaks marked with * correspond to organic salts used in the ligand-stripping process. (b) 2D-SAXS pattern obtained on a CdSe nanocrystal-based mesoporous film. The image shows strong in-plane scattering, indicative of a well-defined pore size, but no long range periodicity of the pores. Scattering vector *S* components are given in 1/nm.

analysis of the peak widths were found to be ~5 nm. This is also consistent with the diameter observed in TEM (Figure 4.1a). Some additional small peaks belonging to BF_4^- salts (NOBF_4 and NO_2BF_4) are observed and these are marked with an asterisk (JCPDS reference cards nos. 17-0252 and 17-0253). These extra peaks disappear after thermal degradation of the polymer to leave behind the pure wurtzite phase of CdSe (B).

Pattern B shows diffraction for the mesoporous CdSe films. For this sample, the peak intensities show more deviation from the ideal wurtzite structure, indicative of increasing zinc blende character. Analysis of the peak widths for the templated films gives a grain size of ~10 nm for the more intense and narrower peaks (i.e. (110) and (112)), and ~5 nm for the less intense and broader peaks (i.e. (102) and (103)). This observation can be explained by a distribution of nanocrystals – some that have fused to yield larger domains and some that did not grow in size during thermal treatments. It is usually difficult to see a distribution of nanocrystal sizes by X-ray diffraction because larger nanocrystals scatter much more strongly than small ones. In this case, however, the nanocrystals that grow in size apparently have more zinc blende character, which allows us to see the presence of the uncoarsened nanocrystals in the wurtzite peaks.⁶³ While this data does indicate that there is some grain growth during the thermal treatment, the data also corroborates the SEM images in Figure 4.2a–d where individual nanocrystals that do not fully fuse can still be seen making up the pore wall. We also note that a comparison of the relative intensities around the diffraction rings for each peak in the raw 2-D data for both (A) and (B) indicates that the nanocrystals embedded

in the pore walls are randomly oriented with respect to the substrate and there is no preferred or oriented growth during the thermal treatment.

Analysis of the templated films further made use of two-dimensional small-angle X-ray scattering (2D-SAXS) measurements performed on beamline 1-4 at SSRL, collected in reflection mode at a grazing angle of incidence, $\beta = 0.8^\circ$. Figure 4.3b shows a 2D-SAXS pattern collected for PBO-*b*-PEO templated CdSe nanocrystals. Little out-of-plane diffraction is observed in the z-direction, but strong in-plane scattering maxima can be seen along the x-direction. Analysis of the observed scattering maxima corresponds to a lengthscale of 28 nm. This type of diffuse scattering is characteristic of a disordered or non-periodic material with homogeneously sized pores. This repeat distance of 28 nm is also in reasonable agreement with the sum of the average pore diameter and wall thickness determined by SEM above.

4.2.3 Optical Properties

The optical properties of the mesoporous CdSe films were investigated by absorption spectroscopy. Figure 4.4 shows UV-visible absorption spectra for oleate-passivated CdSe nanocrystals dispersed in hexane (black line), and CdSe nanocrystals after Et_3OBF_4 treatment dispersed in DMF (dashed black line), both plotted as normalized absorbance versus wavelength. The oleate-capped nanocrystals show a first exciton peak at 578 nm or 2.15 eV, which corresponds to a calculated diameter of ~ 3.8 nm.⁶⁴ The spectrum for the ligand-stripped nanocrystals shows very similar data with the first exciton peak at 573 nm or 2.16 eV, and a calculated diameter of ~ 3.7 nm.⁶⁴ The slight exciton peak shift after the ligand-exchange process may be attributed to differences in surface passivation by oxoanionic ligands versus DMF. Figure 4.4 also

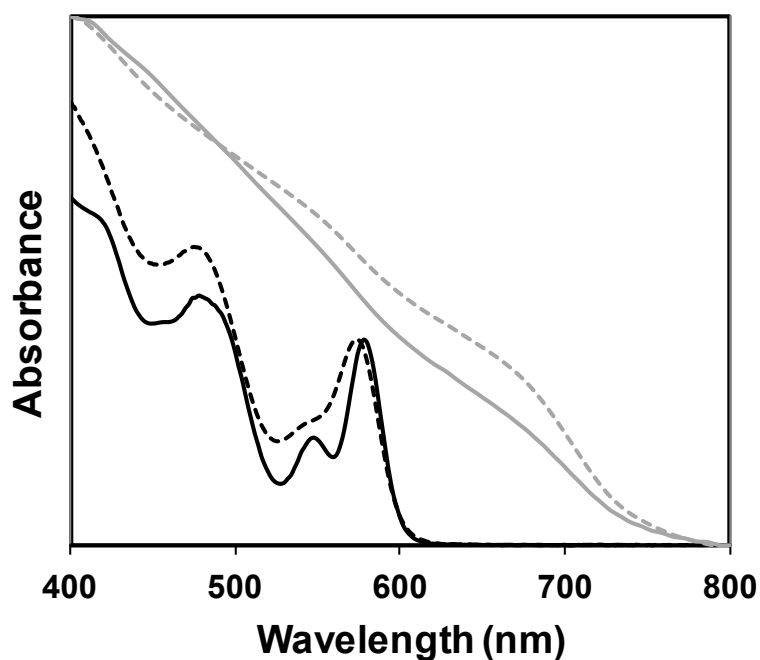


Figure 4.4. UV-visible absorption spectra of CdSe nanocrystals in several environments. As-synthesized samples dispersed in hexane are indicated with a solid black line. Data collected on samples dispersed in DMF after ligand stripping with Et_3OBF_4 are indicated with a dashed black line. Data for a dense film of untemplated CdSe nanocrystals after ligand stripping are indicated by a dashed gray line. Data for a templated mesoporous CdSe nanocrystal-based film are indicated by a solid gray line. All data is plotted as normalized absorbance versus wavelength.

shows absorption for a dense film of untemplated ligand-stripped CdSe nanocrystals (dashed grey line), and a mesoporous CdSe film (gray line). Both films were deposited onto glass heated to 400 °C under argon and data is plotted as normalized absorbance versus wavelength. The porous templated CdSe film was approximately $1.0 \pm 0.1 \mu\text{m}$. Very similar behavior is observed for both films, with bathochromic shifts of the exciton peak to ~675 nm or 1.84 eV for the dense film of untemplated CdSe and to ~680 nm or 1.82 eV for mesoporous templated CdSe are observed. Bathochromic shifts to ~611 nm have been reported in the literature for CdSe nanocrystal dense-films.⁶⁵ The shift to higher wavelength in our materials can be explained by a combination of increases in the interparticle electronic coupling and real grain growth of the nanocrystals in both dense untemplated films and templated films.

To better understand this data, it is worth noting that the room temperature bulk band gap for bulk wurtzite CdSe is 1.74 eV.⁶⁶ For both nanocrystal based films film, a tail of absorption and/or scattering are observed beyond this bulk band edge. The presence of both an excitonic peak and absorption near the bulk band edge is consistent with the 2D-WAXS data from Figure 4.3a which shows the presence of both larger (10 nm, not quantum confined) and smaller (5 nm) domains after annealing. The optical data is also in agreement with the SEM images that show that the nanocrystals are fused together. Moreover, the data shows that thermal processing has the same effect on both templated and untemplated nanocrystals, demonstrating that the CdSe behavior does not change after making it mesoporous. Despite these optical changes, the templated film still shows a distinct size induced blue shift of the absorption, indicating that these nanoporous, nanocrystal-based films can successfully combine

quantum confinement, high surface area, and porosity, a combination that could be beneficial for a range of light driven processes.

4.2.4 Composition

Compositional information on the templated CdSe films was determined from X-ray photoelectron spectroscopy (XPS) measurements. Figure 4.5a shows a high-resolution spectrum taken of the Cd 3d core region which contains two peaks corresponding to the $3d_{3/2}$ and $3d_{5/2}$ core levels. The positions of the peak for the Cd $3d_{3/2}$ and Cd $3d_{5/2}$ core levels are centered on binding energies of 411.9 and 405.2 eV, which are in good agreement with reported values of 411.93 and 405.13 eV for CdSe.^{66,67} More importantly, the data shows that no oxidation of the Cd occurred, as evidenced by the complete absence of CdO_x peaks that typically appear as shoulders at slightly higher binding energies for both $3d_{3/2}$ and $3d_{5/2}$ core levels. The expected positions of the CdO_x $3d_{3/2}$ and $3d_{5/2}$ peaks, reported to be 413.08 and 406.30 eV,⁶⁷ are indicated on the figure with arrows. Figure 4.5b shows a similar high resolution spectrum of the Se 3d core region showing two peaks corresponding to $3d_{3/2}$ and $3d_{5/2}$ core levels centered at binding energies of 54.7 and 53.8 eV. These energies are again in agreement with literature values for Se $3d_{3/2}$ and $3d_{5/2}$ core levels in CdSe, reported as 55.07 and 54.18 eV.^{66,67} Similarly, the spectrum shows the complete absence of an oxidized Se peak, which occurs at higher binding energy, reported at 59.0 eV for SeO_2 .^{67,68} The binding energy of CdSe, measured as the difference between the Cd $3d_{5/2}$ and Se $3d_{5/2}$ peaks, averages 351.4 eV, which is again in good agreement with previous reports for bulk CdSe and CdSe nanocrystals.^{66,67} Taken together, the XPS

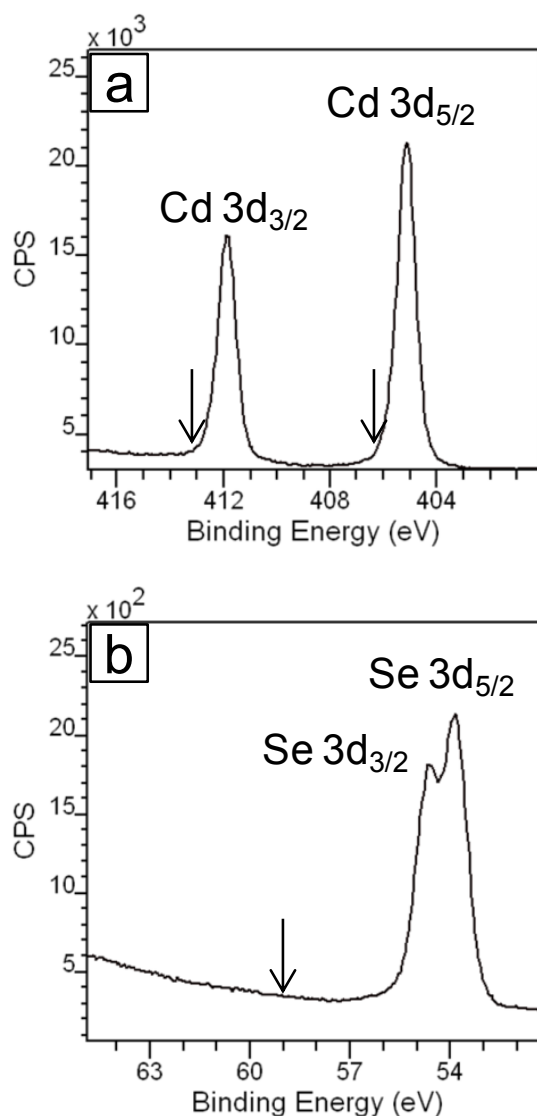


Figure 4.5. XPS collected on a mesoporous CdSe nanocrystal-based film. (a) A high resolution spectrum of the Cd 3d core region shows peaks for the 3d_{3/2} and 3d_{5/2} core levels of Cd in CdSe. No peaks corresponding to CdO_x can be observed (arrows mark expected location). (b) A high resolution spectrum for Se 3d core region shows peaks for the 3d_{3/2} and 3d_{5/2} core levels of Se in CdSe. Again, no peaks corresponding SeO₂ can be observed (arrows mark expected location).

data clearly shows that the CdSe nanocrystals are not oxidized during either the templating process or thermal annealing step.

4.2.5 Ellipsometric Porosimetry Measurements

The micro- and mesoporosity of both template and untemplated CdSe nanocrystal films was analyzed by ellipsometric porosimetry using toluene as the adsorbate.⁶⁹ Figure 4.6a shows a typical adsorption-desorption isotherm for a PBO-*b*-PEO-templated CdSe mesoporous film, demonstrating typical IV behavior.⁷⁰ The templated CdSe mesoporous film shows a 50% overall toluene-accessible pore volume. The appearance of a hysteresis loop in the isotherm at higher relative pressures is representative of a mesoporous material that exhibits an interconnected porosity, where the absorption trace provides information about the size of any cages in the material, and the desorption trace provides information about neck sizes. The mesopore size distribution shown in Figure 4.6b was determined by fitting a Kelvin model to the data to give a cage diameter distribution centered at 18 nm and a neck diameter distribution centered at 9 nm. The mesopore size distribution determined by ellipsometric porosimetry, arising from the PBO-*b*-PEO template, is thus in good agreement with the pore diameter determined by SEM (Figure 4.2a–d) and the average repeat distance determined by 2D-SAXS (Figure 4.3b) measurements. For comparison, data was also collected on a dense film of untemplated ligand-stripped nanocrystals. The dense film exhibited a 4% overall toluene-accessible pore volume with a mesopore size distribution centered around 3 nm. Both films exhibit very similar behavior at lower pressures, indicating similar microporosity. At higher pressures, the templated films deviate

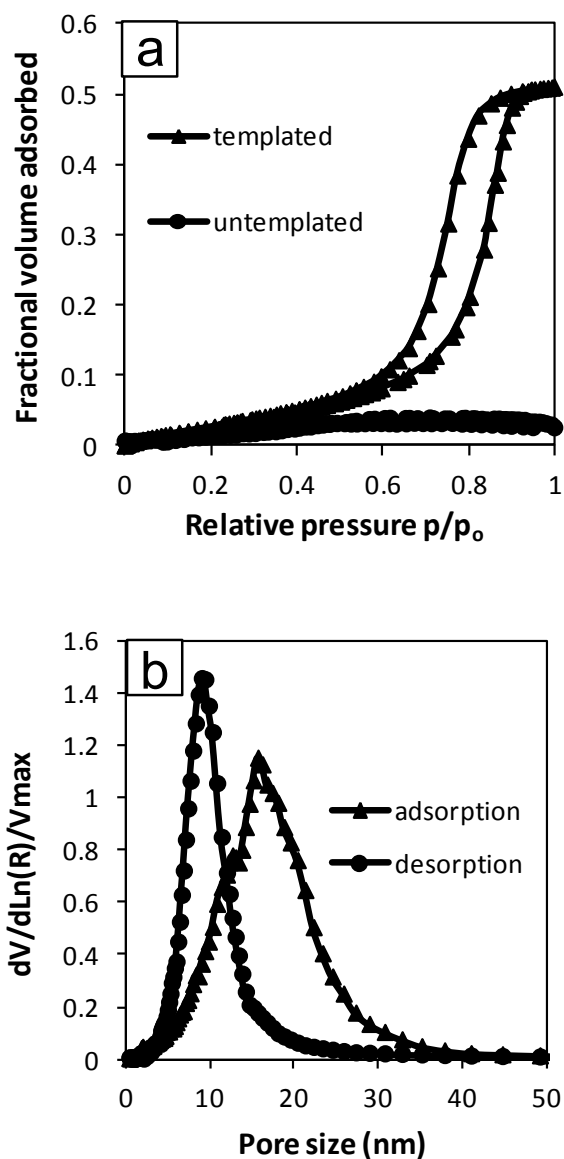


Figure 4.6. (a) Toluene adsorption-desorption isotherm for a templated CdSe nanocrystal-based mesoporous film (filled triangles) and a dense film of untemplated nanocrystals (filled circles). The mesoporous film exhibits a 50% toluene-accessible porous volume while the dense film exhibits a 4% toluene-accessible porous volume. (b) Corresponding pore size distribution data obtained for the templated film in (a).

significantly from the untemplated films, confirming the idea that the mesoporosity arises from the polymer template. As expected, the dense films have a much smaller pore volume, compared to the templated films, because the pores are created only by the random aggregation of the nanocrystal building blocks.

A fit of the Dubinin-Radushkevich model to the isotherm at lower relative pressures gives the micropore size distribution. Here we find a cage diameter of 2.0 nm and a neck diameter of 1.8 nm. The micropores arise from the spaces in between the CdSe nanocrystals that make up the pore walls. The same fit was applied to a dense film of untemplated nanocrystals, and the micropores were found to exhibit a cage size of 2.0 nm and a neck diameter of 1.2 nm. It is likely that the 3 nm mesopores obtained from the Kelvin fit are part of the same continuous distribution of small pores, which lie at the size limits of both models. Based on this result, it is reasonable to speculate that the Dubinin-Radushkevich model may slightly underestimate the micropore size distribution in the template films as well. Overall, we find that both films have similar micropore sizes, suggesting that the nanocrystals retain their nanodimensional character when cast into films, regardless of the presence of polymer derived mesopores. The presence of both meso- and micropores in the templated CdSe films results in the useful combination of high surface area and good accessibility.

4.2.6 Electrical Properties

Finally, to investigate the electrical properties of the templated CdSe nanocrystal-based mesoporous films, dc current-voltage measurements of CdSe nanocrystal-based films deposited onto ITO-coated glass substrate were performed using hanging mercury drop electrodes. Figure 4.7 depicts the current density-voltage characteristics obtained

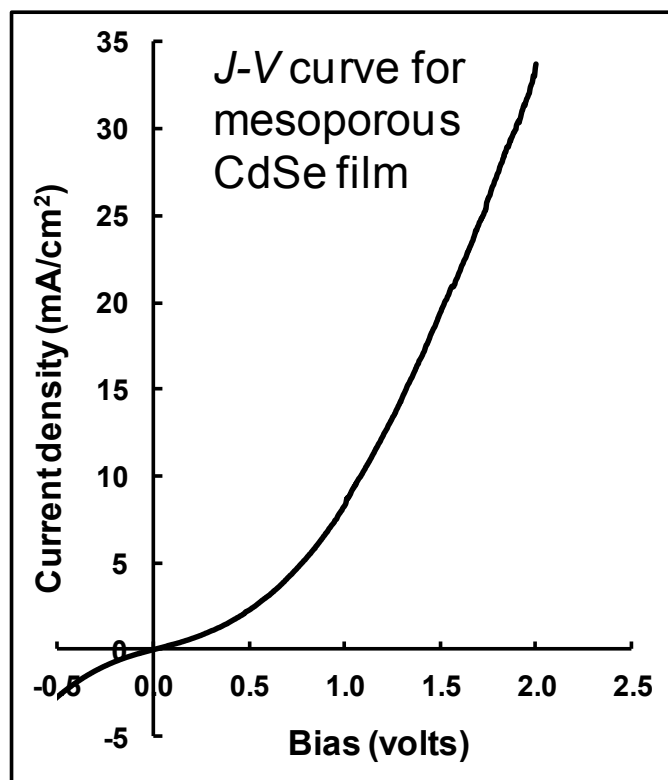


Figure 4.7. Experimental current density-voltage curve for a CdSe nanocrystal-based mesoporous film demonstrating typical diodic behavior. A space-charge limited current model was utilized to calculate a carrier mobility of $10^{-4} \text{ cm}^2 \text{ V}^{-1} \text{ sec}^{-1}$ from this data.

for a 100 nm thick mesoporous CdSe film. Figure 4.7 shows typical diodic behavior, thus allowing us to use a space-charge limited current (SCLC) model to estimate the carrier mobility from this data.⁷¹ A fit to a logarithmic current density-voltage plot to the trap-free (or equivalently trap-filled) space charge limited region where the slope = 2 gives a SCLC mobility of $10^{-4} \text{ cm}^2 \text{ V}^{-1} \text{ s}^{-1}$, which is comparable to reported mobilities of $1.3 \times 10^{-4} \text{ cm}^2 \text{ V}^{-1} \text{ s}^{-1}$ for CdSe nanocrystal-based solid films.⁶⁵ These results demonstrate that in addition to the open porosity observed by porosimetry, these templated CdSe nanocrystal-based mesoporous films are also electrically interconnected. Such connectivity is key to both photovoltaic performance and to electrochemically assisted photocatalysis.

4.3 Conclusions

In this work, we report a solution-phase route for the assembly of ligand-stripped CdSe nanocrystals into mesoporous hierarchical architectures. The ligand-exchange process using Et_3OBF_4 readily produces “bare” CdSe nanocrystals that can be templated with a PBO-*b*-PEO block copolymer. Because the templating process is completely decoupled from the chemistry used to synthesize these nanocrystals, the method should be directly transferable to any other semiconductor or metal nanocrystals that can be ligand-stripped using Meerwein’s salt, regardless of whether they are air-stable. We demonstrate that the crystal structure and composition of the templated CdSe films are retained during the thermal annealing process, and while some grain growth does occur, quantum confined excitonic features are still observed in the final porous material. The mesoporous CdSe films exhibit reasonable charge carrier

mobility, confirming that the nanocrystals are electronically interconnected in the film. By varying the type and size of nanocrystal, block ratio, and total molecular weight of the block copolymer polymer used as the template, it should be possible to tune many of the details of the final architecture. This should make it possible to produce porous materials with varying composition, mesoporosity, and microporosity, which are important for applications where domain size, diffusion length and electronic conductivity effect device performance.

The method is also compositionally flexible – because the nanocrystals are synthesized in a step that is completely separate from the co-assembly, the nanocrystals are more physical objects than chemical species. This means that it should be possible to combine different types of nanocrystals into a single porous network, joining, for example, metals and semiconductors or two semiconductors with different band offsets.^{72,73} More importantly, because the CdSe is porous, it should also be possible to fill the pore volume with other materials.^{74,75} Extending nanocrystal templating methods to systems that are not stable in air thus opens up the potential to produce an incredible diversity of designed composites that could exhibit novel or interesting properties.

4.4 Experimental

4.4.1 Materials

The following chemicals were purchased and used as received: (Poly(butylene oxide)-*b*-poly(ethylene oxide), with a mass ratio of PBO(5000)-*b*-PEO(6500), a block

ratio of PBO₉₀-*b*-PEO₁₁₄, and a PDI = 1.09 was purchased from Advanced Polymer Materials Inc.

CdSe nanocrystals were synthesized using the Workstation for Automated Nanomaterials Discovery and Analysis (WANDA), an automated nanocrystal synthesis robot housed in the Molecular Foundry, Lawrence Berkeley National Laboratory.⁶² To carry out the ligand-exchange process, as-synthesized nanocrystals were treated with Et₃OBF₄ according to recently reported procedures.^{59,61} All ligand-stripping reactions were carried out under inert conditions.

4.4.2 Synthesis of Mesoporous CdSe Films

The synthesis of mesoporous CdSe nanocrystal-based films was carried out under inert conditions, including both film deposition and thermal annealing steps. In a typical procedure, 10 mg of the PBO₉₀-*b*-PEO₁₁₄ diblock copolymer was dissolved in 0.1 mL of DMF with gentle heating. To this solution, 1 mL of CdSe nanocrystals dispersed in DMF (20 mg/mL) was added. From this mixture, thin films were prepared by spin-coating onto desired substrates (silicon, ITO-coated glass, or glass) at 1000 to 2000 rpm for 60 s. Thick films were produced by drop casting onto desired substrates. The films were dried using a 3 h ramp up to 175 °C, followed by a 3 h soak. Thermal decomposition of the template was done after the drying step using a 6 h ramp from 175 °C to 400 °C, followed by a 3 h soak.

4.4.3 Methods

TEM images were obtained using a JEOL-2100 electron microscope operating at 200 kV. TGA measurements were performed under flowing argon gas using a Perkin Elmer Instruments Pyris Diamond TG/DTA Thermogravimetric/Differential Thermal

Analyzer Module. SEM images were obtained using a JEOL model 6700F electron microscope with beam energy 5 kV. 2D-WAXS and 2D-SAXS data were collected at the Stanford Synchrotron Radiation Laboratory using beamlines 11-3 and 1-4. Absorbance spectra were performed on an Agilent HP 8452A UV–Vis Spectrophotometer. XPS analysis was performed using a Kratos Axis Ultra DLD with a monochromatic (K_{α} radiation) source. The charge neutralizer filament was used to control charging of the sample. A 20 eV pass energy was used with a 0.05 eV pass energy. Scans were calibrated using the C 1s peak shifted to 294.8 eV. DC conductivity of the CdSe films on ITO substrates were measured in an argon filled glovebox using a Solartron 1287 potentiostat and 1252A frequency analyzer. Voltage was applied through the CdSe film using two 16 mm² hanging mercury drops separated by 1 cm. Ellipsometric porosimetry was performed on a PS-1000 instrument from Semilab using toluene and as the solvent. A UV–visible CCD detector adapted to a grating spectrograph analyzes the signal reflected by the sample. The light source is a 75 W Hamamatsu Xenon lamp and measurements were performed on the spectral range from 1.24–4.5 eV. Data analysis was performed using the associated WinElli II software with the assumption of slit-like pores. If the actual pores are closer to cylindrical, the real pores sizes will be slightly larger than the values reported here. Data is fit with a contact angle of zero for the solvent.

4.4 References

-
- ¹ Zhang, Y.; Xie, Z.; Wang, J. Supramolecular-Templated Thick Mesoporous Titania Films for Dye-Sensitized Solar Cells: Effect of Morphology on Performance. *Appl. Mater. Inter.* **2009**, *1*, 2789–2795.
 - ² Kim, J.-Y.; Kang, S. H.; Kim, H. S.; Sung, Y.-E. Preparation of Highly Ordered mesoporous Al₂O₃/TiO₂ and its Application in Dye-Sensitized Solar Cells. *Langmuir*, **2010**, *26*, 2864–2870.
 - ³ Zhang, Y.; Yuwono, A. H.; Wang, J.; Li, J. Enhanced Photocatalysis by Doping Cerium into Mesoporous Titania Thin Films. *J. Phys. Chem. C* **2009**, *113*, 21406–21412.
 - ⁴ Sreethawong, T.; Suzuki, Y.; Yoshikawa, S. Photocatalytic Evolution of Hydrogen Over Mesoporous TiO₂ Supported NiO Photocatalyst Prepared by Single-Step Sol-Gel Process with Surfactant Template. *Int. J. Hydrogen Energy* **2005**, *30*, 1053–1062.
 - ⁵ Brezesinski, B.; Wang, J.; Polleux, J.; Dunn, B.; Tolbert, S. H. Templated Nanocrystal-Based Porous TiO₂ Films for Next-Generation Electrochemical Capacitors. *J. Am. Chem. Soc.* **2009**, *131*, 1802–1809.
 - ⁶ Wang, P.; Zakeeruddin, S. M.; Moser, J. E.; Nazeeruddin, M. K.; Sekiguchi, T.; Gratzel, M. A Stable Quasi-Solid-State Dye-Sensitized Solar Cell with an Amphiphilic Ruthenium Sensitizer and Polymer Gel Electrolyte. *Nat. Mater.* **2003**, *2*, 402–407.

-
- ⁷ Wang, P.; Zakeeruddin, S. M.; Comte, P.; Charvet, R.; Humphry-Baker, R.; Gratzel, M. Enhance the Performance of Dye-Sensitized Solar Cells by Co-Grafting Amphiphilic Sensitizer and Hexadecylmalonic Acid on TiO₂ Nanocrystals. *J. Phys. Chem. B* **2003**, *107*, 14336–14341.
- ⁸ Talapin, D. V.; Murray, C. B. PbSe Nanocrystal Solids for n- and p-Channel Thin Film Field-Effect Transistors. *Science* **2005**, *310*, 86–89.
- ⁹ Gur, I.; Fromer, N. A.; Geier, M. L.; Alivisatos, A. P. Air-Stable All-Inorganic Nanocrystal Solar Cells Processed from Solution. *Science* **2005**, *310*, 462–465.
- ¹⁰ Dayal, S.; Kopidakis, N.; Olson, D. C.; Ginley, D. S.; Rumbles, G. Photovoltaic Devices with a Low Band Gap Polymer and CdSe Nanostructures Exceeding 3% Efficiency. *Nano Lett.* **2010**, *10*, 239–242.
- ¹¹ Choi, J. J.; Wenger, W. N.; Hoffman, R. S.; Lim, Y.-F.; Luria, J.; Jasieniak, J.; Marohn, J. A.; Hanrath, T. Solution-Processed Nanocrystal Quantum Dot Tandem Solar Cells. *Adv. Mater.* **2011**, *23*, 3144–3148.
- ¹² Manna, L.; Milliron, D. J.; Meisel, A.; Scher, E. C.; Alivisatos, A. P. Controlled Growth of Tetrapod-Branched Inorganic Nanocrystals. *Nat. Mater.* **2003**, *2*, 382–385.
- ¹³ Peng, X.; Manna, L.; Yang, W.; Wickham, J.; Scher, E.; Kadavanich, A.; Alivisatos, A. P. Shape Control of CdSe Nanocrystals. *Nature*, **2000**, *404*, 59–61.
- ¹⁴ Murray, C. B.; Norris, D. J.; Bawendi, M. G. Synthesis and Characterization of Nearly Monodisperse CdE (E = S, Se, Te) Semiconductor Nanocrystallites. *J. Am. Chem. Soc.* **1993**, *115*, 8706–8715.

-
- ¹⁵ Hines, M. A.; Guyot-Sionnest, P. Synthesis and Characterization of Strongly Luminescing ZnS-Capped CdSe Nanocrystals. *J. Phys. Chem.* **1996**, *100*, 468–471.
- ¹⁶ Peng, X.; Schlamp, M. C.; Kadavanich, A. V.; Alivisatos, A. P. Epitaxial Growth of Highly Luminescent CdSe/CdS Core/Shell Nanocrystals with Photostability and Electronic Accessibility. *J. Am. Chem. Soc.* **1997**, *119*, 7019–7029.
- ¹⁷ Guzelian, A. A.; Banin, U.; Kadavanich, A. V.; Peng, X.; Alivisatos, A. P. Colloidal Chemical Synthesis and Characterization of InAs Nanocrystal Quantum Dots. *Appl. Phys. Lett.* **1996**, *69*, 1432–1434.
- ¹⁸ Kruszynska, M.; Borchert, H.; Parisi, J.; Kolny-Olesiak, J. Synthesis and Shape Control of CuInS₂ Nanoparticles. *J. Am. Chem. Soc.* **2010**, *132*, 15976–15986.
- ¹⁹ Shevchenko, E. V.; Talapin, D. V.; Kotov, N. A.; O'Brien, S. O.; Murray, C. B. Structural Diversity in Binary Nanoparticle Superlattices. *Nature* **2006**, *439*, 55–59.
- ²⁰ Talapin, D. V.; Shevchenko, E. V.; Bodnarchuk, M. I.; Ye, X.; Chen, J.; Murray, C. B. Quasicrystalline Order in Self-Assembled Binary Nanoparticle Superlattices. *Nature* **2009**, *461*, 964–967.
- ²¹ Zhao, H.; Wang, D.; Chaker, M.; Ma, D. Effect of Different Types of Surface Ligands on the Structure and Optical Property of Water-Soluble PbS Quantum Dots Encapsulated by Amphiphilic Polymers. *J. Phys. Chem. C* **2011**, *115*, 1620–1626.
- ²² Aldana, J.; Wang, Y. A.; Peng, X. Photochemical Instability of CdSe Nanocrystals Coated by Hydrophilic Thiols. *J. Am. Chem. Soc.* **2001**, *123*, 8844–8850.

-
- ²³ Law, M.; Luther, J. M.; Song, Q.; Hughes, B. K.; Perkins, C. L.; Nozik, A. J. Structural, Optical, and Electrical Properties of PbSe Nanocrystals Solids Treated Thermally or with Simple Amines. *J. Am. Chem. Soc.* **2008**, *130*, 5974–5985.
- ²⁴ Luther, J. M.; Law, M.; Song, Q.; Perkins, C. L.; Beard, M. C.; Nozik, A. J. Structural, Optical, and Electrical Properties of Self-Assembled Films of PbSe Nanocrystals Treated with 1,2-Ethanedithiol. *ACS Nano* **2008**, *2*, 271–280.
- ²⁵ Zarghami, M. H.; Liu, Y.; Gibbs, M.; Gebremichael, E.; Webster, C.; Law, M. p-Type PbSe and PbS Quantum Dot Solids Prepared with Short-Chain Acids and Diacids. *ACS Nano* **2010**, *4*, 2475–2485.
- ²⁶ Kovalenko, M. V.; Scheele, M.; Talapin, D. V. Colloidal Nanocrystals with Molecular Metal Chalcogenide Surface Ligands. *Science* **2009**, *324*, 1417–1420.
- ²⁷ Wang, R.; Tangirala, R.; Raoux, S.; Jordan-Sweet, J. L.; Milliron, D. J. Ionic and Electronic Transport in Ag₂S Nanocrystal-GeS₂ Matrix Composites with Size-Controlled Ag₂S Nanocrystals. *Adv. Mater.* **2012**, *24*, 99–103.
- ²⁸ Jiang, C.; Lee, J.-S.; Talapin, D. V. Soluble Precursors for CuInSe₂, CuIn_{1-x}Ga_xSe₂, and Cu₂ZnSn(S,Se)₄ Based on Colloidal Nanocrystals and Molecular Metal Chalcogenide Surface Ligands. *J. Am. Chem. Soc.* **2012**, *134*, 5010–5013.
- ²⁹ Tangirala, R.; Baker, J. L.; Alivisatos, A. P.; Milliron, D. J. Modular Inorganic Nanocomposites by Conversion of Nanocrystal Superlattices. *Angew. Chem. Int. Ed.* **2010**, *49*, 2878–2882.
- ³⁰ Mohanan, J. L.; Arachchige, I. U.; Brock, S. L. Porous Semiconductor Chalcogenide Aerogels. *Science* **2005**, *307*, 397–400.

-
- ³¹ Gaponik, N.; Wolf, A.; Marx, R.; Lesnyak, V.; Schilling, K.; Eychmuller, A. Three-Dimensional Self-Assembly of Thiol-Capped CdTe Nanocrystals: Gels and Aerogels as Building Blocks for Nanotechnology. *Adv. Mater.* **2008**, *20*, 4257–4262.
- ³² Yao, Q.; Brock, S. L. Porous CdTe Nanocrystals Assemblies: Ligation Effects on the Gelation Process and the Properties of Resultant Aerogels. *Inorg. Chem.* **2011**, *50*, 9985–9992.
- ³³ Yao, Q. Arachchige, I. U.; Brock, S. L. Brock. Expanding the Repertoire of Chalcogenide Nanocrystal Networks: Ag₂Se Gels and Aerogels by Cation Exchange Reactions. *J. Am. Chem. Soc.* **2009**, *131*, 2800–2801.
- ³⁴ Yanagisawa, T.; Shimizu, T.; Kuroda, K.; Kato, C. The Preparation of Alkyltrimethylammonium-Kanemite Complexes and their Conversion to Microporous Materials. *Bull. Chem. Soc. Jpn.* **1990**, *63*, 988–992.
- ³⁵ Inagaki, S.; Fukushima, Y.; Kuroda, K. J. Synthesis of Highly Ordered Mesoporous Materials from a Layered Polysilicate. *Chem. Soc. Chem. Commun.* **1993**, 680–682.
- ³⁶ Kresge, C. T.; Leonowicz, M. E.; Roth, W. J.; Vartuli, J. C.; Beck, J. S. Ordered Mesoporous Molecular Sieves Synthesized by a Liquid-Crystal Template Mechanism. *Nature* **1992**, *359*, 710–712.
- ³⁷ Beck, J. S.; Vartuli, J. C.; Roth, W. L.; Leonowicz, M. E.; Kresge, C. T.; Schmidt, K. D.; Chu, C. T.-W.; Olson, D. H.; Sheppard, E. W.; McCullen, S. B.; Higgins, J. B.; Schlenker, J. L. A New Family of Mesoporous Molecular Sieves Prepared with Liquid Crystal Templates. *J. Am. Chem. Soc.* **1992**, *114*, 10834–10843.

-
- ³⁸ Zhao, D. Y.; Feng, J. L.; Huo, Q. S.; Melosh, N.; Fredrickson, G. H.; Chmelka, B. F.; Stucky, G. D. Triblock Copolymer Syntheses of Mesoporous Silica with Periodic 50 to 300 Angstrom Pores. *Science* **1998**, *279*, 548–552.
- ³⁹ Monnier, A.; Schuth, F.; Huo, Q.; Kumar, D.; Margolese, D.; Maxwell, R. S.; Stucky, G. D.; Krishnamurty, M.; Petroff, P.; Firouzi, A.; Janicke, M.; Chmelka, B. F. Cooperative Formation of Inorganic-Organic Interfaces in the Synthesis of Silicate Mesostructures. *Science* **1993**, *261*, 1299–1303.
- ⁴⁰ Yang, P.; Deng, T.; Zhao, D.; Feng, P.; Pine, D.; Chmelka, B.; Whitesides, G.; Stucky, G. D. Hierarchically Ordered Oxides. *Science* **1998**, *282*, 2244–2246.
- ⁴¹ Templin, M.; Franck, A.; Chesne, A. D.; Leist, H.; Zhang, Y.; Ulrich, R.; Schadler, V.; Wiesner, U. Organically Modified Aluminosilicate Mesostructures from Block Copolymer Phases. *Science* **1997**, *278*, 1795–1798.
- ⁴² Tian, B. Z.; Liu, X. Y.; Tu, B.; Yu, C. Z.; Fan, J.; Wang, L. M.; Xie, S. H.; Stucky, G. D.; Zhao, D. Y. Self-Adjusted Synthesis of Ordered Stable Mesoporous Minerals by Acid–Base Pairs. *Nat. Mater.* **2003**, *2*, 159–163.
- ⁴³ Antonelli, D. M.; Ying, J. Y. Synthesis of Hexagonally Packed Mesoporous TiO₂ by a Modified Sol–Gel Method. *Angew. Chem., Int. Ed. Engl.* **1995**, *34*, 2014–2017.
- ⁴⁴ Mamak, M.; Coombs, N.; Ozin, G. Mesoporous Yttria–Zirconia and Metal–Yttria–Zirconia Solid Solutions for Fuel Cells. *Adv. Mater.* **2000**, *12*, 198–202.

-
- ⁴⁵ Warren, S. C.; Perkins, M. R.; Adams, A. M.; Kamperman, M.; Burns, A. A.; Arora, H.; Herz, E.; Suteewong, T.; Sai, H.; Li, Z.; Werner, J.; Song, J.; Werner-Zwanziger, U.; Zwanziger, J. W.; Gratzel, M.; DiSalvo, F. J.; Wiesner, U. A Silica Sol–Gel Design Strategy for Nanostructured Metallic Materials. *Nat. Mater.* **2012**, *11*, 60–467.
- ⁴⁶ Brezesinski, B.; Wang, J.; Tolbert, S. H.; Dunn, B. Ordered Mesoporous Alpha-MoO₃ with Iso-Oriented Nanocrystalline Walls for Thin-Film Pseudocapacitors. *Nat. Mater.* **2010**, *9*, 146–151.
- ⁴⁷ Templin, M.; Franck, A.; Chesne, A. D.; Leist, H.; Zhang, Y.; Ulrich, R.; Schadler, V.; Wiesner, U. Organically Modified Aluminosilicate Mesostructures from Block Copolymer Phases. *Science* **1997**, *278*, 1795–1798.
- ⁴⁸ Kuemmel, M.; Smatt, J.-H.; Boissiere, C.; Nicole, L.; Sanchez, C.; Linden, M.; Grosso, D. Hierarchical Inorganic Nanopatterning (INP) Through Direct Easy Block-Copolymer Templating. *J. Mater. Chem.*, **2009**, *19*, 3638–3642.
- ⁴⁹ Brezesinski, K.; Wang, J.; Haetge, J.; Reitz, C.; Steinmueller, S. O.; Tolbert, S. H.; Smarsly, B. M.; Dunn, B.; Brezesinski, T. Pseudocapacitive Contributions to Charge Storage in Highly Ordered Mesoporous Group V Transition Metal Oxides with Iso-Oriented Layered Nanocrystalline Domains. *J. Am. Chem. Soc.* **2010**, *132*, 6982–6990.
- ⁵⁰ Quickel, T. E.; Le, V. H.; Brezensinski, T.; Tolbert, S. H. On the Correlation between Nanoscale Structure and Magnetic Properties in Ordered Mesoporous Cobalt Ferrite (CoFe₂O₄) Thin Films. *Nano Lett.* **2010**, *10*, 2982–2988.

-
- ⁵¹ Rauda, I. E.; Buonsanti, R.; Saldarriaga-Lopez, L. C.; Benjauthrit, K.; Schelhas, L. T.; Stefik, M.; Augustyn, V.; Ko, J.; Dunn, B.; Wiesner, U.; Milliron, D. J.; Tolbert, S. H. General Method for the Synthesis of Hierarchical Nanocrystal-Based Mesoporous Materials. *ACS Nano*, **2012**, *6*, 6386–6399.
- ⁵² Buonsanti, R.; Pick, T. E.; Krins, N.; Richardson, T. J.; Helms, B. A.; Milliron, D. J. Assembly of Ligand-Stripped Nanocrystals into Precisely Controlled Mesoporous Architectures. *Nano Lett.* **2012**, *12*, 3872–3877.
- ⁵³ Warren, S. C.; Messina, L. C.; Slaughter, L. S.; Kamperman, M.; Zhou, Q.; Gruner, S. M.; DiSalvo, F. J.; Wiesner, U. Ordered Mesoporous Materials from Metal Nanoparticle-Block Copolymer Self-Assembly. *Science* **2008**, *320*, 1748–1752.
- ⁵⁴ Ba, J. H.; Polleux, J.; Antonietti, M.; Niederberger, M. Non-aqueous Synthesis of Tin Oxide Nanocrystals and Their Assembly into Ordered Porous Mesostructures. *Adv. Mater.* **2005**, *17*, 2509–2512.
- ⁵⁵ Corma, A.; Atienzar, P.; Garcia, H.; Chane-Ching, J. Y. Hierarchically Mesostructured Doped CeO₂ with Potential for Solar-Cell Use. *Nat. Mater.* **2004**, *3*, 394–397.
- ⁵⁶ Deshpande, A. S.; Pinna, N.; Smarsly, B.; Antonietti, M.; Niederberger, M. Controlled Assembly of Preformed Ceria Nanocrystals into Highly Ordered 3D Nanostructures. *Small* **2005**, *1*, 313–316.
- ⁵⁷ Dong, A.; Ye, X.; Chen, J.; Kang, Y.; Gordon, T.; Kikkawa, J. M.; Murray, C. B. A Generalized Ligand-Exchange Strategy Enabling Sequential Surface Functionalization of Colloidal Nanocrystals. *J. Am. Chem. Soc.* **2011**, *133*, 998–1006.

-
- ⁵⁸ Nag, A.; Kovalenko, M. V.; Lee, J.-S.; Liu, W.; Spokoyny, B.; Talapin, D. V. Metal-Free Inorganic Ligands for Colloidal Nanocrystals: S^{2-} , HS^- , Se^{2-} , HSe^- , Te^{2-} , HTe^- , TeS_3^{2-} , OH^- , and NH_2^- as Surface Ligands. *J. Am. Chem. Soc.* **2011**, *133*, 10612–10620.
- ⁵⁹ Rosen, E. L.; Buonsanti, R.; Llodes, A.; Sawvel, A. M.; Milliron, D. J.; Helms, B. A. Exceptionally Mild Reactive Stripping of Native Ligands from Nanocrystal Surfaces by Using Meerwein's Salt. *Angew. Chem. Int. Ed.* **2012**, *51*, 684–689.
- ⁶⁰ Llodes, A.; Hammack, A. T.; Buonsanti, R.; Tangirala, R.; Aloni, S.; Helms, B. A.; Milliron, D. J. Polyoxometalates and Colloidal Nanocrystals as Building Blocks for Metal Oxide Nanocomposite Films. *J. Mater. Chem.* **2011**, *21*, 11631–11638.
- ⁶¹ Duong, J. T.; Bailey, M. J.; Pick, T. E.; McBride, P. M.; Rosen, E. L.; Buonsanti, R.; Milliron, D. J.; Helms, B. A. Efficient Polymer Passivation of Ligand-Stripped Nanocrystal Surfaces. *J. Polym. Sci. A Polym. Chem.* **2012**, *50*, 3719–3727.
- ⁶² Chan, E. M.; Xu, C.; Mao, A. W.; Han, G.; Owen, J. S.; Cohen, B. E.; Milliron, D. J. Reproducible, High-Throughput Synthesis of Colloidal Nanocrystals for Optimization in Multidimensional Parameter Space. *Nano Lett.* **2010**, *10*, 1874–1885.
- ⁶³ Fedorov, V. A.; Ganshin, V. A.; Korkishko, Y. N. Determination of the Point of the Zincblende-to-Wurtzite Structural Phase Transition in Cadmium Selenide Crystals. *Phys. Stat. Sol. A.* **1991**, *126*, K5–K7.
- ⁶⁴ Jasieniak, J.; Smith, L.; van Embden, J.; Mulvaney, P.; Califano, M. Re-Examination of the Size-Dependent Absorption Properties of CdSe Quantum Dots. *J. Phys. Chem. C* **2009**, *113*, 19468–19474.

-
- ⁶⁵ Webber, D. H.; Brutchey, R. L. Ligand Exchange on Colloidal CdSe Nanocrystals using Thermally Labile tert-Butylthiol for Improved Photocurrent in Nanocrystal Films. *J. Am. Chem. Soc.* **2012**, *134*, 1085–1092.
- ⁶⁶ Katari, J. E. B.; Colvin, V. L.; Alivisatos, A. P. X-ray Photoelectron Spectroscopy of CdSe Nanocrystals with Applications to Studies of the Nanocrystal Surface. *J. Phys. Chem.* **1994**, *98*, 4109–4117.
- ⁶⁷ Vesely, C. J.; Langer, D. W. Electronic Core Levels of the IIB-VIA Compounds. *Phys. Rev. B* **1971**, *4*, 451–462.
- ⁶⁸ Tsuchiya, K.; Sakata, M.; Funyu, A.; Ikoma, H. Selenium Passivation of GaAs with Se/NH₄OH Solution. *Jpn. J. Appl. Phys.* **1995**, *34*, 5926–5932.
- ⁶⁹ Baklanov, M. R.; Mogilnikov, K. P.; Polovinkin, V. G.; Dultsev, F. N. Determination of Pore Size Distribution in Thin Films by Ellipsometric Porosimetry. *J. of Vac. Sci. & Tech. B* **2000**, *18*, 1385–1391.
- ⁷⁰ Gregg, S. J.; Sing, K. S. W. Adsorption, Surface Area, and Porosity. 2nd ed. (Academic, London, **1982**).
- ⁷¹ Hikmet, R. A. M.; Talapin, D. V.; Weller, H. Study of Conduction Mechanism and Electroluminescence in CdSe/ZnS Quantum Dot Composites. *J. Appl. Phys.* **2003**, *93*, 3509–3514.
- ⁷² Nakayama, T.; Murayama, M. Chemical Trend of Band Offsets at Wurtzite/Zinc-Blende Heterocrystalline Semiconductor Interfaces. *Phys. Rev. B* **1994**, *49*, 4710–4724.

-
- ⁷³ Wei, S.-H.; Zunger, A. Calculated Natural Band Offsets of all II-VI and II-V Semiconductors: Chemical Trends and the Role of Cation *d* Orbitals. *Appl. Phys. Lett.* **1998**, *72*, 2011–2013.
- ⁷⁴ Coakley, K. M.; Liu, Y.; McGehee, M. D.; Frindell, K. L.; Stucky, G. D. Infiltrating Semiconducting Polymers into Self-Assembled Mesoporous Titania Films for Photovoltaic Applications. *Adv. Funct. Mater.* **2003**, *13*, 301–306.
- ⁷⁵ Coakley, K. M.; McGehee, M. D. Photovoltaic Cells Made from Conjugated Polymers Infiltrated into Mesoporous Titania. *Appl. Phys. Lett.* **2003**, *83*, 3380–3382.

CHAPTER 5

Enhancing Pseudocapacitive Charge Storage in Polymer Templated Mesoporous Materials

5.1 Introduction

The growing global energy demands coupled with environmental concerns have increased the need for renewable energy sources, which, due to their intermittent nature, will require energy storage devices. Batteries and supercapacitors, also known as electrochemical capacitors (ECs), represent the most widely used energy storage devices. Supercapacitors are frequently overlooked as an energy storage technology despite the fact that these devices provide greater power, much faster response times, and longer cycle life than batteries. This occurs because the energy density of ECs is significantly lower than batteries, and this has limited their potential applications.

This chapter reviews our recent work on mesoporous transition metal oxide architectures that store charge through surface or near surface redox reactions, a phenomenon termed pseudocapacitance. The faradaic nature of pseudocapacitance leads to significant increases in energy density and thus represents an exciting future direction for ECs. We show that both the choice of material and electrode architecture is important for producing the ideal pseudocapacitor device. In particular, we focus on simple design rules that, when integrated into our materials, lead to significant improvements to capacitive energy storage.

In this work, the current state of electrode architectures for pseudocapacitors, from slurry electrodes to carbon/metal oxide composites, is briefly reviewed. We then describe the synthesis of mesoporous films made with amphiphilic diblock copolymer templating agents. We specifically examine templated films optimized for pseudocapacitive charge storage – that is, films synthesized from nanoparticle building blocks, and films made from traditional battery materials with a flexible architecture that is designed to minimize the strain associated with lithium intercalation. Electrochemical analysis of these mesoporous films then allows for a detailed understanding of the origin of the charge storage by separating capacitive contributions from traditional diffusion controlled intercalation processes. We also discuss methods to separate double-layer capacitance from pseudocapacitance. From this analysis, we show that nanocrystal based nanoporous materials offer an architecture optimized for high levels of redox or surface pseudocapacitance. Interestingly, in some cases, materials engineered to minimize the strain associated with lithium insertion can also show intercalation pseudocapacitance, where insertion processes become so kinetically facile that they appear capacitive. Finally, we conclude with a summary of design rules that should result in high power, high energy density electrode architectures. These design rules include the assembly of small nanosized building blocks to increase surface area, maintaining an interconnected open mesoporosity to facilitate solvent diffusion, flexibility in the structure to facilitate volume expansion during lithium insertion, optimized crystalline domain size and orientation, and the creation of effective electron transport pathways.

5.2 Electrochemical Capacitors

The projected doubling of world-wide energy consumption over the next 50 years presents one of the great scientific, technological, and environmental challenges of our times.¹ This predicament has brought increased awareness of the need for a sustainable energy future based on renewable sources. In order to realize the large-scale solar or wind-based electrical generation that will be critical in meeting future energy demands, new electrical energy storage (EES) systems must be developed to supply energy continuously.

The leading EES technologies today are batteries and electrochemical capacitors (ECs). Both are based on electrochemistry and the power and energy relationship between the two is shown in a Ragone Plot (Figure 5.1a).² The success of lithium-ion batteries in consumer electronics and the first generation of plug-in hybrids has led to significant advances. Nonetheless, it is evident that ECs possess a number of very attractive properties that complement or exceed the capabilities of batteries: fast charging within seconds, cycle life in excess of 500,000 cycles, and the ability to deliver > 10x more power.³ As a result, there are areas where ECs can find unique applications. For example, the fast charging properties of ECs are needed for regenerative braking in light rail, frequency regulation in smart grids, and they are well suited for storing the intermittent energy profiles of renewable energy sources.³ Limiting the widespread use of ECs is their energy density: currently, commercial devices store less than 10 Wh·kg⁻¹,¹ while state of the art asymmetric EC devices can achieve ~30 Wh·kg⁻¹.⁴

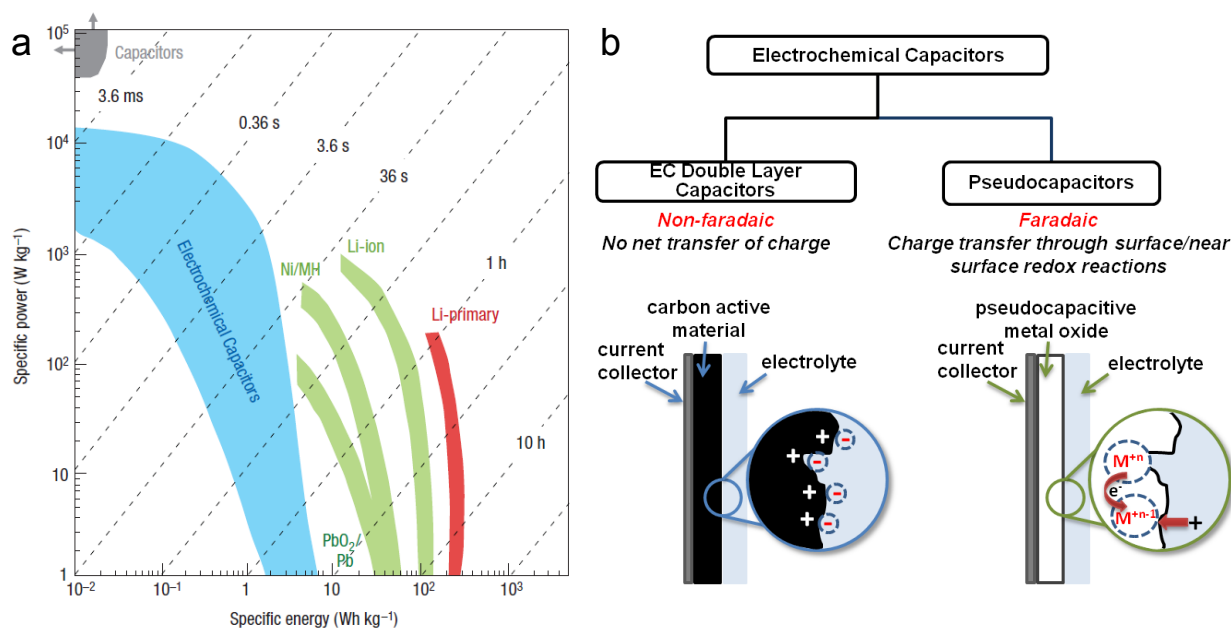


Figure 5.1. (a) A power vs. energy density graph (Ragone Plot) of energy storage devices (Adapted from ref 2. Copyright Nature 2008). (b) Mechanisms for capacitive charge storage at an electrode surface.

Based on their energy storage mechanisms, ECs may be divided into two main categories (Figure 5.1b): electric double-layer capacitors (EDLCs) and pseudocapacitors. EDLCs store charge in a thin double-layer located at the interface between the electrolyte and the electrode. This type of capacitance (C) occurs on every electrode surface and is dependent upon the surface area of the electrode:

$$C = \frac{\epsilon S}{d}$$

where ϵ is the relative permittivity, S is the surface area, and d is the thickness of the double-layer. Since d is small (a few Å, depending on the electrolyte ion and solvent dimensions),⁵ the capacitances exhibited by EDLCs are much higher than those found in traditional dielectric capacitors. Carbon-based materials are used as EDLC electrodes due to their high surface areas and electronic conductivities, and capacitance values of 100–150 F g⁻¹ have been achieved in some materials.⁶ In an ideal capacitor, the current is independent of potential and therefore a cyclic voltammogram (CV) will exhibit rectangular or “mirror” behavior. In an EDLC, the adsorption of ions on the surface results in mostly rectangular CVs; however, potential dependence may exist due to such effects as overscreening and crowding at the double layer.⁷

Pseudocapacitance is a faradaic process that involves surface or near-surface redox reactions. The interest in utilizing pseudocapacitance is that the energy density associated with faradaic reactions is at least one order of magnitude greater than that of double-layer processes – above 100 $\mu\text{F cm}^{-2}$ for pseudocapacitance vs. 10 $\mu\text{F cm}^{-2}$ for EDLCs.⁸ Traditionally, most pseudocapacitive materials are transition metal oxides, whose specific capacitance values exceed 1,000 F·g⁻¹. Pseudocapacitance often

exhibits a dependence on potential due to the redox reactions occurring on the metal oxides. This may lead to peaks in the CV curves.

Over the past few years, we have been using the soft-templating of transition metal oxides to create mesoporous films that provide a novel architecture for high-quality pseudocapacitor materials.^{9–12} Our materials contain a number of features which are beneficial for surface or near-surface charge storage reactions: high surface area, ordered porosity, nanosized crystalline domains, and iso-orientation. The mesoporous morphologies enable electrolyte access to the redox-active walls and enhanced kinetics due to the relatively short diffusion paths for electrons and ions. In this review, we describe the current understanding of surface redox reactions for charge storage, how porous electrode architectures have been used in ECs, analysis techniques to determine surface charge storage, and how a mesoporous electrode architecture can enhance this behavior.

The origin of pseudocapacitance has been described thoroughly by Conway.⁵ In this description, pseudocapacitance occurs whenever the amount of charge insertion (Q) depends on the voltage (V), giving the form of a capacitance (Q/V). Based on this theory, we identified three common charge storage processes that occur when a redox-active material is immersed in electrolyte. (1) Ions can intercalate into preferred crystallographic sites, often in materials characterized by layered or tunnel structures. The intercalation is accompanied by metal valence change to preserve electrical neutrality. (2) Ions are electrochemically adsorbed onto the surface of the material. In this mechanism, referred to as redox pseudocapacitance, adsorption is associated with a change in the metal valence state. This process is kinetically facile because of the

short-range nature of ion transport. (3) In our research, we have also observed mesoporous oxides in which the intercalation is facile, giving rise to a capacitive response. This third process is referred to as intercalation pseudocapacitance.

In the case of intercalation pseudocapacitance, the material's behavior is sometimes described as “transitional” between batteries and ECs because while the ion insertion may be facile, bulk solid-state diffusion still leads to slow processes.⁵ Widely used intercalation materials such as LiCoO_2 show charging time of over one hour, which is substantially beneath the EC power density regime. However, in the case of nanostructured materials such as the mesoporous films, diffusion distances are drastically decreased from the bulk and intercalation can kinetically behave in a more capacitive manner. In this class of materials, the distinction between capacitive and diffusive mechanisms is particularly important. We will elaborate later on such analysis techniques.

5.3 Architectures for fast energy storage

It is now well established that controlling the architecture of electrode materials plays a pivotal role in enhancing the performance of energy storage devices. As discussed above, the reactions that govern charge storage in pseudocapacitive materials are dependent on a combination of fast electron- and ion-transfer to the active sites. Consequently, there has been a push to use nanostructured materials to create porosity and increase surface area. The combination of high surface area and nanoscale dimensions allows for short diffusion lengths and easy access to surface redox sites. Porosity is needed for solvent diffusion and the pores size can have a

significant influence on the capacitance.⁶ Small domain sizes can also lead to suppression of phase transitions and reduced intercalation stress.¹³

5.3.1 Slurry-cast electrodes

The traditional method for characterizing the electrochemical properties of EC materials involves fabricating an electrode from a slurry consisting of active material, a conductive additive, and a binder. This approach enables electrodes to be made from virtually any powdered material. Electrodes have been produced from transition metal oxides in the form of nanoplates, nanorods, and nanoparticles, as well as powders of mesoporous materials.¹⁴ In many cases, these mesoporous powders are made using hard templates such as opals and surfactant-templated silica.¹⁵ The versatility of hard-templating is demonstrated by the wide range of materials that can be prepared including β -MnO₂, Li₄Ti₅O₁₂, and LiCoO₂.¹⁶ The disadvantage is the multistep processing.

One of the principal disadvantages of slurry-cast electrodes is that it tends to “bury” the surface of the active material,¹⁷ so that the electrolyte cannot reach all the surface redox sites, thus leading to poor rate capabilities. In addition, a significant percentage of the electrode (>15 weight %) is made up of inactive materials. Moreover, slurry-electrodes may contain large interparticle distances that lead to a low volume of active material. It can also be difficult to deconvolute the electrochemical properties of the active material from the electrochemical response of the electrode.

5.3.2 Nanomaterials on conductive scaffolds

There are many examples of composite materials that utilize a nanostructured version of a good electronic conductor that is coated with a transition metal oxide. One

example utilizes porous metal foams coated with transition metal oxides.¹⁸ A more popular approach is to use high surface area carbons as the scaffold, including carbon nanotubes, graphene, or fibers.¹⁹ For most of these types of composites, fast charge/discharge kinetics are observed due to a good conductive network throughout the electrode, however, both volumetric and gravimetric capacitances are greatly decreased when the mass of the inactive conductive scaffold is considered.²⁰

5.3.3 Thin-film electrodes

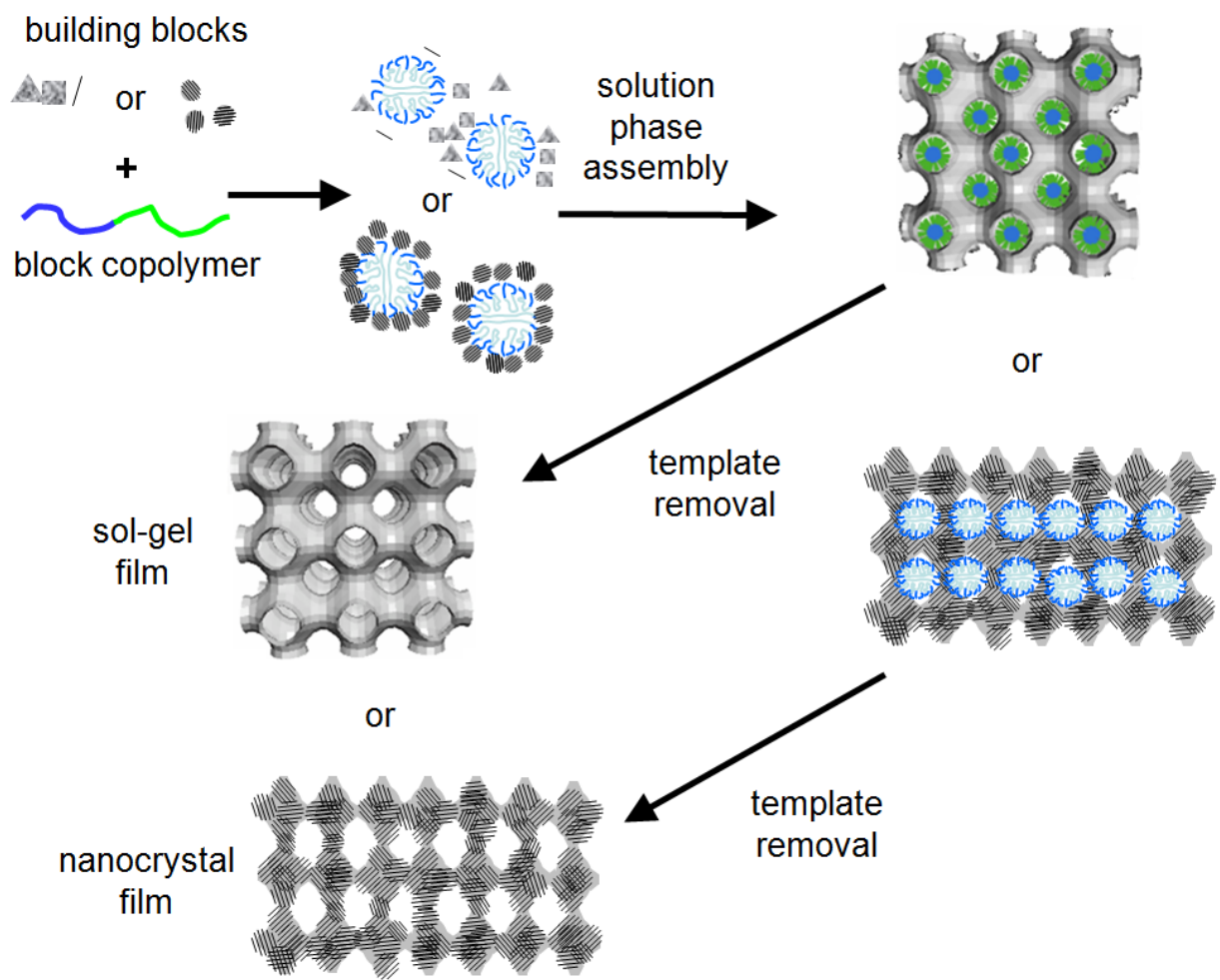
Another popular approach is to deposit a thin-film of the charge storage material onto a conductive substrate, such as a metal foil or tin-doped indium oxide (ITO) coated glass. Films can be deposited by a variety of solution-phase methods including drop-casting, dipping, and electrodeposition.²¹ Since no conductive additives or binders are used, the electrochemical properties of thin films can generally be unequivocally assigned to the active material, making these systems particularly useful for fundamental studies. In addition, if the films are thin, the capacitance and rate capabilities can be high as problems with electrical conductivity are minimized. Of course, the drawback is that the total energy storage of such electrodes is small.

Mesoporous architectures can be directly produced as thin-film electrodes using the soft-templating method. Here, we specifically focus on materials made using amphiphilic templates, including ionic and non-ionic surfactants, small triblock copolymers (specifically the pluronic family of polymers) and more recently, a growing family of larger diblock copolymers (DCP) that readily form micelles in solution and self-organize into lamellar, hexagonal or cubic structures via an evaporation induced self assembly (EISA) process.²²⁻²⁴ Casting a solution of template and inorganic precursor

onto a substrate results in an inorganic-organic composite. The template can be subsequently removed to produce a mesoporous inorganic material. While there are numerous reports of metal oxide films produced by EISA methods, the challenge of producing electrode materials is that crystalline oxides are generally needed. When metal oxides are prepared with small ionic surfactants or pluronics, the materials are often amorphous because the pore walls are too thin to crystallize without destruction of the nanoscale architecture. In the next section, we demonstrate that large DCP can circumvent this problem by producing thicker pore walls that effectively allow for crystallization of virtually any material. Such polymers also allow larger building blocks, such as preformed nanocrystals, to be organized into porous networks.

5.4 Synthesis of mesoporous films

In order to examine applications of mesoporous films for pseudocapacitive charge storage, we must first review the synthetic methods used to make these materials. The general method is depicted in Scheme 5.1. In this process, inorganic building blocks are coassembled with an amphiphilic DCP using an EISA process. Sol-gel chemistries are well suited for such polymer-templated techniques. In a typical synthesis, inorganic precursors, often metal alkoxides or metal salts, are dissolved in polar media along with the DCP to form the *sol*. The sol generally contains some water and a more volatile organic solvent such as methanol. When the solution is cast onto a substrate, either through dip-coating or spin-coating, the volatile solvent evaporates and the solution becomes richer in water. This causes the DCP to form micelles and the precursors coassemble around the micelles where they undergo a series of hydrolysis



Scheme 5.1. Evaporative-induced self-assembly process for producing cubic mesoporous films. The building blocks can be either molecular precursors leading to sol-gel-based films, or pre-formed nanocrystals, leading to nanocrystal-based films.

and condensation reactions.²⁵ The micelles then self-organize into a cubic or hexagonal structure as the remainder of the solvent evaporates and a dry film forms on the substrate.^{22–25} The film can be thermally treated to decompose the polymer template, leaving behind a mesoporous film.

Figure 5.2a–b shows scanning electron microscope (SEM) and transmission electron microscope (TEM) images of a sol-gel derived nanoporous Nb₂O₅ film that was crystallized at 600 °C. The film is macroscopically homogeneous with a well-defined cubic architecture and ordered networks of open pores averaging 13–15 nm in diameter. The film was templated with poly(ethylene-co-butylene)-*b*-poly(ethylene oxide), a DCP referred to as KLE. A unique property of these large DCPs, when compared to surfactants and pluronics, is their ability to produce materials with thicker pore walls. During heating of a film with thick walls, crystallization can nucleate with a domain that has a critical size smaller than the pore wall. Nucleation and grain-growth can then both occur within the oxide wall, leading to a highly ordered mesoporous, yet crystalline structure.

In agreement with these ideas, most crystalline, polymer-templated mesoporous materials contain randomly oriented domains with diameters similar to or slightly larger than the average wall thickness. Nanoporous niobia, however, shows unique crystallization behavior that may positively influence in its electrochemical performance. In Figure 5.2c, an electron diffraction pattern from the same KLE-templated Nb₂O₅ film shows the presence of diffraction spots indicating that the crystalline domains are oriented relative to the substrate. The data specifically indicates oriented crystal growth along the [0*k*0] direction of the orthorhombic *T*-Nb₂O₅ nanodomains. To further

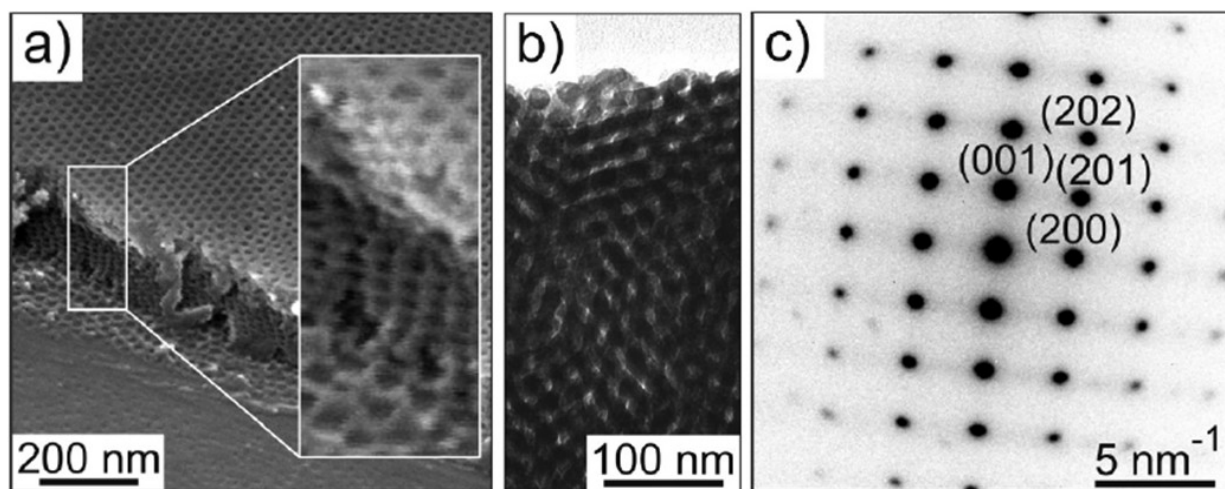


Figure 5.2. Morphology of KLE-templated $T\text{-Nb}_2\text{O}_5$ films with iso-oriented nanocrystalline pore walls. (a) Cross-sectional FESEM image of a razor-blade cut in a film held at a tilt of 45° . A higher-magnification image is shown in the inset of (a) confirming that the periodic structure observed on the top-surface persists throughout the film. (b) Bright-field TEM image. (c) Electron diffraction pattern obtained from the same sample shown in (b). The lattice-spacings correspond well with orthorhombic Nb_2O_5 (T -phase). (Adapted from ref 12. Copyright American Chemical Society 2010.)

characterize the crystal structure of these materials, wide-angle X-ray diffraction (WAXD) can be used. In Figure 5.3a, 1D-WAXD taken on mesoporous $T\text{-Nb}_2\text{O}_5$, $L\text{-Ta}_2\text{O}_5$, and TaNbO_5 films shows only one distinct peak, the (1 8 0) reflection, for all three samples indicating an iso-oriented crystallographic orientation with respect to the substrate. The inset shows a 2D-WAXD pattern which shows the other orthorhombic $T\text{-Nb}_2\text{O}_5$ peaks at off-normal angles. Similar oriented crystal growth has also been achieved in polymer-templated mesoporous $\alpha\text{-MoO}_3$, which crystallizes into a 2D layered structure with van der Waal gaps in between the stacked layers (Figure 5.6a). The interlayer gaps in these systems can be used for Li^+ intercalation. A more detailed discussion of the role of these oriented structures in Li^+ intercalation is given in section 5.6.

Another route to synthesizing crystalline, nanoporous films is to use preformed nanocrystals as building blocks.^{9,26-28} Templated nanocrystal-based materials show much higher surface areas than the sol-gel derived systems discussed above, and are thus an ideal way to build redox pseudocapacitance into a material. Figure 5.4a shows an example of a nanocrystal-based mesoporous TiO_2 architecture. The high magnification SEM image (inset) shows TiO_2 nanocrystals embedded in the pore walls. A detailed pore analysis on the nanocrystal-based TiO_2 system was obtained by toluene physisorption based on gravimetric measurements with a quartz crystal microbalance device or by ellipsometric porosimetry. Figure 5.4b–d shows typical adsorption-desorption isotherms for (b) templated sol-gel TiO_2 , (c) templated nanocrystal-based TiO_2 , and (d) untemplated TiO_2 nanocrystals. The main point to draw from these data is the templated nanocrystal film exhibits a bimodal porosity with larger mesopores, left

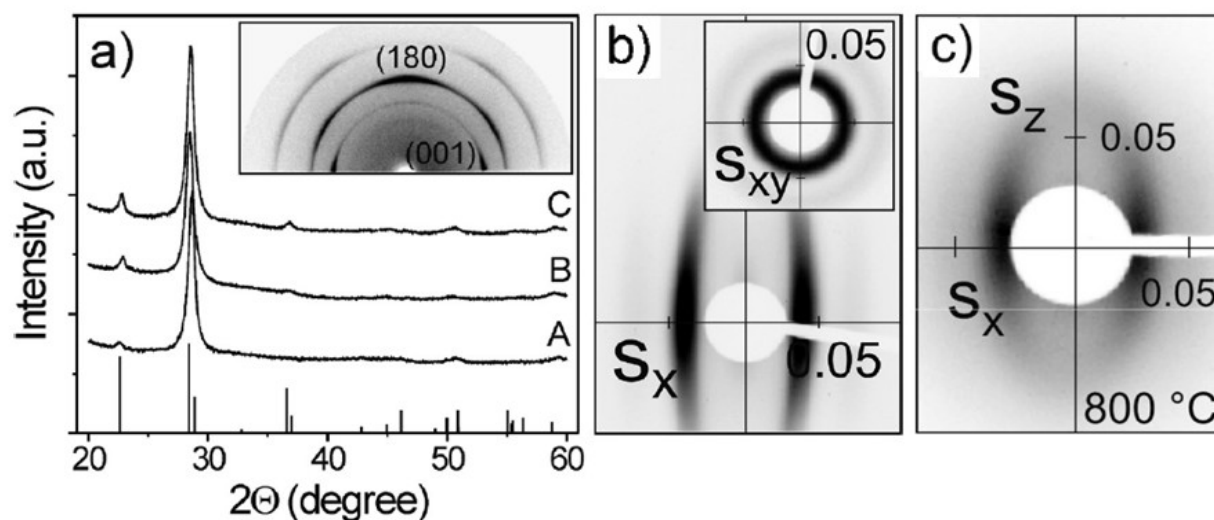


Figure 5.3. (a) 1D-WAXD data obtained on KLE-templated $T\text{-Nb}_2\text{O}_5$ (A), $L\text{-Ta}_2\text{O}_5$ (B), and TaNbO_5 (C) films. The stick pattern shows orthorhombic $T\text{-Nb}_2\text{O}_5$ according to JCPDS reference card no. 30-0873. A typical 2D-WAXD pattern for mesoporous $T\text{-Nb}_2\text{O}_5$ is shown in the inset of (a). (b) 2D-SAXS data obtained on cubic mesoporous Nb_2O_5 collected at angles of incidence $\beta = 10^\circ$ and 90° (inset). (c) 2D-SAXS pattern of KLE22-templated nanocrystal-based cubic mesoporous TiO_2 film acquired at an angle of incidence $\beta = 7^\circ$. (b–c) Scattering vector, s , components are given in $1/\text{nm}$. (Adapted from ref 9. and 12. Copyright American Chemical Society 2009 and 2010.)

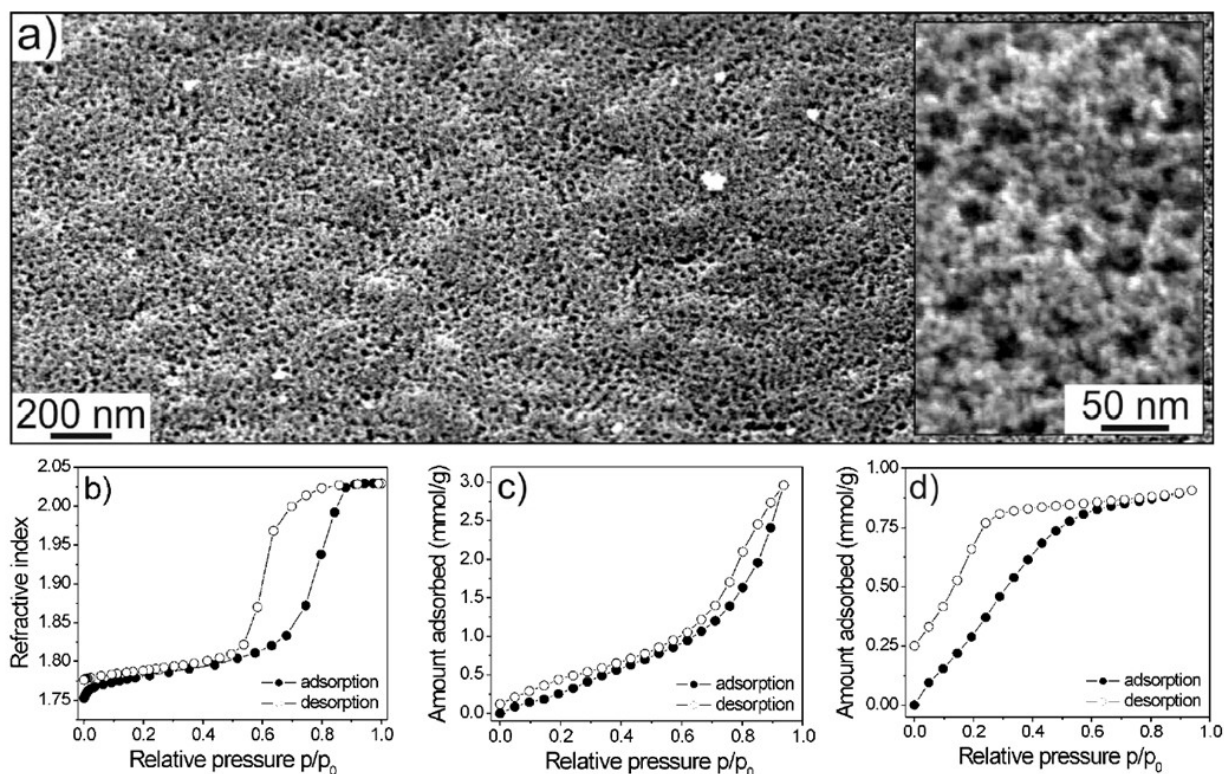


Figure 5.4. (a) Low-magnification top-view FESEM images of a KLE23-templated nanocrystal-based mesoporous TiO₂ film. The inset in (a) shows a high-magnification top-view FESEM image; the porosity is bimodal with 1–4 and 20–25 nm diameter pores. (b–d) Toluene adsorption-desorption isotherms for self-organized TiO₂ thin-films. (b) KLE22-templated sol-gel film, showing a standard isotherm for a sol-gel derived film with a monomodal pore structure. (c) KLE23-templated nanocrystal film with bimodal porosity. (d) Untemplated nanocrystal film with sub-4 nm pores that are formed by random nanocrystal aggregation. (Adapted from ref 9. Copyright American Chemical Society 2009.)

behind by the template, and smaller micropores, formed between the nanocrystals, leading to a substantial increase in surface area which can in turn produce an increase in pseudocapacitance.

For mesoporous films, the nanoscale structure can be examined by two-dimensional small-angle X-ray scattering (2D-SAXS). Figure 5.3b shows 2D-SAXS data obtained on a cubic mesoporous Nb₂O₅ film heated to 600 °C, and Figure 5.3c shows patterns for a nanocrystal-based TiO₂ film. The Nb₂O₅ film produces diffraction patterns with distinct in-plane maxima that can be indexed to a body centered cubic (bcc) pore system with a (110) orientation relative to the plane of the substrate and a lattice parameter of 33–35 nm. The TiO₂ nanocrystal film, by contrast, produces a more diffuse ellipsoidal ring which is characteristic of a more distorted pore system with a characteristic lengthscale of 35 nm. Taken together, these synthetic routes and characterization methods allow us to produce redox active materials with a diverse set of structures. Electrochemical analysis of these materials (described below) then lets us develop general design rules for fabricating polymer-templated mesoporous metal oxide electrode materials.

5.5 Quantifying capacitive properties

We have investigated the electrochemical behavior of mesoporous thin-films of TiO₂, CeO₂, MoO₃, and Nb₂O₅ in a non-aqueous Li⁺ electrolyte with several analysis techniques that allow us to use kinetic behavior to distinguish between surface and bulk charge storage. These materials can all intercalate Li⁺ and therefore careful analysis is needed to separate capacitive charge storage from diffusive contributions. Here we

describe three ways to do that. First, the current at a particular potential is kinetically separated into capacitive and diffusive contributions. Second, double-layer capacitance is directly measured by performing cyclic voltammetry in a bulky electrolyte. Finally, electrochemical impedance spectroscopy (EIS) at different potentials is used to analytically estimate pseudocapacitive and double-layer contributions.

5.5.1 Differentiating between capacitance and diffusion currents

In a cyclic voltammetry experiment, the current is a function of the sweep rate and can generally be expressed as:

$$i(V) = av^b$$

where i is the current, V is the potential, v is the sweep rate of the experiment (in mV s^{-1}), and a and b are adjustable constants. For the analysis, we assume that currents arising from bulk intercalation processes follow semi-infinite linear diffusion kinetics, and therefore will vary as $v^{1/2}$. In contrast, currents resulting from surface charge storage processes will have a capacitive response and vary linearly with v . The b -value in the above equation is therefore an estimate of the type of charge storage occurring in the material: if b is 0.5, then the current is diffusion-controlled; if b is 1, then the current is capacitive.

For nanocrystal-templated mesoporous TiO_2 , CV curves collected at scan rates from 10 to $0.5 \text{ mV}\cdot\text{s}^{-1}$, and b -values as a function of potential are shown in Figure 5.5a and 5.5b, respectively. The b -value at the peak potentials of 1.75 and 1.95 V (cathodic and anodic sweeps, respectively), is approximately 0.5 while away from the peaks, the b -value increases until it reaches ~ 1 . This analysis demonstrates that while the peak

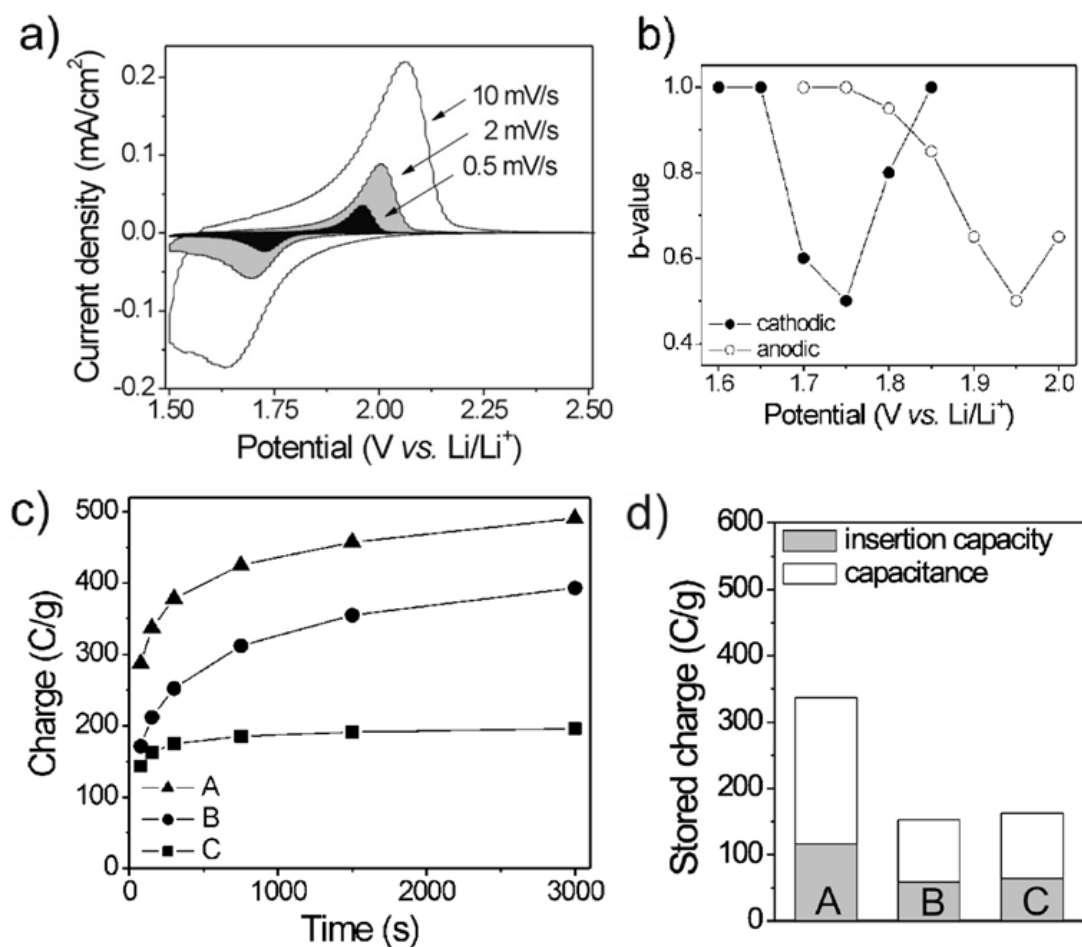


Figure 5.5. (a) Typical cyclic voltammetric responses of KLE-templated nanocrystal-based TiO_2 films at various sweep rates. (b) Calculated b -values for a KLE-templated nanocrystal-based TiO_2 film as a function of potential for the cathodic (Li^+ insertion) and anodic sweep (Li^+ extraction). (c–d) Comparison of charging rates (c) and total stored charge at a sweep rate of 10 mV s^{-1} (d) for various TiO_2 films. A and C refer to KLE-templated and untemplated nanocrystal films, while B refers to KLE-templated sol-gel films. (Adapted from ref 9. Copyright American Chemical Society 2009.)

potential currents are primarily due to diffusion processes, the capacitive contribution dominates away from the peaks.

The current behavior can be described in a more precise manner by separating the diffusion and capacitive contributions at a particular potential, as proposed by Liu, *et al.*²⁹

$$i(V) = k_1 v^{1/2} + k_2 v$$

Solving for the values of k_1 and k_2 allows for estimation of the capacitive and diffusion contributions to the current.

Figure 5.6b shows how this analysis is applied to iso-oriented crystalline mesoporous α -MoO₃. The pseudocapacitive contribution (shaded-region) is characterized by broad peaks characteristic of surface-confined charge storage.¹⁰ Such a response is unique to the mesoporous, iso-oriented architecture. From this curve, the charge storage due to capacitive processes can be estimated and the results can then be compared at different sweep rates and charging times, as shown in Figure 5.6c for MoO₃.

5.5.2 Estimating double-layer capacitance

Capacitive charge storage is expected to have contributions from both pseudocapacitive and double-layer effects. One way to estimate the amount of double-layer capacitance in a material that also exhibits pseudocapacitance is to perform cyclic voltammetry experiments with a bulky cation electrolyte, such as tetrabutylammonium (TBA⁺) perchlorate.¹² Figure 5.7 demonstrates the CV response of mesoporous T-Nb₂O₅ in both Li⁺ and TBA⁺ electrolytes. Clearly, in the bulkier electrolyte, the overall charge storage is smaller. This result indicates that only ~10% of the charge storage in

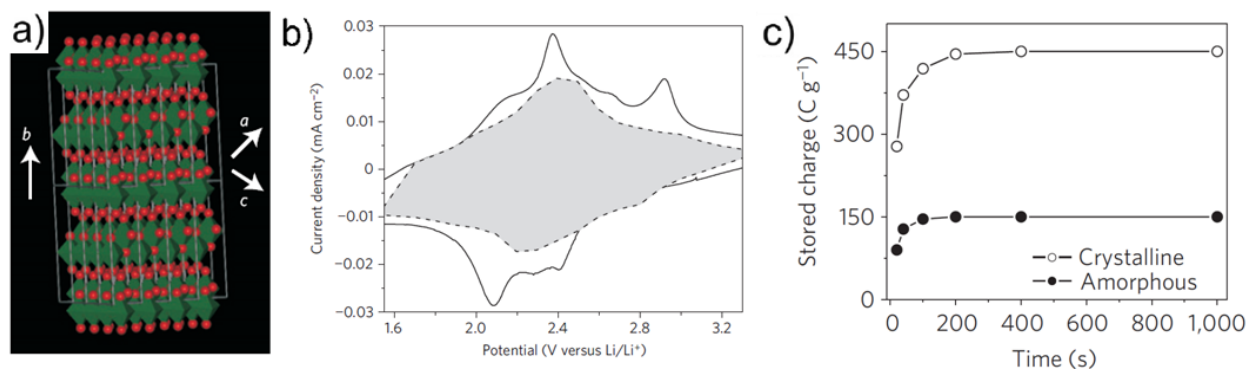


Figure 5.6. (a) Molybdenite (α - MoO_3) unit cells showing the layer-like arrangement of molybdenum (green) and oxygen atoms (red). (b) Cyclic voltammetry at 0.1 mV s^{-1} of mesoporous crystalline α - MoO_3 : the pseudocapacitive contribution is shaded, as deduced from current analysis. (c) The capacitive contribution to the total stored charge plotted as function of charging time for a mesoporous amorphous MoO_3 film and a mesoporous crystalline α - MoO_3 film. The capacitive contribution for the mesoporous crystalline film is three times larger than the amorphous analogue. (Adapted from ref 10. Copyright Macmillan Publishers 2010.)

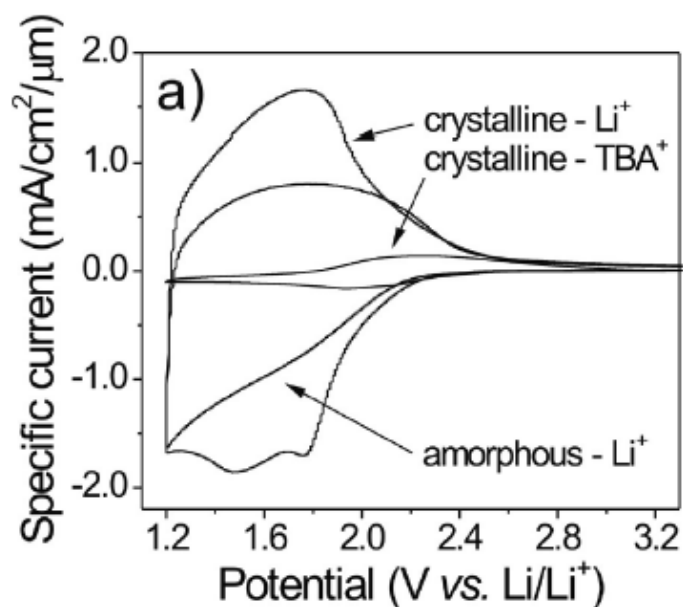


Figure 5.7. Cyclic voltammetry ($\nu = 10$ mV/s) of mesoporous $T\text{-Nb}_2\text{O}_5$ in Li^+ and TBA^+ non-aqueous electrolytes, where TBA^+ is used to estimate the double-layer capacitance. The results demonstrate the small contribution of double-layer capacitance to the overall charge storage (Adapted from ref 12. Copyright American Chemical Society 2010).

$T\text{-Nb}_2\text{O}_5$ is due to double-layer capacitance. The rest is due to faradaic redox processes.

Another way to separate the double-layer and pseudocapacitance is to use analytical modeling based on EIS. An example of this technique applied to mesoporous CeO_2 is shown in Figure 5.8a–c. A simple circuit is used to model the response at different points during lithiation, as shown in the inset of Figure 5.8a. Upon lithium insertion into the CeO_2 film, the electronic conductivity increases and charge is accumulated through capacitive processes. The double-layer capacitance is found to be independent of the potential, whereas the pseudocapacitance does depend on the applied voltage (Figure 5.8c). EIS can be used to corroborate the role of pseudocapacitance in charge storage of metal oxide films.

5.6 Design rules for pseudocapacitor electrodes

The advantage of working with thin-films of transition metal oxides is that it allows us to investigate the fundamental charge storage properties of several mesoporous materials. This, along with the work of others on porous electrodes, has led to a better understanding of what type of architectures can be used to optimize pseudocapacitive charge storage. The attributes required for an effective pseudocapacitive architecture include high surface area, interconnected porosity, mechanical flexibility, nanodimensionality, and effective electron transport. We illustrate these design principles through examples from our work on mesoporous transition metal oxides.

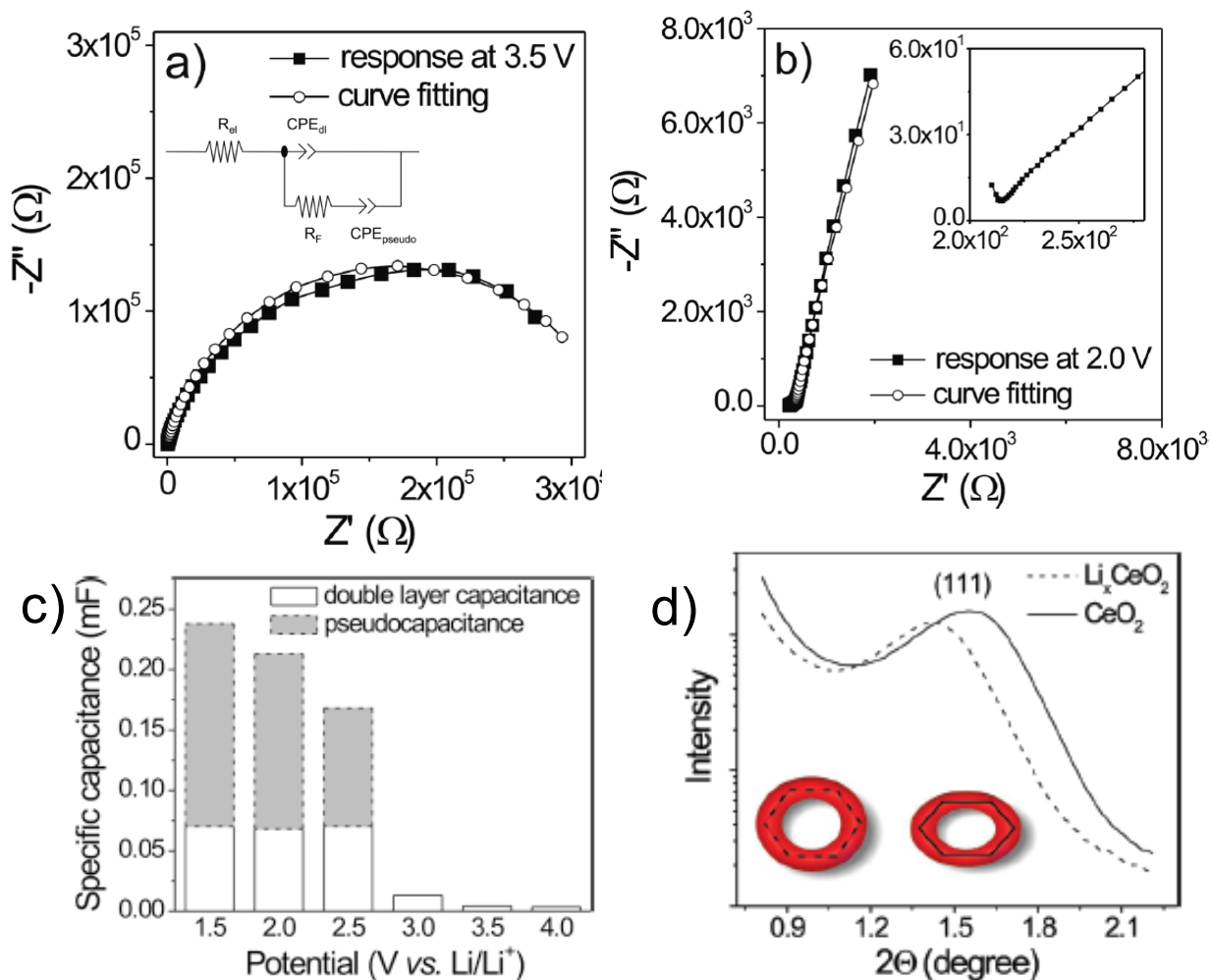


Figure 5.8. Use of electrochemical impedance spectroscopy to separate pseudocapacitance and double-layer capacitance in mesoporous crystalline CeO_2 : (a) impedance response at 3.5 V and (b) after lithiation to 2 V. The inset in (a) represents the proposed circuit model. (c) Results of the fitting analysis demonstrate that pseudocapacitance accounts for a significant fraction of the charge storage. (d) Typical 1D-SAXS pattern for KLE-templated CeO_2 and Li_xCeO_2 films. (Adapted from ref 11. Copyright American Chemical Society 2010).

5.6.1 Small nanosized building units for high surface area

Perhaps the most obvious requirement for pseudocapacitive charge storage is to utilize materials with a high surface area in order to expose more of the active surface redox sites. An effective electrode architecture should maintain the high surface area of the nanocrystals without burying them in conductive additives or binders. Polymer-templated nanocrystals with bimodal porosity (Figure 5.4a) demonstrate the dramatic effect of increased surface area on the charge storage properties of anatase TiO_2 . Figure 5.5c and 5.5d compares the charge storage behavior observed for (A) polymer-templated nanocrystal films, (B) polymer-templated sol-gel films, and (C) untemplated nanocrystal films. The pseudocapacitive contribution to charge storage is nearly 65% of the total stored charge for the templated nanocrystal film at faster sweep rates. In addition, the data suggests the total amount of stored charge and charging/discharging rates improve significantly for the templated nanocrystals architecture. These results can be attributed to the bimodal porosity with larger mesopores that allow for electrolyte diffusion, and smaller micropores that expose many redox active sites on the surface of the TiO_2 to the electrolyte.

5.6.2 Mesoporosity to facilitate solvent diffusion

The work on templated porous TiO_2 films also underscores the advantage of creating mesoporous architecture with a three-dimensional interconnected porosity (Figure 5.5c). The significance of maintaining an open porosity is apparent from the larger stored charge in the templated nanocrystal film. The data suggest that the electrochemical charge/discharge properties are enhanced by (1) minimizing the solid-

state diffusion path lengths and (2) facilitating mass transport of ions and solvent to the electrochemically active sites.

It can also be inferred from the data that in order to obtain fast solvent transport pathways, a minimum pore size is needed. This is evident by comparing the templated and untemplated nanocrystal-based films. In the latter case, the pore spaces between the nanocrystals (micropores) are too small and diffusion of ions and solvent through the film is hindered. The significant feature of this work is that the combination of the mesoporous morphology and the use of small nanosized building blocks provide a general synthetic route for improving both the surface area and the diffusion of electrolyte through the electrode structure.

5.6.3 Flexible architectures to facilitate volume expansion

One unique aspect of mesoporous films is that the ordered porosity, nanodimensions, and in some cases, iso-orientation, allow the structure to be flexible. This feature may be particularly beneficial for systems that exhibit intercalation pseudocapacitance. As ions incorporate into the layers and tunnels of such materials, size constraints and electrostatic repulsions result in lattice expansion. In bulk materials, high-rates of lithiation produce uneven lithium distribution in the material, leading to significant stress and eventually fracture.³⁰ In EC applications, the charging rates are much higher than in batteries; as the physical mechanism of intercalation pseudocapacitance is similar to that of lithium-ion batteries, the stresses can be very high. Despite this fact, materials like mesoporous orthorhombic $T\text{-Nb}_2\text{O}_5$ can be charged and discharged reversibly in a matter of seconds.

The ordered porosity and nanodimensions of mesoporous films can be modeled as a nanotruss architecture. To investigate their effects, one-dimensional small-angle X-ray scattering (1D-SAXS) experiments were carried out on mesoporous crystalline CeO_2 to see how the nanoscale repeat distance changes with cycling.¹¹ These experiments demonstrated that after fully lithiating the material for 2 hours, the film expanded by about 10% normal to the substrate, as measured by changes in the pore-to-pore distance. In Figure 5.8d the low angle diffraction peak does not broaden upon Li^+ intercalation, indicating that the framework can easily flex to accommodate the volume expansion associated with insertion.

In addition to the nanotruss architecture of all these sol-gel mesoporous films, $\alpha\text{-MoO}_3$ and $T\text{-Nb}_2\text{O}_5$ preferentially crystallize in an iso-oriented manner, with the preferred intercalation planes parallel to the substrate.^{10,12} The advantage of iso-orientation in such layered and tunnel materials is to allow uniform expansion during lithiation normal to the substrate, in addition to the tensile stress alleviation mentioned above.

5.6.4 Nanosized domains

Thus far we have established that as the dimensions of electroactive materials approach the nanoscale, the total surface area and therefore the availability of redox active sites of the material increases substantially. We have also demonstrated how maintaining an interconnected open mesoporous architecture leads to facile diffusion of ions/electrolyte to the electrochemically active sites. We now return to the concept of “iso-oriented” crystalline domains. Figure 5.6c compares the capacitive charge storage as a function of charging time for an iso-oriented mesoporous MoO_3 crystalline film with

a mesoporous amorphous MoO_3 film. The mesoporous crystalline film shows faster charging and higher capacity than the amorphous film. While surface-confined redox pseudocapacitance should occur in both types of films, the capacitive contribution is significantly higher for the crystalline film (almost 70%), compared to the amorphous film (only 35%). Therefore, in this system, it appears that intercalation pseudocapacitance associated with the fast insertion of Li^+ into the van der Waal gaps of the MoO_3 occurs on the same timescale as redox pseudocapacitance. The unique combination of a high surface area, open porosity and the nearly perfect crystallographic alignment of the intercalation layers provide very short diffusion path lengths that allow facile insertion into layers without compromising kinetics.

An important question that has yet to be addressed with mesoporous materials is their lifetime and cyclability. In general, the behavior of pseudocapacitor materials has received only limited study, however, the results are very promising. Asymmetric capacitors which incorporate one pseudocapacitive electrode show stable device operation in excess of 8,000 cycles,⁴ well beyond the performance of batteries. We expect mesoporous materials to perform similarly to these pseudocapacitors.

5.7 Conclusions

The significance of the work reviewed here is to outline systematic ways to improve the electrochemical properties of capacitive storage devices through careful design of the electrode architecture. Enhanced device performance is realized through integration of one or more of the following design rules into electrode architecture: assembling small nanosized building blocks to increase surface area, maintaining an

interconnected open mesoporosity to facilitate solvent diffusion, flexibility in the structure to facilitate volume expansion during ion transport, well defined nanodimensional domains, possibly with oriented crystalline layers to facilitate ion intercalation into the lattice, and creation of effective electron transport pathways. The latter is especially important because good electronic conductivity is essential for creating thicker architectures that can store more energy per area and volume. Several groups have already demonstrated the significant benefits of combining pseudocapacitive materials with good electron conductors,¹⁹ but these architectures usually contain a significant amount of inactive material. The goal for the next generation of mesoporous supercapacitors is to scale these optimized architectures to bulk form. Through exploration of new and optimized electrode architectures, the advancement of electrochemical capacitors to the forefront of next-generation energy storage devices can become a realization.

5.8 References

- ¹ Basic Research Needs for Electrical Energy Storage. Office of Basic Sciences, U.S. Department of Energy, Washington, DC, July 2007.
- ² Simon, P.; Gogotsi, Y. Materials for Electrochemical Capacitors. *Nat. Mater.* **2008**, 7, 845–854.
- ³ Miller, J. R.; Simon, P. Electrochemical Capacitors for Energy Management. *Science* **2008**, 321, 651–652.
- ⁴ Naoi, K. Nanohybrid Capacitor: The Next Generation Electrochemical Capacitors. *Fuel Cells* **2010**, 10, 825–833.
- ⁵ Conway, B. E. *Electrochemical Supercapacitors: Scientific Fundamentals and Technological Applications*; Kluwer Academic: New York, 1999.
- ⁶ Largeot, C.; Portet, C.; Chmiola, J.; Taberna, P.-L.; Gogotsi, Y.; Simon, P. Relation between Ion Size and Pore Size for an Electric Double-Layer Capacitor. *J. Am. Chem. Soc.* **2008**, 130, 2730–2731.
- ⁷ Bazant, M. Z.; Storey, B. D.; Kornyshev, A. Double Layer in Ionic Liquids: Overscreening versus Crowding. *Phys. Rev. Lett.* **2011**, 106, 046102(1–4).
- ⁸ Conway, B. E.; Pell, W. G. Double-layer and Pseudocapacitance Type of Electrochemical Capacitors and their Applications to the Development of Hybrid Devices. *J. Solid State Electrochem.* **2003**, 7, 637–644.
- ⁹ Brezesinski, T.; Wang, J.; Polleux, J.; Dunn, B.; Tolbert, S. H. Templated Nanocrystal-Based Porous TiO₂ Films for Next-Generation Electrochemical Capacitors. *J. Am. Chem. Soc.* **2009**, 131, 1802–1809.

-
- ¹⁰ Brezesinski, T.; Wang, J.; Tolbert, S. H.; Dunn, B. Ordered Mesoporous α -MoO₃ with Iso-Oriented Nanocrystalline Walls for Thin-Film Pseudocapacitors. *Nature Mater.* **2010**, *9*, 146–151.
- ¹¹ Brezesinski, T.; Wang, J.; Senter, R.; Brezesinski, K.; Dunn, B.; Tolbert, S. H. On the Correlation between Mechanical Flexibility, Nanoscale Structure, and Charge Storage in Periodic Mesoporous CeO₂ Thin Films. *ACS Nano* **2010**, *4*, 967–977.
- ¹² Brezesinski, K.; Wang, J.; Haetge, J.; Reitz, C.; Steinmueller, S. O.; Tolbert, S. H.; Smarsly, B. M.; Dunn, B.; Brezesinski, T. Pseudocapacitive Contributions to Charge Storage in Highly Ordered Mesoporous Group V Transition Metal Oxides with Iso-Oriented Layered Nanocrystalline Domains. *J. Am. Chem. Soc.* **2010**, *132*, 6982–6990.
- ¹³ Brezesinski, K.; Haetge, J.; Wang, J.; Mascotto, S.; Reitz, C.; Rein, A.; Tolbert, S. H.; Perlich, J.; Dunn, B.; Brezesinski, T. Ordered Mesoporous α -Fe₂O₃ (Hematite) Thin-Film Electrodes for Application in High Rate Rechargeable Lithium Batteries. *Small* **2011**, *7*, 407–414.
- ¹⁴ Tiwari, J. N.; Tiwari, R. N.; Kim, K. S. Zero-Dimensional, One-Dimensional, Two-Dimensional and Three-Dimensional Nanostructured Materials for Advanced Electrochemical Energy Devices. *Prog. Mater. Sci.* **2012**, *57*, 724–803 and references therein.
- ¹⁵ Ren, Y.; Ma, Z.; Bruce, P. G. Ordered Mesoporous Metal Oxides: Synthesis and Applications. *Chem. Soc. Rev.* **2012**, *41*, 4909–4927 and references therein.

-
- ¹⁶ Cheng, F.; Tao, Z.; Liang, J.; Chen, J.; Template-Directed Materials for Rechargeable Lithium-Ion Batteries. *Chem. Mater.* **2008**, *20*, 667–681 and references therein.
- ¹⁷ Dong, W.; Rolison, D. R.; Dunn, B. Electrochemical Properties of High Surface Area Vanadium Oxide Aerogels. *Electrochem. Solid State Lett.* **2000**, *3*, 457–459.
- ¹⁸ Zhang, H.; Yu, X.; Braun, P. V. Three-Dimensional Bicontinuous Ultrafast-Charge and-Discharge Bulk Battery Electrodes. *Nature Nanotech.* **2011**, *6*, 277–281.
- ¹⁹ Liu, R.; Duay, J.; Lee, S. B. Heterogeneous Nanostructured Electrode Materials for Electrochemical Energy Storage. *Chem. Commun.* **2010**, *47*, 1384–1404 and references therein.
- ²⁰ Gogotsi, Y.; Simon, P. True Performance Metrics in Electrochemical Energy Storage. *Science* **2011**, *334*, 917–918.
- ²¹ Lokhande, C. D.; Dubal, D. P.; Joo, O.-S.; Metal Oxide Thin Film Based Supercapacitors. *Curr. Appl. Phys.* **2011**, *11*, 255–270 and references therein.
- ²² Kresge, C. T.; Leonowicz, M. E.; Roth, W. J.; Vartuli, J. C.; Beck, J. S. Ordered Mesoporous Molecular Sieves Synthesized by a Liquid-Crystal Template Mechanism. *Nature* **1992**, *359*, 710–712.
- ²³ Zhao, D. Y.; Feng, J. L.; Huo, Q. S.; Melosh, N.; Fredrickson, G. H.; Chmelka, B. F.; Stucky, G. D. Triblock Copolymer Synthesis of Mesoporous Silica with Periodic 50 to 300 Angstrom Pores. *Science* **1998**, *279*, 548–552.
- ²⁴ Templin, M.; Franck, A.; Du Chesne, H.; Leist, H.; Zhang, Y.; Ulrich, R.; Schadler, V.; Wiesner, U. Organically Modified Aluminosilicate Mesostructures from Block Copolymer Phases. *Science* **1997**, *278*, 1795–1798.

-
- ²⁵ Lu, Y. F.; Ganguli, R.; Drewien, C. A.; Anderson, M. T.; Brinker, C. J.; Gong, W. L.; Guo, Y. X.; Soye, H.; Dunn, B.; Huang, M. H.; Zink, J. I. Continuous Formation of Supported Cubic and Hexagonal Mesoporous Films by Sol Gel Dip-Coating. *Nature* **1997**, *389*, 364–368.
- ²⁶ Warren, S. C.; Messina, L. C.; Slaughter, L. S.; Kamperman, M.; Zhou, Q.; Gruner, S. M.; DiSalvo, F. J.; Wiesner, U. Ordered Mesoporous Materials from Metal Nanoparticle–Block Copolymer Self-Assembly. *Science* **2008**, *320*, 1748–1752.
- ²⁷ Deshpande, A. S.; Pinna, N.; Smarsly, B.; Antonietti, M.; Niederberger, M.; Controlled Assembly of Preformed Ceria Nanocrystals into Highly Ordered 3D Nanostructures. *Small* **2005**, *1*, 313–316.
- ²⁸ Ba, J. H.; Polleux, J.; Antonietti, M.; Niederberger, M. Non-aqueous Synthesis of Tin Oxide Nanocrystals and Their Assembly into Ordered Porous Mesoporous Structures. *Adv. Mater.* **2005**, *17*, 2509–2512.
- ²⁹ Liu, T.-C.; Pell, W. G.; Roberson, S. L.; Conway, B. E. Behavior of Molybdenum Nitrides as Materials for Electrochemical Capacitors. *J. Electrochem. Soc.* **1998**, *145*, 1882–1888.
- ³⁰ Zhao, K.; Pharr, M.; Vlassak, J. J.; Suo, Z. Fracture of Electrodes in Lithium-Ion Batteries caused by Fast Charging. *J. Appl. Phys.* **2010**, *108*, 073517(1–6).

CHAPTER 6

General Method for the Synthesis of Hierarchical Nanocrystal-Based Mesoporous Materials

6.1 Introduction

One of the key goals of nanoscience research over the past 2 decades has been the development of methods to precisely control structure at the nanometer length scale. One route to this control that has met with significant success is amphiphilic templating of inorganic materials. In this method, soluble inorganic oligomers co-assemble with amphiphilic organic species to produce a structured inorganic/organic composite material. Thermal or chemical removal of the organic component leaves behind an inorganic material with porosity on the nanometer length scale, and an architecture that is determined by co-assembly of the organic and inorganic components.¹⁻⁹ Common structure directing agents include surfactants and block copolymers, and these have been used to prepare a broad range of mesoporous architectures from soluble inorganic building blocks, in most cases utilizing sol-gel chemistries.¹⁰⁻²⁸

While this method provides beautiful control of nanometer scale architecture, there is much less control of the atomic scale structure in most templated nanoporous materials. Pore walls can be crystallized by thermal processing, but in many cases the walls do not fully crystallize during template removal, resulting in a partially crystalline or amorphous pore wall.^{29,30} Moreover, the lack of control of grain growth during the

crystallization process can result in the destruction of the pore-solid architecture and the interconnected porosity. Creating materials with this type of nanometer scale architecture is a worthwhile goal, however, as this architecture imparts the unique combination of high surface area, an electrically interconnected structure, and good accessibility to the surface area.

One approach to mitigate the problems associated with crystallization of the inorganic framework is to start not with sol-gel type molecular precursors, but with preformed nanocrystals. Using this method, crystalline nanoporous materials can be produced, and because thermal processing is needed only to remove the polymer template and network the nanocrystals, not to crystallize the inorganic phase, open, interconnected porosity is well retained. A few examples of this type of nanocrystal templating exist in the literature.^{31–36} The problem is that while the literature is full of beautiful routes to soluble nanocrystals with well-defined chemical composition, size, shape, and distinctive optical, electronic, and chemical properties,^{37–50} the vast majority of those nanocrystals are coated with organic surface ligands that provide solubility and prevent nanocrystal agglomeration. In order to substitute sol-gel type precursors with pre-formed nanocrystals in typical template-driven syntheses, the ligands must be removed from the nanocrystals while maintaining nanocrystal solubility and preventing aggregation. Most of the previous results for nanocrystal templating utilized nanocrystals with hydrolysable surface groups that could be removed by the addition of small quantities of water to produce metastable, hydroxyl-terminated nanocrystals.^{51,52} Such methods are not general, however, because in many cases removal of the surface

groups leads to agglomerated nanocrystals that cannot be templated, limiting the types of nanocrystal-based nanoporous materials that can be produced.

One reason that nanocrystal-templating is so important is that we have recently shown that nanocrystal-based nanoporous titania demonstrates high levels of pseudocapacitive charge storage accompanied by fast charging/discharging rates.³⁵ These materials were synthesized from nanocrystals that contained hydrolysable surface ligands, as discussed above.^{51,52} In that work, enhancement of electrochemical properties resulted from the unique combination of open porosity, which allowed facile electrolyte diffusion throughout the material, and the high density of electrochemically active surface redox sites, which results from the high surface area of the nanocrystal building blocks that made up the pore walls.³⁵ In order to be able to extend this approach to a broader array of nanocrystals, a more broadly applicable method for templating ligand-stripped nanocrystals is needed. Because of this interest in materials for electrochemical supercapacitors, the materials that we have chosen to explore in this work are either conductors or redox active transition metal oxides. The technique should be applicable, however, to any nanocrystal system that is stable under the calcination conditions required to remove the polymer template.

Recently, there have been few reports on methods to strip native ligands off the surface of nanocrystals to produce bare, soluble nanocrystals that can be dissolved in polar solvents.^{53–55} The first example was work by Murray and co-workers, who reported a method that employed nitrosonium tetrafluoroborate (NOBF_4).⁵³ The authors speculate that NO^+ reacts with trace water to form nitrous and/or fluoroboric acid which protonate basic ligands such as carboxylic acids and amines so that they desorb from

the surface of nanocrystals, accompanied by phase transfer of the nanocrystals from nonpolar to polar solvents.⁵³ In that work, the native organic ligands are removed and replaced by some combination of protons and dimethylformamide (DMF), to produce dispersible, cationic nanocrystals that are charge-balanced by BF_4^- anions. Milliron and coworkers used this method to prepare nanocomposite films containing Sn-doped In_2O_3 (ITO) nanocrystals in transition metal oxide matrices.⁵⁶ Recently, related but milder ligand stripping methods have also been reported, so that ligands can now be removed non-destructively from a broad range of nanocrystals.⁵⁵

In this work, we build from our previous work on templating nanocrystals into porous architectures and describe a general route to prepare hierarchical nanocrystal-based mesoporous films of various systems. The NOBF_4 ligand-exchange strategy is utilized to prepare dispersible nanocrystals of various oxide systems including ITO,^{56–58} manganese oxide (Mn_3O_4),⁵⁹ and manganese ferrite (MnFe_2O_4).⁶⁰ We demonstrate the generality of this approach by varying the composition and size of the nanocrystals, and in each case, nearly identical porous networks are produced with no modification of the synthetic procedure. This statement cannot be made of sol-gel derived porous materials, as the reactivity of each sol-gel precursor is different and so synthetic procedures must be reoptimized for each materials system. In the present case, formation of each nanocrystal building block requires materials specific optimization, but the formation of the porous network does not. Because this method focuses on assembly, decoupled from molecular scale reactivity, synthetic procedures scale across materials systems without adjustment. In addition, nanocrystals are templated with a range of di-block copolymers containing variable block compositions and molecular

weights. Films are produced by various coating methods including dip-coating, spin-coating, and drop-casting. We further show that even greater material diversity is accessible through solid-state conversion reactions. For example, the MnFe_2O_4 system can be converted to a mixed manganese-iron oxide $(\text{Mn,Fe})_2\text{O}_3$ with retention of the original porous architecture. Taken together, the results demonstrated in this work describe a powerful approach to templating diverse nanocrystal systems and, therefore, a simple recipe for preparing functional nanoscale architectures from preformed nanocrystal building blocks.

6.2 Results and Discussion

6.2.1 Preparation of Mesoporous Nanocrystal-based Films

The synthesis of mesoporous nanocrystal-based materials is described in detail in the experimental section. The key steps in the process, however, are discussed here. The overall synthetic process involves nanocrystal synthesis, ligand removal, and templating of the desired nanocrystal system. In all cases, nanocrystals were synthesized using previously reported high-temperature solution-phase syntheses that utilize organic ligands with either amine or carboxylic acid functional groups to stabilize the nanocrystal surface.^{56–60} As-synthesized nanocrystals dispersed in hexane were then stripped of their surface ligands and phase transferred into polar media by treatment with NOBF_4 in DMF, as described above.⁵³ In a typical film synthesis, ethanolic dispersions of the ligand-exchanged pre-formed nanocrystals, with ~10% DMF (v/v), were mixed with a block copolymer template, dissolved in pure ethanol, to prepare the coating solution. Thin-films were dip-coated onto clean polar substrates through an

evaporation-induced self-assembly process.⁶¹ In solution, the polymer forms micelles and, upon evaporation of the solvent, the micelles co-assemble with the pre-formed nanocrystals and both components self-organize into a mesostructured organic/inorganic composite. Next, the organic polymer template is thermally decomposed in air to leave behind a mesoporous inorganic architecture that exhibits three-dimensionally interconnected porosity.

Dispersible, ligand-free nanocrystal building blocks are essential to this process. Figure 6.1 shows the transmission electron microscopy (TEM) images of three different compositions of nanocrystals, both before and after ligand-stripping with NOBF_4 . The images show ITO (Figure 6.1a–b), MnFe_2O_4 (Figure 6.1c–d), and Mn_3O_4 (Figure 6.1e–f) nanocrystals with ligand-stripped samples in panels b, d, and f. As can be seen in Figure 6.1b, NOBF_4 -treated ITO nanocrystals are not agglomerated or fused together, suggesting they form stable dispersions.⁵³ A closer look at the particles after NOBF_4 treatment reveals a shorter inter-particle distance which is consistent with removal of the native ligands.⁵³ In addition, the average particle size (7.3 ± 0.7 nm) does not change suggesting no etching of the surface of the nanocrystals during the NOBF_4 treatment. Similar results were observed for both MnFe_2O_4 (Figure 6.1c–d) and Mn_3O_4 (Figure 6.1e–f) nanocrystals. There is no apparent agglomeration or change in particle size for either MnFe_2O_4 (4.6 ± 0.5 nm) or Mn_3O_4 (4.8 ± 0.5 nm) nanocrystals after NOBF_4 treatment. Taken together, the TEM data for all three systems reveal the nanocrystals have a uniform size and shape that is not altered by the ligand removal process. These data suggest that NOBF_4 stripping is a viable method that can be

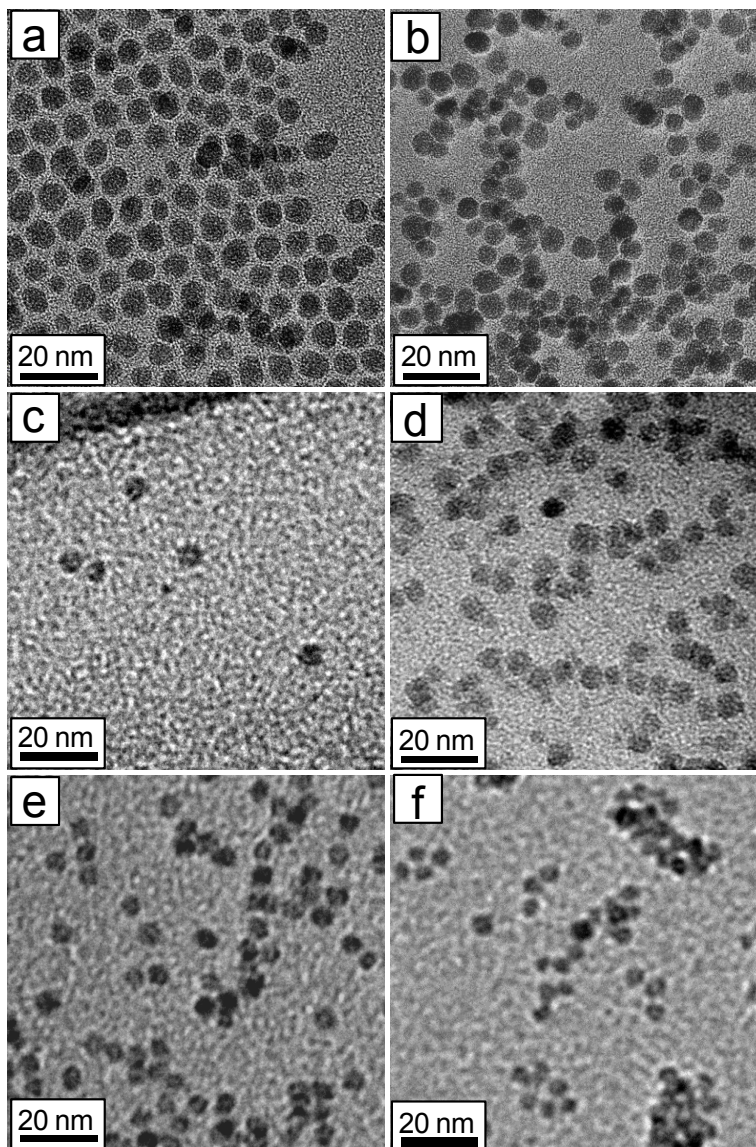


Figure 6.1. TEM images of ITO nanocrystals as-synthesized (a) and after the ligand-exchange process (b); MnFe_2O_4 nanocrystals as-synthesized (c) and after the ligand-exchange process (d); and Mn_3O_4 nanocrystals as-synthesized (e) and after the ligand-exchange process (f). In all cases, the particles do not agglomerate and maintain a uniform size and shape after the ligand removal process.

utilized to prepare dispersions of many nanocrystals compositions for use in polymer templating.

To this end, figure 6.2 shows top view scanning electron microscope (SEM) images of mesoporous films produced from these same three nanocrystal systems including: ITO (Figure 6.2a–b), Mn_3O_4 (Figure 6.2c–d) and MnFe_2O_4 (Figure 6.2e–f). For all three systems the block copolymer template utilized was poly(ethylene-*alt*-propylene)-*block*-poly(ethylene oxide), (PEP-*b*-PEO) (polydispersity index (PDI) = 1.05), which was thermally decomposed between 350 and 450 °C in air to produce the porous materials. This class of amphiphilic block copolymers has been shown to produce well-ordered, periodic mesoporous inorganic materials.^{16,35,62–72} In the synthesis, we begin with ligand-exchanged nanocrystals that are stabilized in solution by a combination of dative bonds from the DMF solvent and electrostatic repulsion from the charged nanocrystal surface. Upon addition of the polymer, the PEO block likely coordinates to the nanocrystal surface so that upon solvent evaporation the nanocrystals preferentially segregate to the PEO region of the composite film. Thermal treatment is then used to thermally degrade the polymer and fuse the nanocrystals together. The thermal stability of the hydrophobic polymer block ensures that the nanocrystals are well fused before full thermal decomposition of the template, resulting in a rigid inorganic porous structure.

The films in Figure 6.2a–b were prepared from ITO nanocrystals with a diameter of 7.3 ± 0.7 nm.⁵⁶ Figure 6.2a shows a low-magnification image of an ITO film where the mesopores are locally disordered, but they are macroscopically homogeneous with an average diameter of 15 ± 3 nm. The pore walls range from 1–3 nanocrystals across,

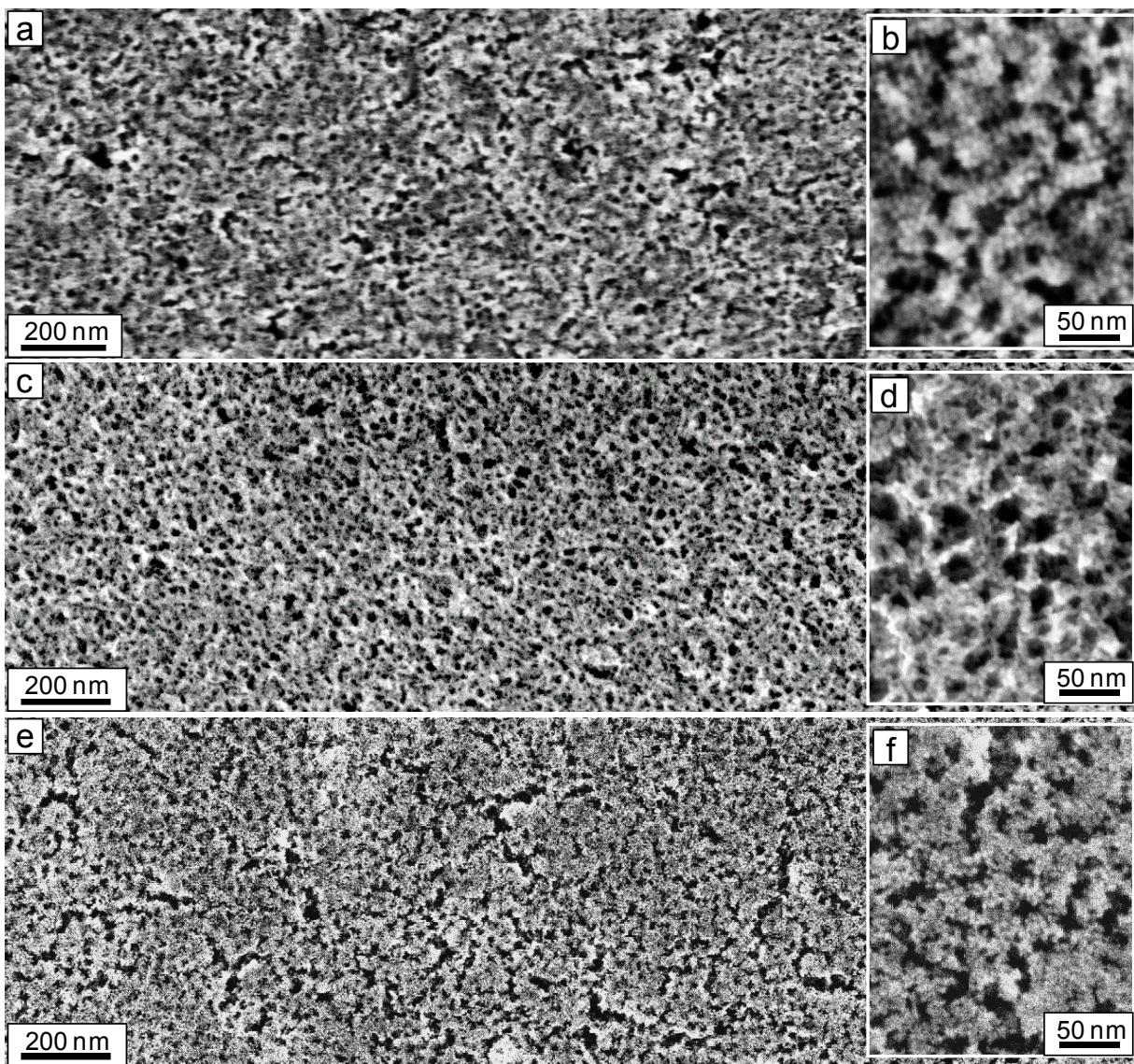


Figure 6.2. SEM images of various templated nanocrystal-based porous films. (a) Low-magnification and (b) high-magnification top-view SEM images of PEP-*b*-PEO templated ITO nanocrystals. (c) Low-magnification and (d) high-magnification top-view SEM images of PEP-*b*-PEO templated Mn_3O_4 nanocrystals. (e) Low-magnification and (f) high-magnification top-view SEM images of PEP-*b*-PEO templated MnFe_2O_4 nanocrystals.

with approximately 2 nanocrystals representing the majority of pore walls in the film. Given an average nanocrystal diameter of 7.3 ± 0.7 nm, the sum of the pore diameter and the average wall thickness is in reasonable agreement with two-dimensional small-angle X-ray scattering (see below, 2D-SAXS, Figure 6.6a) data where the average repeat distance was found to be 32 nm. These films are crack-free and the pores are open at the surface. Figure 6.2b shows a high-magnification image where the presence of individual nanocrystals can also be seen; the voids between these nanocrystals give rise to micropores that significantly increase surface area.

Figure 6.2c shows a top view low-magnification image of PEP-*b*-PEO templated Mn_3O_4 nanocrystals with an average diameter of 4.8 ± 0.5 nm.⁵⁹ A high-magnification image of Mn_3O_4 films is shown in Figure 6.2d. Similarly, low-magnification (Figure 6.2e) and high magnification (Figure 6.2f) images of MnFe_2O_4 nanocrystal-based films with an average particle diameter of 4.6 ± 0.5 nm⁶⁰ are also shown. For these two films, just as for ITO, the mesopores are locally disordered, with an average pore diameter of 17 ± 4 nm for Mn_3O_4 films and 16 ± 2 nm for MnFe_2O_4 films. In the high-magnification images for both Mn_3O_4 and MnFe_2O_4 , the presence of individual nanocrystals that give rise to micropores are again visible. In all three types of nanocrystal-based films, ITO, Mn_3O_4 , and MnFe_2O_4 , the pore walls are comprised of nanocrystals that fuse only at point contact and retain their generally spherical shape. Because the nanocrystals in the pore walls do not fully fuse to form a dense wall, microporosity is generated.

Figure 6.2 thus demonstrates that our templating approach can be applied to nanocrystals with a broad range of compositions, producing films with nearly identical nanometer scale architecture. As discussed above, previous work has been published

on block co-polymer templating of nanocrystals, but in those reported syntheses, the chemistries used have been specific to a small class of nanocrystals and the methods have not scaled across materials.^{35,51,52} In those cases, nanocrystals were formed with benzyl alkoxide on the surface, and those alkoxide ligands could be hydrolyzed off to produce metastable, ligand free nanocrystals that could also be coassembled with diblock copolymers. Only a few nanocrystal types can be synthesized in truly soluble form using this chemistry, however, so the method is not general. The beauty of the NOBF_4 chemistry used here⁵³ is that it is quite general, and recent variations on the method have now extended this ligand-stripping process to even more nanocrystals types,⁵⁵ further increasing the range of materials that can be formed into porous networks.

6.2.2 Synthetic and Structural Tunability

To demonstrate the extent of synthetic tunability in our approach we explored several different parameters including choice of block copolymer, coating technique and size of the nanocrystal. In addition to the PEP-*b*-PEO polymer used to prepare the films in Figure 6.2, we can template films with poly(butadiene(1,2 addition))-*block*-poly(ethylene oxide) (PB-*b*-PEO),⁷² and poly(butylene oxide)-*block*-poly(ethylene oxide) (PBO-*b*-PEO). Chemically speaking, all three polymers have a PEO hydrophilic block that may vary in length and a hydrophobic block which may also vary in length. To investigate the architectural effects from each polymer template the differences in the weight fraction and molecular weight for each block must also be considered. Here, the weight fraction for the PEO block, $f_w \text{ PEO}$, in PEP-*b*-PEO is defined as $f_w \text{ PEO} = M_n \text{ PEO} / (M_n \text{ PEO} + M_n \text{ PEP})$, where $M_n \text{ PEO}$ and $M_n \text{ PEP}$ are the molecular weights for the

individual blocks. Using this definition, the weight fractions for PEP-*b*-PEO are $f_w \text{ PEP} = 0.49$ ($M_n = 3900$ g/mol) and $f_w \text{ PEO} = 0.51$ ($M_n = 4000$ g/mol), for PB-*b*-PEO they are $f_w \text{ PB} = 0.52$ ($M_n = 5500$ g/mol) and $f_w \text{ PEO} = 0.48$ ($M_n = 5000$ g/mol), and for PBO-*b*-PEO they are $f_w \text{ PBO} = 0.57$ ($M_n = 6500$ g/mol) and $f_w \text{ PEO} = 0.43$ ($M_n = 5000$ g/mol). All polymers have similar hydrophilic:hydrophobic block ratios, but the total molecular weights and the chemical nature of the hydrophobic block varies significantly. A more detailed description of the block length, molecular weight and weight fraction for each block in all three block copolymers can be found in the experimental section.

Figure 6.3a–b shows top-view SEM images of PB-*b*-PEO templated ITO nanocrystals with an average diameter of 7.3 ± 0.7 nm prepared by dip-coating (Figure 6.3a) and spin-coating (Figure 6.3b). Similar to the PEP-*b*-PEO templated ITO nanocrystals in Figure 6.2a–b, these films demonstrate a locally disordered mesostructure with macroscopically homogeneous porosity. PB-*b*-PEO templated films have an average pore diameter of 28 ± 3 nm and the pore walls are approximately one to three nanocrystals thick. In agreement with these values, the average distance between pores was found to be fairly large (around 36 nm) from 2D-SAXS data, Figure 6.6e. The variation in pore diameter and pore wall thickness for PB-*b*-PEO- versus PEP-*b*-PEO-templated ITO films can be explained by their structural difference. Our PB-*b*-PEO is a larger polymer with $M_n = 10500$ g/mol, compared to PEP-*b*-PEO with $M_n = 7900$ g/mol. Therefore, it is expected to form larger micelles in solution leading to larger pores. In addition, the PEO block in PB-*b*-PEO is larger than the PEO block in PEP-*b*-PEO which should lead to thicker pore walls, since the particles co-assemble with the PEO block of the micelles to form the pore walls during synthesis.

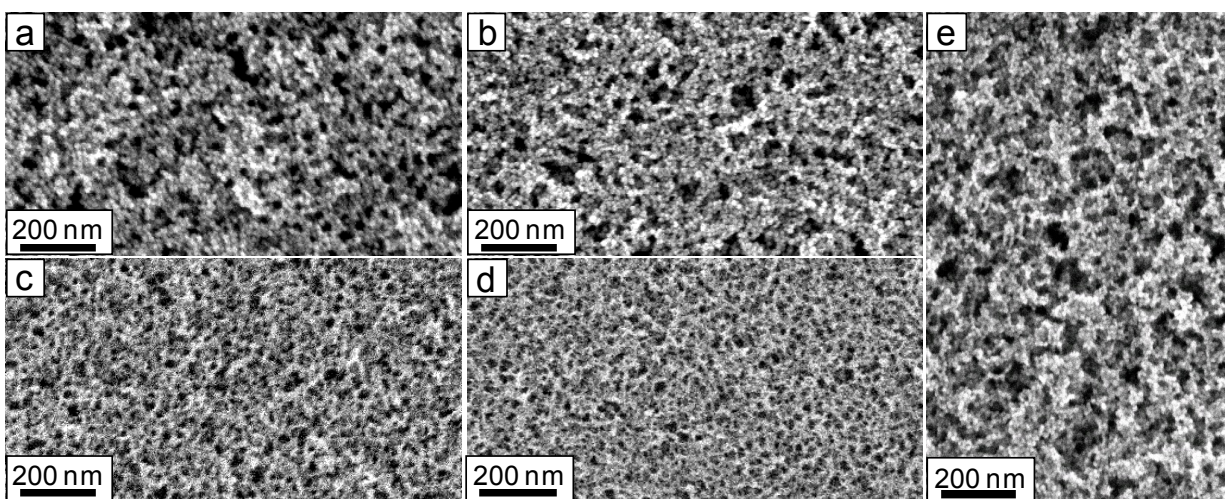


Figure 6.3. SEM images of templated nanocrystal-based porous films demonstrating variability of the template and coating method. Low-magnification top-view SEM images of PB-*b*-PEO templated ITO nanocrystals prepared by dip-coating (a) and spin-coating (b). Low-magnification top-view SEM images of PBO-*b*-PEO templated Mn₃O₄ nanocrystals prepared by dip-coating (c) and spin-coating (d). (e) SEM image of PEP-*b*-PEO templated ITO nanocrystals prepared by drop-casting.

Figure 6.3c–d shows top-view SEM images of Mn_3O_4 nanocrystals with an average diameter of 4–5 nm that were templated with PBO-*b*-PEO by dip-coating (Figure 6.3c) and spin-coating (Figure 6.3d). Both PB-*b*-PEO and PBO-*b*-PEO templates were thermally decomposed at 450 °C in air. Interestingly, the total molecular weight of our PBO-*b*-PEO is larger than that of our PB-*b*-PEO and PEP-*b*-PEO. However, the average pore diameter for the PBO-*b*-PEO system was found to be 13 ± 1 nm with an average pore wall thickness of 6–8 nm, which are both smaller than values determined for PB-*b*-PEO and PEP-*b*-PEO templated systems. This is corroborated with 2D-SAXS data (Figure 6.6f), which shows an average pore-to-pore distance of 28 nm for PBO-*b*-PEO materials, which is smaller than the averages for the PB-*b*-PEO- or PEP-*b*-PEO-templated systems. The smaller mesostructure can be attributed to the less hydrophobic/more hydrophilic nature of the PBO block compared to PB and PEP. Some nanocrystals may associate with the nominally hydrophobic block, leading to a smaller pore. More likely, because of the increased solubility of the PBO-*b*-PEO polymer in polar solvents, the polymer may have a lower aggregation number, which could also lead to smaller-sized micelles in solution. Lower aggregation number also explains the combination of a smaller average pore diameter and a smaller pore wall thickness, which would lead to the shorter pore-to-pore distance observed in SAXS.

Figure 6.3e shows a top-view SEM image of ITO nanocrystals with an average diameter of 7.3 ± 0.7 nm that were templated with PEP-*b*-PEO by drop-casting. To prepare these films, nanocrystal/polymer solution was drop cast onto a polar substrate and the solvent was allowed to evaporate in air at room temperature. The films were heated to 450 °C to thermally decompose the polymer template. The film in Figure 6.3e

had an average thickness of $2.0 \pm 0.1 \mu\text{m}$ based on profilometry measurements. The average pore diameter was found to be $15 \pm 3 \text{ nm}$, which is in agreement with the films in Figure 6.2 that were also templated with PEP-*b*-PEO. The drop-cast films show somewhat more disordered porosity, compared with dip-coated and spin-coated films. However, it is important to note that these films are at least one order of magnitude thicker than either dip-coated or spin-coated films and from a macroscopic perspective, the porosity is still homogeneous.

As described above, the method used to deposit films plays a role in the final film architecture. On average, spin-coating produces the thinnest films ranging from 100 to 120 nm thick after calcination by profilometry measurements. A single dip-coating process produces films ranging from 120 to 220 nm after calcination. It was also found that multiple coatings could be used to make thicker films; for example, double-dipped films up to 400 nm could be produced. To produce thicker films, drop-casting can be used. Drop casting is a viable method for generating films in the 1–5 μm range.

A comparison of films prepared by dip-coating (Figure 6.3a and 6.3c), spin-coating (Figure 6.3b and 6.3d) and drop-casting (Figure 6.3e) reveals that surface roughness increases from spin-coated < dip-coated < drop-casted films. This can be explained by differences in the drying kinetics for each coating technique. In drop-casted films, the solvent evaporates very slowly and this can lead to inhomogeneous drying, especially near the surface of the film. During dip-coating, the solvent evaporates faster than for drop-casted films but slower than spin-coated films, and these variations in evaporation rate can lead to small variations in surface roughness. On the other hand, spin-coating involves very fast evaporation of the solvent, producing

films with a more homogeneous thickness. For most sol-gel based block copolymer templated materials, spin coating produces significantly less ordered materials because there is not enough time for hydrolysis and condensation reactions to occur during the film deposition process.^{73–75} In this case, however, no chemistry occurs during film deposition, and so the pore structure in all cases is similar, indicating that all methods are viable routes to film deposition. This combination of results demonstrates the robustness of this nanocrystal-templating strategy and indicates that homogeneous, nanoporous nanocrystal-based films can likely be made by any solution phase deposition route, including industrially scalable methods such as doctor-blading or roll-to-roll deposition.

Another route to structural variation in these materials focuses on the ability to perform thermally induced solid-state conversion reactions in nanoporous materials with retention of the intrinsic nanostructure.^{68,76} While many different kinds of nanocrystals can be synthesized, there are still more materials that have not yet been made as soluble nanocrystals. Solid state transformation thus provides a route to expand the palette of accessible materials. Thermal treatments stringent enough to drive a solid-solid transformation can, however, lead to destruction of the periodicity and obstruction of the porosity from grain growth particularly at high temperatures. Here, we show one example of a transformation that can occur with-in our nanocrystal based nanoporous materials with retention of nanometer scale architecture.

It is well known that spinel structured ferrites can be converted to materials with a hematite structure upon thermal treatment in air.⁷⁷ The data in Figure 6.4 demonstrates this type of solid-state conversion reaction in a PEP-*b*-PEO-templated MnFe_2O_4

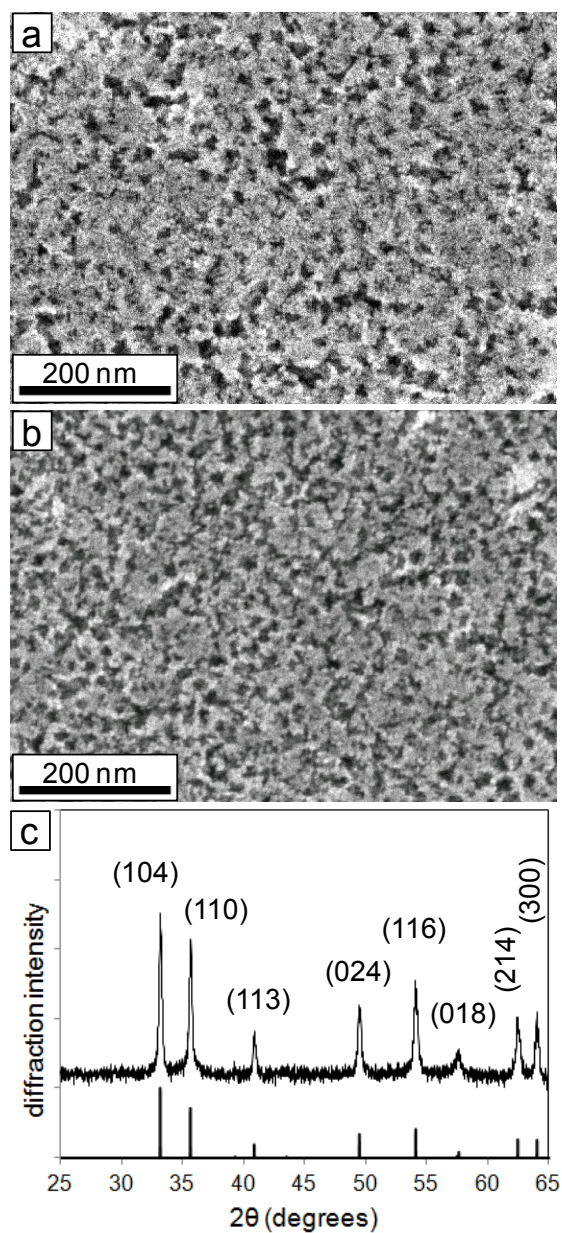


Figure 6.4. (a) SEM image of PEP-*b*-PEO templated MnFe_2O_4 nanocrystal-based films. (b) SEM image of MnFe_2O_4 films in (a) that were thermally converted to $(\text{Mn,Fe})_2\text{O}_3$ at 400 °C demonstrating retention of mesostructure. (c) WAXD data showing full conversion from MnFe_2O_4 to $(\text{Mn,Fe})_2\text{O}_3$.

nanocrystal thin-film. The spinel ferrite (Figure 6.4a), is converted to a mixed oxide (Mn,Fe)₂O₃ system (Figure 6.4b). The conversion of bulk spinel (cubic) MnFe₂O₄ phase to the hematite (rhombohedral) (Mn,Fe)₂O₃ phase in air at elevated temperatures (>650 °C) has been reported to occur by oxidation of the Mn²⁺ in the spinel to Mn³⁺ resulting in a solid solution of Fe₂O₃ and Mn₂O₃ with a hematite crystal structure.⁷⁷ The films in Figure 6.4a were heated to 350 °C to thermally decompose the polymer template while still retaining the ferrite phase. Interestingly, in the templated nanocrystal-based films, thermal conversion to hematite occurs at only 400 °C which is significantly lower than the bulk conversion temperature. This result is consistent with the established fact that phase transitions in nanocrystals can occur at very different temperatures than those in the bulk systems.^{78,79} More importantly, the films retain the nanoscale architecture and open porosity. Figure 6.4c shows WAXD data collected on converted (Mn,Fe)₂O₃ films. The peaks can be indexed to the hematite phase of iron oxide with a rhombohedral crystal structure (JCPDS reference card no. 08-2902) with no indication of the spinel phase suggesting complete conversion. Scherrer analysis of the peak widths gives an average grain size of ~40 nm indicating that there is grain growth during thermal conversion. Some nanocrystals can still be seen in Figure 6.4b, however, suggesting an inhomogeneous distribution of grain sizes. Interestingly, the grain growth observed during the ferrite to hematite transition implies that the many nanocrystals of ferrite can convert into larger single hematite crystals with large diameters and while preserving the pore structure. The key feature to note is that the nanostructure is not destroyed, and that comparison of Figure 6.4a–b shows qualitatively similar porosity. This type of

conversion reaction can become important when recipes for producing nanocrystals of a particular composition are not available.

6.2.3 Structural Characterization

While the SEM images presented in Figures 6.2 – 6.4 provide the most direct route to visualize these porous networks, they provide information only about a small surface region of the film, and they provide no information about the atomic scale structure of the films. To further characterize the structure of these nanocrystal-based nanoporous materials, we utilize a combination of low and high angle X-ray scattering, combined with ellipsometric porosimetry. Analysis of the crystal structure was carried out using wide angle X-ray diffraction (WAXD) measurements. Figure 6.5a shows WAXD patterns for ITO nanocrystals as-synthesized (A), after NOBF_4 treatment (B) and after templating with PEP-*b*-PEO (C). In all three patterns (A–C), the evolution of the main peaks can be indexed to the cubic phase (bixbyite) of In_2O_3 with Sn doped into the lattice (JCPDS reference card no. 06-0416). Scherrer analysis of the peak widths for ITO nanocrystals as-synthesized (A) and after NOBF_4 treatment (B) gives in an average domain size of 7–8 nm which is consistent with the particle size found in TEM data (Figure 6.1a–b). In (C), the average domain size of nanocrystals does not change after templating with PEP-*b*-PEO which is consistent with SEM data (Figure 6.2a–b) that shows individual nanocrystals comprising the pore walls of the films. The relative intensities of the peaks also suggest the nanocrystals embedded in the pore walls are randomly oriented. The fact that there is no phase-transformation or grain growth during thermal decomposition of the polymer suggests the nanocrystals are thermally stable.

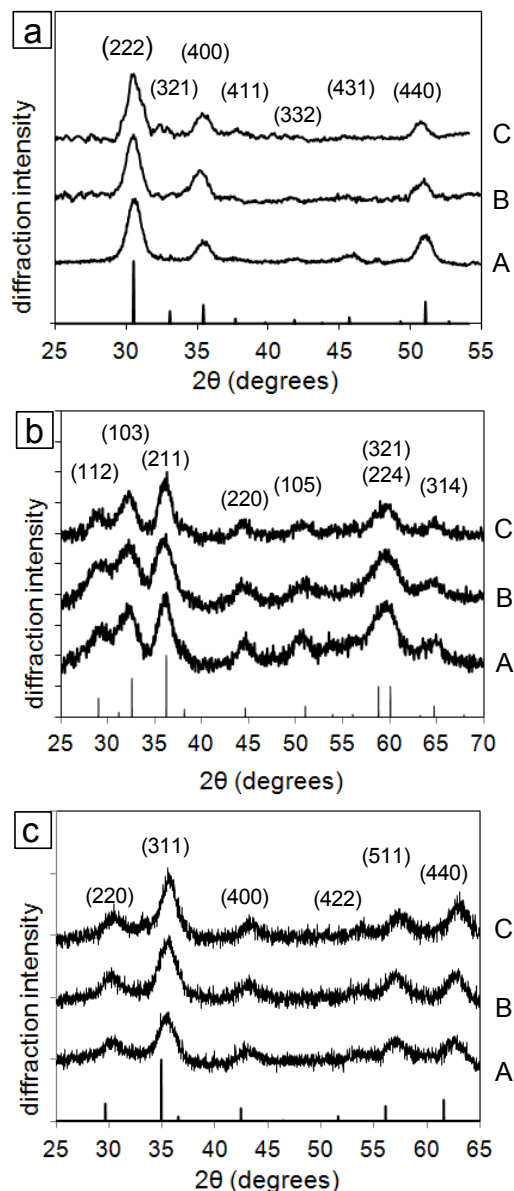


Figure 6.5. (a) WAXD patterns of as-synthesized ITO nanocrystals (A), ITO nanocrystals after the ligand-exchange process (B) and a templated ITO nanocrystal-based film (C). (b) WAXD patterns of as-synthesized Mn_3O_4 nanocrystals (A), Mn_3O_4 nanocrystals after the ligand-exchange process (B), and a templated Mn_3O_4 nanocrystal-based film (C). (c) WAXD patterns of as-synthesized $MnFe_2O_4$ nanocrystals (A), $MnFe_2O_4$ nanocrystals after the ligand-exchange process (B), and a templated $MnFe_2O_4$ nanocrystal-based film (C).

Similar trends were observed in both Mn_3O_4 (Figure 6.5b) and MnFe_2O_4 (Figure 6.5c) systems when examined by WAXD. Figure 6.5b shows patterns for Mn_3O_4 nanocrystals as-synthesized (A), after NOBF_4 treatment (B) and after templating with PEP-*b*-PEO (C). The XRD patterns for (Figure 6.5b (A–C)) can be assigned to the tetragonal Mn_3O_4 (hausmannite) structure (JCPDS reference card no. 80-0382). Scherrer analysis of the peak widths in all three patterns gives an average size of 4–5 nm, which is in agreement with TEM data (Figure 6.1e–f). Finally, for the MnFe_2O_4 system (Figure 6.5c), the main peaks in all three patterns, as-synthesized (A), after NOBF_4 treatment (B) and after templating with PEP-*b*-PEO (C), can be indexed to the cubic phase of manganese ferrite (JCPDS reference card no. 02-8666). The average grain size for (A–C) was found to be 4–5 nm (Scherrer analysis) again confirming that the particle size is not affected by the NOBF_4 treatment⁵³ or thermal treatments, corroborating TEM (Figure 6.1c–d) and SEM data (Figure 6.4a). As in the case for ITO, analysis of the peak intensities for both Mn_3O_4 and MnFe_2O_4 also reveals that the pore walls are made up of nanocrystals with random orientations. Overall, the WAXD data shown here confirm the nanocrystals for all three systems are chemically stable during NOBF_4 treatment⁵³ and thermally stable during the decomposition of the polymer. In addition, the data indicates that the nanocrystals are fully crystalline before the templating step, confirming they are in fact pre-formed and ready to serve as architectural building blocks.

The nanoscale architecture was further characterized by 2D-SAXS experiments, which were collected on beamline 1-4 at the Stanford Synchrotron Radiation Laboratory. Measurements were carried out in reflection mode with the incoming beam

at grazing or near grazing incidence. Here we define the incident angle (*i.e.* the angle between the X-ray beam and the plane of the substrate) as β . Higher β angles bias the diffraction against the out-of-plane scattering and are thus used for the more ordered samples to produce more even intensities around the ring. Figure 6.6 shows 2D-SAXS patterns collected for PEP-*b*-PEO templated films of ITO at $\beta = 1.25^\circ$ (a), Mn_3O_4 at $\beta = 2.25^\circ$ (b), MnFe_2O_4 $\beta = 0.80^\circ$ (c) and $(\text{Mn,Fe})_2\text{O}_3$ $\beta = 0.80^\circ$ (d). In the ITO-based films (a) the evolution of a diffuse ellipsoidal ring with a strong in-plane scattering maxima along the x-direction is observed corresponding to an average repeat distance of 32 nm. The observed pattern is characteristic of a disordered material with a homogeneous length scale. During thermal decomposition of the polymer template, the films experience anisotropic contraction of the pores in the direction perpendicular to the plane of the substrate, which also explains the ellipsoidal shape.

The observed 2D-SAXS data for Mn_3O_4 (Figure 6.6b) shows strong in-plane scattering maxima with an average repeat distance of 32 nm. The pattern shows a less-defined ellipsoidal ring with less scattering in the z-direction. This type of pattern often occurs in partly disordered thin film systems. Because there are only 10–20 pore repeats through the thickness of the film, this is insufficient to produce strong constructive interference in the out-of plane direction when disorder is included. The scattering length in the x- and y-directions is much greater, however, so constructive interference is observed even in partly disordered systems. The in-plane scattering maxima for both MnFe_2O_4 (Figure 6.6c) and $(\text{Mn,Fe})_2\text{O}_3$ (Figure 6.6d) films also corresponds to an average repeat distance 32 nm.

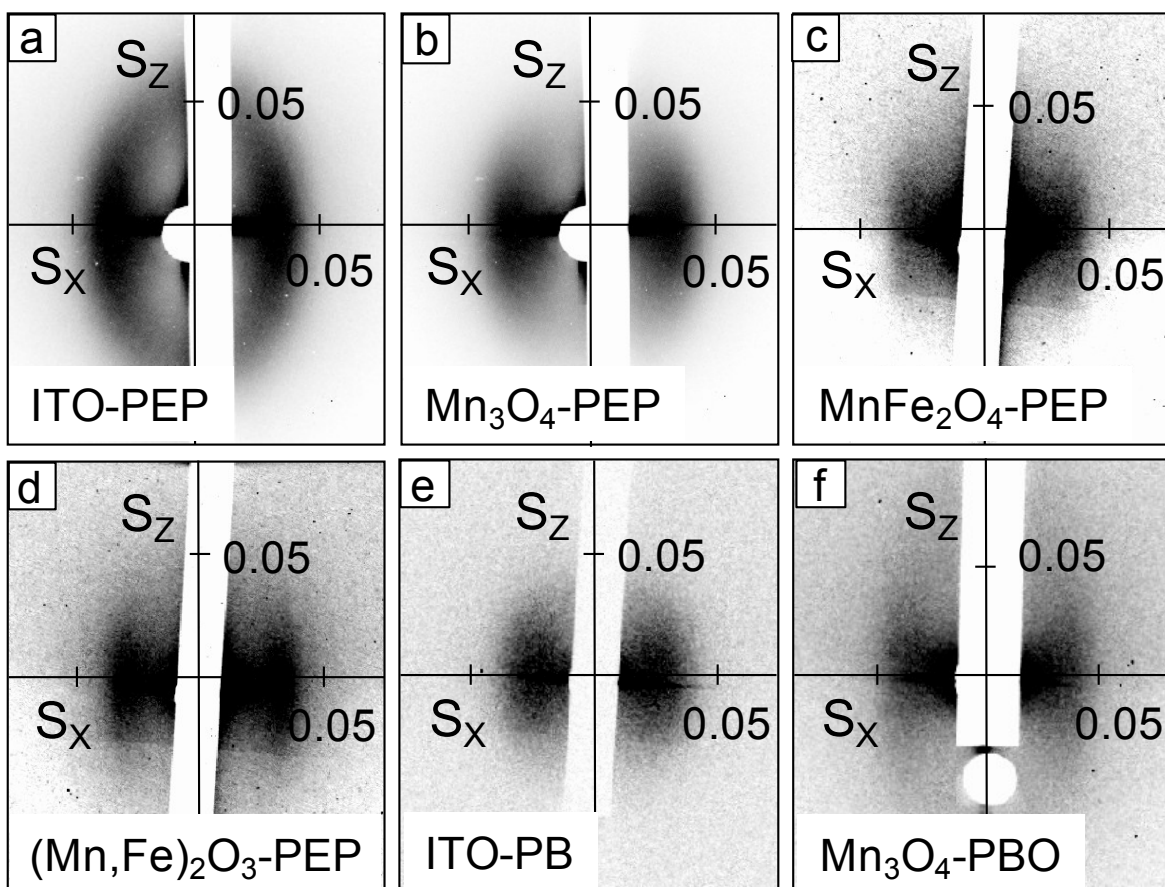


Figure 6.6. 2D-SAXS patterns obtained on PEP-*b*-PEO templated ITO-based films (a), Mn_3O_4 -based films (b), MnFe_2O_4 -based films (c), and $(\text{Mn,Fe})_2\text{O}_3$ -based films (d). Patterns for PB-*b*-PEO templated ITO nanocrystal-based films (e) and PBO-*b*-PEO templated Mn_3O_4 nanocrystal-based films. Data were collected at an angle of incidence $\beta = 1.25^\circ$ for (a), $\beta = 2.25^\circ$ for (b), $\beta = 0.80^\circ$ for (c), $\beta = 0.80^\circ$ for (d), $\beta = 0.80^\circ$ for (e), and $\beta = 0.60^\circ$ for (f). Scattering vector S components are given in $1/\text{nm}$.

The fact that all four types of films exhibit a similar average repeat distance is consistent with the fact that the PEP-*b*-PEO template directs the mesostructure and nanoscale architecture. Moreover, an average repeat distance of 32 nm is approximately commensurate with the sum of the average pore diameter and pore wall thickness that was estimated from SEM for all the PEP-*b*-PEO templated nanocrystal-based materials discussed thus far. For the PB-*b*-PEO film shown in Figure 6.6e, a large repeat distance (36 nm) is observed, again consistent with SEM and the large polymer size employed in the synthesis. Finally, for the PBO-*b*-PEO templated samples shown in Figure 6.6f, a smaller repeat distance (28 nm) is found. The reasons this polymer produces a smaller repeat distance were discussed above. While the specific repeat distances shown in Figure 6.6 corroborate the conclusions from SEM, the SAXS data also provide additional information. Specifically, all of the SEM images in Figures 6.2 – 6.4 appear to show similar levels of disorder. Examination of the SAXS data, however, shows that PEP-*b*-PEO templated films are actually somewhat more ordered at the nanometer scale than films synthesized using PB-*b*-PEO or PBO-*b*-PEO. Perhaps more importantly, the fact that scattering data can be observed for all films in 2D-SAXS regardless of the level of disorder, confirms that all films show homogeneity of the structure at the nanoscale. For most applications, it is this homogeneity of pore size and wall thickness, rather than pore periodicity that is most important.³⁵

To study the effects of nanocrystal size on the porous architecture, ITO nanocrystals with an average diameter of 4.6 ± 0.4 nm (Figure 6.7a) and 7.3 ± 0.7 nm (Figure 6.7e)^{56–58} were templated with PEP-*b*-PEO. For both films the average size of the mesopores by SEM was found to be 17 ± 3 nm arising from the template. TEM

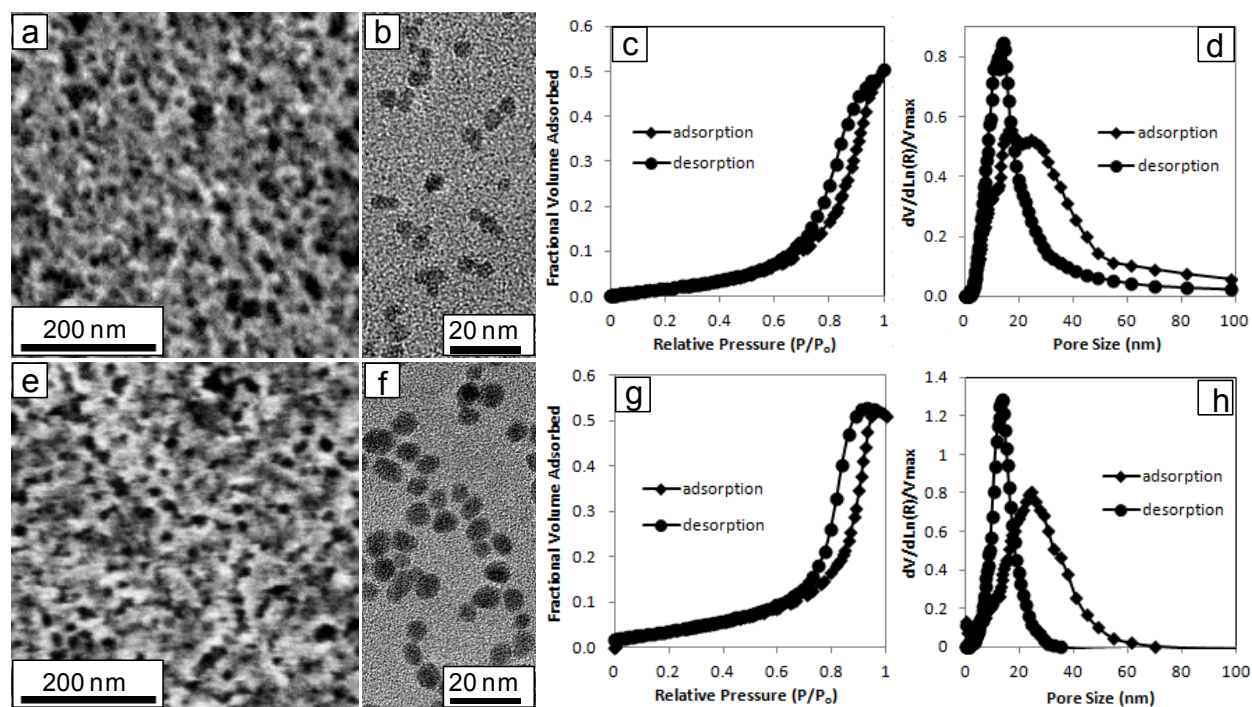


Figure 6.7. (a) SEM image of PEP-*b*-PEO templated ITO nanocrystals with a diameter of 4–5 nm. (b) TEM image of the NOBF₄-treated ITO nanocrystals. (c) A typical toluene adsorption-desorption isotherm showing characteristic mesoporous behavior for films shown in (a). (d) Pore size distribution data obtained from the isotherm in (c). (e) SEM image of 7–8 nm ITO nanocrystals templated with PEP-*b*-PEO. (f) TEM image of the NOBF₄-treated ITO nanocrystals. (g) Toluene adsorption-desorption isotherm showing characteristic mesoporous behavior. (h) Pore size distribution data obtained from the isotherm in (g).

images of 4.6 ± 0.4 nm ITO (Figure 6.7b) and 7.3 ± 0.7 nm ITO (Figure 6.7f) nanocrystals after NOBF_4 treatment show the particles are free of agglomeration with a uniform size and shape.⁵³ The micro- and mesoporosity was further analyzed by ellipsometric porosimetry measurements using toluene as the adsorbate.⁸⁰ Adsorption-desorption isotherms for both templated 4.6 ± 0.4 nm ITO (Figure 6.7c) and 7.3 ± 0.7 nm ITO (Figure 6.7g) nanocrystals show typical type IV behavior.⁸¹ For this type of physisorption behavior, the presence of a hysteresis loop at higher relative pressures is representative of a mesoporous structure with interconnected porosity. The adsorption curve describes the pore size of the cages, and the desorption curve reveals the pore size of the necks. For 4.6 ± 0.4 nm ITO, a Kelvin model fit to the isotherm (Figure 6.7c) produces a pore diameter distribution centered at 22 nm and a neck-diameter distribution centered at 12 nm, as shown in Figure 6.7d. The Dubinin-Radushkevich model was further fit to the isotherm at lower relative pressures to examine the micropores in these materials. Average micropore sizes for films made from 4.6 ± 0.4 nm ITO nanocrystals were 1.2 nm (cage diameter from adsorption) and 0.8 nm (neck diameter from desorption). These micropores arise from the spaces in between the randomly agglomerated nanocrystals that make up the pore walls. A fit to the 7.3 ± 0.7 nm ITO isotherm (Figure 6.7g) gives a mesopore diameter size distribution centered on 22 nm with an average neck diameter centered on 12 nm as shown in Figure 6.7h, as expected, since both films were prepared with the same polymer template. Interestingly, the micropores in this case were found to have 1.6 nm cages and 1.0 nm necks, which are larger, confirming that the size of the nanocrystals defines the micropore structure. The isotherm for the templated 4.6 ± 0.4 nm ITO films shows a 55% toluene-accessible

porous volume, while for the templated 7.3 ± 0.7 nm ITO films it shows a 50% total pore volume.

Additional ellipsometric porosimetry measurements were carried out for PB-*b*-PEO templated 7.3 ± 0.7 nm ITO nanocrystals (Figure 6.8a–b) and PEP-*b*-PEO templated 4.8 ± 0.5 nm Mn_3O_4 nanocrystals (Figure 6.8c–d). For PB-*b*-PEO ITO, a fit to the isotherm (Figure 6.8a) gives a pore diameter size distribution centered on 30 nm with an average neck diameter centered on 15 nm as shown in Figure 6.8b. The larger mesopores determined by porosimetry are in reasonable agreement with SEM and 2D-SAXS discussed earlier arising from the larger size of the PB-*b*-PEO template. The micropores, however, show 1.6 nm cages and 1.0 nm necks, similar to that of 7.3 ± 0.7 nm ITO templated with PEP-*b*-PEO, again confirming that the nanocrystal size dictates the microporous structure. Figure 6.8c shows a typical isotherm obtained for PEP-*b*-PEO templated Mn_3O_4 films. In this case, the mesopores were found to be similar to those obtained from the data in Figure 6.7d and h, with an average pore and neck size of 23 nm and 13 nm – as expected from the fact that all three samples used the same PEP-*b*-PEO template. The micropores were found to have 1.4 nm cages and 1.0 nm necks. The isotherm for the PB-*b*-PEO ITO shows a 45% toluene-accessible porous volume, while PEP-*b*-PEO Mn_3O_4 shows a 70% total pore volume. Table 6.1 summarizes the porosity data showing nanocrystal-based templated films exhibit a bimodal porosity where the micropore size can be tuned by changing the size of the pre-formed nanocrystals and the mesopore size can be tuned by changing the size and chemical nature of the template. Overall, the pore analyses found here corroborate the

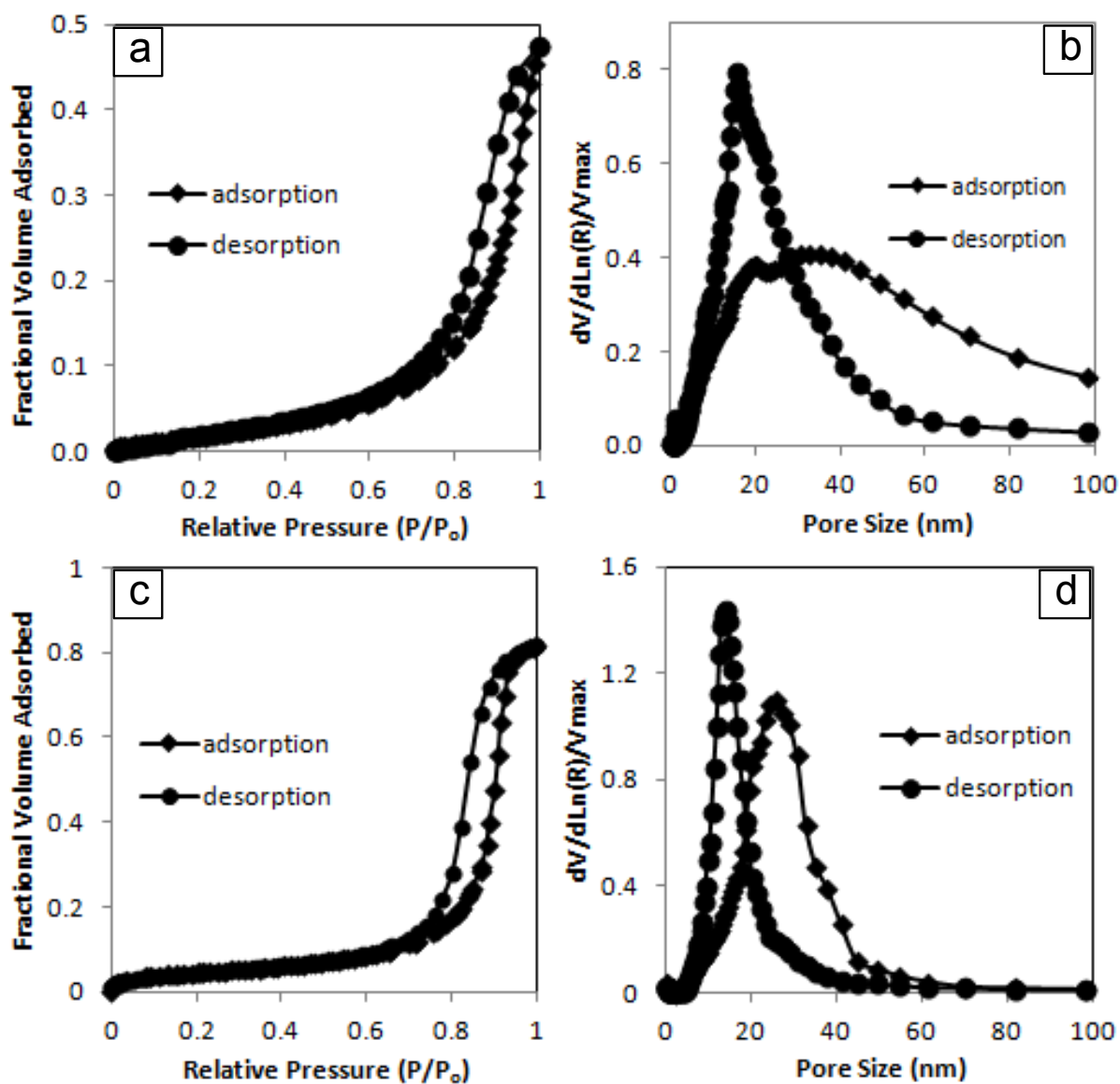


Figure 6.8. Toluene adsorption-desorption isotherms for PB-*b*-PEO templated ITO nanocrystals with a diameter of 7–8 nm (a) and PEP-*b*-PEO templated Mn_3O_4 nanocrystals with a diameter of 4–5 nm (c). Corresponding pore size distribution data for PB-*b*-PEO templated ITO (b) and PEP-*b*-PEO templated Mn_3O_4 (d) obtained from the isotherms.

Table 6.1. Summary of mesopore size arising from the block copolymer template and micropore size arising from nanocrystal size.

Polymer/Nanocrystal Size	M_n^a (g/mol)	f_w hydrophobic block ^b	f_w PEO block ^c	Cage Size (nm) ^d (micropore from Polymer) (micropore from Nanocrystal)	Neck Size (nm) ^e (mesopore from Polymer) (micropore from Nanocrystal)
PEP- <i>b</i> -PEO	7900	0.49	0.51	22	12
PB- <i>b</i> -PEO	10500	0.52	0.48	30	15
PBO- <i>b</i> -PEO	11500	0.57	0.43	16	9
ITO – 4.6 nm				1.2	0.8
ITO – 7.3 nm				1.6	1.0
Mn ₃ O ₄ – 4.8 nm				1.4	1.0

^a Total molecular weight of the block copolymer template, ^b weight fraction for the hydrophobic block, ^c weight fraction for the PEO block, ^d average cage size for mesopores arising from the template or micropores arising from the nanocrystal size, ^e average neck size for mesopores arising from the template or micropores arising from the nanocrystal size.

observations from SEM, TEM, WAXD and 2D-SAXS described earlier in all systems studied.

To demonstrate the advantage of our high surface area mesoporous architecture materials we examined the electrochemical properties of a templated Mn_3O_4 nanocrystal-based mesoporous film and compared it to an untemplated film, cast from the same ligand-free nanocrystals. Figure 6.9 shows a comparison of charging times calculated from cyclic voltammetric data at various sweep rates for a PEP-*b*-PEO templated Mn_3O_4 nanocrystal-based mesoporous film (squares) and an untemplated Mn_3O_4 nanocrystal film (circles) cycled in a non-aqueous electrolyte. The data shows significant differences in charging behavior for the two films. The most obvious trend is the total capacity – after 500 s, the total charge stored in the templated film is about 300 C/g, twice the amount of charge compared to the untemplated film (150 C/g). Perhaps more important is the time dependant trends. After 1200 s the templated film is fully charged while the capacity in the untemplated films is still increasing at 2500 s. The templated film stores more charge than the untemplated film because the pore structure maximizes surface area and thus accessible redox sites. Moreover, comparison of the templated film to the untemplated film shows that the open and interconnected porosity enhances charge storage kinetics by facilitating ion/electrolyte diffusion to the redox sites.

In considering the implications of this work, some perspective is needed. The purpose of this work is not focused on Mn_3O_4 as a material for capacitive charge storage, particularly since the capacity observed here is lower than reported values for TiO_2 ,³⁵ MoO_3 ,⁶³ and Nb_2O_5 ⁷⁰ mesoporous materials. Rather, we propose a general

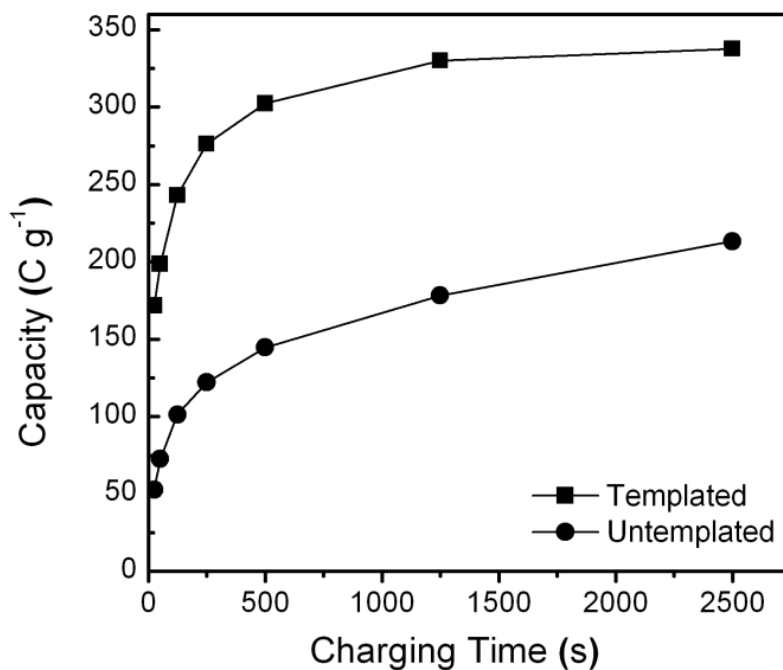


Figure 6.9. Comparison of capacity at various charging times calculated from cyclic voltammetric data at various sweep rates for a PEP-*b*-PEO templated Mn₃O₄ nanocrystal-based mesoporous film (squares) and an untemplated Mn₃O₄ nanocrystal film (circles).

strategy to produce nanoscale architectures that combines key features that could lead to significant improvements in not only electrochemical charge storage, but in other applications such as catalysis and photovoltaics, among others.

6.3 Conclusions

In this work, we describe a general route for assembling pre-formed nanocrystals into hierarchical mesoporous architectures. By tailoring the nanocrystal composition and size along with the block copolymer template type and size, the methodology presented here can offer a high degree of synthetic and structural control over the final architecture of the material. In addition, the ability to perform solid state conversion reactions while retaining the structure/porosity was also demonstrated. The NOBF_4 ligand-exchange method used here resulted in soluble nanocrystals without any particle etching or growth, or change in crystal structure, suggesting this general method may be extended to a wider range of functional nanocrystals. As a demonstration of the utility of these materials we show enhanced charge storage kinetics for porous Mn_3O_4 films. Many of the polymer templates used here are commercially available, indicating that this is a generally accessible route to the production of nanocrystal based nanoporous materials. Moreover, while the materials presented here showed homogeneous, but disordered porosity, recent advances using custom synthesized polymers indicate that highly ordered materials can also be produced from ligand-stripped nanocrystals.⁸²

Taken together, this work provides a general strategy for harnessing the incredible synthetic diversity of nanocrystal-based materials and using it for the

production of nanoporous materials. This general route should be applicable to many nanocrystals systems for a wide range of applications.

6.4 Experimental

6.4.1 Materials

The following chemicals were purchased and used as received: oleylamine (90% Aldrich), oleic acid (90%, Aldrich), stearic acid (95%, Aldrich), xylene (98%, Aldrich), manganese(II) acetate (98%, Aldrich), indium acetylacetonate (99.99+%, Aldrich), tin bis(acetylacetonate) dichloride (98%, Aldrich), manganese(II) acetylacetonate (Aldrich), iron(III) acetylacetonate (97% Aldrich), 1,2-hexadecanediol (90%, aldrich), benzyl ether (98%, aldrich), nitrosonium tetrafluoroborate (95%, Aldrich). Poly(butadiene(1,2 addition))-*b*-poly(ethylene oxide), with a mass ratio of PB(5500)-*b*-PEO(5000), a block ratio of PB₁₀₂-*b*-PEO₁₁₄, and with a polydispersity index (PDI) = 1.05, was purchased from Polymer Source, Inc. Poly(butylene oxide)-*b*-poly(ethylene oxide), with a mass ratio of PBO(5000)-*b*-PEO(6500), a block ratio PBO₉₀-*b*-PEO₁₁₄, and with a PDI = 1.09 was purchased from Advanced Polymer Materials Inc. Poly((ethylene-*alt*-propylene)-*block*-poly(ethylene oxide), with a mass ratio of PEP(3900)-*b*-PEO(4000), a block ratio of PEP₅₆-*b*-PEO₉₁, and with a PDI = 1.05, was synthesized using reported methods.^{83,84} Briefly, polyisoprene was grown by anionic polymerization, terminated with an -OH group and then hydrogenated over Pd/C. The resulting PEP-OH was subsequently extended by anionic polymerization of ethylene oxide.

6.4.2 Synthesis and Ligand-Exchange of Nanocrystals

Previously reported procedures were followed to synthesize 7–8 nm and 4–5 nm ITO nanocrystals,^{56–58} 4–5 nm MnFe_2O_4 nanocrystals,⁶⁰ and 4–5 nm Mn_3O_4 nanocrystals,⁵⁹ all of which were stabilized by either oleylamine or oleic acid ligands. All as-synthesized nanocrystals were purified and dispersed in hexane (10–15 mg/mL). To carry out the ligand-exchange process, as-synthesized nanocrystals were treated with NOBF_4 according to a recently reported procedure.⁵³ In a typical ligand-exchange reaction, 5 mL of nanocrystal dispersion in hexane was combined with 5 mL of NOBF_4 solution in N, N-dimethylformamide (DMF) (10 mg/mL) with stirring (5 min), or until the nanocrystals were transferred to the DMF phase. The nanocrystals were precipitated with toluene then centrifuged, followed by multiple washings with DMF/toluene. The ligand-stripped nanocrystals were dispersed in DMF/ethanol (1:10 v/v) to give a final concentration of 15–20 mg/mL.

6.4.3 Synthesis of Mesoporous Nanocrystal-based Films

In a typical synthesis, 40 mg of the desired diblock copolymer was dissolved in 0.5 mL of ethanol with gentle heating. To this solution, 3 mL of the desired nanocrystals in DMF/ethanol (20 mg/mL) was added. From this mixture, thin films were produced by dip-coating onto polar substrates at a constant withdrawal rate of 1–10 mm/s with a constant 30% relative humidity. Thin films were also prepared by spin-coating onto polar substrates at 1000 to 2000 rpm for 60 s. Finally, thick films could be produced by drop casting onto polar substrates. In most cases, some optimization of the exact concentration of diblock copolymer and nanocrystal was required for mesostructure optimization. The films were dried using a 3 h ramp up to 175 °C, followed by a 3 h

soak. Thermal decomposition of the template was done after the drying step using a 6 h ramp from 175 °C to 450 °C for ITO and Mn₃O₄ films and to 350 °C for MnFe₂O₄ films, followed by a 3 h soak.

6.4.4 Methods

Transmission electron microscopy (TEM) images were obtained using an FEI/PHILIPS CM120 electron microscope operating at 120 kV, as well as a JEOL-2100 electron microscope operating at 200 kV. Scanning electron microscopy (SEM) images were obtained using a JEOL model 6700F electron microscope with beam energy 5 kV, and with a Zeiss Gemini Ultra-55 Analytical electron microscope with beam energy 5 kV. Conventional wide-angle X-ray diffraction (WAXD) measurements were carried out on a Bruker D8-GADDS diffractometer with Cu_{Kα} radiation, and on a Panalytical XPert PRO MPD diffractometer, again with Cu_{Kα} radiation. 2D small-angle X-ray scattering (2D-SAXS) data were collected at the Stanford Synchrotron Radiation Laboratory using beamline 1-4 using the Rayonix165 large angle CCD detector. All measurements were performed in reflection geometry. Ellipsometric porosimetry was performed on a PS-1000 instrument from Semilab using toluene and as the adsorbate. A UV–visible CCD detector adapted to a grating spectrograph analyzes the signal reflected by the sample. The light source is a 75 W Hamamatsu Xenon lamp and measurements were performed on the spectral range from 1.24–4.5 eV. Data analysis was performed using the associated WinElli II software. Electrochemical measurements were carried out in a three-electrode cell using a PAR EG&G 273A potentiostat in an argon-filled glovebox, with oxygen and water levels <1 ppm. The working electrode consisted of ITO glass upon which Mn₃O₄ films were deposited. The electrolyte solution used was 1.0 M

LiClO₄ in propylene carbonate (PC) and lithium metal foils were used as the counter and reference electrodes. Cyclic voltammetry was performed using cutoff voltages at 4 and 1.5 V vs. Li/Li⁺.

6.5 References

- ¹ Kresge, C. T.; Leonowicz, M. E.; Roth, W. J.; Vartuli, J. C.; Beck, J. S. Ordered Mesoporous Molecular Sieves Synthesized by a Liquid-Crystal Template Mechanism. *Nature* **1992**, 359, 710–712.
- ² Beck, J. S.; Vartuli, J. C.; Roth, W. L.; Leonowicz, M. E.; Kresge, C. T.; Schmidt, K. D.; Chu, C. T.-W.; Olson, D. H.; Sheppard, E. W.; McCullen, S. B.; *et al.* A New Family of Mesoporous Molecular Sieves Prepared with Liquid Crystal Templates. *J. Am. Chem. Soc.* **1992**, 114, 10834–10843.
- ³ Zhao, D. Y.; Feng, J. L.; Huo, Q. S.; Melosh, N.; Fredrickson, G. H.; Chmelka, B. F.; Stucky, G. D. Triblock Copolymer Syntheses of Mesoporous Silica with Periodic 50 to 300 Angstrom Pores. *Science* **1998**, 279, 548–552.
- ⁴ Yanagisawa, T.; Shimizu, T.; Kuroda, K.; Kato, C. The Preparation of Alkyltrimethylammonium-Kanemite Complexes and Their Conversion to Microporous Materials. *Bull. Chem. Soc. Jpn.* **1990**, 63, 988–992.
- ⁵ Inagaki, S.; Fukushima, Y.; Kuroda, K. Synthesis of Highly Ordered Mesoporous Materials from a Layered Polysilicate. *J. Chem. Soc. Chem. Commun.* **1993**, 680–682.
- ⁶ Ogawa, M. Formation of Novel Oriented Transparent Films of Layered Silica-Surfactant Nanocomposites. *J. Am. Chem. Soc.* **1994**, 116, 7941–7942.
- ⁷ Antonelli, D. M.; Ying, J. Y. Synthesis of Hexagonally Packed Mesoporous TiO₂ by a Modified Sol-Gel Method. *Angew. Chem., Int. Ed. Engl.* **1995**, 34, 2014–2017.

-
- ⁸ Yang, H.; Kuperman, A.; Coombs, N.; Mamiche-Afara, S.; Ozin, G. A. Synthesis of Oriented Mesoporous Silica Films on Mica. *Nature* **1996**, *379*, 703–705.
- ⁹ Monnier, A.; Schuth, F.; Huo, Q.; Kumar, D.; Margolese, D.; Maxwell, R. S.; Stucky, G. D.; Krishnamurty, M.; Petroff, P.; Firouzi, A.; *et al.* Cooperative Formation of Inorganic-Organic Interfaces in the Synthesis of Silica Mesostructures. *Science* **1993**, *261*, 1299–1303.
- ¹⁰ Brezesinski, K.; Haetge, J.; Wang, J.; Mascotto, S.; Reitz, C.; Rein, A.; Tolbert, S. H.; Perlich, J.; Dunn, B.; Brezesinski, T. Ordered Mesoporous α -Fe₂O₃ (Hematite) Thin-Film Electrodes for Application in High Rate Rechargeable Lithium Batteries. *Small* **2011**, *7*, 407–414.
- ¹¹ Sun, D.; Riley, A. E.; Cadby, A. J.; Richman, E. K.; Korlann, S. D.; Tolbert, S. H. Hexagonal Nanoporous Germanium Through Surfactant-Driven Self-Assembly of Zintl Clusters. *Nature* **2006**, *441*, 1126–1130.
- ¹² Stefik, M.; Sai, H.; Epps, T. H.; Bates, F. S.; Gruner, S. M.; DiSalvo, F. J.; Wiesner, U. Ordered Three- and Five-Ply Nanocomposites from ABC Block Terpolymer Microphase Separation with Niobia and Aluminosilicate Sols. *Chem. Mater.* **2009**, *21*, 5466–5473.
- ¹³ Deng, Y.; Yu, T.; Wan, Y.; Shi, Y.; Meng, Y.; Gu, D.; Zhang, L.; Huang, Y.; Liu, C.; Wu, X.; *et al.* Ordered Mesoporous Silicas and Carbons with Large Accessible Pores Templated from Amphiphilic Diblock Copolymer Poly(ethylene oxide)-b-Polystyrene. *J. Am. Chem. Soc.* **2007**, *129*, 1690–1697.

-
- ¹⁴ Cheng, Y. J.; Gutmann, J. S. Morphology Phase Diagram of Ultrathin Anatase TiO₂ Films Templated by a Single PS-*b*-PEO Block Copolymer. *J. Am. Chem. Soc.* **2006**, *128*, 4658–4674.
- ¹⁵ Mamak, M.; Coombs, N.; Ozin, G. Mesoporous Yttria-Zirconia and Metal-Yttria-Zirconia Solid Solutions for Fuel Cells. *Adv. Mater.* **2000**, *12*, 198–202.
- ¹⁶ Warren, S. C.; Perkins, M. R.; Adams, A. M.; Kamperman, M.; Burns, A. A.; Arora, H.; Herz, E.; Suteewong, T.; Sai, H.; Li, Z.; *et al.* Silica Sol-Gel Design Strategy for Nanostructured Metallic Materials. *Nat. Mater.* **2012**, *11*, 460–467.
- ¹⁷ Stefik, M.; Lee, J.; Wiesner, U. Nanostructured Carbon-Crystalline Titania Composites from Microphase Separation of Poly(ethylene oxide-*b*-acrylonitrile) and Titania Sols. *Chem. Commun.* **2009**, 2532–2534.
- ¹⁸ Tian, B. Z.; Liu, X. Y.; Tu, B.; Yu, C. Z.; Fan, J.; Wang, L. M.; Xie, S. H.; Stucky, G. D.; Zhao, D. Y. Self-Adjusted General Synthesis of Ordered Stable Mesoporous Minerals by Acid-Base Pairs. *Nat. Mater.* **2003**, *2*, 159–163.
- ¹⁹ Finnemore, A. S.; Scherer, M. R. J.; Langford, R.; Mahajan, S.; Ludwigs, S.; Meldrum, F.; Steiner, U. Nanostructured Calcite Single Crystals with Gyroid Morphologies. *Adv. Mater.* **2009**, *21*, 3928–3932.
- ²⁰ Brezesinski, B.; Wang, J.; Senter, R.; Brezesinski, K.; Dunn, B.; Tolbert, S. H. On the Correlation Between Mechanical Flexibility, Nanoscale Structure, and Charge Storage in Periodic Mesoporous CeO₂ Thin Films. *ACS Nano* **2010**, *4*, 967–977.
- ²¹ Yang, P.; Deng, T.; Zhao, D.; Feng, P.; Pine, D.; Chmelka, B.; Whitesides, G.; Stucky, G. D. Hierarchically Ordered Oxides. *Science* **1998**, *282*, 2244–2246.

-
- ²² Freer, E. M.; Krupp, L. E.; Hinsberg, W. D.; Rice, P. M.; Hedrick, J. L.; Cha, J. N.; Miller, R. D.; Kim, H. C. Oriented Mesoporous Organosilicate Thin Films. *Nano Lett.* **2005**, *5*, 2014–2018.
- ²³ Brezesinski, T.; Groenewolt, M.; Gibaud, A.; Pinna, N.; Antonietti, M.; Smarsly, B. M. Evaporation-Induced Self-Assembly (EISA) at Its Limit: Ultrathin, Crystalline Patterns by Templating of Micellar Monolayers. *Adv. Mater.* **2006**, *18*, 2260–2263.
- ²⁴ Grosso, D.; Boissière, C.; Smarsly, B.; Brezesinski, T.; Pinna, N.; Albouy, P. A.; Amenitsch, H.; Antonietti, M.; Sanchez, C. Periodically Ordered Nanoscale Islands and Mesoporous Films Composed of Nanocrystalline Multimetallic Oxides. *Nat. Mater.* **2004**, *3*, 787–792.
- ²⁵ Kuemmel, M.; Grosso, D.; Boissière, U.; Smarsly, B.; Brezesinski, T.; Albouy, P. A.; Amenitsch, H.; Sanchez, C. Thermally Stable Nanocrystalline γ -Alumina Layers with Highly Ordered 3D Mesoporosity. *Angew. Chem., Int. Ed.* **2005**, *44*, 4589–4592.
- ²⁶ Docamp, P.; Guldin, S.; Stefik, M.; Tiwana, P.; Orilall, M. C.; Huttner, S.; Sai, H.; Wiesner, U.; Steiner, U.; Snaith, H. J. Control of Solid-State Dye-Sensitized Solar Cell Performance by Block-Copolymer-Directed TiO_2 Synthesis. *Adv. Func. Mater.* **2010**, *20*, 1787–1796.
- ²⁷ Zhao, D.; Huo, Q.; Feng, J.; Chmelka, B. F.; Stucky, G. D. Nonionic Triblock and Star Diblock Copolymer and Oligomeric Surfactant Syntheses of Highly Ordered, Hydrothermally Stable, Mesoporous Silica Structures. *J. Am. Chem. Soc.* **1998**, *120*, 6024–6036.

-
- ²⁸ Kondo, J. N.; Domen, K. Crystallization of Mesoporous Metal Oxides. *Chem. Mater.* **2008**, *20*, 835–847.
- ²⁹ Crepaldi, E. L.; Soler-Illia, G. J. A. A.; Grosso, D.; Sanchez, C. Nanocrystallised Titania and Zirconia Mesoporous Thin Films Exhibiting Enhanced Thermal Stability. *New J. Chem.* **2003**, *27*, 9–13.
- ³⁰ Crepaldi, E. L.; Soler-Illia, G. J. A. A.; Grosso, D.; Cagnol, F.; Ribot, F.; Sanchez, C. Controlled Formation of Highly Organized Mesoporous Titania Thin Films: from Mesostructured Hybrids to Mesoporous Nano-anatase TiO₂. *J. Am. Chem. Soc.* **2003**, *125*, 9770–9786.
- ³¹ Warren, S. C.; Messina, L. C.; Slaughter, L. S.; Kamperman, M.; Zhou, Q.; Gruner, S. M.; DiSalvo, F. J.; Wiesner, U. Ordered Mesoporous Materials from Metal Nanoparticle-Block Copolymer Self-Assembly. *Science* **2008**, *320*, 1748–1752.
- ³² Corma, A.; Atienzar, P.; Garcia, H.; Chane-Ching, J. Y. Hierarchically Mesostructured Doped CeO₂ with Potential for Solar-Cell Use. *Nat. Mater.* **2004**, *3*, 394–397.
- ³³ Deshpande, A. S.; Pinna, N.; Smarsly, B.; Antonietti, M.; Niederberger, M. Controlled Assembly of Preformed Ceria Nanocrystals into Highly Ordered 3D Nanostructures. *Small* **2005**, *1*, 313–316.
- ³⁴ Ba, J. H.; Polleux, J.; Antonietti, M.; Niederberger, M. Non-aqueous Synthesis of Tin Oxide Nanocrystals and Their Assembly into Ordered Porous Mesostructures. *Adv. Mater.* **2005**, *17*, 2509–2512.

-
- ³⁵ Brezesinski, B.; Wang, J.; Polleux, J.; Dunn, B.; Tolbert, S. H. Templated Nanocrystal-Based Porous TiO₂ Films for Next-Generation Electrochemical Capacitors. *J. Am. Chem. Soc.* **2009**, *131*, 1802–1809.
- ³⁶ Szeifert, J. M.; Feckl, J. M.; Fattakhova-Rohlfing, D.; Liu, Y.; Kalousek, V.; Rathousky, J.; Bein, T. Ultrasmall Titania Nanocrystals and Their Direct Assembly into Mesoporous Structures Showing Fast Lithium Insertion. *J. Am. Chem. Soc.* **2010**, *132*, 12605–12611.
- ³⁷ Sun, S.; Murray, C. B. Synthesis of Monodisperse Cobalt Nanocrystals and Their Assembly Into Magnetic Superlattices. *J. Appl. Phys.* **1999**, *85*, 4325–4330.
- ³⁸ Boyer, J.-C.; Vetrone, F.; Cuccia, L. A.; Capobianco, J. A. Synthesis of Colloidal Upconverting NaYF₄ Nanocrystals Doped with Er³⁺, Yb³⁺ and Tm³⁺, Yb³⁺ via Thermal Decomposition of Lanthanide Trifluoroacetate Precursors. *J. Am. Chem. Soc.* **2006**, *128*, 7444–7445.
- ³⁹ Shevchenko, E. V.; Talapin, D. V.; Rogach, A. L.; Kornowski, A.; Haase, M.; Weller, H. Colloidal Synthesis and Self-Assembly of CoPt₃ Nanocrystals. *J. Am. Chem. Soc.* **2002**, *124*, 11480–11485.
- ⁴⁰ Manna, L.; Milliron, D. J.; Meisel, A.; Scher, E. C.; Alivisatos, A. P. Controlled Growth of Tetrapod-Branched Inorganic Nanocrystals. *Nat. Mater.* **2003**, *2*, 382–385.
- ⁴¹ Hines, M. A.; Guyot-Sionnest, P. Synthesis and Characterization of Strongly Luminescing ZnS-Capped CdSe Nanocrystals. *J. Phys. Chem.* **1996**, *100*, 468–471.

-
- ⁴² Peng, X.; Schlamp, M. C.; Kadavanich, A. V.; Alivisatos, A. P. Epitaxial Growth of Highly Luminescent CdSe/CdS Core/Shell Nanocrystals with Photostability and Electronic Accessibility. *J. Am. Chem. Soc.* **1997**, *119*, 7019–7029.
- ⁴³ Xia, Y.; Xiong, Y. J.; Lim, B.; Skrabalak, S. E. Shape-Controlled Synthesis of Metal Nanocrystals: Simple Chemistry Meets Complex Physics? *Angew. Chem., Int. Ed.* **2009**, *48*, 60–103.
- ⁴⁴ Yu, W. W.; Falkner, J. C.; Shih, B. S.; Colvin, V. L. Preparation and Characterization of Monodisperse PbSe Semiconductor Nanocrystals in a Noncoordinating Solvent. *Chem. Mater.* **2004**, *16*, 3318–3322.
- ⁴⁵ Murray, C. B.; Norris, D. J.; Bawendi, M. G. Synthesis and Characterization of Nearly Monodisperse CdE (E = Sulfur, Selenium, Tellurium) Semiconductor Nanocrystallites. *J. Am. Chem. Soc.* **1993**, *115*, 8706–8715.
- ⁴⁶ Chen, O.; Chen, X.; Yang, Y.; Lynch, J.; Wu, H.; Zhuang, J.; Cao, Y. C. Synthesis of Metal-Selenide Nanocrystals Using Selenium Dioxide as the Selenium Precursor. *Angew. Chem., Int. Ed.* **2008**, *47*, 8638–8641.
- ⁴⁷ Sun, Y.; Xia, Y. Shape-Controlled Synthesis of Gold and Silver Nanoparticles. *Science* **2002**, *298*, 2176–2179.
- ⁴⁸ Peng, X.; Manna, L.; Yang, W.; Wickham, J.; Scher, E.; Kadavanich, A.; Alivisatos, A. P. Shape Control of CdSe Nanocrystals. *Nature*, **2000**, *404*, 59–61.

-
- ⁴⁹ Gaponik, N.; Talapin, D. V.; Rogach, A. L.; Hoppe, K.; Shevchenko, E. V.; Kornowski, A.; Eychmuller, A.; Weller, H. Thiol-Capping of CdTe Nanocrystals: An Alternative to Organometallic Synthetic Routes. *J. Phys. Chem. B* **2002**, *106*, 7177–7185.
- ⁵⁰ Talapin, D. V.; Yu, H.; Shevchenko, E. V.; Lobo, A.; Murray, C. B. Synthesis of Colloidal PbSe/PbS Core-Shell Nanowires and PbS/Au Nanowire-Nanocrystal Heterostructures. *J Phys. Chem. C* **2007**, *111*, 14049–14054.
- ⁵¹ Niederberger, M.; Bartl, M. H.; Stucky, G. D. Benzyl Alcohol and Titanium Tetrachloride – A Versatile Reaction System for the Nonaqueous and Low-temperature Preparation of Crystalline and Luminescent Titania Nanoparticles. *Chem. Mater.* **2002**, *14*, 4364–4370.
- ⁵² Niederberger, M.; Garnweitner, G.; Krumeich, F.; Nesper, R.; Colfen, H.; Antonietti, M. Tailoring the Surface and Solubility Properties of Nanocrystalline Titania by a Nonaqueous In Situ Functionalization Process. *Chem. Mater.* **2004**, *16*, 1202–1208.
- ⁵³ Dong, A.; Ye, X.; Chen, J.; Kang, Y.; Gordon, T.; Kikkawa, J. M.; Murray, C. B. A Generalized Ligand-Exchange Strategy Enabling Sequential Surface Functionalization of Colloidal Nanocrystals. *J. Am. Chem. Soc.* **2011**, *133*, 998–1006.

-
- ⁵⁴ Nag, A.; Kovalenko, M. V.; Lee, J.-S.; Liu, W.; Spokoyny, B.; Talapin, D. V. Metal-free Inorganic Ligands for Colloidal Nanocrystals: S^{2-} , HS^- , Se^{2-} , HSe^- , Te^{2-} , HTe^- , TeS_3^{2-} , OH^- , and NH_2^- as Surface Ligands. *J. Am. Chem. Soc.* **2011**, *133*, 10612–10620.
- ⁵⁵ Rosen, E. L.; Buonsanti, R.; Llodes, A.; Sawvel, A. M.; Milliron, D. J.; Helms, B. A. Exceptionally Mild Reactive Stripping of Native Ligands from Nanocrystal Surfaces by Using Meerwein's Salt. *Angew. Chem. Int. Ed.* **2012**, *51*, 684–689.
- ⁵⁶ Llodes, A.; Hammack, A. T.; Buonsanti, R.; Tangirala, R.; Aloni, S.; Helms, B. A.; Milliron, D. J. Polyoxometalates and Colloidal Nanocrystals as Building Blocks for Metal Oxide Nanocomposite Films. *J. Mater. Chem.* **2011**, *21*, 11631–11638.
- ⁵⁷ Choi, S. I.; Nam, K. M.; Park, B. K.; Seo, W. S.; Park, J. T. Preparation and Optical Properties of Colloidal, Monodisperse, and Highly Crystalline ITO Nanoparticles. *Chem. Mater.* **2008**, *20*, 2609–2611.
- ⁵⁸ Giltisrap, R. A.; Capozzi, C. J.; Carson, C. G.; Gerhardt, R. A.; Summers, C. J. Synthesis of a Nonagglomerated Indium Tin Oxide Nanoparticle Dispersion. *Adv. Mater.* **2008**, *20*, 4163–4166.
- ⁵⁹ Yu, T.; Moon, J.; Park, J.; Park, Y. I.; Bin Na, H.; Kim, B. H.; Song, I. C.; Moon, W. K.; Hyeon, T. Various-Shaped Uniform Mn_3O_4 Nanocrystals Synthesized at Low Temperature in Air Atmosphere. *Chem. Mater.* **2009**, *21*, 2272–2279.
- ⁶⁰ Masala, O.; Seshadri, R. Magnetic Properties of Capped, Soluble $MnFe_2O_4$ Nanoparticles. *Chem. Phys. Lett.* **2005**, *402*, 160–164.

-
- ⁶¹ Lu, Y.; Ganguli, R.; Drewien, C. A.; Anderson, M. T.; Brinker, C. J.; Gong, W.; Guo, Y.; Soye, H.; Dunn, B.; Huang, M. H.; *et al.* Continuous Formation of Supported Cubic and Hexagonal Mesoporous Films by Sol-Gel Dip-Coating. *Nature* **1997**, *389*, 364–368.
- ⁶² Garcia, B. C.; Kamperman, M.; Ulrich, R.; Jain, A.; Gruner, S. M.; Wiesner, U. Morphology Diagram of a Diblock Copolymer-Aluminosilicate Nanoparticle System. *Chem. Mater.* **2009**, *21*, 5397–5405.
- ⁶³ Brezesinski, T.; Wang, J.; Tolbert, S. H.; Dunn, B. Ordered Mesoporous Alpha-MoO₃ with Iso-Oriented Nanocrystalline Walls for Thin-Film Pseudocapacitors. *Nat. Mater.* **2010**, *9*, 146–151.
- ⁶⁴ Haetge, J.; Hartmann, P.; Brezesinski, K.; Janek, J.; Brezesinski, T. Ordered Large-Pore Mesoporous Li₄Ti₅O₁₂ Spinel Thin Film Electrodes with Nanocrystalline Framework for High Rate Rechargeable Lithium Batteries: Relationships among Charge Storage, Electrical Conductivity, and Nanoscale Structure. *Chem. Mater.* **2011**, *23*, 4384–4393.
- ⁶⁵ Sallard, S.; Brezesinski, T.; Smarsly, B. M. Electrochromic Stability of WO₃ Thin Films with Nanometer-Scale Periodicity and Varying Degrees of Crystallinity. *J. Phys. Chem. C* **2007**, *111*, 7200–7206.
- ⁶⁶ Quickel, T. E.; Le, V. H.; Brezesinski, T.; Tolbert, S. H. On the Correlation Between Nanoscale Structure and Magnetic Properties in Ordered Mesoporous Cobalt Ferrite (CoFe₂O₄) Thin Films. *Nano Lett.* **2010**, *10*, 2982–2988.

-
- ⁶⁷ Haetge, J.; Suchomski, C.; Brezesinski, T. Ordered Mesoporous MFe_2O_4 ($M = Co, Cu, Mg, Ni, Zn$) Thin Films with Nanocrystalline Walls, Uniform 16 nm Diameter Pores and High Thermal Stability: Template-Directed Synthesis and Characterization of Redox Active Trevorite. *Inorg. Chem.* **2010**, *49*, 11619–11626.
- ⁶⁸ Richman, E. K.; Kang, C. B.; Brezesinski, T.; Tolbert, S. H. Ordered Mesoporous Silicon through Magnesium Reduction of Polymer Templated Silica Thin Films. *Nano Lett.* **2008**, *8*, 3075–3079.
- ⁶⁹ Suchomski, C.; Reitz, C.; Brezesinski, K.; Tavares de Sousa, C.; Rohnke, M.; Iimura, K.; Esteves de Araujo, J. P.; Brezesinski, T. Structural, Optical, and Magnetic Properties of Highly Ordered Mesoporous MCr_2O_4 and $MCr_{2-x}Fe_xO_4$ ($M = Co, Zn$) Spinel Thin Films with Uniform 15 nm Diameter Pores and Tunable Nanocrystalline Domain Sizes. *Chem. Mater.* **2012**, *24*, 155–165.
- ⁷⁰ Brezesinski, K.; Wang, J.; Haetge, J.; Reitz, C.; Steinmueller, S. O.; Tolbert, S. H.; Smarsly, B. M.; Dunn, B.; Brezesinski, T. Pseudocapacitive Contributions to Charge Storage in Highly Ordered Mesoporous Group V Transition Metal Oxides with Iso-Oriented Layered Nanocrystalline Domains. *J. Am. Chem. Soc.* **2010**, *132*, 6982–6990.
- ⁷¹ Templin, M.; Franck, A.; Chesne, A. D.; Leist, H.; Zhang, Y.; Ulrich, R.; Schadler, V.; Wiesner, U. Organically Modified Aluminosilicate Mesostructures from Block Copolymer Phases. *Science* **1997**, *278*, 1795–1798.

-
- ⁷² Kuemmel, M.; Smatt, J.-H.; Boissiere, C.; Nicole, L.; Sanchez, C.; Linden, M.; Grosso, D. Hierarchical Inorganic Nanopatterning (INP) Through Direct Easy Block-Copolymer Templating. *J. Mater. Chem.*, **2009**, *19*, 3638–3642.
- ⁷³ Baroch, P.; Hieda, J.; Saito, N.; Takai, O. Atmospheric Plasma-Calcination of Mesoporous Tungsten Oxide Utilizing Plasma Dielectric Barrier Discharge. *Thin Solid Films* **2007**, *515*, 4905–4908.
- ⁷⁴ Maruo, T.; Tanaka, S.; Nishiyama, N.; Motoda, K.; Funayama, K.; Egashira, Y.; Ueyama, K. Low-Index Mesoporous Silica Films Modified With Trimethylethoxysilane. *Colloids and Surfaces A* **2008**, *318*, 84–87.
- ⁷⁵ Besson, S.; Gacoin, T.; Jacquiod, C.; Ricolleau, C.; Babonneau, D.; Boilot, J.-P. Structural Study of 3D-Hexagonal Mesoporous Spin-coated Sol-Gel Films. *J. Mater. Chem.* **2000**, *10*, 1331–1336.
- ⁷⁶ Brezesinski, T.; Groenewolt, M.; Antonietti, M.; Smarsly, B. Crystal-to-Crystal Phase Transition in Self-Assembled Mesoporous Iron Oxide Films. *Angew. Chem. Int. Ed.* **2006**, *45*, 781–784.
- ⁷⁷ Schleich, D. M.; Zhang, Y. Preparation of Some Metal Ferrite MFe_2O_4 Thin Films Through a Nonaqueous Sol Method. *Mater. Res. Bull.* **1995**, *30*, 447–452.
- ⁷⁸ Jiang, X.; Xie, Y.; Lu, J.; He, W.; Zhu, L.; Qian, Y. Preparation and Phase Transformation of Nanocrystalline Copper Sulfides (Cu_9S_8 , Cu_7S_4 and CuS). *J. Mater. Chem.*, **2000**, *10*, 2193–2196.

-
- ⁷⁹ Chernyshova, I. V.; Hochella, M. F.; Madden, A. S. Size-dependent Structural Transformations of Hematite Nanoparticles. 1. Phase transition. *Phys. Chem. Chem. Phys.* **2007**, *9*, 1736–1750.
- ⁸⁰ Baklonov, M. R.; Mogilnikov, K. P.; Polovinkin, V. G.; Dultsev, F. N. Determination of Pore Size Distribution in Thin Films by Ellipsometric Porosimetry. *J. of Vac. Sci. & Tech. B* **2000**, *18*, 1385–1391.
- ⁸¹ Gregg, S. J.; Sing, K. S. W. *Adsorption, Surface Area, and Porosity*, 2nd ed.; Academic: London, 1982.
- ⁸² Buonsanti, R.; Pick, T. E.; Krins, N.; Richardson, T. J.; Helms, B. A.; Milliron, D. J.; Assembly of ligand-stripped nanocrystals into precisely controlled mesoporous architectures. *Nano Lett.* **2012**, *12*, 3872–3877.
- ⁸³ Hillmyer, M. A.; Bates, F. S. Synthesis and Characterization of Model Polyalkane-Poly(ethylene oxide) Block Copolymers. *Macromolecules* **1996**, *29*, 6994–7002.
- ⁸⁴ Allgaier, J.; Poppe, A.; Willner, L.; Richter, D. Synthesis and Characterization of Poly[1,4-Isoprene-*b*-(ethylene oxide)] and Poly[ethylene-co-propylene-*b*-(ethylene oxide)] Block Copolymers. *Macromolecules* **1997**, *30*, 1582–1586.

CHAPTER 7

High-Performance Pseudocapacitors Based on Atomic Layer Deposition of V_2O_5 onto Conductive Nanocrystal-Based ITO Mesoporous Scaffolds

7.1 Introduction

Electrochemical energy storage devices known as pseudocapacitors have attracted much attention because they have the ability to attain high energy densities while maintaining high power densities.¹ Pseudocapacitors store charge through fast and reversible faradaic processes that involve surface or near the surface redox reactions. These charge storage mechanisms are different than those in traditional batteries because they are not limited by the diffusion of ions/electrolyte into the bulk. Therefore, pseudocapacitors can offer several benefits that parallel or even exceed those of batteries including fast charge/discharging within seconds, good charge/discharge cycling stability, and the ability to deliver >10x more power.² An ideal pseudocapacitor electrode architecture should comprise a redox-active material (i.e. metal oxide) that has a nanodimensional structure to accommodate shorter ion diffusion lengths. In addition, the material should have a high surface area in order to maximize all the redox-active sites, and, have an open interconnected porosity to facilitate solvent diffusion to all the redox-active sites. Finally, electrical conductivity should be integrated and wired into the redox-active component in order to simultaneously achieve both higher energy and power densities in one structure. The improvements to electrochemical energy storage resulting from building electrical conductivity into

electrode materials are well established in the literature. Carbon-based materials such as carbon nanotubes (CNT) and graphene have been shown to act as good conductive platforms for the construction of composite electrodes. For example, CNT-based composites of manganese oxide (MnO_2),³ titanium oxide (TiO_2),⁴ tin oxide (SnO_2),⁴ lithium manganese oxide (LiMn_2O_4),⁵ and vanadium oxide (V_2O_5)⁶⁻⁸ have been reported. Graphene-based composites of LiMn_2O_4 ,⁵ iron oxide (Fe_3O_4),⁹ SnO_2 ,¹⁰ $\text{Ni}(\text{OH})_2$,¹¹ and MnO_2 ¹² have also been produced. In addition to carbon-based conductors, metals have also been integrated into composite electrodes with unique architectures including an interpenetrated nickel inverse opal,¹³ nanoporous gold,¹⁴ nickel porous foam,^{15,16} copper pillar arrays,¹⁷ and stainless steel mesh.¹⁸ In the examples above, the conductive component provided a network for good electrical transport throughout the active material which resulted in improvements to the electrochemical performance.

While electrical conductivity is important, for redox pseudocapacitance, interfacial area in contact with the electrolyte appears to be the most important factor. For example, we reported significant enhancements to the capacitive charge storage behavior in nanocrystal-based mesoporous TiO_2 pseudocapacitors templated using poly(ethylene oxide-*block*-hydrocarbon) [PEO-XXX] type polymers.¹⁹ In that work, the porous titania architectures demonstrated high levels of pseudocapacitive charge storage that were accompanied by rapid charging/discharging rates.¹⁹ The improved performance resulted from the unique architecture, which exhibited an open interconnected porosity that facilitated rapid solvent diffusion throughout the material, as well as a high density of redox-active surface sites arising from the nanocrystals within

the pores walls. Bein and coworkers have also reported the preparation of mesoporous films from TiO_2 nanocrystalline particles that demonstrated high Li insertion capacities and fast charging rates resulting from the high surface to bulk ratio of the nanocrystals and the easily accessible mesoporous structures.²⁰ The literature includes a few more examples of this type of polymer templated nanocrystal-based co-assembly to prepare porous architectures.^{21–24}

More recently, we developed a general route for assembling pre-formed nanocrystals into hierarchical mesoporous architectures by extending this synthetic approach to a wider range of nanocrystal systems including, Mn_3O_4 , MnFe_2O_4 , and tin-doped indium oxide (ITO).²⁵ We used an established ligand-exchange method using NOBF_4 ²⁶ to strip ligands off of the surface of nanocrystals, allowing us to template them with similar PEO based diblock copolymers. Similar to our TiO_2 nanocrystal-based materials,¹⁹ when we used nanodimensional building blocks and assembled them into hierarchical architectures, the materials exhibited a bimodal porosity that combined mesopores, arising from the block copolymer template, and micropores, created by the spaces in between the nanocrystals embedded in the pore walls. In that work, we showed that templated Mn_3O_4 nanocrystal-based films exhibited enhanced charge storage behavior compared to untemplated nanocrystals, again demonstrating the efficacy of the electrode architecture.²⁵ Moreover, we demonstrated high synthetic tunability where the mesoporosity could be tuned by varying the polymer template, and the microporosity could be tuned by varying the size of the nanocrystal. Other recent studies show that this method also works with polymers containing non-PEO polar blocks.²⁷

While our polymer templated nanocrystal-based mesoporous materials provide an attractive and effective electrode architecture, they will ultimately be limited by electrical conductivity when scaled up to prepare thick electrodes. Therefore, in order to build electrodes with more ideal architectures, we need to integrate a conductor into our materials while still retaining the high surface area and open interconnected porosity. Here, we use solution-phase methods to construct porous conductive scaffolds by templating ITO nanocrystals into mesoporous architectures and subsequently coat the ITO with V_2O_5 via atomic layer deposition (ALD) to produce pseudocapacitor electrode composites. The Rubloff group recently developed and optimized a new ALD V_2O_5 process that resulted in highly conformal and crystalline V_2O_5 films that demonstrated high performance electrochemical energy storage.^{28,29} We use this process to coat porous ITO with two different thicknesses: 2 nm and 7 nm V_2O_5 layers. We also study crystallinity effects in the V_2O_5 layers by heating to various temperatures and examine the pseudocapacitive response.

In addition to our examination of model pseudocapacitor structures, this work allows us to explore some fundamental questions related to pseudocapacitive charge storage. For example, by using two different vanadia film thicknesses, this unique system allows us to explore the kinetics of Li^+ motion into a film. Specifically, we try to answer the question – how thick can a vanadia film be before the charge storage has a significant non-capacitive contribution? The answer should have significant ramifications on the rational design of nanoscale pseudocapacitors.

7.2 Results and Discussion

7.2.1 Synthesis of ITO-V₂O₅ Composites

We previously reported the synthesis of mesoporous ITO nanocrystal-based films.²⁵ Here, we use poly(ethylene-*alt*-propylene)-*block*-poly(ethylene oxide), (PEP-*b*-PEO) as the block copolymer template. ITO nanocrystals capped with amine functional ligands were synthesized according to literature procedures.^{30–32} Next, the as-synthesized nanocrystals were stripped of their ligands using an NOBF₄ treatment to produce bare nanocrystals that were charge-stabilized.²⁶ Figure 7.1b shows a TEM image of ligand-stripped ITO nanocrystals with an average diameter of 4.6 ± 0.4 nm demonstrating they are uniform in shape and size, and free of agglomeration. Ligand-stripped ITO nanocrystals, dispersed in ethanol with ~10% dimethylformamide (DMF) (v/v), were mixed with PEP-*b*-PEO, dissolved in pure ethanol, to prepare the coating solution. Thin-films were then either dip-coated or spin-coated onto clean polar substrates through an evaporation-induced self-assembly process.³³ In solution, the polymer self-assembles to form micelles and, upon evaporation of the solvent, the ITO nanocrystals associate with the polar PEO block to yield a mesostructured organic/inorganic composite. The polymer template was then thermally decomposed by heating the films to 450 °C, resulting in ITO nanocrystal-based mesoporous architectures.

Figure 7.1a shows a low-magnification SEM image of a mesoporous ITO film exhibiting a bimodal porosity with a combination of mesopores, created by the polymer template, and micropores, arising from the nanocrystals embedded in the pore walls. The mesopores, with an average pore size of 15 ± 3 nm, are locally disordered;

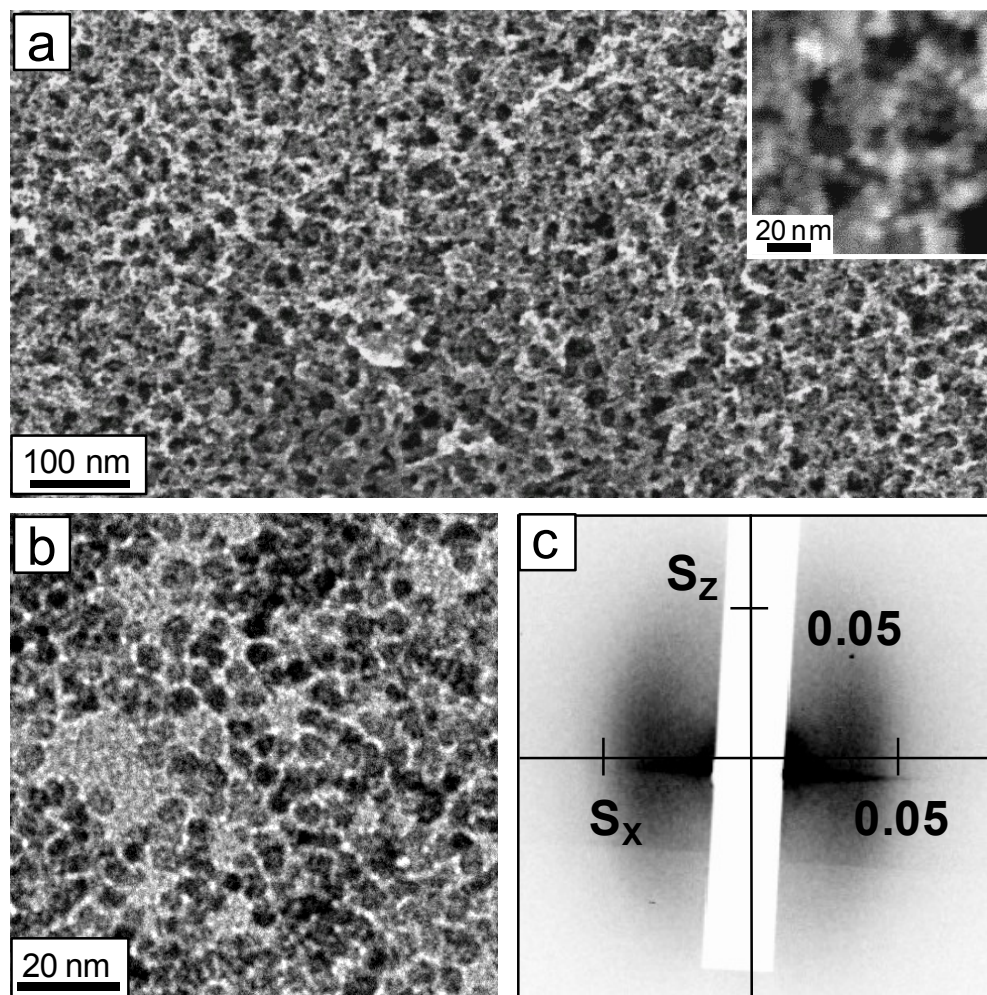


Figure 7.1. (a) Low-magnification SEM image of PEP-*b*-PEO templated ITO nanocrystal-based mesoporous films. Inset: higher-magnification image showing pore walls comprising individual ITO nanocrystals. (b) TEM image of ligand-stripped ITO nanocrystals with an average diameter of 4.6 ± 0.4 nm. (c) 2D-SAXS pattern obtained on a PEP-*b*-PEO templated ITO nanocrystal-based film, collected at an angle of incidence $\beta = 1.25^\circ$. The pattern shows strong in-plane scattering, indicative of a well-defined pore size, but no long range periodicity of the pores. Scattering vector S components are given in 1/nm.

however, they do retain a macroscopically homogeneous porosity. The films are crack-free and maintain open porosity at the surface. A closer look at a high-magnification image (inset of Figure 7.1a) shows individual ITO nanocrystals that comprise the pore walls, which are approximately 1 – 3 nanocrystals thick. Because the nanocrystals do not completely fuse to form a dense wall, the voids between them gives rise to micropores that significantly increase the surface area of the material.

To further characterize the nanoscale architecture we performed two-dimensional small-angle X-ray scattering (2D-SAXS) and ellipsometric porosimetry measurements. Figure 7.1c shows the 2D-SAXS pattern obtained for mesoporous ITO films, collected at an angle of incidence $\beta = 1.25^\circ$. The pattern shows a diffuse ellipsoidal ring with strong in-plane scattering, indicative of a homogenous but non-periodic pore structure with a characteristic pore + wall distance of 32 nm. The porosity of the ITO films was analyzed by ellipsometric porosimetry using toluene as the adsorbate.³⁴ Figure 7.4a shows an adsorption-desorption isotherm for a mesoporous ITO film that exhibits typical type IV behavior.³⁵ The hysteresis present at higher relative pressures is indicative of a mesostructured material with an open interconnected porosity. The adsorption and desorption curves describes the cage and neck sizes of the mesopores. A Kelvin model fit to the isotherm produces pore size distributions centered at 40 nm \pm 20 nm (cages) and 20 nm \pm 10 nm (necks), as shown in Figure 7.4b. The microporosity was determined by fitting a Dubinin-Radushkevich model, producing micropores with an average size of 1 – 2 nm. The data confirm the ITO films exhibit a bimodal porosity that leads to a high surface area with an interconnected open porosity. The isotherm in Figure 7.4a shows a 60% toluene-accessible pore volume. It should be noted that the

average mesopore sizes found by porosimetry (Figure 7.4 a – b) are larger than those determined by 2D-SAXS (Figure 7.1c) and SEM (Figure 7.2 b – c). This variation is a result from different batches of mesoporous ITO films that were produced. In addition, the pore size can be varied by changing the polymer to nanocrystal ratio; therefore, many pores sizes can be made.

The ITO films represent high surface area, porous, conductive scaffolds constructed from ITO nanocrystals. In the next step, we coated the ITO scaffolds with thin-film layers of V_2O_5 via an ALD process.²⁸ ALD is a low temperature thin-film growth technique by which sequentially pulsed precursors are exposed to a surface, leading to predictable monolayer growth with superb uniformity even over demanding topography, such as high-aspect ratio nanostructures.³⁶ In this process, we explored two ALD processes using different oxidants- water and ozone. We also studied two different thicknesses, ~2 nm and ~7 nm V_2O_5 layers controlled by different ALD cycles (see experimental details). The composites were then annealed by a rapid thermal annealing (RTA) process in air at various temperatures allowing us to study the effects of crystallinity in the V_2O_5 layers.

7.2.2 Structure and Electrochemical Properties of 2 nm V_2O_5

Figure 7.2 a – c shows top-view SEM images of smaller-pore ITO films that were coated with a 2 nm layer of V_2O_5 (ozone-based, 100 ALD cycles) as-deposited (Figure 7.2a), heated to 200 °C (Figure 7.2b), and heated to 450 °C (Figure 7.2c). All three composites feature an open porosity with visible mesopores with average diameters of 18 ± 3 nm (Figure 7.2a), 16 ± 3 nm (Figure 7.2b), and 15 ± 3 nm (Figure 7.2c). These values are all equivalent, given the statistical error, and are in agreement with the

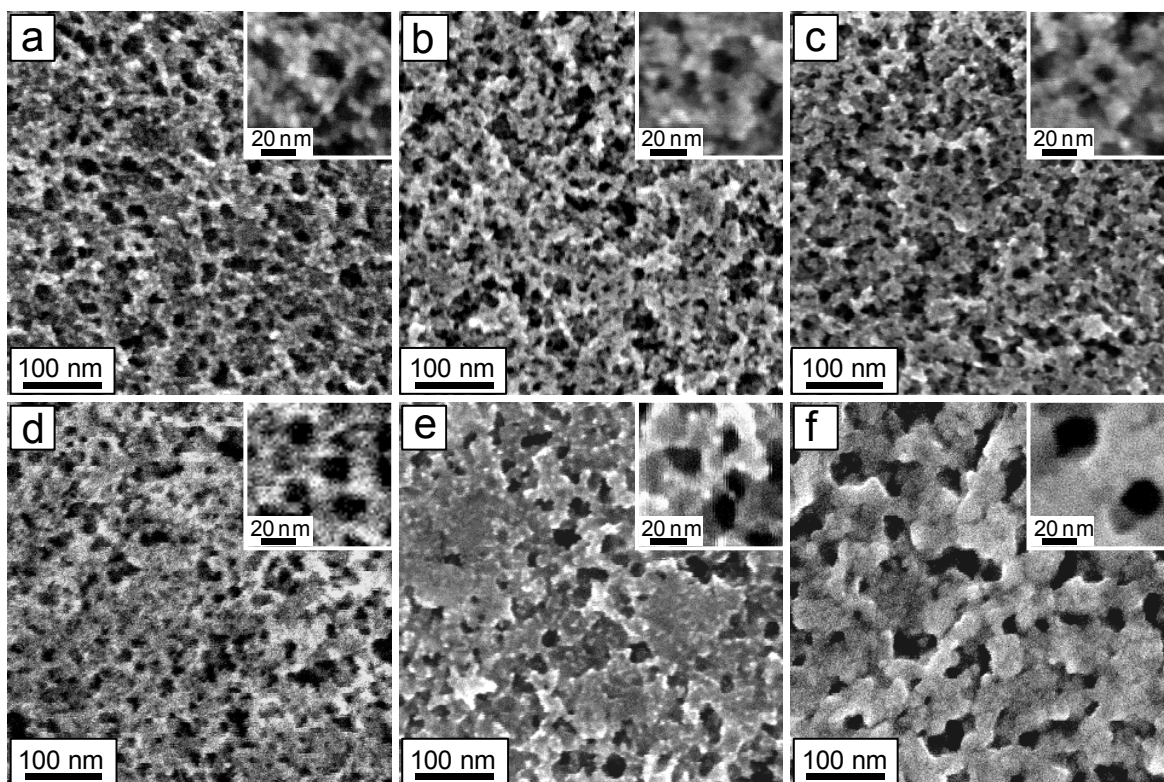


Figure 7.2. (a–c) Low-magnification SEM images of mesoporous ITO films coated with a 2 nm layer of V_2O_5 as-deposited (a) (inset: higher-magnification image showing individually coated nanocrystals); heated to 200 °C (b) (inset: higher-magnification image showing grain growth of the V_2O_5 around the nanocrystals); and, heated to 450 °C (c) (inset: higher-magnification image showing grain growth of the V_2O_5 around the nanocrystals). (d–f) Low-magnification SEM images of mesoporous ITO films coated with a 7 nm layer of V_2O_5 as-deposited (d) (inset: higher-magnification image showing spaces in between nanocrystals are filled in with V_2O_5); heated to 200 °C (e) (inset: higher-magnification image showing grain growth of V_2O_5 leads to partially fused pores); and, heated to 350 °C (f) (inset: higher-magnification image showing grain growth of the V_2O_5 leads to significant loss of mesostructure).

average diameter, 15 ± 3 nm, determined for mesoporous ITO (Figure 7.1a). More importantly is that in the higher-magnification images (insets) of Figure 7.2 a – c, the presence of individually coated nanocrystals is visible demonstrating that this process produces conformal layers around the ITO scaffold. It should be noted, however, that there appears to be some grain growth of the V_2O_5 around the nanocrystals in the layers heated to 200 °C, and the layers heated 450 °C show clear grain growth. These results suggest that as the layers are crystallized at higher temperatures, there is some corresponding grain growth of the V_2O_5 leading to a smaller mesopore pore size and some filling of the micropores.

To further characterize 2 nm V_2O_5 layers we performed X-ray photoelectron spectroscopy (XPS) measurements. Figure 7.3a shows a high-resolution spectrum taken of the V 2p core region for 2 nm layer of V_2O_5 . The binding energies for V 2p_{3/2} and V 2p_{1/2}, observed at 517.3 and 524.6 eV for 2nm V_2O_5 , are in good agreement with reported values of 517.2 and 524.5 eV for V^{5+} in V_2O_5 .³⁷ Deconvolution of the V2p_{3/2} peak reveals that vanadium is found as 91 % in the 5+ valence state (red arrow) and 9 % in the 4+ valence state (blue arrow).

We used ellipsometric porosimetry to analyze the porosity of composites after coating fairly large-pore ITO with 2 nm of V_2O_5 . For this sample, the uncoated porous ITO film showed a pore size distribution for the cages centered at 40 ± 20 nm, and for the necks at 20 ± 10 nm, (Figure 7.4b). Adsorption-desorption isotherms for vanadia coated films heated to 200 °C (Figure 7.4c) and 450 °C (Figure 7.4e) show typical type IV behavior with a hysteresis at higher relative pressures suggesting the composites are mesoporous with an open interconnected porosity. A Kelvin model fit to the isotherms

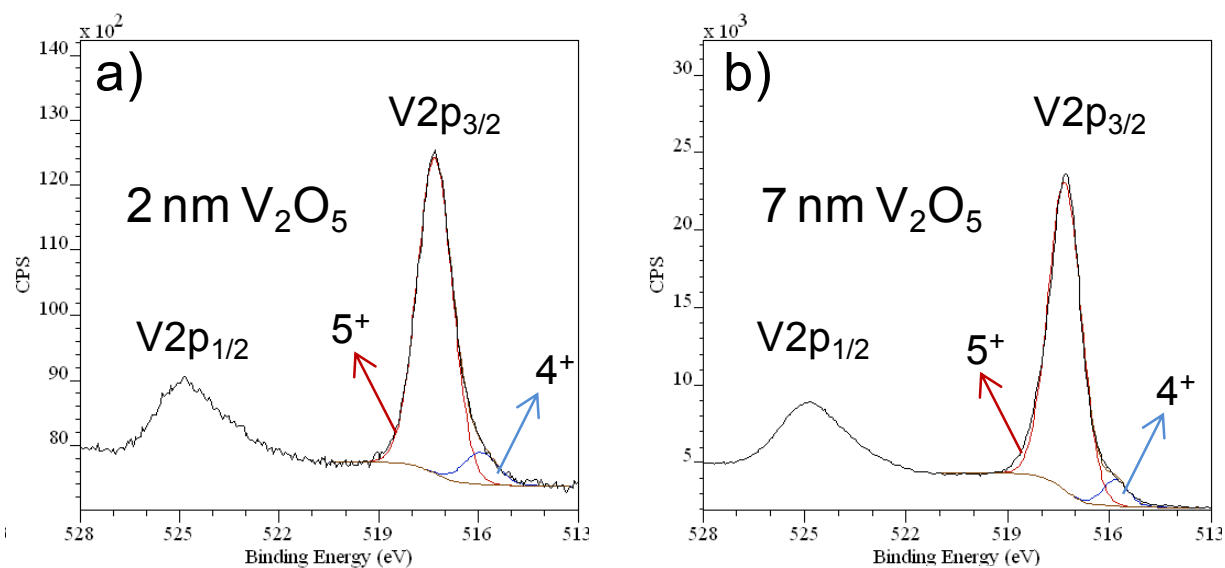


Figure 7.3. XPS spectra for porous ITO films coated with a 2 nm (a) and 7 nm (b) layer of V_2O_5 . The survey scans show the V 2p core regions, with peaks for both $2p_{3/2}$ and $2p_{1/2}$ core levels. The red arrows point to the V^{5+} peak and the blue arrows points to the V^{4+} peak after deconvolution of the $V_2p_{3/2}$ peak.

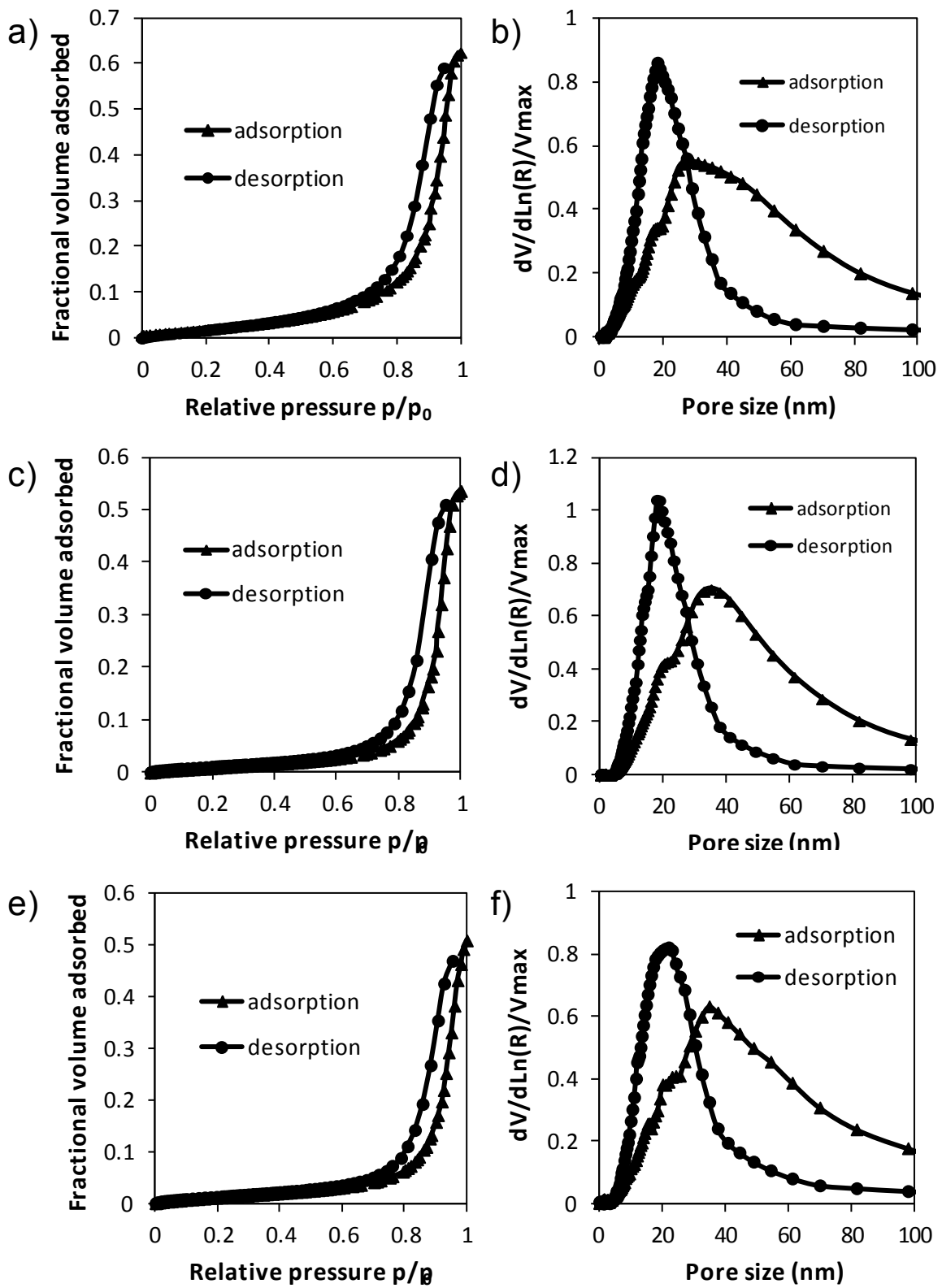


Figure 7.4. Toluene adsorption-desorption isotherms showing characteristic mesoporous behavior for a mesoporous ITO nanocrystal-based film (a), mesoporous ITO film coated with a 2 nm layer of V_2O_5 heated to 200 °C (c), mesoporous ITO film coated with a 2 nm layer of V_2O_5 heated to 450 °C (e). Pore size distribution data obtained from the isotherms for a mesoporous ITO nanocrystal-based film (b), mesoporous ITO film coated with a 2 nm layer of V_2O_5 heated to 200 °C (d), mesoporous ITO film coated with a 2 nm layer of V_2O_5 heated to 450 °C (f).

produces pore size distributions of 36 ± 16 nm (cage) and 18 ± 8 nm (neck) for films heated to 200 °C (Figure 7.4d), and 37 ± 17 nm (cage) and 19 ± 9 nm (neck) for films heated to 450 °C (Figure 7.4f). The overall decrease in the mesopore size is consistent with the fact that the pore walls have been coated with a thin layer of V_2O_5 . The fact that low T and high T samples show the same pores size within error is also consistent with observations from SEM described above. The microporosity was determined by fitting a Dubinin-Radushkevich model, producing micropores with an average size of 1 – 2 nm for both films, suggesting the microporosity is retained after coating the ITO nanocrystals. The isotherms in Figure 7.4 c – e show a 50% toluene-accessible pore volume for both films, which is lower than the pore volume calculated for uncoated ITO of 60%, consistent with ITO that has been coated with a thin layer of V_2O_5 .

Cyclic voltammetry (CV) was performed to examine the charge storage behavior of the 2nm V_2O_5 layers. The Li^+ insertion process can be expressed by $V_2O_5 + xLi^+ + xe^- \leftrightarrow Li_xV_2O_5$, where x represents the mole fraction of inserted lithium ions.³⁸ Figure 7.5a compares the charge storage dependence of 2 nm V_2O_5 heated to 200 and 450 °C at sweep rates in the range between 0.5 – 100 mV/s. In both curves, the capacity increases with decreasing sweep rate indicating that full storage has not been reached, even at the slower sweep rates used here. The V_2O_5 layer heated to 200 °C stores almost twice as much charge than the 2 nm layer heated to 450 °C at all the various sweep rates. Figure 7.5b shows the charge storage dependence of 2 nm V_2O_5 heated to 200 and 450 °C plotted as capacity versus charging times calculated from the various sweep rates in Figure 7.5a. Again, significant differences in the charging behavior are

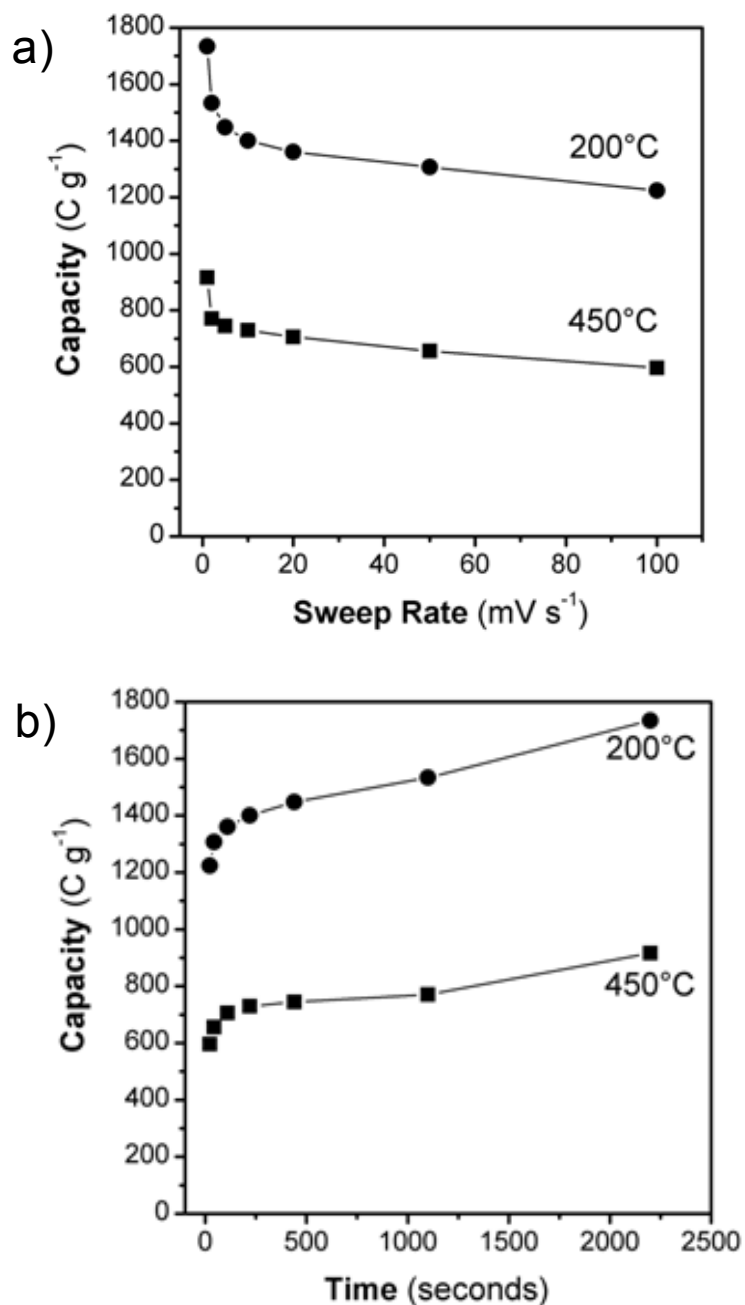


Figure 7.5. (a) Charge storage dependence on sweep rate for mesoporous ITO films coated with a 2 nm layer of V_2O_5 heated to 200 and 450 °C. (b) Comparison of charging rates calculated from cyclic voltammetric data at various sweep rates for mesoporous ITO films coated with a 2 nm layer of V_2O_5 heated to 200 and 450 °C.

observed when comparing the 2 nm V_2O_5 heated to 200 and 450 °C. After a charging time of 200 s, the total charge stored at 200 °C is 1400 C/g, almost twice the amount of charge compared to 450 °C. While the majority of charge is stored in only 200 s, there is an easily measureable increase in capacity going to longer times, again indicating that not all redox sites in these materials are kinetically accessible.

Because the mesoporosity and microporosity of the composites does not change significantly when the V_2O_5 is heated to higher temperatures, as discussed above, it is unlikely that the decrease in the gravimetrically normalized capacity can be attributed to a change in the architecture. Rather, the difference in the capacity observed between films heated to 200 and 450 °C is likely explained by the atomic structure and bonding of the V_2O_5 layer. At 200 °C, the V_2O_5 should have a structure related to the orthorhombic phase, which is known to show facile Li^+ intercalation.³⁹ The material should also be less ordered, which can also increase redox sites.³⁹ When V_2O_5 is heated to 450 °C, a phase transition to the monoclinic crystalline structure occurs in bulk samples, leading to a reduction in Li^+ intercalation sites.⁴⁰ While redox pseudocapacitance is generally assumed to be a surface phenomenon, this data suggest that near-surface intercalation sites also contribute to redox pseudocapacitance and the lack of those near surface sites can cause a dramatic decrease in capacity.

We also investigated the effects of using different oxidants during the ALD process by comparing both water- and ozone-based 2 nm V_2O_5 coatings. Figure 7.6a compares the charge storage behavior in 2 nm V_2O_5 coated ITO synthesized using both water and ozone, and heated to 200 °C, cycled at sweep rates ranging from 0.5 – 100 mV/s. For both water- and ozone-based 2 nm V_2O_5 the capacity increases with

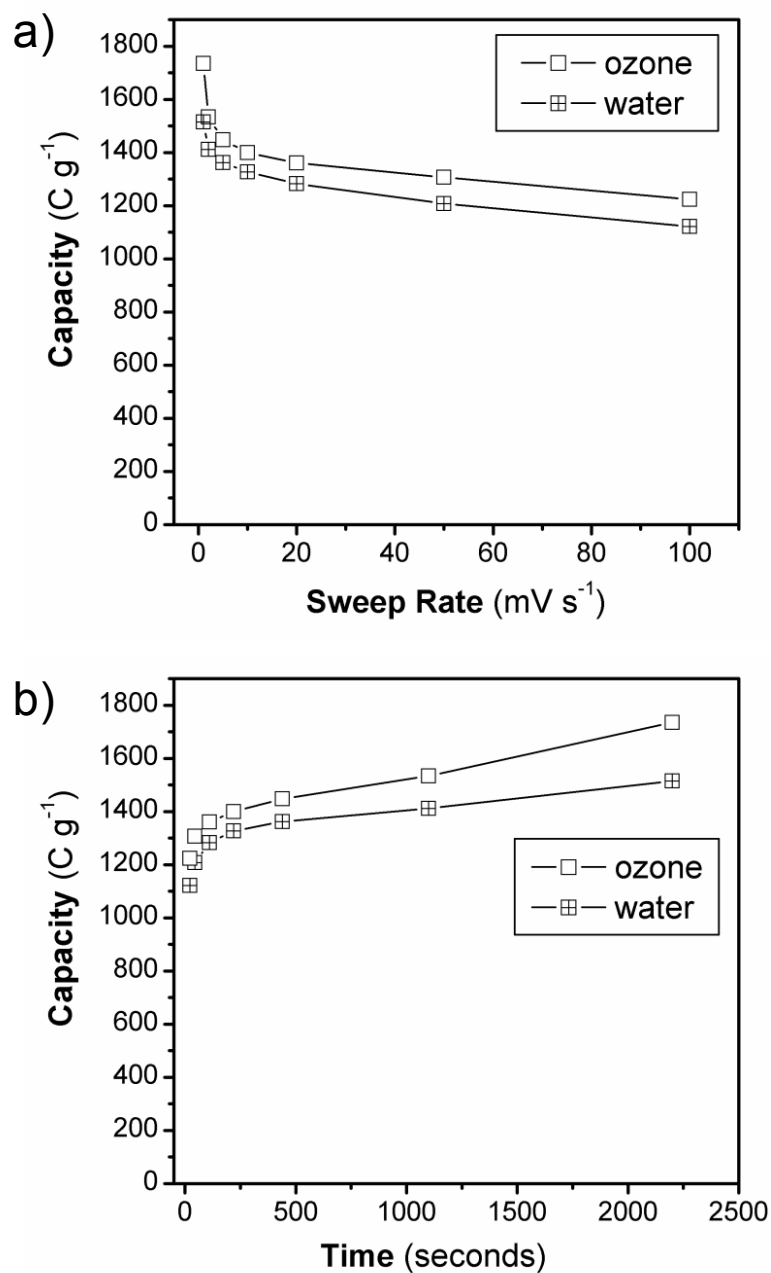


Figure 7.6. (a) Charge storage dependence on sweep rate for porous ITO films coated with a 2 nm of V_2O_5 via ALD using water and ozone as the oxidant, both were heated to 200 °C. (b) Comparison of capacity versus charging times for porous ITO films coated with a 2 nm of V_2O_5 via ALD using water and ozone as the oxidant, both were heated to 200 °C.

decreasing sweep rate, suggesting that full charge storage is not reached in both films, and, there is slow diffusion of Li^+ ions observed in both cases. Figure 7.6b shows the charge storage dependence plotted as capacity versus charging time. Similar trends are observed for both types of films where the gravimetrically normalized capacity increases with charging time. In Figure 7.6b, after a charging time of ~ 200 s, the total charge stored in ozone-based V_2O_5 is ~ 50 C/g larger than water-based V_2O_5 . After ~ 1200 s, the total charge stored in ozone-based V_2O_5 is ~ 100 C/g larger than water-based V_2O_5 . These results suggest that ozone-based V_2O_5 films exhibit better charge storage behavior than water-based V_2O_5 .

7.2.3 Structure and Electrochemical Properties of 7 nm V_2O_5

We also investigated the effects of a thicker (7nm) V_2O_5 layer. Figure 7.2 d – e shows top-view SEM images of porous ITO films that were coated with a 7 nm layer of (ozone-based) V_2O_5 (ozone-based, 250 ALD cycles) as-deposited (Figure 7.2d), heated to 200°C (Figure 7.2e), and heated to 350°C (Figure 7.2f). Figure 7.2d shows that the thicker V_2O_5 has filled most of the micropores while retaining most of the mesopores. When the V_2O_5 layer is heated to 200°C , as shown in Figure 7.2e, all of the micropores are filled and grain growth of V_2O_5 is filling most of the mesopores. In Figure 7.2f, when the V_2O_5 is heated to 350°C the significant amount of grain growth of the V_2O_5 leads to significant loss of mesostructure and most of the pores are clogged. In this case, the 7 nm V_2O_5 layers appear too thick to maintain the bimodal porosity that was retained in the 2 nm V_2O_5 layers. Because significant grain growth was observed by 350°C , these films were not heated hot enough to drive the phase transition to the monoclinic phase

because it was determined that it would not be possible to separate the effects of the phase transition from the effects of grain growth.

We also performed XPS measurements on the 7 nm V_2O_5 layers. Figure 7.3b shows the high-resolution spectrum taken of the V 2p core regions. The binding energies for the V 2p_{3/2} and V 2p_{1/2} peaks observed at 517.3 and 524.7 eV are also in good agreement with reported values for V^{5+} in V_2O_5 , respectively.³⁷ Deconvolution of the V2p_{3/2} peak reveals that vanadium is found as 96 % in the 5+ valence state (red arrow) and 4 % in the 4+ valence state (blue arrow).

Ellipsometric porosimetry was also performed on large-pore ITO coated with 7 nm V_2O_5 . Adsorption-desorption isotherms for films heated to 200 °C (Figure 7.7a) and 300 °C (Figure 7.7c) show typical type IV behavior with a hysteresis at higher relative pressures indicating the films are mesoporous. A Kelvin model fit to the isotherms produces pore size distributions of 45 ± 25 nm (cage) and 18 ± 8 nm (neck) for films heated to 200 °C (Figure 7.4b), and 35 ± 15 nm (cage) and 22 ± 12 nm (neck) for films heated to 300 °C (Figure 7.4d). Interestingly, the mesopore size distributions are slightly larger than those obtained in Figure 7.4 for bare ITO and 2 nm V_2O_5 coated ITO. This can be explained by the fact that in thicker layers, there is more structural rearrangement in the V_2O_5 layer, leading to opening of the pores and resulting in larger pore sizes. The isotherms in Figure 7.4a and c show a ~25 and ~30% toluene-accessible pore volume, which is lower than the pore volume calculated for uncoated ITO (60%, Figure 7.4a) and 2 nm V_2O_5 coated ITO (50%, Figure 7.4 c and e), consistent with ITO that has been coated with a thicker layer of V_2O_5 . As expected, the microporosity is lost in films coated with thicker vanadia layers.

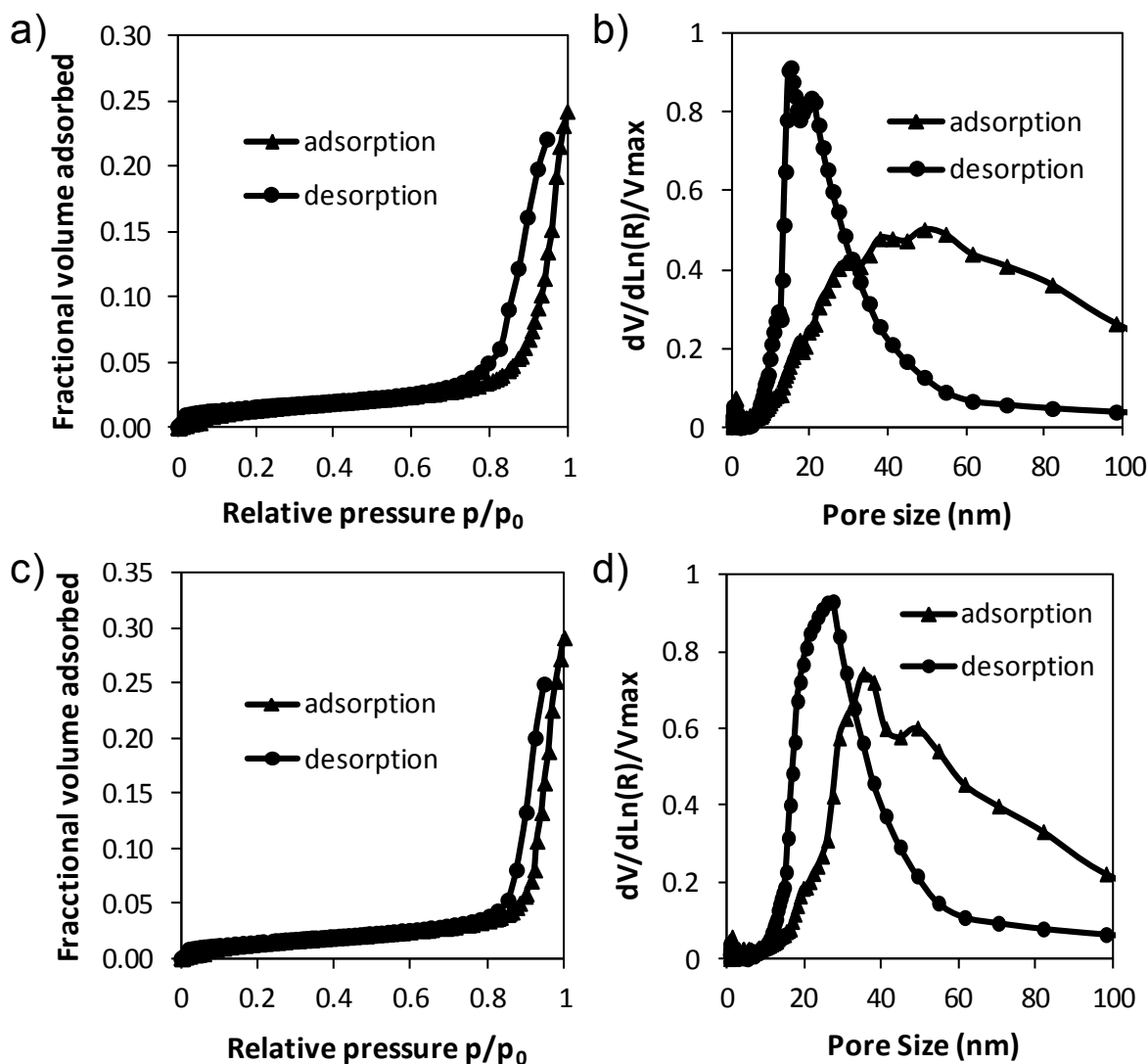


Figure 7.7. Toluene adsorption-desorption isotherms showing characteristic mesoporous behavior for a mesoporous ITO film coated with a 7 nm layer of V_2O_5 heated to 200 °C (a), and a mesoporous ITO film coated with a 7 nm layer of V_2O_5 heated to 300 °C (c). Pore size distribution data obtained from the isotherms for a mesoporous ITO film coated with a 7 nm layer of V_2O_5 heated to 200 °C (b), and a mesoporous ITO film coated with a 7 nm layer of V_2O_5 heated to 300 °C (d).

The charge storage behavior of the 7 nm V_2O_5 layers was also studied by CV. Figure 7.8a compares the charge storage dependence of 7 nm V_2O_5 heated to various temperatures (200, 250, 300, and 350 °C) at sweep rates ranging from 0.5 – 100 mV/s. As with the thinner films, for all temperatures, the gravimetrically normalized capacity increases with decreasing sweep rate, suggesting the V_2O_5 layer is not fully charged because of slow diffusion of Li^+ ions into the structure, even at the slowest sweep rates used here. At all sweep rates, the films heated to 200 °C have the highest capacity and the capacity decreases by half at 250 °C. The capacity is nearly lost at both 300 and 350 °C. Figure 7.8c shows the charge storage dependence plotted as capacity versus charging times at all temperatures. The same trend is observed for all temperatures, where the capacity increases with longer charging times, again suggesting V_2O_5 is not fully charged at shorter charging times due to slow diffusion of Li^+ ions. In Figure 7.8c, after a charging time of ~200 s, the total charge stored at 200 °C is 900 C/g, compared to 600 C/g 250 °C, and ~200 C/g for both 300 and 350 °C.

We also performed CV measurements on flat films of V_2O_5 coated onto flat ITO substrates and heated to the same temperatures (200, 250, 300, and 350 °C). Figure 7.8b compares the charge storage dependence of flat 7 nm V_2O_5 heated to various at sweep rates ranging from 0.5 – 100 mV/s. Interestingly, the capacity at all temperatures is less dependent on the sweep rate for flat films in Figure 7.8b compared to porous films in Figure 7.8a, suggesting that solvent diffusion through the pore system or electrical conductivity in the porous ITO network may contribute to the kinetic limitations. In addition, the capacity is similar at all temperatures to within experimental error, a result that makes sense given that grain growth cannot block pores in a flat film, and

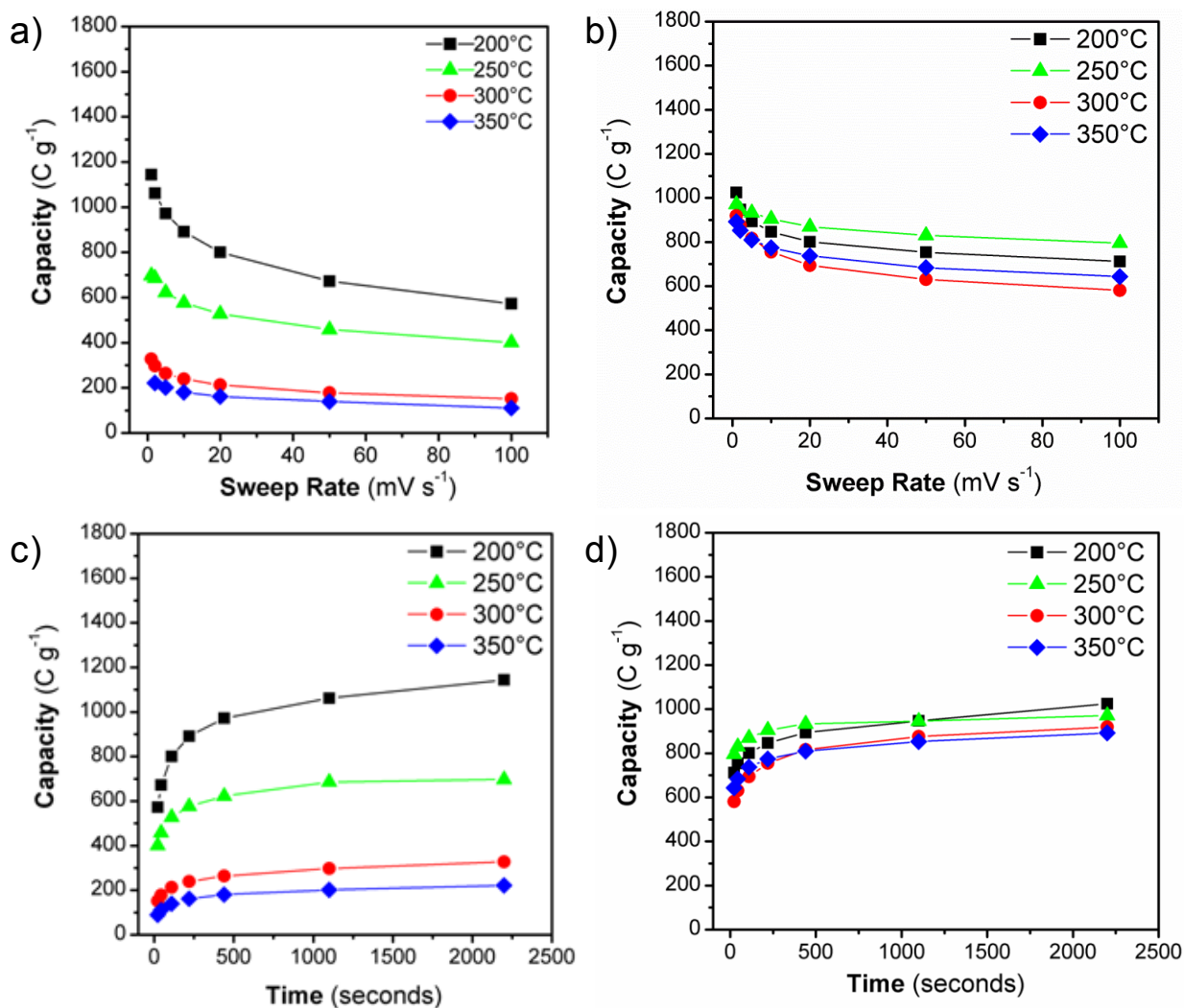


Figure 7.8. (a) Charge storage dependence on sweep rate for mesoporous ITO films coated with a 7 nm layer of V₂O₅ heated to 200, 250, 300 and 350 °C. (b) Charge storage dependence on sweep rate for flat ITO coated with a 7 nm layer of V₂O₅ heated to 200, 250, 300 and 350 °C. (c) Comparison of charging rates calculated from cyclic voltammetric data at various sweep rates for mesoporous ITO films coated with a 7 nm layer of V₂O₅ heated to 200, 250, 300 and 350 °C. (d) Comparison of charging rates calculated from cyclic voltammetric data at various sweep rates for flat ITO coated with a 7 nm layer of V₂O₅ heated to 200 , 250, 300 and 350 °C.

none of these films were heated hot enough to drive a phase transition to the monoclinic phase. Figure 7.8d shows the charge storage dependence plotted as capacity versus charging times for the flat V_2O_5 films. At all temperatures, the V_2O_5 is fully charged by ~200 s, to within experimental error. This suggests the storage of Li^+ ions occurs by fast surface redox reactions at all temperatures, and the kinetic limitations in the porous films result from architectural factors. Similar experiments were also performed on 2 nm V_2O_5 layers on flat ITO heated to 200 and 450 °C. Unfortunately, the mass loading for flat 2 nm V_2O_5 layers was too low to obtain meaningful gravimetrically normalized capacity data. While the data is not included here and cannot be discussed in detail, it is worth noting that the general trend in the data was very similar to the trends observed in figures 7.5 a and c with high temperature sample showing about half the capacity of the low temperature, likely due to a phase transition to a less redox active high T phase.

7.2.4 Pseudocapacitance in ITO- V_2O_5 composites

We follow previously reported work to determine quantitatively the capacitive contribution to the current response by using the voltammetric sweep rate dependence of the total stored charge as shown in Figure 7.5a and Figure 7.8a.⁴¹ In this analysis, the total stored charge can be separated into three components: the faradaic contribution from the Li^+ insertion process, the faradaic contribution from charge transfer processes with surface atoms (referred to as pseudocapacitance),⁴² and the non-faradaic contribution from the double-layer capacitance. In our analysis, the latter two capacitive components are not separated and are both referred to as the capacitive contribution to the total charge, while the remaining charge is referred to as the insertion contribution. The current response (i) at a fixed potential (V) can be described as the

combination of two separate mechanisms, namely surface capacitive effects and (k_1v) and diffusion-controlled Li⁺ insertion ($k_2v^{1/2}$) according to⁴³:

$$i(V) = k_1v + k_2v^{1/2}$$

where v is the sweep rate. By determining both k_1 and k_2 , we can use the above equation to distinguish between the currents arising from Li⁺ insertion and those from capacitive effects, as previously demonstrated.⁴¹

Figure 7.9 shows the total stored charge for mesoporous ITO coated with 2 nm and 7 nm V₂O₅ layers heated to 200 °C at two different sweep rates, 1 and 10 mV/s. The total current or stored charge (total area integrated under the CV curves) is divided into diffusion-controlled and capacitive (non-diffusion) charge storage. In Figure 7.9 a – b and d – e, the shaded area represents the capacitive current and the white area represents the diffusion-controlled current contributions to the total stored charge. The gravimetrically normalized stored charge divided into capacitive (shaded area) and diffusion-controlled (white area) contributions is represented in Figure 7.9c (1 mV/s) and Figure 7.9f (10 mV/s).

At a slow sweep rate of 1 mV/s, 2 nm V₂O₅ features a slightly higher diffusion-controlled capacity (~500 C/g) than 7 nm V₂O₅ (~400 C/g). This can be explained by the higher porosity observed in 2 nm V₂O₅ (Figure 7.4c) compared to 7 nm V₂O₅ (Figure 7.7a), resulting in more accessible redox sites with shorter diffusion path lengths for the electrolyte. In addition, 2 nm V₂O₅ shows a higher amount of total stored charge (~1700 C/g) compared to 7 nm V₂O₅ (~1100 C/g), as well as a higher capacitive charge storage (~1200 C/g) compared to 7 nm V₂O₅ (~700 C/g). These results suggest that there are more redox sites available for fast charge storage in 2 nm V₂O₅, likely due to a higher

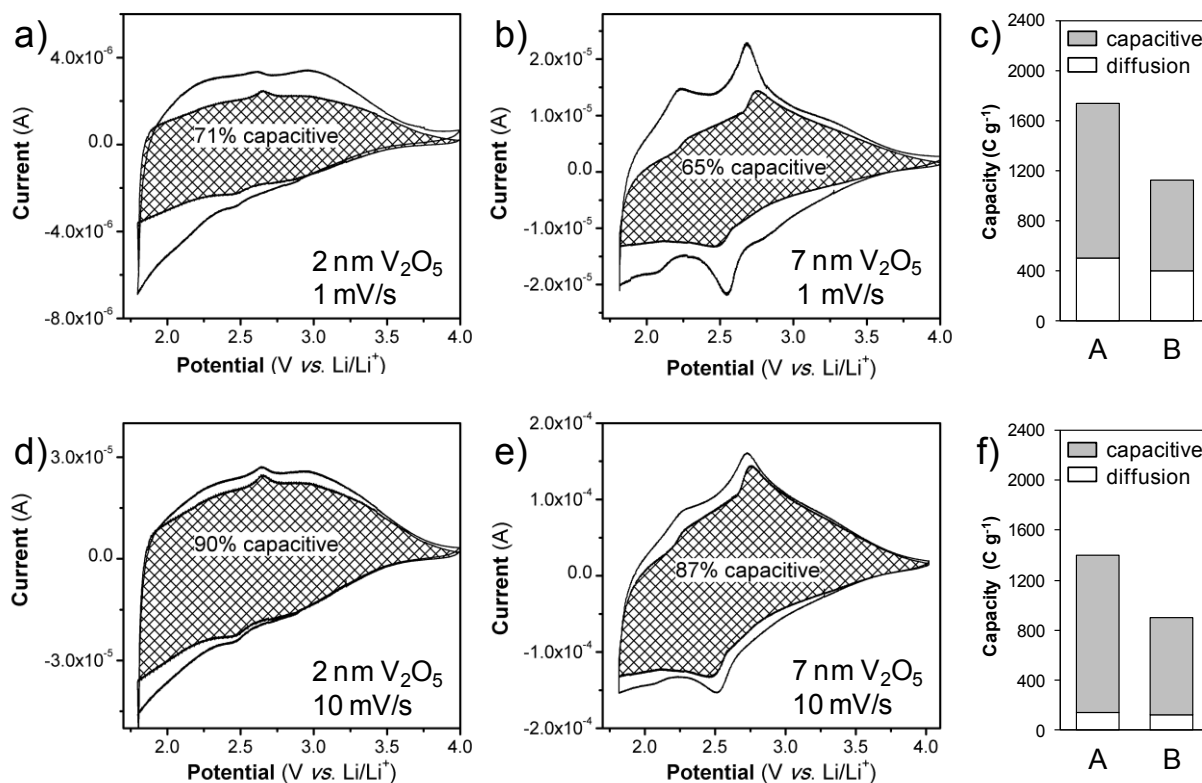


Figure 7.9. Cyclic voltammetric responses for porous ITO films coated with 2 nm (a) and 7 nm (b) layer of V_2O_5 heated to $200^\circ C$ at sweep rates of 1 mV/s. Cyclic voltammetric responses for the same films, 2 nm (d) and 7 nm (e) layer of V_2O_5 , at sweep rates of 10 mV/s. The capacitive contribution to the current is represented as the shaded area. Corresponding comparison of the total stored charge at sweep rates of 1 (c) and 10 (f) mV/s, where A and B represent 2 and 7 nm layer of V_2O_5 heated to $200^\circ C$.

surface area resulting from a higher pore volume (Figure 7.4c). These results also reveal that the loss of bimodal porosity that is observed in 7 nm V_2O_5 , due to significant grain growth that clogs the pores (Figure 7.2e and Figure 7.7a), both inhibit capacitive charge storage and impede diffusion-controlled processes.

Figure 7.9f shows the gravimetrically normalized capacities for 2 and 7 nm V_2O_5 cycled at a faster sweep rate (10 mV/s). The capacitive stored charge is unaffected by the increase in sweep rate leading to similar values. This can be explained by the presence of both double-layer and pseudocapacitive processes that are not kinetically limited. By contrast, the slow diffusion of Li^+ ions into V_2O_5 leads to a significant reduction in the diffusion-controlled contribution to the total stored charge; this can be attributed to Li^+ ions having less time to diffuse into the V_2O_5 network. Therefore, the capacitive contribution to the total stored charge or is greater for both 2 and 7 nm V_2O_5 compared to the contribution from diffusion-controlled mechanisms. Overall, these results demonstrate that both 2 and 7 nm V_2O_5 layers allow for high rate charging/discharging, as seen by the fact that 90% and 87% of the total stored charge is coming from capacitive contributions at a faster sweep rate.

A comparison of the CV curves in Figure 7.9 a – b and d – e reveals that the total stored charge (area under CV curve, not gravimetrically normalized) is greater for 7 nm V_2O_5 compared to 2 nm V_2O_5 . Moreover, the fact that 7 nm V_2O_5 shows much lower gravimetrically normalized charge storage at both slow and fast sweep rates compared to 2 nm V_2O_5 suggests that the grain growth that clogs the pores blocks electrolyte access to the V_2O_5 and only some fraction of the film near the liquid interface is electrochemically active. This was demonstrated by the significant decrease in surface

area and porosity that was observed by SEM and porosimetry experiments. Therefore, because only a fraction of the 7 nm V_2O_5 at the surface is storing charge, overall, 7 nm V_2O_5 must be storing more charge in the lattice. If we look at the shape of CVs for 2 nm versus 7 nm V_2O_5 , there are more defined redox peaks for 7 nm V_2O_5 suggesting the structure is more ordered and features more specific redox sites in the V_2O_5 lattice.

To further investigate the rate capability of the ITO- V_2O_5 composites, we examine the normalized capacity versus sweep rate for all conditions as shown in Figure 7.10a. For each curve, the capacity is normalized by setting the total stored charge to a value of 1.0. The 2 nm layer heated to 200 °C shows the best rate capability, followed by 2 nm V_2O_5 heated to 450 °C. Interestingly, 7 nm V_2O_5 heated to 250 °C shows better rate capability than 200 °C, followed by 300 and 350 °C. If we recall in Figure 7.8a, 7 nm V_2O_5 heated to 200 °C showed higher capacity at all sweep rates. This suggests that heating 7 nm V_2O_5 to 250 °C leads to structural rearrangement or ordering of bonds that improves the diffusion of Li^+ ions into the V_2O_5 network, but also leads to grain growth that blocks access to some of the pores.

Figure 7.10b compares the charge storage and rate capability of mesoporous ITO coated 2 nm and 7 nm layer of V_2O_5 , bare mesoporous ITO, and ITO- V_2O_5 composites including the mass loading for both ITO and V_2O_5 . As expected, the bare mesoporous ITO electrode shows very high rate capability but low gravimetrically normalized capacity and capacitance arising only from the electrical double-layer. When the mass of mesoporous ITO scaffold is included in the calculated gravimetrically normalized capacity and capacitance, as expected, the amounts decrease significantly since both 2 nm and 7 nm V_2O_5 layers account for only a small fraction of the total

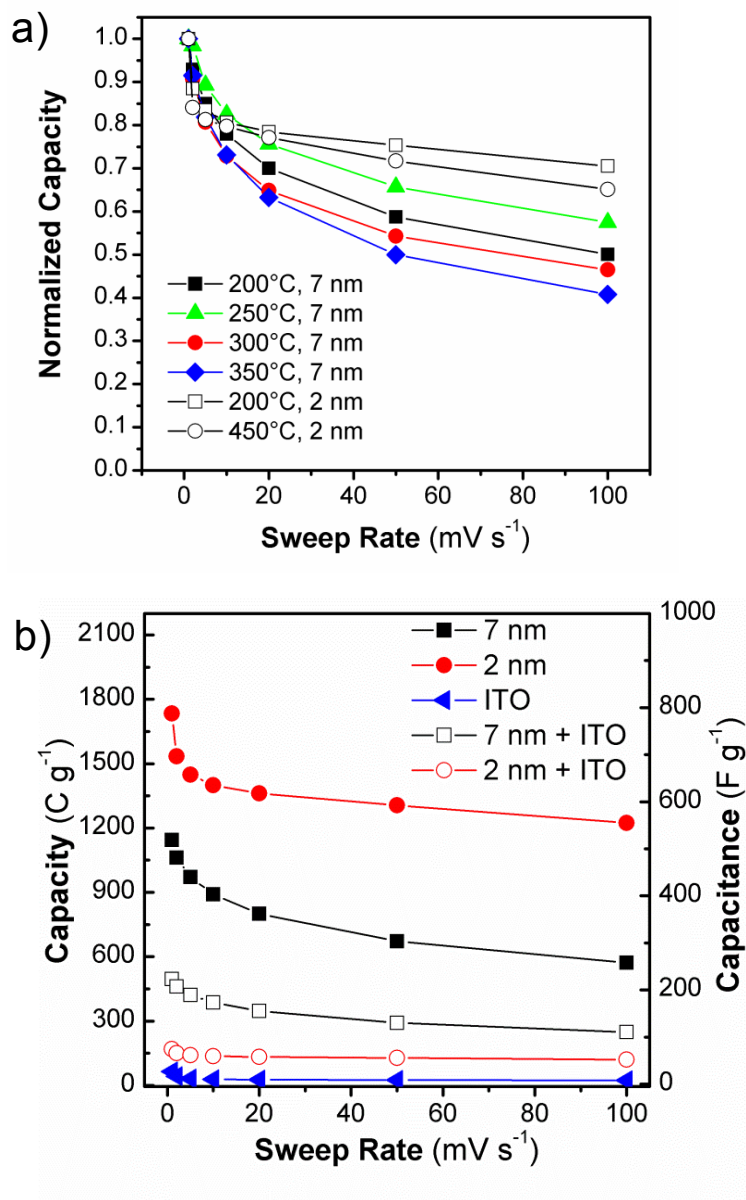


Figure 7.10. (a) Comparison of normalized capacity versus sweep rate calculated from cyclic voltammetric data at various sweep rates for porous ITO coated with a 2 nm and 7 nm layer of V₂O₅ via ALD heated to various temperatures. (b) Comparison of the rate capability of porous ITO coated with a 2 nm and 7 nm layer of V₂O₅, bare mesoporous ITO, and ITO-V₂O₅ composites including the mass loading for both ITO and V₂O₅.

electrode mass. The 2 nm ITO- V_2O_5 composite shows better rate capability than the 7 nm ITO- V_2O_5 composite which can be attributed to having a higher surface area that is accessible to the electrolyte. As discussed above, the surface area and pore volume decreases significantly for the 7 nm V_2O_5 layers. It should be noted, however, that the capacity at all sweep rates is about twice as high for the 7 nm ITO- V_2O_5 composite compared to the 2 nm ITO- V_2O_5 , stemming from the fact that the thicker layer has a higher V_2O_5 mass loading.

While the mass normalized capacities that include the ITO mass are not particularly high, it is important to note that this is not meant to be a commercial battery system, but rather a proof-of-concept exploration of architecture. The mass of ITO, which includes two heavy elements, is anomalously high for a conductor, so its total effect on the mass normalized capacity is disproportionately high. The more important results of this work are an increased understanding of the important factors needed to design a core-shell porous network for pseudocapacitive charge storage.

7.3 Conclusions

Herein, we have designed a new nanoscale pseudocapacitor architecture, constructed using templating of conducting ITO nanocrystals to form a high surface area mesoporous scaffold, followed by coating these porous conductors with a redox-active layer of V_2O_5 to produce nanoporous composites for pseudocapacitive energy storage. By varying the thickness of the V_2O_5 layer as well as the extent of crystallization through various annealing temperatures, the charge storage behavior and rate capability of the composites was examined. Thin V_2O_5 layers (2 nm) feature on

open interconnected porosity and a high surface area, leading to charge storage arising from capacitive processes. Thicker layers showed increased capacity on an area normalized basis, but reduced capacity on a mass normalized basis, indicating that not all of the material in the thick films was accessible to the electrolyte.

The crystal structure was also found to play a role in the charge storage behavior in our composites. In general, modest heating to crystallize the V_2O_5 to the orthorhombic phase ($\sim 250^\circ\text{C}$) led to higher pseudocapacitance. Heating V_2O_5 to temperatures high enough to form a monoclinic phase ($>400^\circ\text{C}$) led to a decrease in total charge storage and rate capability. In thick porous layers, heating V_2O_5 led to significant grain growth that blocked access of the electrolyte to the redox sites, which led to a significant drop in capacity. However, the capacity of flat V_2O_5 films did not decrease with heating. Therefore, it was not possible to separate grain growth effects from crystal structure effects in thick porous layers.

Taken together, these results provide significant insight on the design of pseudocapacitive materials using a core-shell architecture. Thin shells retain the high surface area of the host conductor and show good kinetics, but the total mass loading of redox active material is not high. Thicker films solve the problem of low mass loading, and if the crystal structure is optimized for Li^+ insertion, near surface redox sites several nm into the material can show fast redox kinetics. Thick films in a core-shell structure can lead to a loss of surface area and pore access, however, and have significant potential for grain growth and structural rearrangement upon thermal processing. To construct an ideal architecture, the initial conductive scaffold must be designed so that

thick films can lead to materials that combine high active mass loading with microporosity (for high surface area) and high conductivity.

While the electrodes discussed here are based on thin-films with a modest mass loading of active material, the significance of our study here emphasizes the importance of the crystal structure of the active material as well as the architecture of the electrode, and, how these features affect pseudocapacitive charge storage. Based on our findings, an ideal pseudocapacitor architecture features a high surface area conductor that is coated with an moderately thick layer of active material to form a high surface area core-shell structure that exhibits an open interconnected porosity. In the vanadia system, the layer should be thick enough to allow formation of the orthorhombic phase while maintaining the high surface area of the porous conductor, and in our system, the layer should be between 2 – 7 nm. By applying these fundamental design rules, it may become possible to build pseudocapacitor materials that will achieve high charge storage while maintaining fast charging/discharging kinetics.

7.4 Experimental

7.4.1 Materials

The following chemicals were purchased and used as received: oleylamine (90% Aldrich), oleic acid (90%, Aldrich), indium acetylacetonate (99.99+%, Aldrich), tin bis(acetylacetonate) dichloride (98%, Aldrich), nitrosonium tetrafluoroborate (95%, Aldrich), Vanadium tri-isopropoxide, (96%, Alfa Aesar). Poly((ethylene-*alt*-propylene)-*block*-poly(ethylene oxide), with a mass ratio of PEP(3900)-*b*-PEO(4000), a block ratio of PEP₅₆-*b*-PEO₉₁, and with a PDI = 1.05, was synthesized using reported methods.^{44,45}

Briefly, polyisoprene was grown by anionic polymerization, terminated with an -OH group and then hydrogenated over Pd/C. The resulting PEP-OH was subsequently extended by anionic polymerization of ethylene oxide.

7.4.2 Synthesis and Ligand-exchange of Nanocrystals

Previously reported procedures were followed to synthesize 7–8 nm and 4–5 nm ITO nanocrystals that were stabilized by either oleylamine or oleic acid ligands.⁴⁶⁴⁷⁴⁸ All as-synthesized nanocrystals were purified and dispersed in hexane (10–15 mg/mL). To carry out the ligand-exchange process, as-synthesized nanocrystals were treated with NOBF₄ according to a recently reported procedure.²⁶ In a typical ligand-exchange reaction, 5 mL of nanocrystal dispersion in hexane was combined with 5 mL of NOBF₄ solution in N, N-dimethylformamide (DMF) (10 mg/mL) with stirring (5 min), or until the nanocrystals were transferred to the DMF phase. The nanocrystals were precipitated with toluene then centrifuged, followed by multiple washings with DMF/toluene. The ligand-stripped nanocrystals were dispersed in DMF/ethanol (1:10 v/v) to give a final concentration of 15–20 mg/mL.

7.4.3 Synthesis of Mesoporous Nanocrystal-based Films

The synthesis of mesoporous ITO nanocrystal-based films was previously reported.²⁵ Briefly, in a typical synthesis, 40 mg of the desired diblock copolymer was dissolved in 0.5 mL of ethanol with gentle heating. To this solution, 3 mL of the desired nanocrystals in DMF/ethanol (20 mg/mL) was added. From this mixture, thin films were produced by dip-coating onto polar substrates at a constant withdrawal rate of 1–10 mm/s with a constant 30% relative humidity. Thin films were also prepared by spin-coating onto polar substrates at 1000 to 2000 rpm for 60 s. The films were dried using

a 3 h ramp up to 175 °C, followed by a 3 h soak. Thermal decomposition of the template was done after the drying step using a 6 h ramp from 175 °C to 450 °C, followed by a 3 h soak.

7.4.4 Synthesis of V₂O₅-ITO composites

The ALD V₂O₅ process was performed in a commercial BENEQ TFS 500 reactor, which has a base pressure of 2 mbar. Vanadium tri-isopropoxide, VO(OC₃H₇)₃, was used as the vanadium precursor, which was kept at 45°C giving a vapor pressure of ~0.29 torr. Ozone or water was used as the oxidant. O₃ with 18wt% was generated from pure O₂ source by a MKS O3MEGA ozone delivery system. Ozone ALD was done at 170 °C while water ALD was done at 120 °C. The film thickness was measured ex-situ using a SOPRA GES5 spectroscopic ellipsometer. The 2 and 7 nm V₂O₅ film was done with 100 and 250 ALD cycles respectively. One ALD cycle includes 0.5 s VTOP pulse, 1 s N₂ purge, 2 s oxidant pulse and 1 s N₂ purge. After coated with V₂O₅, the ITO films were post-annealed in oxygen for 60 s using an AG Associates 410 rapid thermal annealer at 200, 250, 300, 350 and 450 °C.

7.4.5 Methods

Transmission electron microscopy (TEM) images were obtained using an FEI/PHILIPS CM120 electron microscope operating at 120 kV. Scanning electron microscopy (SEM) images were obtained using a JEOL model 6700F electron microscope with beam energy 5 kV. 2D small-angle X-ray scattering (2D-SAXS) data were collected at the Stanford Synchrotron Radiation Laboratory using beamline 1-4 using the Rayonix165 large angle CCD detector. All measurements were performed in reflection geometry. XPS analysis was performed using a Kratos Axis Ultra DLD with a

monochromatic (K_{α} radiation) source. The charge neutralizer filament was used to control charging of the sample. A 20 eV pass energy was used with a 0.05 eV pass energy. Scans were calibrated using the C 1s peak shifted to 294.8 eV. Ellipsometric porosimetry was performed on a PS-1000 instrument from Semilab using toluene and as the adsorbate. A UV–visible CCD detector adapted to a grating spectrograph analyzes the signal reflected by the sample. The light source is a 75 W Hamamatsu Xenon lamp and measurements were performed on the spectral range from 1.24–4.5 eV. Data analysis was performed using the associated WinElli II software with the assumption of slit-like pores. If the actual pores are closer to cylindrical, the real pores sizes will be slightly larger than the values reported here. Data is fit with a contact angle of zero for the solvent. Electrochemical measurements were carried out in a three-electrode cell using a PAR EG&G 273A potentiostat in an argon-filled glovebox, with oxygen and water levels <1 ppm. The working electrode consisted of ITO glass upon which ITO- V_2O_5 films were deposited. The electrolyte solution used was 1.0 M $LiClO_4$ in propylene carbonate (PC) and lithium metal foils were used as the counter and reference electrodes. Cyclic voltammetry was performed using cutoff voltages at 4 and 1.8 V vs. Li/Li^+ .

7.5 References

- ¹ Conway, B. E.; Pell, W. G. Double-layer and Pseudocapacitance Type of Electrochemical Capacitors and their Applications to the Development of Hybrid Devices. *J. Solid State Electrochem.* **2003**, 7, 637–644.
- ² Miller, J. R.; Simon, P. Electrochemical Capacitors for Energy Management. *Science* **2008**, 321, 651–652.
- ³ Nam, K.-W.; Lee, C.-W.; Yang, X.-Q.; Cho, B. W.; Yoon, W.-S.; Kim, K.-B. Electrodeposited Manganese Oxides on Three-Dimensional Carbon Nanotubes Substrate: Supercapacitive Behavior in Aqueous and Organic Electrolytes. *J. Power Sources* **2002**, 188, 323–331.
- ⁴ Reddy, A. L. M.; Ramaprabhu, S. Nanocrystalline Metal Oxides Dispersed Multiwalled Carbon Nanotubes as Supercapacitor Electrodes. *J. Phys. Chem. C* **2007**, 111, 7727–7734.
- ⁵ Zhao, X.; Hayner, C. M.; Kung, H. H. Self-Assembled Lithium Manganese Oxide Nanoparticles on Carbon Nanotubes or Graphene as High-Performance Cathode Material for Lithium-Ion Batteries. *J. Mater. Chem.* **2011**, 21, 17297–17303.
- ⁶ Sathiya, M.; Prakash, A. S.; Ramesha, K.; Tarascon, J.-M.; Shukla, A. K. V₂O₅-Anchored Carbon Nanotubes for Enhanced Electrochemical Energy Storage. *J. Am. Chem. Soc.* **2011**, 133, 16291–16299.
- ⁷ Chen, Z.; Augustyn, V.; Wen, J.; Zhang, Y.; Shen, M.; Dunn, B.; Lu, Y. High-Performance Supercapacitors based on Intertwined CNT/V₂O₅ Nanowire Nanocomposites. *Adv. Mater.* **2011**, 23, 791–795.

-
- ⁸ Kim, I.-H.; Kim, J.-H.; Cho, B.-W.; Kim, K.-B. Pseudocapacitive Properties of Electrochemically Prepared Vanadium Oxide on Carbon Nanotubes Film Substrate. *J. Electrochem. Soc.* **2006**, *153*, A1451–A1458.
- ⁹ Chen, W.; Li, S.; Chen, C.; Yan, L. Self-Assembly and Embedding of Nanoparticles by In Situ Reduced Graphene for Preparation of a 3D Graphene/Nanoparticle Aerogel. *Adv. Mater.* **2011**, *23*, 5679–5683.
- ¹⁰ Wang, D.; Kou, R.; Choi, D.; Yang, Z.; Nie, Z.; Li, J.; Saraf, L. V.; Hu, D.; Zhang, J.; Graff, G. L.; Liu, J.; Pope, M. A.; Aksay, I. A. Ternary Self-Assembly of Ordered Metal Oxide-Graphene Nanocomposites for Electrochemical Energy Storage. *ACS Nano* **2010**, *4*, 1587–1595.
- ¹¹ Wang, H.; Casalongue, H. S.; Liang, Y.; Dai, H. Ni(OH)₂ Nanoplates Grown on Graphene as Advanced Electrochemical Pseudocapacitor Materials. *J. Am. Chem. Soc.* **2010**, *132*, 7472–7477.
- ¹² Yu, G.; Hu, L.; Liu, N.; Wang, H.; Vosgueritchian, M.; Yang, Y.; Cui, Y.; Bao, Z. Enhancing the Supercapacitor Performance of Graphene/MnO₂ Nanostructured Electrodes by Conductive Wrapping. *Nano Lett.* **2011**, *11*, 4438–4442.
- ¹³ Zhang, H.; Yu, X.; Braun, P. V. Three-Dimensional Bicontinuous Ultrafast-Charge and -Discharge Bulk Battery Electrodes. *Nat. Nanotech.* **2011**, *6*, 277–281.
- ¹⁴ Lang, X.; Hirata, A.; Fujita, T.; Chen, M. Nanoporous Metal/Oxide Hybrid Electrodes for Electrochemical Supercapacitors. *Nat. Nanotech.* **2011**, *6*, 232–236.

-
- ¹⁵ Li, J.; Yang, Q. M.; Zhitomirsky, I. Nickel Foam-Based Manganese Dioxide-Carbon Nanotubes Composite Electrodes for Electrochemical Supercapacitors. *J. Power Sources* **2008**, *185*, 1569–1574.
- ¹⁶ McDonough, J. R.; Choi, J. W.; Yang, Y.; La Mantia, F.; Zhang, Y.; Cui, Y. Carbon Nanofiber Supercapacitors with Large Areal Capacitances. *Appl. Phys. Lett.* **2009**, *95*, 243109(1–3).
- ¹⁷ Taberna, P. L.; Mitra, S.; Poizot, P.; Simon, P.; Tarascon, J.-M. High Rate Capabilities Fe₃O₄-Based Cu Nano-Architected Electrodes for Lithium-Ion Battery Applications. *Nat. Mater.* **2006**, *5*, 567–573.
- ¹⁸ Kim, J.-H.; Myung, S.-T.; Sun, Y.-K. Molten Salt Synthesis of LiNi_{0.5}Mn_{1.5}O₄ Spinel for 5V Class Cathode Material of Li-Ion Secondary Battery. *Electrochem. Acta* **2004**, *49*, 219–227.
- ¹⁹ Brezesinski, T.; Wang, J.; Polleux, J.; Dunn, B.; Tolbert, S. H. Templated Nanocrystal-Based Porous TiO₂ Films for Next-Generation Electrochemical Capacitors. *J. Am. Chem. Soc.* **2009**, *131*, 1802–1809.
- ²⁰ Szeifert, J. M.; Feckl, J. M.; Fattakhova-Rohlfing, D.; Liu, Y.; Kalousek, V.; Rathousky, J.; Bein, T. Ultrasmall Titania Nanocrystals and Their Direct Assembly into Mesoporous Structures Showing Fast Lithium Insertion. *J. Am. Chem. Soc.* **2010**, *132*, 12605–12611.
- ²¹ Warren, S. C.; Messina, L. C.; Slaughter, L. S.; Kamperman, M.; Zhou, Q.; Gruner, S. M.; DiSalvo, F. J.; Wiesner, U. Ordered Mesoporous Materials from Metal Nanoparticle-Block Copolymer Self-Assembly. *Science* **2008**, *320*, 1748–1752.

-
- ²² Corma, A.; Atienzar, P.; Garcia, H.; Chane-Ching, J. Y. Hierarchically Mesoporous Doped CeO₂ with Potential for Solar-Cell Use. *Nat. Mater.* **2004**, *3*, 394–397.
- ²³ Deshpande, A. S.; Pinna, N.; Smarsly, B.; Antonietti, M.; Niederberger, M. Controlled Assembly of Preformed Ceria Nanocrystals into Highly Ordered 3D Nanostructures. *Small* **2005**, *1*, 313–316.
- ²⁴ Ba, J. H.; Polleux, J.; Antonietti, M.; Niederberger, M. Non-aqueous Synthesis of Tin Oxide Nanocrystals and Their Assembly into Ordered Porous Mesoporous Structures. *Adv. Mater.* **2005**, *17*, 2509–2512.
- ²⁵ Rauda, I. E.; Buonsanti, R.; Saldarriaga-Lopez, L. C.; Benjauthrit, K.; Schelhas, L. T.; Stefik, M.; Augustyn, V.; Ko, J.; Dunn, B.; Wiesner, U.; Milliron, D. J.; Tolbert, S. H. A General Method for the Synthesis of Hierarchical Nanocrystal-Based Mesoporous Materials. *ACS Nano*, **2012**, *6*, 6386–6399.
- ²⁶ Dong, A.; Ye, X.; Chen, J.; Kang, Y.; Gordon, T.; Kikkawa, J. M.; Murray, C. B. A Generalized Ligand-Exchange Strategy Enabling Sequential Surface Functionalization of Colloidal Nanocrystals. *J. Am. Chem. Soc.* **2011**, *133*, 998–1006.
- ²⁷ Buonsanti, R.; Pick, T. E.; Krins, N.; Richardson, T. J.; Helms, B. A.; Milliron, D. J.; Assembly of ligand-stripped nanocrystals into precisely controlled mesoporous architectures. *Nano Lett.* **2012**, *12*, 3872–3877.

-
- ²⁸ Chen, X.; Pomerantseva, E.; Banerjee, P.; Gregorczyk, K.; Ghodssi, R.; Rubloff, G. Ozone-Based Atomic Layer Deposition of Crystalline V₂O₅ Films for High Performance Electrochemical Energy Storage. *Chem. Mater.* **2012**, *24*, 1255–1261.
- ²⁹ Chen, X.; Zhu, H.; Chen, Y.-C.; Shang, Y.; Cao, A.; Hu, L.; Rubloff, G. MWCNT/V₂O₅ Core/Shell Sponge for High Areal Capacity and Power Density Li-Ion Cathodes. *ACS Nano* **2012**, DOI: 10.1021/nn302417x.
- ³⁰ Giltisrap, R. A.; Capozzi, C. J.; Carson, C. G.; Gerhardt, R. A.; Summers, C. J. Synthesis of a Nonagglomerated Indium Tin Oxide Nanoparticle Dispersion. *Adv. Mater.* **2008**, *20*, 4163–4166.
- ³¹ Choi, S. I.; Nam, K. M.; Park, B. K.; Seo, W. S.; Park, J. T. Preparation and Optical Properties of Colloidal, Monodisperse, and Highly Crystalline ITO Nanoparticles. *Chem. Mater.* **2008**, *20*, 2609–2611.
- ³² Choi, S. I.; Nam, K. M.; Park, B. K.; Seo, W. S.; Park, J. T. Preparation and Optical Properties of Colloidal, Monodisperse, and Highly Crystalline ITO Nanoparticles. *Chem. Mater.* **2008**, *20*, 2609–2611.
- ³³ Lu, Y.; Ganguli, R.; Drewien, C. A.; Anderson, M. T.; Brinker, C. J.; Gong, W.; Guo, Y.; Soyeze, H.; Dunn, B.; Huang, M. H.; *et al.* Continuous Formation of Supported Cubic and Hexagonal Mesoporous Films by Sol-Gel Dip-Coating. *Nature* **1997**, *389*, 364–368.

-
- ³⁴ Baklonov, M. R.; Mogilnikov, K. P.; Polovinkin, V. G.; Dultsev, F. N. Determination of Pore Size Distribution in Thin Films by Ellipsometric Porosimetry. *J. of Vac. Sci. & Tech. B* **2000**, *18*, 1385–1391.
- ³⁵ Gregg, S. J.; Sing, K. S. W. *Adsorption, Surface Area, and Porosity*, 2nd ed.; Academic; London, **1982**.
- ³⁶ George, S. M. Atomic Layer Deposition: An Overview. *Chemical Reviews* **2010**, *110*, 111–131.
- ³⁷ Silversmit, G.; Depla, D.; Poelman, H.; Marin, G. B.; De Gryse, R. Determination of the V2p XPS Binding Energies for Different Vanadium Oxidation States (V^{5+} to V^{0+}). *J. Electron. Spectrosc. Relat. Phenom.* 2004, *135*, 167–175.
- ³⁸ Livage, J. Vanadium Pentoxide Gels. *Chem. Mater.* **1991**, *3*, 578–593.
- ³⁹ Wang, Y.; Takahashi, K.; Lee, K.; Cao, G. Nanostructured Vanadium Oxide Electrodes for Enhanced Lithium-Ion Intercalation. *Adv. Funct. Mater.* **2006**, *16*, 1133–1144.
- ⁴⁰ Talledo, A.; Valdivia, H. Investigation of Oxide (V_2O_5) Thin Films as Electrodes for Rechargeable Microbatteries Using Li. *J. Va. Sci. Technol. A* **2003**, *21*, 1494–1499.
- ⁴¹ Wang, J.; Polleux, J.; Lim, J.; Dunn, B. Pseudocapacitive Contributions to Electrochemical Energy Storage in TiO_2 (Anatase) Nanoparticles. *J. Phys. Chem. C* **2007**, *111*, 14925–14931.
- ⁴² Conway, B. E.; Birss, V.; Wojtowicz, J. The Role and Utilization of Pseudocapacitance for Energy Storage by Supercapacitors. *J. Power Sources* **1997**, *66*, 1–14.

-
- ⁴³ Bard, A. J.; Faulkner, L. R. *Electrochemical Methods: Fundamentals and Applications*; John Wiley and Sons; New York, **1980**.
- ⁴⁴ Hillmyer, M. A.; Bates, F. S. Synthesis and Characterization of Model Polyalkane-Poly(ethylene oxide) Block Copolymers. *Macromolecules* **1996**, *29*, 6994–7002.
- ⁴⁵ Allgaier, J.; Poppe, A.; Willner, L.; Richter, D. Synthesis and Characterization of Poly[1,4-Isoprene-b-(ethylene oxide)] and Poly[ethylene-co-propylene-b-(ethylene oxide)] Block Copolymers. *Macromolecules* **1997**, *30*, 1582–1586.
- ⁴⁶ Llordes, A.; Hammack, A. T.; Buonsanti, R.; Tangirala, R.; Aloni, S.; Helms, B. A.; Milliron, D. J. Polyoxometalates and Colloidal Nanocrystals as Building Blocks for Metal Oxide Nanocomposite Films. *J. Mater. Chem.* **2011**, *21*, 11631–11638.
- ⁴⁷ Choi, S. I.; Nam, K. M.; Park, B. K.; Seo, W. S.; Park, J. T. Preparation and Optical Properties of Colloidal, Monodisperse, and Highly Crystalline ITO Nanoparticles. *Chem. Mater.* **2008**, *20*, 2609–2611.
- ⁴⁸ Giltstrap, R. A.; Capozzi, C. J.; Carson, C. G.; Gerhardt, R. A.; Summers, C. J. Synthesis of a Nonagglomerated Indium Tin Oxide Nanoparticle Dispersion. *Adv. Mater.* **2008**, *20*, 4163–4166.

CHAPTER 8

Conclusions

The work presented here demonstrates that solution-phase methods provide simple yet effective routes to produce highly functional nanostructured materials with good control of the final architecture. The general solution-phase assembly of unique and versatile building blocks, ranging from atomic scale metal chalcogenide molecular precursors to nanometer scale preformed nanocrystals, into complex architectures was accomplished through various solvent-driven chemistries.

Highly soluble molecular precursors were solution-processed and melt-processed using a hard template. The solvent driven assembly process led to architectures that were defined by the dimensions of the porous template. The hydrazine-based molecular precursor method resulted in CuInSe_2 nanotubes and nanowires from single and multiple infiltrations. Because the final architecture was controlled mostly by the wetting of the hydrazine solution along the walls of the template, wire formation does not require that all of the multiple incorporations make use of the same precursor solutions. Therefore, by infiltrating the tubes with a variety of different solutions, it should be possible to construct hetero-structured materials that may exhibit unique properties. Perhaps more importantly, this method should be general to all of the metal chalcogenide semiconductors that can be prepared by this hydrazinium salt chemistry because incorporation and wetting are controlled by hydrazine and not the precursor.

Anisotropic layered organic-inorganic semiconductors were melt-processed into hard templates where the architecture was again dictated by the dimensions of the hard template. Preferential self-assembly of the organic-inorganic layers into highly oriented concentric 2D multilayered arrays was achieved. The embedded semiconductor exhibited charge transport in the direction out-of-plane with respect to the substrate. This simple approach may be extended to other organic-inorganic layered perovskites that are prepared by similar solution/melt processes. But more importantly, the method describes a means to control the crystallographic orientation of these layered materials in porous channels leading to the ability to manipulate the anisotropic conductivity along this orientation. This work could have important implications for a variety of newly designed high-performance devices that rely on materials with anisotropic properties.

The solution-phase assembly of preformed nanocrystals into mesoporous hierarchical architectures by soft templating methods was described. New chemistries using various salts, including NOBF_4 and Et_3OBF_4 , made it possible to strip native ligands off of the surface of colloidal nanocrystals to prepare bare and highly dispersible nanocrystals or building blocks. A broad range of nanocrystals were templated with block copolymers including redox-active metal oxides, conductive metal oxides, and metal-chalcogenide semiconductors. These materials exhibit a bimodal porosity with mesopores, arising from the block copolymer template, and micropores, arising from the nanocrystals embedded in the pore walls. Interestingly, the micropore size can be tuned by changing the size of the nanocrystal and the mesopore size can be tuned by changing the size and chemical nature of the template. Therefore, by tailoring the nanocrystal composition and size, along with the block copolymer template type and

size, the methodology presented here offers a high degree of synthetic and structural control over the final architecture of these materials.

Because the templating process is independent from the chemistry used to synthesize these nanocrystals, the method should be applicable to other metal-oxides, semiconductor or metal nanocrystals that can be ligand-stripped using the described methods. It was demonstrated that these materials retain the properties of the individual nanocrystals in film form. For example, the mesoporous CdSe semiconductor materials retain the quantum confined excitonic features of CdSe nanocrystals as well as reasonable charge carrier transport, confirming that the nanocrystals are electronically interconnected in the film. These types of highly functional materials have the potential to find new and exciting applications in areas from catalysis and photocatalysis to solar energy harvesting, among others.

It was also demonstrated that electrochemical energy storage performance can greatly benefit from these nanocrystal-based mesoporous materials. In particular, the high surface area and open interconnected porosity in these nanoporous materials was found to greatly enhance pseudocapacitance in metal oxide redox-active based nanocrystals. In addition, conductive nanocrystals were assembled into high surface area architectures providing an effective conductive platform that can be coated with a suitable redox-active material by atomic layer deposition. These newly designed composites can be used to answer some very important fundamental questions about pseudocapacitive behavior in redox-active materials. For example, the limitations of film thickness on capacitive charge storage are of great interest in designing the ideal pseudocapacitor. Understanding the dependence of pseudocapacitance on the

morphology and crystal structure of a material can provide information that is key to developing good battery materials.

The nanocrystal-based assembly work described here provides a general and versatile strategy where the combination of synthetically diverse building blocks and complex mesoporous architectures leads to the construction of highly functional materials. This general route should be applicable to many nanocrystals systems for a wide range of applications. In addition, other interesting and more complex synthetic strategies should be possible. For example, assembling more than one type of nanocrystal into a single mesoporous film or filling the pore volume of a mesoporous film with other materials could lead to diverse multifunctional composites that could exhibit novel and/or interesting properties. Hence, the construction of a highly functional mesoporous architecture that combines a semiconductor and metal-oxide may be realized. This synthetic versatility may become more important for developing devices that rely on the intimate contact of various functional components.

Taken together in its entirety, the work presented here follows a universal theme that in order for any building block to be assembled into a desired architecture it must be highly soluble in a suitable solvent that can be solution-processed with a structure directing template. The template is very important because it ultimately dictates the final structure and dimensions of the material. A wide range of templates can be utilized including both hard (i.e. anodic alumina) and soft (diblock copolymer) templates. It should, therefore, be possible to construct more complex architectures if more complex templates are available. The significance of this work is that the solvent-driven processes were found to be general in each case and independent of the make-up of

the building blocks themselves; rather, it was the assembly process itself, in combination with the template, which dictated the final architecture. Therefore, the make-up of the building block, whether it is a compositionally different molecular precursor or nanocrystal, can be varied, leading to architectures with unique properties and/or functionalities.

APPENDIX A

Detailed Experimental Procedures for the Synthesis of Hydrazine-based Metal Chalcogenide Precursors and Templated Nanocrystal-Based Mesoporous Films

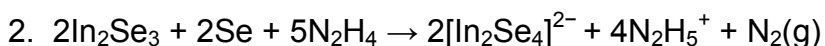
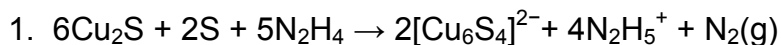
This section describes the detailed experimental procedures for the synthesis of the hydrazine-based CuInSe_2 and Sb_2S_3 precursors as well as the synthesis of templated nanocrystal-based mesoporous films discussed in this dissertation. The first two sections describe the synthesis of the hydrazine-based CuInSe_2 and Sb_2S_3 precursors. The third section describes the synthesis of CdSe nanocrystal-based mesoporous films, including details of the Meerwein's salt (Et_3OBF_4) ligand-exchange process. Finally, the fourth section describes the synthesis of Mn_3O_4 nanocrystal-based mesoporous films, including details of the NOBF_4 ligand-exchange process.

A.1 Detailed Synthesis of the Hydrazine-Based CuInSe_2 Precursor

The hydrazine-based CuInSe_2 precursor was synthesized according to a previously established procedure.¹ The reagents/solvents required for the synthesis are: Cu_2S , S, In_2Se_3 , Se, and anhydrous hydrazine. *Caution: hydrazine is highly toxic and should be handled with appropriate protective equipment to prevent contact with either the vapors or liquid.* All reagents/solvents should be stored inside a glovebox and all procedures should be carried out in a glove box. The hydrazine is clear if it is pure; however, if it is slightly yellow, it is impure and should not be used for the synthesis. The hydrazine reagent bottle comes with a sure seal so it is best to not expose the

hydrazine too much to the box air or it turns slightly yellow over time. The best thing to do is to aliquot 8 mL portions of hydrazine from the reagent bottle into separate 20 mL scintillation vials to keep the hydrazine as clean as possible and use each aliquot for one synthesis reaction.

In a typical synthesis of the hydrazine-based CuInSe_2 precursor, Cu_2S (159 mg, 1.0 mmol), S (64 mg, 2.0 mmol), In_2Se_3 (467 mg, 1.0 mmol) and Se (79 mg, 1.0 mmol) were dissolved in 8 mL of anhydrous hydrazine in a single reaction in a 20 mL scintillation vial and this solution was stirred overnight on a stir plate. The reaction is highly exothermic so the vial should not be sealed completely to allow N_2 gas to evolve. The dissolution reactions are as follows:



The reaction may be scaled down by dissolving Cu_2S (79.5 mg, 0.5 mmol), S (32 mg, 1.0 mmol), In_2Se_3 (233.5 mg, 0.5 mmol) and Se (39.5 mg, 0.5 mmol) in 4 mL of anhydrous hydrazine in a single reaction. The soluble CuInSe_2 precursor in hydrazine formed a yellow-green solution that had some dark green product that crashed out of solution during the synthesis. This dark green product resulted from impurities in the mixture that reacted with hydrazine, therefore, this product was filtered using a PTFE 0.2 μm filter using a plastic syringe. The yellow-green solution is the highly soluble pure hydrazine-based CuInSe_2 precursor. If the solution clogs the filter, the best thing to do is let the mixture sit over night so all the big particles settle down at the bottom of the vial. The next day, the top layer should be free of big particles and then it can be filtered.

If a dry powder is desired for analysis (e.g. XRD, EDX), a small amount of the filtered yellow-green solution can be heated gently to evaporate out the hydrazine. The boiling point of hydrazine is 114 °C, so heating it close to this temperature ensures it evaporates out. *Caution: hydrazine is highly explosive and extra care should be taken when heating hydrazine to high temperatures.* At the bottom of the vial you now have the dry precursor with the formula: $(\text{N}_2\text{H}_5)^+_3 (\text{In}_2\text{Cu}_2\text{Se}_4\text{S}_3)^{3-}$. This dry powder can be re-dissolved in anhydrous hydrazine if desired. The next step is to thermally anneal the dry powder at 350 °C under inert atmosphere for 20 minutes to convert the precursor to CuInSe_2 powder. The thermally annealed CuInSe_2 crystalline powder is metallic in color and is now air stable and can be handled outside of the glovebox.

A.2 Detailed Synthesis of the Hydrazine-Based Sb_2S_3 Precursor

There are two different methods to produce the Sb_2S_3 precursor. The reagents/solvents required for the first method are: Sb_2S_3 , S, and anhydrous hydrazine. The reagents/solvents required for the second method are: Sb, S, and anhydrous hydrazine. *Caution: hydrazine is highly toxic and should be handled with appropriate protective equipment to prevent contact with either the vapors or liquid.* All reagents/solvents should be stored inside a glovebox and all procedures should be carried out in a filled glove box. The hydrazine should be clear if it is pure; however, if it is slightly yellow, it is impure and should not be used for the synthesis. The hydrazine reagent bottle comes with a sure seal so it is best to not expose the hydrazine too much to the box air or it turns slightly yellow over time. The best thing to do is to aliquot 4 mL

portions of hydrazine from the reagent bottle into separate 20 mL scintillation vials to keep the hydrazine as clean as possible and use each aliquot for one synthesis reaction.

In a typical synthesis using the first method: Sb_2S_3 (340 mg, 1.0 mmol) and S (128 mg, 4.0 mmol) were dissolved in 4 mL of anhydrous hydrazine in a single reaction in a 20 mL scintillation vial. In a typical synthesis using the second method: Sb (244 mg, 2.0 mmol) and S (244 mg, 7.0 mmol) were dissolved in 4 mL of anhydrous hydrazine in a single reaction in a 20 mL scintillation vial. The reaction is highly exothermic so the vial was not sealed completely to allow the gas to evolve. The reaction was allowed to sit overnight with stirring. The soluble Sb_2S_3 precursor in hydrazine formed a clear yellow solution. If a dark precipitate forms, it needs to be filtered because it forms from impurities in the mixture that react with hydrazine. Therefore, it should be filtered using a PTFE 0.2 μm filter using a plastic syringe. The yellow solution is the pure highly soluble hydrazine-based Sb_2S_3 precursor.

If a dry powder is desired for analysis (e.g. XRD, EDX), a small amount of the filtered yellow solution can be heated gently to evaporate out the hydrazine. The boiling point of hydrazine is 114 °C, so heating it close to this temperature ensures it evaporates out. *Caution: hydrazine is highly explosive and extra care should be taken when heating hydrazine to high temperatures.* This dry powder can be re-dissolved in anhydrous hydrazine if desired. The next step is to thermally anneal the dry powder at 450 °C under inert atmosphere for 30 minutes to convert the precursor to CuInSe_2 powder. The thermally annealed Sb_2S_3 crystalline powder is metallic in color and is now air stable and can be handled outside of the glovebox.

A.3 Detailed Synthesis of CdSe Nanocrystal-Based Mesoporous Films

A.3.1 Procedure for Meerwein's Salt Ligand-Exchange

This procedure should be applicable to any colloidal nanocrystals that are not stable under oxidative conditions, e.g. main group semiconductors, metal chalcogenides and metals. This procedure is also applicable to all colloidal nanocrystals that are air-stable. Previously reported procedures were followed to synthesize oleate-capped CdSe nanocrystals dispersed in hexane.² To carry out the ligand-exchange process, as-synthesized oleate-capped CdSe nanocrystals were treated with Et₃OBF₄ according to recently reported procedures.^{3,4}

The reagents/solvents required for the ligand-exchange process are: Meerwein's salt (Et₃OBF₄), acetonitrile (MeCN), chloroform and dimethylformamide (DMF). Meerwein's salt should be stored in the glovebox and all the solvents must be dry in order to bring them into the glovebox. For nanocrystals that are not stable under oxidative conditions (e.g. CdSe) all steps must be carried out under inert conditions in a glove box. Make sure all the required materials are brought inside the glovebox ahead of time. In a typical ligand-exchange reaction, Et₃OBF₄ (15 mg, 0.10 mmol) was dissolved in MeCN (1 mL) in a 20 mL scintillation vial. To this solution, the oleate-capped CdSe nanocrystals dispersed in hexanes (1 mL, 1–20 mg/mL) was added to form a biphasic solution. The reaction was scaled accordingly as needed for the amount of nanocrystals that were ligand-exchanged. The vial was sealed properly and this solution was taken out of the glove box and vortexed for several seconds resulting in the precipitation of the nanocrystals from solution. Next, the vial was brought back inside the glovebox and the mixture was transferred to a centrifuge tube. Chloroform (1

mL) was added to the tube and it was brought out of the glovebox and then the solution was centrifuged for 10–15 minutes. The centrifuge tube was brought back inside the glove box and the solution phase was removed and the pelleted nanocrystals were then washed with additional 1 mL chloroform. The resultant “bare” or BF_4^- -stabilized CdSe nanocrystals were dispersed in DMF to give a final concentration of 20 mg/mL. The ligand-stripped nanocrystals were sealed properly, brought out of the glovebox and sonicated for 1–2 hours. Finally, they were brought back into the glovebox and this solution was stored inside the glovebox.

For air-stable nanocrystals, the main difference is that the dissolution of Et_3OBF_4 in MeCN must be carried out inside a glove box, then, this solution can be taken out of the glovebox. The nanocrystals dispersed in hexane can be added to the Et_3OBF_4 in MeCN solution outside of the glovebox. The rest of the steps, vortexing, centrifugation and washing can all be done outside of the glove box. Note that for air-stable nanocrystals that are ligand-stripped, they can be dissolved in a mixture of DMF/ethanol. This can be done after the last chloroform washing step, take the pelleted nanocrystals (e.g. 20 mg of BF_4^- -capped nanocrystals) and dispersed them in 0.2 mL DMF. If the nanocrystals do not disperse in the DMF, heat the centrifuge tube in a water bath at $\sim 60^\circ\text{C}$ for 30 min or until the nanocrystals completely dissolve in the DMF. Once the nanocrystals are completely dissolved in the DMF, 0.8 mL of ethanol can be slowly added until the nanocrystals go into solution. If the nanocrystals crash out during the addition of ethanol, centrifuge them and disperse them again in 0.2 mL DMF under heating. Next, add the 0.8 mL ethanol slowly while keeping the solution $\sim 60^\circ\text{C}$ until all the nanocrystals go into solution. The resulting nanocrystals are now

dispersed in a total of 1 mL of DMF/ethanol (1:5 v/v) to give a final concentration of ~20 mg/mL. The reaction can be scaled accordingly as needed for the amount of nanocrystals that are ligand-exchanged.

Note: the DMF/ethanol ratio can be varied if desired, for example, the nanocrystals can be dispersed in 0.1 mL of DMF and diluted with 0.9 mL of ethanol to give a final ratio of DMF/ethanol (1:10 v/v). The final DMF/ethanol solution must have at least 10 % DMF v/v. There can be solubility problems when insufficient DMF is present, therefore, some trial and error must be done in order to determine the minimum amount of DMF that is required in order to completely dissolve the nanocrystals in a DMF/ethanol mixture.

A.3.2 Procedure for Polymer Templating of CdSe Nanocrystals

In order to template nanocrystals that are not air-stable (e.g. CdSe), a block copolymer that has ether functionalities on both blocks is required because this class of polymer can be degraded under inert conditions. Here, the polymer used is: Poly(butylene oxide)-*b*-poly(ethylene oxide), with a mass ratio of PBO(5000)-*b*-PEO(6500), a block ratio of PBO₉₀-*b*-PEO₁₁₄, and a PDI = 1.09.

The synthesis of mesoporous CdSe nanocrystal-based films was carried out under inert conditions inside a glovebox, including both film deposition and thermal annealing steps. Make sure all the required materials are brought inside the glovebox ahead of time including spin-coater, substrates, pipette, etc. In a typical procedure, 10 mg of the PBO₉₀-*b*-PEO₁₁₄ diblock copolymer was weighed out in a small 4 mL vial outside of the glovebox and this vial was brought inside the glovebox uncapped. Once the vial was inside the glovebox, 0.1 mL of DMF was added to dissolve the polymer.

Next, the vial was capped and brought outside the glovebox and placed on a warm plate with gentle heating overnight.

The next day, the CdSe nanocrystals dispersed in DMF were brought outside of the glovebox and sonicated for 1 hour to produce a good dispersion. After sonication, the CdSe nanocrystals and the dissolved polymer were brought inside the glove box. Next, 1 mL of CdSe nanocrystals dispersed in DMF (20 mg/mL) was added to the dissolved polymer. The mixture was stirred on a warm plate for 30 minutes before film deposition.

From this mixture, thin films were prepared by spin-coating onto desired substrates (silicon, ITO-coated glass, or glass) at 1000 to 2000 rpm for 60 s. A pipette with tip was used to dropcast ~100 μ L of the mixture onto clean substrates and the solution was spread to cover the entire substrate before spinning. Thicker films (~100–150 nm) were prepared at slower speeds, and thinner films at faster speeds (~80–100 nm). The substrates were cleaned before bringing into the glovebox using a KOH base wash and dried using compressed air. Thicker films (~ 1–2 μ m) were also produced by drop-casting onto desired substrates and allowing the solvent to evaporate. The films were then sealed in an air-tight vial and transferred to a glovebox with a furnace. The films were then placed inside the furnace hooked up to a temperature controller. The films were dried using a 3 h ramp up to 175 °C, followed by a 3 h soak. Thermal decomposition of the template was done after the drying step using a 6 h ramp from 175 °C to 400 °C, followed by a 3 h soak. The calcined films were then stored in a sealed vial inside the glovebox.

A.4 Detailed Synthesis of Mn₃O₄ Nanocrystal-Based Mesoporous Films

A.4.1 Synthesis of Mn₃O₄ Nanocrystals

A previously reported procedure was followed to synthesize 4–5 nm Mn₃O₄ nanocrystals.⁵ The reagents/solvents required for the synthesis are: manganese(II) acetate, stearic acid, oleylamine, hexanes, xylenes and ethanol. In a typical synthesis, manganese(II) acetate (0.17 g, 1.0 mmol), oleylamine (3.28 mL or 2.67 g, 10.0 mmol) and stearic acid (0.57 g, 2.0 mmol) were dissolved in 15 mL of xylenes in air atmosphere in a 150 mL round bottom flask. The flask was sealed using a rubber septum stopper and a needle was inserted through the septum to allow pressure to equilibrate. The flask was immersed in an oil bath using a temperature controller connected to a variac. The mixture was stirred and slowly heated to 90 °C for 1 hour. When the mixture reached 90 °C, 1 mL of DI water was injected into the solution under vigorous stirring using a 1mL plastic syringe and needle. The mixture was allowed to age at 90 °C for 3 h. A brown product (Mn₃O₄ nanocrystals) formed at the bottom of the flask which was precipitated with 100 mL of ethanol and centrifuged. The nanocrystals were washed with 5 mL hexanes and precipitated with 25 mL of ethanol and centrifuged again. The washed Mn₃O₄ nanocrystals were dispersed in 10 mL of hexanes and sonicated for 2 hours. The reaction yields about 60 mg of Mn₃O₄ nanocrystals.

A.4.2 Procedure for NOBF₄ Ligand-Exchange

This procedure should be applicable to any colloidal nanocrystals that are stable under oxidative conditions, e.g. metal-oxides like Mn₃O₄ and ITO. To carry out the ligand-exchange process, as-synthesized Mn₃O₄ nanocrystals were treated with NOBF₄ according to a recently reported procedure.⁶

The reagents/solvents required for the synthesis are: oleylamine-capped Mn_3O_4 nanocrystals in hexane, DMF, toluene and NOBF_4 . In a typical ligand-exchange reaction, 60 mg of Mn_3O_4 nanocrystals dispersed in 10 mL of hexane (6 mg/mL) was added to a 20 mL scintillation vial. To this mixture, 10 mL of dimethylformamide (DMF) was added and biphasic mixture was formed with the clear DMF phase at the bottom and the brown Mn_3O_4 phase on top. Next, 100 mg of NOBF_4 salt was added to the vial and the mixture was stirred vigorously for (5 min), or until the nanocrystals were transferred to the DMF phase. The mixture was transferred to a centrifuge tube and precipitated with 20 mL of toluene and centrifuged for 10–15 minutes. The $\text{Mn}_3\text{O}_4\text{-BF}_4$ nanocrystals were then redispersed in 1.0 mL of DMF and precipitated with 20 mL toluene and centrifuged again. This washing step was repeated 3 more times to ensure that the nanocrystals are washed from excess ligands. Finally, after the last centrifugation step, the ligand-stripped Mn_3O_4 nanocrystals were dispersed in 0.5 mL DMF. If the nanocrystals do not disperse in the DMF, heat the centrifuge tube in a water bath at $\sim 60^\circ\text{C}$ for 30 min or until the nanocrystals completely dissolve in the DMF. Once the nanocrystals were completely dissolved in the DMF, 2.5 mL of ethanol was slowly added until the nanocrystals go into solution. If the nanocrystals crash out during the addition of ethanol, centrifuge them one more time and disperse them again in 0.5 mL DMF under heating. Next, add the ethanol 0.5 mL at a time while keeping the solution $\sim 60^\circ\text{C}$ until all the nanocrystals go into solution. The resulting nanocrystals are now dispersed in a total of 3 mL of DMF/ethanol (1:6 v/v) to give a final concentration of ~ 20 mg/mL.

Note: the DMF/ethanol ratio can be varied if desired, for example, the nanocrystals can be dispersed in 0.3 mL of DMF and diluted with 2.7 mL of ethanol to give a final ratio of DMF/ethanol (1:10 v/v). The final DMF/ethanol solution must have at least 10 % DMF v/v. There can be solubility problems when insufficient DMF is present, therefore, some trial and error must be done in order to determine the minimum amount of DMF that is required in order to completely dissolve the nanocrystals in a DMF/ethanol mixture.

A.4.3 Procedure for Polymer Templating of Mn_3O_4 Nanocrystals

In order to template nanocrystals that are air-stable (e.g. metal oxides), an amphiphilic diblock copolymer was used. The synthesis of polymer-templated mesoporous nanocrystal-based films of Mn_3O_4 , MnFe_2O_4 and ITO was previously published.⁷ Three different types of block copolymers were used: Poly(butadiene(1,2 addition))-*b*-poly(ethylene oxide), with a mass ratio of PB(5500)-*b*-PEO(5000), a block ratio of PB_{102} -*b*- PEO_{114} , and with a polydispersity index (PDI) = 1.05; Poly(butylene oxide)-*b*-poly(ethylene oxide), with a mass ratio of PBO(5000)-*b*-PEO(6500), a block ratio PBO_{90} -*b*- PEO_{114} , and with a PDI = 1.09; Poly((ethylene-*alt*-propylene)-*block*-poly(ethylene oxide), with a mass ratio of PEP(3900)-*b*-PEO(4000), a block ratio of PEP_{56} -*b*- PEO_{91} , and with a PDI = 1.05. Here, the polymer used is: PEP(3900)-*b*-PEO(4000) or PEP-*b*-PEO to template Mn_3O_4 nanocrystals.

This procedure is applicable to any air-stable metal oxide nanocrystals (e.g. Mn_3O_4 , MnFe_2O_4 and ITO) that have been ligand-exchanged using either Meerwein's salt (Et_3OBF_4) or NOBF_4 that are dispersed in a DMF/ethanol mixture as previously described. Here, 60 mg of BF_4 -capped Mn_3O_4 nanocrystals dispersed in 3 mL of

DMF/ethanol (1:6 v/v) to give a final concentration of ~20 mg/mL was used. In a typical synthesis, 40 mg of PEP-*b*-PEO diblock copolymer was dissolved in 0.35 mL of ethanol in a 4mL vial and placed on a warm plate with gentle heating overnight. To this solution, 3 mL of the Mn₃O₄ nanocrystals in DMF/ethanol (20 mg/mL) was added. This final solution has a total volume of 3.35 mL, therefore, the final concentration of nanocrystals is ~18 mg/mL and the final concentration of polymer is ~12 mg/mL. The mixture was stirred on a warm plate for 30 minutes, then it was filtered using a 0.2 μ m PTFE filter before deposition.

From this mixture, thin films were produced by dip-coating onto polar substrates (silicon, ITO-coated glass, or glass) at a constant withdrawal rate of 1–10 mm/s with a constant 30% relative humidity. The substrates were cleaned using a KOH base wash and dried using compressed air. Thinner films (~80–100 nm) were produced at slower pulling rates and thicker films at faster pulling rates (~100–150 nm). For nanocrystal-based films, it is best to pull at the fastest speed possible or ~4 V to give a film that is ~150 nm thick. If the films looked either cloudy or not homogeneously dried, the humidity was modified between 10 % up to 40 % until good films were produced. Thin films were also prepared by spin-coating onto polar substrates at 1000 to 2000 rpm for 60 s. A pipette with tip was used to dropcast ~100 μ L of the mixture onto clean substrates and the solution was spread to cover the entire substrate before spinning. Thicker films were prepared at slower spinning speeds, and thinner films at faster spinning speeds. Thicker films (~ 1–2 μ m) could be produced by drop casting onto polar substrates and allowing the solvent to evaporate. The films were then placed inside a furnace hooked up to a temperature controller. The films were dried using a 3 h ramp up to 175 °C,

followed by a 3 h soak. Thermal decomposition of the template was done after the drying step using a 6 h ramp from 175 °C to 450 °C followed by a 3 h soak.

Note: in most cases, some optimization of the exact concentration of diblock copolymer and nanocrystals was required for mesostructure optimization. In the case described above, the ratio by mass of nanocrystals to polymer is 60:40 or 1.5; this ratio can be varied accordingly if after film analysis the films do not look porous or are very inhomogeneous. The ratio can be varied from, for example, 60 mg nanocrystals and 60 mg polymer giving a ratio of 1, as well as 80 mg nanocrystals and 40 mg polymer giving a ratio of 2. It is worthwhile to vary the ratio to find the ideal conditions in order to make the best ordered mesoporous films. This includes varying the concentration of nanocrystals from 20 mg/mL up to 30 mg/mL, for example. The conditions described above for PEP-*b*-PEO templated Mn₃O₄ films were found to be the optimal conditions to give good quality films; however, variations are possible depending on the nanocrystals and polymer. Finally, the thermal degradation step will vary accordingly by the block copolymer that is used since each has a different TGA profile.

A.5 References

- ¹ Milliron, D. J.; Mitzi, D. B.; Copel, M.; Murray, C. E. Solution-Processed Metal Chalcogenide Films for p-Type Transistors. *Chem. Mater.* **2006**, *3*, 587–590.
- ² Chan, E. M.; Xu, C.; Mao, A. W.; Han, G.; Owen, J. S.; Cohen, B. E.; Milliron, D. J. Reproducible, High-Throughput Synthesis of Colloidal Nanocrystals for Optimization in Multidimensional Parameter Space. *Nano Lett.* **2010**, *10*, 1874–1885.
- ³ Rosen, E. L.; Buonsanti, R.; Llodes, A.; Sawvel, A. M.; Milliron, D. J.; Helms, B. A.; Exceptionally Mild Reactive Stripping of Native Ligands from Nanocrystal Surfaces by Using Meerwein's Salt. *Angew. Chem. Int. Ed.* **2012**, *51*, 684–689.
- ⁴ Duong, J. T.; Bailey, M. J.; Pick, T. E.; McBride, P. M.; Rosen, E. L.; Buonsanti, R.; Milliron, D. J.; Helms, B. A.; Efficient Polymer Passivation of Ligand-Stripped Nanocrystal Surfaces. *J. Polym. Sci. A Polym. Chem.* **2012**, *50*, 3719–3727.
- ⁵ Yu, T.; Moon, J.; Park, J.; Park, Y. I.; Bin Na, H.; Kim, B. H.; Song, I. C.; Moon, W. K.; Hyeon, T. Various-Shaped Uniform Mn₃O₄ Nanocrystals Synthesized at Low Temperature in Air Atmosphere. *Chem. Mater.* **2009**, *21*, 2272–2279.
- ⁶ Dong, A.; Ye, X.; Chen, J.; Kang, Y.; Gordon, T.; Kikkawa, J. M.; Murray, C. B. A Generalized Ligand-Exchange Strategy Enabling Sequential Surface Functionalization of Colloidal Nanocrystals. *J. Am. Chem. Soc.* **2011**, *133*, 998–1006.
- ⁷ Rauda, I. E.; Buonsanti, R.; Saldarriaga-Lopez, L. C.; Benjauthrit, K.; Schelhas, L. T.; Stefik, M.; Augustyn, V.; Ko, J.; Dunn, B.; Wiesner, U.; Milliron, D. J.; Tolbert, S. H.; General Method for the Synthesis of Hierarchical Nanocrystal-Based Mesoporous Materials. *ACS Nano*, **2012**, *6*, 6386–6399.